NASA/CR—2000-209812

Effects of Thermal and Mechanical Processing on Microstructures and Desired Properties of Particle-Strengthened Cu-Cr-Nb Alloys

Kenneth Reed Anderson
University of California at Davis, Davis, California

February 2000

The NASA STI Program Office . . . in Profile

Since its founding, NASA has been dedicated to the advancement of aeronautics and space science. The NASA Scientific and Technical Information (STI) Program Office plays a key part in helping NASA maintain this important role.

The NASA STI Program Office is operated by Langley Research Center, the Lead Center for NASA's scientific and technical information. The NASA STI Program Office provides access to the NASA STI Database, the largest collection of aeronautical and space science STI in the world. The Program Office is also NASA's institutional mechanism for disseminating the results of its research and development activities. These results are published by NASA in the NASA STI Report Series, which includes the following report types:

- TECHNICAL PUBLICATION. Reports of completed research or a major significant phase of research that present the results of NASA programs and include extensive data or theoretical analysis. Includes compilations of significant scientific and technical data and information deemed to be of continuing reference value. NASA's counterpart of peer-reviewed formal professional papers but has less stringent limitations on manuscript length and extent of graphic presentations.

- TECHNICAL MEMORANDUM. Scientific and technical findings that are preliminary or of specialized interest, e.g., quick release reports, working papers, and bibliographies that contain minimal annotation. Does not contain extensive analysis.

- CONTRACTOR REPORT. Scientific and technical findings by NASA-sponsored contractors and grantees.

- CONFERENCE PUBLICATION. Collected papers from scientific and technical conferences, symposia, seminars, or other meetings sponsored or cosponsored by NASA.

- SPECIAL PUBLICATION. Scientific, technical, or historical information from NASA programs, projects, and missions, often concerned with subjects having substantial public interest.

- TECHNICAL TRANSLATION. English-language translations of foreign scientific and technical material pertinent to NASA's mission.

Specialized services that complement the STI Program Office's diverse offerings include creating custom thesauri, building customized data bases, organizing and publishing research results . . . even providing videos.

For more information about the NASA STI Program Office, see the following:

- Access the NASA STI Program Home Page at ***http://www.sti.nasa.gov***

- E-mail your question via the Internet to help@sti.nasa.gov

- Fax your question to the NASA Access Help Desk at (301) 621-0134

- Telephone the NASA Access Help Desk at (301) 621-0390

- Write to:
  NASA Access Help Desk
  NASA Center for AeroSpace Information
  7121 Standard Drive
  Hanover, MD 21076

NASA/CR—2000-209812

Effects of Thermal and Mechanical Processing on Microstructures and Desired Properties of Particle-Strengthened Cu-Cr-Nb Alloys

Kenneth Reed Anderson
University of California at Davis, Davis, California

National Aeronautics and
Space Administration

Glenn Research Center

February 2000

Acknowledgments

I gratefully acknowledge the NASA/OAI Collaborative Student Snmmer Internship at the John Glenn Research Center at Lewis Field (formerly the NASA Lewis Research Center), Cleveland, Ohio, for providing and allowing me the research opportunity which made at least half this dissertation possible. I extend my deepest gratitude to Dr. David L. Ellis for his crucial role in providing material and supporting experimental data. The initial extensive TEM help from Dr. Anita Garg at NASA is also greatly appreciated. Much of the second half of this dissertation comes from work at the Rockwell Science Center, Thousand Oaks, California. I gratefully acknowledge the Graduate Student Industrial Fellowship granted by NSF-CTS (Dr. M. Roco, program director) that made this work possible. I'm indebted to the Rockwell Science Center, and especially Drs. Don Ulmer (at Rocketdyne Division of Boeing), Dallis Hardwick (now at Boeing) and Cliff Bampton (at Rocketdyne Division of Boeing), for their insightful discussion and support in providing necessary resources and facilities. I would also like to give special thanks to Professors Jeffery C. Gibeling and James F. Shackelford for kindly taking part in my Dissertation Committee, for which they showed great patience and understanding! Finally, I would like to, again, give greatest thanks possible to my advisor, Prof. Joanna Groza for her continuous support, assistance to me and confidence in me.

Available from

NASA Center for Aerospace Information
7121 Standard Drive
Hanover, MD 21076
Price Code: A09

National Technical Information Service
5285 Port Royal Road
Springfield, VA 22100
Price Code: A09

Effects of Thermal and Mechanical Processing on Microstructures and Desired Properties of Particle-Strengthened Cu-Cr-Nb Alloys

ABSTRACT

Ternary Cu-Cr-Nb alloys, particularly Cu-8 Cr-4 Nb (in at.%), have demonstrated good thermal stability as well as high strength and high conductivity at low and high temperatures. This behavior – due to the insoluble and strong Cr_2Nb intermetallic phase that forms from the 2:1 Cr/Nb ratio – has put Cu-Cr-Nb alloys at the forefront as the next-generation particle-strengthened Cu alloys for aerospace applications. The initial powder material, produced by Ar-gas atomization, has a bimodal size distribution of Cr_2Nb precipitates. Primary Cr_2Nb precipitates, formed congruently from the melt, are typically ~1 μm in size, and secondary Cr_2Nb particles, precipitated from atomized solid solution, are typically 30-200 nm in size. This study provides the first detailed examination of the stability and strengthening effects of these particles in Cu-Cr-Nb alloys. Extruded Cu-8 Cr-4 Nb exposed to temperatures of up to 1323 K for up to 100 hr sustained a drop in strength of only 25-30%. Such behavior was mainly a manifestation of Cu grains stabilized by primary and secondary Cr_2Nb dispersoids, which remained in their initial size range due to their inherently sluggish coarsening. The modest particle coarsening was analyzed in terms of and found to follow LSW-type behavior.

This investigation also revealed that the primary particles, usually situated at grain boundaries and triple points, provide a direct grain boundary pinning effect, and moreover, an indirect, grain boundary strengthening effect, but virtually no Orowan strengthening effect. The secondary Cr_2Nb particles, typically found within grains (and to a lesser extent, at grain boundaries), do provide Orowan strengthening. For extruded material, it was established that grain-boundary strengthening (Hall-Petch effect) accounts for about two-thirds of the overall strength of material, with Orowan effects essentially contributing the remainder. The proven thermal stability, strengthening

effects and, more importantly, strength retention, was the driving force to further improve upon these attributes via microstructural refinement of Cu-Cr-Nb alloys. Thus, mechanical milling was carried out on as-received powders, especially novel Cu-4 Cr-2 Nb.

Mechanical milling (MM) of Cu-4 Cr-2 Nb and Cu-8 Cr-2 Nb produced an increase in hot pressed Vickers hardness of 122% and 96%, respectively. However, MM also inadvertently produced a corresponding decrease in electrical conductivity of ~33% for both alloys. The increase in hardness was more due to Cu grain-size refinement than to second-phase particle-size refinement. The drop in conductivity was due to second-phase particle-size refinement, which increased both particle/matrix interfacial area and solute solubility. This novel detailed study also proved the enhanced stability of mechanically processed Cu-4 Cr-2 Nb. Hot pressed 4 hr-milled Cu-4 Cr-2 Nb experienced a 30% increase in conductivity with only a 22% drop in hardness when annealed at 1273 K for 50 hr. Such changes were largely due to an increase in dispersed-particle size (decrease in solute and interfacial electron scattering) and Cu grain size (reduced Hall-Petch effect), respectively.

Altogether, the goal of improving the strength and stability of Cu-4 Cr-2 Nb to better than such properties for as-extruded Cu-8 Cr-4 Nb has been met. In addition, a figure-of-merit (FOM) coupling hardness and thermal conductivity was developed during this stage of the investigation. This FOM was found to be maximum for the case of 4-hr milled and hot pressed Cu-4 Cr-2 Nb material. Thus, this entire study comprising processing, microstructure and property characterization of Cu-Cr-Nb alloys has demonstrated that these alloys not only inherently possess high strength, conductivity and thermal stability, but can also be further developed to improve their strength and stability.

TABLE OF CONTENTS

I. INTRODUCTION

1.1. BACKGROUND

1.1.1. Cu-Cr-Nb Alloy Genesis

Within the last 10-15 years, a variety of dispersion-strengthened (DS) copper alloys have been developed and studied due to their unique proclivity to provide a good combination of high mechanical strength and thermal/electrical conductivity. Strengthening is usually achieved by the introduction of a stable *ceramic*, *carbide* or *refractory metal* secondary phase, e.g., [1-10]. One highly sought achievement is the latest development of high-strength alloys with high-temperature stability. In particular, novel Cu-Cr-Nb alloys, recently designed at NASA-Lewis with the Cr:Nb ratio of 2:1, have received special attention as the next generation of elevated temperature DS alloys [11-13]. The strengthening is provided by the precipitation of hard Cr_2Nb *intermetallic* particles, which are stable up to the congruent melting point of 2043 K (see Fig. 1 for Cr-Nb phase diagram). Cr_2Nb-strengthened Cu is a strong candidate material for potential uses ranging from welding electrode and high-voltage switch applications to more advanced active-cooling applications, such as first wall and divertor interactive components in fission and magnetic confinement fusion reactors, combustion chamber liners for next-generation reusable launch vehicle (RLV) engines, and rocket nozzle liners.

The Cr:Nb ratio of 2:1 was selected such that all Cr and Nb combine to form the insoluble Cr_2Nb compound to preserve the excellent thermal conductivity of a virtually pure copper matrix. The negligible solubilities of BCC refractory Cr and Nb in Cu up to 1200 K [15], their complete solubility in liquid Cu above solvus, and their Cr_2Nb formation provide the thermodynamic rationale behind the design of this alloy. Furthermore, this Cr-Nb behavior in solid copper indicates the likelihood for maximum

thermal stability of Cu-Cr-Nb alloys. Finally, it should be pointed out that the high temperature stability of DS alloys is largely dictated by the extent of particle coarsening and dissolution.

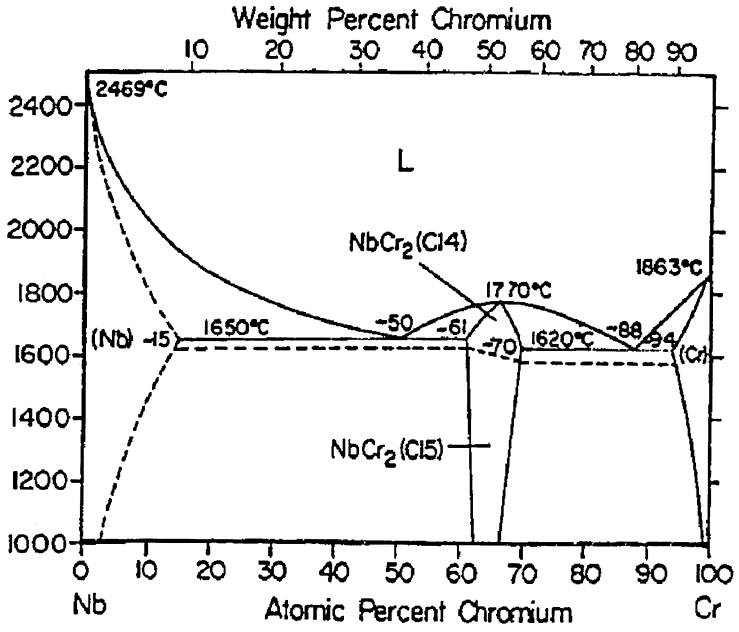

Figure 1 - The most recent Assessment of the Cr-Nb Phase Diagram (Drawn From Ref. [14]).

1.1.2. Indication of Thermal Stability

1.1.2.1. Thermodynamic Aspects

The thermodynamic driving force for virtually all particle coarsening is the minimization of the total free energy, G, via the evolution of a lower overall specific particle/matrix interfacial area due to the coarser precipitates. In other words, irrespective of the mechanism that controls Ostwald ripening, it is reduction in total (surface) energy in the system that drives the reaction. That is, the system is driven by the minimization of the total interfacial energy, $\Sigma\gamma A$, where γ and A are the interfacial energy per unit area and area of the respective particles. Furthermore, it has been shown by differential scanning calorimetry traces [16] that the free energy reduction associated

with decreasing total surface area is manifested by heat evolution; in other words, coarsening is an exothermic reaction.

In any precipitation-hardened material there will be a range of particle sizes due to differences in the nucleation time and growth rates. Due to a capillarity effect or the Gibbs-Thomson effect, the solute concentration in the matrix adjacent to a particle will increase as the radius of curvature decreases. This follows from the fact that solute solubility depends exponentially on a free energy difference, ΔG. This Gibbs free energy difference is increased by the factor $2\gamma/r$—which is due to associated interfacial energies and radii of particles (r) – which subsequently increases the solute solubility [17]. Figure 2 below shows two adjacent spherical particles with different diameters. The smaller particle will experience a greater

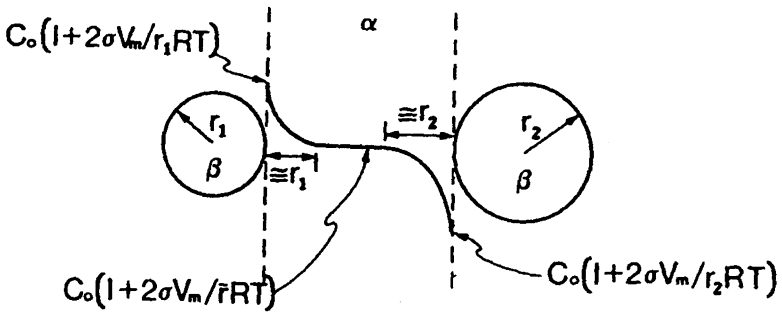

Figure 2 - Two β particles (radii r_1 and r_2) in an α matrix. Local equilibrium is assumed to exist at the respective particle-matrix interfaces so that $C(r_1) > C(r) > C(r_2)$. This leads to transfer of β atoms to the matrix from the smaller particle and its subsequent dissolution. The opposite process occurs in the region of the matrix/large particle interface. The characteristic diffusion distance is proportional to the particle radius (taken from [18]).

increase in free energy (larger capillarity effect, $2\gamma/r$) than the larger particle - compared to a particle of infinite radius - causing the enhanced solute concentration in the matrix at the smaller particle. This effect of $2\gamma/r$, or particle radius, on solubility is given in the following equation form:

$$C_r = C_{e,\infty}\left(1+\frac{2\gamma V_m}{rRT}\right) \quad (1)$$

where C_r = equilibrium solubility of a particle of radius r (m);

$C_{e,\infty}$ = equilibrium solubility of infinite radius;

γ = dispersoid/matrix interfacial energy in J/m^2;

V_m = molar volume of the particle in m^3/mole;

r = radius of particle

R = 8.314 J/mol·K; and

T = absolute temperature in Kelvin (K).

Thus, the particle-size (Gibbs-Thomson) effect thermodynamically induces a concentration gradient, which drives the diffusion and the means by which the microstructure strives towards equilibrium, or minimization of system free energy.

Based on the above, the microstructure of a two-phase alloy is necessarily out of equilibrium if the total interfacial free energy per unit volume is not minimized. In other words, a system with particles of *different sizes* is thermodynamically unstable due to large surface energy effects. Larger particles having lower overall interfacial area tend to grow at the expense of smaller precipitates, which tend to dissolve and shrink, thus giving an overall lower system free energy. Therefore, a high density of small precipitates will tend to coarsen into a relatively lower density of larger particles. The thermal stability of microstructure and, of coarse, the retention of strength at elevated temperatures, are obviously enhanced by slowing this coarsening process.

1.1.2.2. Kinetic Aspects

It is, in fact, a low tendency for Cr_2Nb precipitate coarsening that is the advantage of Cu-Cr_2Nb alloys. This resistance to coarsening is predicted by application of the coarsening kinetics described by the Lifshitz-Slyozov-Wagner (LSW) theory [19, 20]. The development of the LSW theory was the first real effort to theoretically and

quantitatively describe the coarsening behavior of a dispersed second phase in a parent matrix. The LSW theory was developed to model the kinetics of precipitate growth from supersaturated solid solutions after the completion of nucleation, but it may also apply to other methods of particle incorporation (e.g. mechanical alloying and internal oxidation), as well as to coarsening of grains in liquid-phase sintering [21-24] and to the coarsening of pores in solid state sintering [25,26]. It is based on a zero volume percent of coarsening phase approximation. One important prediction of the LSW theory is the existence and specific shape of an asymptotic particle size distribution (PSD), or histogram. In fact, LSW theory 'predicts' this phenomenon of a "quasi steady state" particle-size distribution evolving regardless of the initial distribution.

The classical LSW expression for volume diffusion controlled coarsening kinetics typically used is given by:

$$\bar{r}_t^3 - \bar{r}_o^3 = \frac{8\gamma V_m D C_{e,\infty}}{9RT} t = kt \ \ [m^3] \qquad (2)$$

where $\bar{r}_t$ = average particle radius at time t [s] in m;

$\bar{r}_o$ = average particle radius at the onset of coarsening;

γ = dispersoid/matrix interfacial energy in J/m^2;

V_m = molar volume of the particle in m^3/mole;

D = diffusivity of rate controlling solute in the matrix in m^2/s;

$C_{e,\infty}$ = equilibrium solubility of the rate-controlling solute in the matrix;

R = 8.314 J/mol·K; and

T = absolute temperature in Kelvin (K).

It is clear from this formula that the coarsening rate is minimal for a given alloy if D, γ and $C_{e,\infty}$ are minimized. Table I gives the diffusivities and solubilities of several elements in copper at 1300 K. These elements are the reactants of various compounds that may be possible candidate dispersoids in DS copper alloys, e.g., Al_2O_3, TiB_2, Si_3N_4,

MgO, B_4C, and, of course, Cr_2Nb. As seen in the far-right column, Cr and Nb have the lowest combination of D and C – at least for elements for which data were available. This low D-C combination was, again, crucial in the design of Cu-Cr-Nb.

Table I* - Diffusivities and Solubilities of Elements in Copper at 1300 K

Element	D_o (cm^2/s)	Q (kJ/mol)	Diffusivity, D (cm^2/s)	Solubility, C (wt%)	DC, (cm^2/s·wt%)
Al	0.0455	165.3	1.04×10^{-8}	7.6	7.90×10^{-8}
O	0.0176	66.9	3.6×10^{-5}	<0.009	3.24×10^{-7}
Cr	0.337	195	4.9×10^{-9}	0.37	1.81×10^{-9}
Nb	2.04	251.3	1.63×10^{-10}	~ 0.14	2.28×10^{-11}
Ce	$2.38\text{x}10^{-8}$	111.7	7.7×10^{-13}	negligible	--
Ti	0.693	195.8	9.4×10^{-9}	1.8	1.69×10^{-8}
Si	0.037	167.4	7.0×10^{-9}	2	1.40×10^{-8}
N	--	--	--	negligible	--
Ca	--	--	--	negligible	--
Mg	0.016	155	--	0.52	--
Be	0.73	196	9.7×10^{-9}	0.6	5.82×10^{-9}
B	6.42	190	1.5×10^{-7}	0.08	1.19×10^{-8}
C	~0.008	~95.5	$\sim1.16\times10^{-6}$	~0.005	$\sim5.82\times10^{-9}$
Zr	--	--	--	0.13	--

*Based on a similar table originally developed for a particle selection article by Groza and Gibeling [27].

Again, Cr and Nb have very low solubilities in solid copper and Nb also has a very low diffusivity in solid copper [28], which renders it the rate-limiting species. Thus, for the very low D and $C_{e,\infty}$ values for Nb in Cu as given in Table I, Eq. (2) predicts sluggish coarsening for Cu-Cr-Nb alloys. In contrast, for other classical precipitation-strengthened copper alloys, such as Cu-Cr [29], Cu-Zr [30], and Cu-Cr-Zr [31], mechanical strength and thermal conductivity are both adversely affected by excessive coarsening and dissolution of precipitates into the matrix. For example, aging studies of Cu-Cr by Tenwick and Davies [32] show a significant decrease in room temperature (RT) hardness after aging only 1 to 2 hrs at up to 773 K. The relatively high diffusivity of Cr in Cu [28], which promotes rapid coarsening and overaging, is most likely the cause of

such behavior. Again, these adverse effects above 773 K would be greatly reduced when considering Cu-Cr-Nb (Cu-Cr_2Nb) alloys. Based on the stability and high volume fraction of Cr_2Nb particles, Cu-Cr-Nb alloys are expected to provide high strength at room and elevated temperatures. When considering that a role of second-phase particles is to impede dislocation motion, particle stability becomes imperative. Dislocation bypass of impenetrable, incoherent particles via dislocation bowing (and looping), i.e. the Orowan mechanism, and more importantly, the extra component of strength gained from such Orowan bypass, are distinctly controlled by the separation, thus **size** and volume fraction, of dispersed particles.

1.1.3. Relevant Strengthening Mechanisms

Strengthening mechanisms considered most relevant in particle strengthened copper include the Orowan and Hall-Petch effects. Thus, a brief description of each is given next.

Orowan strengthening due to a random distribution of impenetrable particles is typically estimated using the Orowan-Ashby formula [33, 34]:

$$\Delta\sigma = \frac{0.84MG\mathbf{b}}{2\pi(1-\nu)^{0.5}(\lambda-2r)}\ln\frac{r}{\mathbf{b}} \text{ [MPa]} \qquad (3)$$

where M is the Taylor factor (≈3.0 for a polycrystalline FCC metals), G is the shear modulus of the copper matrix [MPa], **b** is the matrix Burgers vector [nm], r is the (average) particle radius [nm], ν is Poisson's ratio of the matrix and λ is mean planar particle spacing expressed as

$$\lambda = r\sqrt{\frac{2\pi}{3f}} \text{ [nm]}, \qquad (4)$$

where f is volume fraction of particles. Eq. (3) is the most reliable, proven and accepted expression for particle size/spacing effects on flow stress for certain important reasons: It assumes a random particle distribution, takes into account dispersoid size for interparticle spacing; and when considering variations in dislocation line tension it averages the nature of dislocations (screw, edge and/or mixed), as well as incorporates interactions of dislocation segments/dipoles encountered when bowing between particles. Thus, the additional direct strengthening provided by particle/dislocation interactions is more pronounced the smaller the particles, at constant f. Therefore, if a small average particle size and high strength initially exists, hindering particle growth is critical in preserving this initial microstructure and strength. Moreover, dispersed particles also provide an "indirect" strengthening effect, i.e. matrix grain boundary/size strengthening via boundary pinning. In other words, the Hall-Petch effect is fostered.

The Hall-Petch expression relating flow stress to grain size is given as [35,36]:

$$\sigma = \sigma_o + k_y d^{-\frac{1}{2}} \quad \text{[MPa]} \tag{5}$$

where d is (measured) grain size, k_y is a material constant related to the ease of slip transfer across a grain boundary, and σ_o is the yield, or friction, stress of essentially a single crystal (or infinite grain size). This strengthening effect is essentially due to stress concentrations at and slip transfer across grain boundaries due to pile-ups of dislocations generated mainly by Frank-Read sources. Smaller grains would require higher applied stresses to generate enough dislocations to induce slip transfer, or flow. It turns out that the grain size d of a DS alloy will be effectively governed by particle size and volume fraction. Thus, an equilibrium, limiting size to which grains coarsen (in the absence of abnormal grain growth) can be calculated with respect to the Hillert-Gladman relation [37,38] based on the Zener model [39]. Such a relation for grain size is based on a distribution of incoherent, spherical particles and can be given as

$$d_{calc} = \frac{4r}{3f} \tag{6}$$

where d is grain size, r is mean particle radius, and f is volume fraction of particles. This expression suggests that as r is reduced, the grain size is reduced and strength increased; or, if r is increased strength is decreased. That is, minimal particle coarsening means minimal matrix grain growth and a consistent Hall-Petch effect. It can be stressed again that the desire for maximum particle stability and strengthening effect in a copper alloy is the driving force in the choice and pursuit of Cu-Cr-Nb alloys. Finally, there is no real consensus as to which mechanism contributes the most to dispersion strengthening, as will be expanded on later.

1.1.4. Thermal/Electrical Conductivity (Resistivity)

It is well known that thermal conductivity in a crystalline solid, the transport of heat through such a solid, is controlled by the conduction of electrons and lattice vibrations (phonons) through the lattice structure. The structure of metals can be viewed as a lattice of fixed positive ion cores surrounded by a "gas" of relatively free and very mobile, delocalized electrons. These freely moving electrons are the valence/conduction electrons, which provide metals their relatively high electrical conductivity. Moreover, for metals, these same electrons are almost entirely responsible for the flow of heat, or, thermal conductivity, making the thermal role of phonons essentially insignificant. Therefore, only expressions for the electrical and thermal conductivity of metals due to such electrons are given next.

An expression for electrical conductivity in a metal can be given as [40]:

$$\sigma_e = \frac{n_e e^2 \lambda_{el}}{m_e \bar{V}_F} \ [(\Omega \cdot m)^{-1}] \tag{7}$$

where n_e = the electron density [m^{-3}],

e = the charge of an electron [1.602×10^{-19} C],

λ_{el} = mean free path of electrons [m],

m_e = mass of an electron [9.11×10^{-31} kg], and

$\overline{V}_F$ = Fermi velocity of electrons [m/s].

An analogous equation for thermal conductivity in metals due to conduction electrons is given by Poirier and Geiger [41] as:

$$\kappa_e = \frac{\pi^2 n_e k_B^2 T \lambda_{el}}{3 m_e \overline{V}_F} \text{ [W/m-K]} \qquad (8)$$

where k_B = Boltzmann's constant [1.3807×10^{-23} J/K],

T = absolute temperature [K], and

the remaining constants and variables have been defined above.

The dependent variable on the right hand side common to both formulas is the electron mean free path, λ_{el}. From this, it is clear that a long λ_{el} permits high conductivities. Thus, it is directly evident how deleterious deviations from perfect lattice periodicity - atom vibrations, solute atoms, dislocations, grain boundaries, etc. - are to the conductivity of metals, since they can only serve to decrease λ_{el}. The ease, as well as the obstruction, of electron flow through an atomic lattice is a manifestation of the periodic wave nature of electrons. Increases in electron wave scattering and their effects on resistivity are addressed below.

The Wiedemann-Franz law relates thermal and electrical conductivity via a constant of proportionality known as the Lorentz number, L. Equation (9) below is the "quantum form" of the Wiedemann-Franz relation [40]:

$$L = \frac{\kappa_{el}}{\sigma_e T} = \frac{\pi^2}{3}\left(\frac{k_B}{e}\right)^2 = 2.45 \times 10^{-8} \text{ W} \cdot \Omega/\text{K}^2 \qquad (9)$$

(Note: Eq. (9) was derived and is valid only for metals.)

The value of L for copper has been empirically determined to be ~2.25×10^{-8} $W \cdot \Omega/K^2$ at room temperature [40]. It can be noted here that this L value for Cu being close to the theoretical L is, in itself, a strong indication that the electronic contribution to the thermal conductivity predominates. Thus, thermal conductivity can be estimated from L and the measured electrical conductivity. This is conveniently done since electrical conductivity, or rather, resistivity, of a material specimen is typically much simpler to measure than thermal conductivity. Usually, thermal conductivity determination requires measurements of two thermal properties of a material, as shown next.

An expression used for the experimental determination of thermal conductivity, which involves two thermal properties – thermal diffusivity and specific heat – is typically given as:

$$\kappa = \rho \alpha_d C_p \quad \text{[W/m-K]} \tag{10}$$

where ρ = the density, in kg/m^3,

α_d = the thermal diffusivity [m^2/s]; and

C_p = the heat capacity (specific heat) [J/kg-K].

Thus, once the thermal diffusivity and heat capacities are measured, thermal conductivity can be directly calculated. Note that measured values of α_d and C_p do not distinguish between components transferring the heat, i.e. electrons and/or phonons. In other words, Eq. (10) applies to metals, ceramics, etc., whereas the previous three expressions are valid only for metals, since they are based on concentration, velocities and mean free paths of strictly valence/conduction band electrons. Again, the critical variable is the electron mean free path, λ_{el}, which is governed by microstructural and atomic-level defects.

Expressions for electrical resistivity and conductivity based on microstructural constituents (e.g. second phases) and features (e.g., grain and dispersoid sizes) can be and

have been established empirically. First, what immediately follows is a look at two derived conductivity expressions relating overall alloy conductivity to volume fraction and conductivity of a dispersed second phase.

The Schroder formula below expresses the electrical or thermal conductivity of an alloy with a dispersed spherical second phase inclusions, e.g., dispersoids and/or precipitates [42]:

$$\sigma_{DS} = \sigma_m \frac{1 + 2f_p \dfrac{1 - \sigma_m/\sigma_p}{2\sigma_m/\sigma_p + 1}}{1 - f_p \dfrac{1 - \sigma_m/\sigma_p}{2\sigma_m/\sigma_p + 1}} \tag{11}$$

where σ_m = the conductivity of the matrix (in this case Cu),

σ_p = the conductivity of the dispersed particles, and

f_p = the volume fraction of dispersed phase.

Another model for thermal conductivity of a continuous metal matrix with a random distribution of non-interacting spherical second-phase particles, known as the Maxwell model [41], is given below as:

$$\kappa_{mix} = \kappa_m \frac{\dfrac{\kappa_p}{\kappa_m} + 2 - 2V_p\left[1 - \dfrac{\kappa_p}{\kappa_m}\right]}{\dfrac{\kappa_p}{\kappa_m} + 2 + V_p\left[1 - \dfrac{\kappa_p}{\kappa_m}\right]} \tag{12}$$

where the subscripts represent the same as those in Eq. (11) and V_p is the volume fraction of second-phase particles.

Equations (11) and (12) are effectively valid for V_p up to ~0.10. Also, since Eqs. (11) and (12) are basically based on a 'rule of mixtures' they do not (directly) take into account microstructural aspects, such as grain size and particle size, spacing, and matrix interface effects, which makes it a first order approximation, at best.

The total resistivity of a metal alloy can be expressed by [43]:

$$\rho_{tot} = \rho_{ph} + \rho_{imp} + \rho_{int} + \rho_{dis} \quad (13)$$

The contribution of phonon scattering is given as ρ_{ph} (essentially ρ of pure Cu), impurity scattering as ρ_{imp}, particle-matrix and Cu grain interface scattering as ρ_{int}, and dislocation scattering as ρ_{dis}. All of these additions to resistivity arise due to the effects of the associated microstructural features on reducing the mean free path of conducting electrons, or increasing electron scattering centers. Again, these interruptions from crystalline ideality impede electron propagation through the lattice. Finally, it is also worth mentioning that the first contribution, ρ_{ph}, is temperature dependent (atomic displacements about mean/equilibrium lattice positions increase with temperature), whereas the remaining contributions to ρ_{tot} are effectively temperature independent. Also, electron-electron interactions are considered insignificant for Cu, thus, have relatively negligible scattering effects.

1.1.5. Mechanical Milling/Alloying

Mechanical alloying/milling (MA/MM), is a solid-state process in which a blend of elemental or alloyed powders (of metals A and B) is subjected to highly energetic compressive kneading forces and stresses in a ball mill (e.g., a planetary ball-mill, a stirred ball-mill, a shaker mill or a vibratory ball-mill). These high impact forces on the powder particles coming between two balls or a ball and the vial wall cause repeated micro-fracturing and cold welding of the particles; in other words, severe working and plastic deformation of material (see Figures 3 and 4 below for schematics). When

powders are mechanically alloyed/milled, a convoluted lamellar structure usually arises in the powder particles due to this microfracturing and cold welding of the particles. This microstructure is typical for early MM/MA stages. In late MM stages, this lamellar structure gives way to a refined, equiaxed subgrain/grain structure through dynamic recovery/recrystallization processes. When such a structure is reached, the MM process is considered essentially at steady-state.

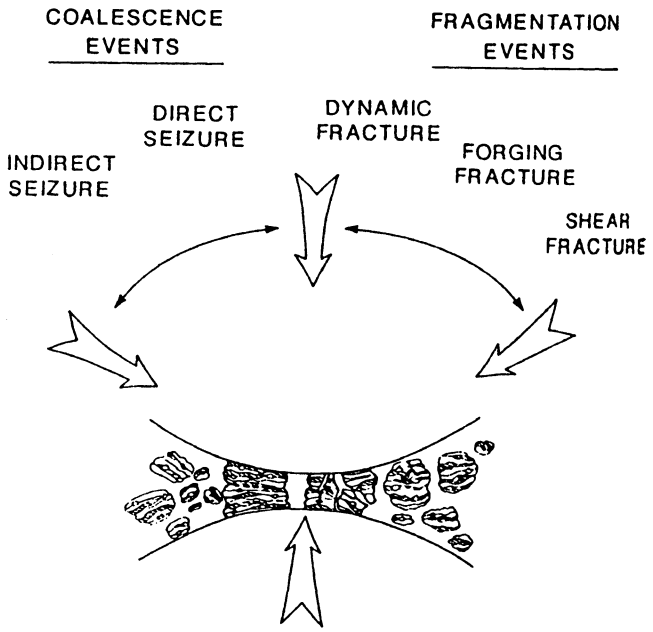

Figure 3 - Ball-Powder-Ball Schematic indicating the dynamics of powder particle micro-racturing/welding and "kneading" during Mechanical Milling Process. (Adapted from ref. [44].)

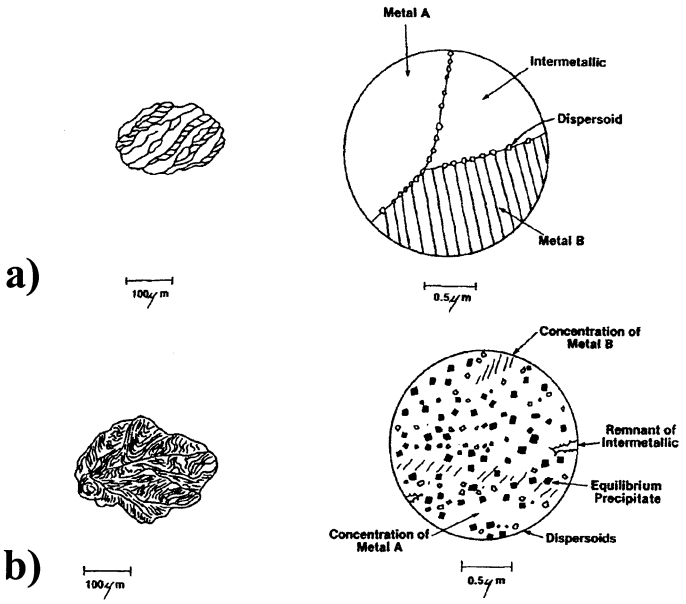

Figure 4 - Schematic Depicting (a) Early Stages and (b) Final Stages of Processing of Microstructure Containing Dispersoids. (Adapted from ref. [45].)

It may be noted here that the kinetic energy ($\sim\frac{1}{2}m_b v_b^2$; m_b = mass of ball, v_b = velocity of ball) dissipated during impact transforms mainly into heat. A minor fraction of the energy will be stored into the material as structural disorder resulting from plastic deformation, e.g., excess vacancies, dislocations, grain boundaries, etc. [46]. Furthermore, this excess energy derived from the MA/MM process leads inevitably to out-of-equilibrium, or metastable structures, including an increase in the solid solubility of alloying elements in a parent matrix. That is, MA can generate a supersaturated solid solution of, for example, B atoms in an A metal lattice structure, at relatively low temperatures. Below is a summary of the attributes of and benefits stemming from the MA/MM process in general, including DS Cu alloying/milling:

- Very fine (intimate/atomic-level) mixing of powders;
- Controlled, (more) homogeneous dispersion of second-phase particles;
- Extremely fine microstructure;
- Freedom to choose particles that are ***stable at high temperatures;***
- Flexibility in choosing the alloy composition;
- No dependence on usual processing limitations (ability to choose the alloy and

phase compositions without regard to liquid and solid solubility limits or densities).

Finally, Figure 4 also shows schematically how MM/MA is effective at producing a refinement and uniform distribution of a (usually refractory) secondary strengthening phase. Also, usually when mechanical milling has reached this steady-state realm, secondary particles are largely found at grain boundaries in DS alloys, i.e. grain size values effectively take on interparticle spacing values.

Several studies involving MM/MA of (DS) copper alloys have been carried out, largely by Morris and Morris [3,4,6,9,47,48]. These experiments dealt primarily with milling Cu with bcc elements (Cr, Mo, Nb, Ta, V) and ceramic particles (TiB_2, CrB_2, ZrB_2). The authors attribute strength increases more to an increased Orowan effect due to a dispersion of refined particles (<30 nm) than to grain size refinement ($\lesssim$300 nm). This is in contrast to Hazzledine's contention that in dispersion hardened materials, it is the "indirect hardening" of particles coming from fine grains being pinned by the particle [49]. This contradiction requires further exploration, which can be achieved with a detailed microstructural study following processing with relation to strength. Finally, even though the concept of "high-strength high-conductivity" copper alloys has been frequently advanced, e.g., refs. [1-10], the effects of *milling* on conductivity have been addressed only once. Morris, *et al.* [9] addressed conductivities of MM Cu alloys, but only briefly and qualitatively. This gives great impetus for important fundamental studies of the detailed effects of MM on not only mechanical properties, but conductivity as well.

A final aspect of DS Cu alloys involves improved creep and fatigue behavior. Sauer *et al.* [50], recently reported the creep behavior of a MM DS Cu alloy (Cu-TiC). Despite sub-micron grain sizes (<300 nm) the alloy exhibited unexpectedly high creep strengths and stress exponents, which were attributed to particles impeding grain

boundary dislocation glide. (As mentioned earlier, grain size and interparticle spacing become essentially equal in mechanical milled DS alloys.) In addition, creep studies of another DS Cu alloy (Cu-Al_2O_3) show the benefits of even intragranular dispersoids on enhancing creep properties [51]. This same DS Cu alloy has also proven to be micro-structurally stable and stronger under low-cycle fatigue (LCF) compared to pure copper [52]. Finally, Cu-8 Cr-4 Nb has shown better LCF properties than pure copper and even another DS Cu alloy, NARloy-Z (Cu-3wt.% Ag-0.5wt.% Zr), used in aerospace applications [53]. These results reveal the benefits of dispersions on the important creep and fatigue properties of structural Cu alloys and, therefore, the importance of optimally strong and stable DS Cu alloys.

1.2. Research Objectives/Approach

The collective objective of this work is to characterize the microstructures and specific properties of Cu-8 Cr-4 Nb and Cu-4 Cr-2 Nb as a function of thermal and mechanical processing. What follows can be considered a two-part approach. The first goal is to demonstrate the high strength and stability of Cu-Cr-Nb alloy(s) through detailed characterization of microstructures and strengthening mechanisms corresponding to such behavior. In addition, this study justifies the choice of the Cu-Cr-Nb system. The second goal is to improve upon these salient attributes through additional mechanical and thermal processing of these alloys.

1.2.1. Part One: High-Temperature Stability and Related Strength:

When this study on a commercially Ar-gas-atomized (P/M) Cu-8 Cr-4 Nb (Cr and Nb in at%) alloy originated, the goal was to assess and demonstrate the design principles for and attributes of Cu-Cr_2Nb alloys. Thus, "part one" of this investigation focuses on the effects of thermal treatments on microstructures and strength of extruded material. It includes and relies on detailed microstructural characterization (e.g., precipitate phase

identification/analysis, analysis of grain and precipitate size and morphology, dislocation/particle interactions) and direct correlation with mechanical properties for a better understanding of thermal stability behavior. In addition to stability aspects, strengthening mechanisms based on microstructural features, i.e. Orowan and Hall-Petch effects, are examined. It was expected *a priori* that the unshearable precipitates add strength as obstacles to dislocation movement (Orowan effect) and the Cr_2Nb particles provide indirect strengthening as grain-boundary pinners (Hall-Petch effect). Moreover, to what degree each effect contributes to overall alloy strength is estimated. It is also presumed that the Cr_2Nb particles increase resistivity as additional electron scattering centers. In addition, solute atoms (Cr and Nb) certainly add to overall alloy resistivity. These individual contributions are estimated separately, in turn. Thus, this segment of the interrogation of Cu-Cr-Nb demonstrates the effects of the dispersed Cr_2Nb phase on the strength and conductivity/resistivity relative to Cu. Strength and stability properties of Cu-Cr-Nb are also briefly compared to those of other existing particle-strengthened Cu alloys.

Observations of initial and aged microstructures inspired the initial concept of modifying the starting material so as to produce more effective microstructures. But, the outcome of this first-ever stability and strengthening-mechanism study of Cu-Cr-Nb necessarily determined whether or not to pursue additional P/M processing for microstructural, thus, strength enhancement. The extents of thermal stability, grain-size strengthening and particle-strengthening are initially proven (in "part one") for a particular DS Cu-Cr_2Nb alloy in the as-atomized, extruded condition. Based on this finding, Cu-Cr-Nb alloys having a more refined microstructure are predicted to be not only stronger, but also sufficiently stable to preserve such enhanced behavior and, therefore, do warrant pursuing.

1.2.2. Part Two: Strength and Stability Enhancement via Mechanical Processing

The proven thermal stability, low- and high-temperature strength and conductivity behavior of the Cu-8 Cr-4 Nb alloy, and basic understanding of strengthening effects justify the subsequent goal of strength enhancement via the processing of starting Cu-Cr-Nb powders. In addition to strength, enhancing alloy conductivity is also desired. This ultimate goal and novel concept of improving both strength and conductivity can be achieved through the investigation of not only P/M processed Cu-8 Cr-4 Nb, but also another P/M Cu-Cr-Nb alloy having less Cr and Nb, thereby offering a higher conductivity. This novel alloy, Cu-4 Cr-2 Nb, satisfies this objective with its lower Cr and Nb content and, of course, lower volume percent of the strengthening Cr_2Nb phase. However, the lower Cr_2Nb content has an inevitable adverse effect on strength based on Eqs. (3)-(5). Therefore, an improvement of low and high temperature mechanical strength to at least the level of, if not above, that of Cu-8 Cr-4 Nb is sought via mechanical milling (MM). In effect, as-extruded Cu-8 Cr-4 will ultimately be used as a base line for which to gauge the strength, stability and conductivity achieved in this mechanical processing work comprising the second-stage, or "part two" of the present overall study of Cu-Cr-Nb alloys.

For as-atomized pre-alloyed and pure starting powders, MM offers a relatively simple, feasible and proven means of inducing intense plastic deformation into the material to *refine* the microstructure, specifically, large *Cr_2Nb precipitate* and *grain* sizes. From this refinement by MM, it is anticipated that the improved Orowan and Hall-Petch strengthening would more than compensate for the reduced precipitate volume fraction in the Cu-4 Cr-2 Nb alloy. In fact, a directly related aspect of this MM study involves the quantification and analysis of the microstructural evolution/development associated with the MM process. This includes precipitate, grain and subgrain/cell sizes, and relative

extent to which each microstructural feature contributes to the strength and conductivity of processed Cu-Cr-Nb alloys.

In addition, mechanical milling has the capability to achieve a more uniform distribution of an initially inhomogeneous Cr_2Nb particle distribution. MM should also drive an initial bimodal particle size distribution (PSD) to a single PSD. Such a resultant uniform size of Cr_2Nb will also decrease the driving force for coarsening (Gibbs-Thomson effect) by decreasing the particle size differences; refer to Fig. 2 and Eq. (1). This control of particle size and distribution to obtain fine and uniform particles should provide optimum mechanical properties sustained by thermally stable microstructures. In other words, inherent to this latest work is tailoring a desired stable microstructure for a desired (optimum) strength and conductivity combination through examination of the effects of the mechanical milling on the microstructure, strength and conductivity of particularly the Cu-4 Cr-2 Nb alloy. Again, an important and relevant indicator of property enhancement is how such MM material compares to as-extruded Cu-8 Cr-4 Nb, which is the most characterized of the Cu-Cr-Nb alloys heretofore.

In summary, the overriding goal of "part two" is to produce an improved Cu-Cr-Nb variant, and, in the process, gain a fundamental understanding of the micro-mechanisms operating prior, subsequent and due to an induced sub-micron structure in Cu-Cr-Nb alloys via mechanical milling. This microstructural refinement is driven to exploit the dependence of the Hall-Petch and Orowan strengthening mechanisms on grain and dispersed particle size, while hopefully mitigating adverse effects on conductivity. Furthermore, this microstructural processing is performed in conjunction with detailed microstructural characterization to gain insight into the *property-enhancing,* inherently *stable microstructures*. Finally, establishment of processing-microstructure-property relationships and a figure-of-merit, such as strength times thermal conductivity, particular to DS copper alloys is an implicit aim.

II. EXPERIMENTAL

2.1. STARTING MATERIAL

Argon atomized Cu-8 Cr-4 Nb and Cu-4 Cr-2 Nb pre-alloyed powders were supplied by Special Metals, Inc. to NASA Lewis Research Center. Melting procedures were based on the methods developed at NASA Lewis for similar Cu-Cr-Nb alloys [12]. (From here on, 8 Cr-4 Nb and 4 Cr-2 Nb will also be designated (8/4) and (4/2), respectively.) The chemical composition of the powders were 6.45 wt.% (7.91 at.%) Cr and 5.79 wt.% (3.98 at.%) Nb - for Cu-8 Cr-4 Nb and 3.27 wt.% (4.0 at.%) Cr and 2.92 wt.% (2.0 at.%) Nb - for Cu-4 Cr-2 Nb. Oxygen levels were 640 ppm and 450 ppm, respectively. Although the chromium content is slightly off stoichiometric, the Cr:Nb ratio (65:35) is still adequate to form only the Cr_2Nb (β) phase, according to the Cr_2Nb phase range in the Cr-Nb phase diagram.

2.2. MATERIAL PROCESSING

2.2.1. As-Extruded Material

At NASA-Lewis, atomized powders (<106 μm) were canned in 5.08 cm diameter mild (low-carbon) steel cans. The cans were then extruded for powder consolidation at 1133 K using a round die with 16:1 reduction in area. The final diameter of the extruded can was approximately 12.7 mm with a Cu-Cr-Nb (8/4 and 4/2) core approximately 9.5 mm. To minimize the coarsening of the Cr_2Nb precipitates, the soak time for the cans was limited to 1 h. Samples used were from these Cu-8 Cr-4 Nb extruded bars. At NASA-Lewis, the extruded specimens were thermally processed for 1, 10, 50 and 100 hours at 773, 973, 1073, 1173, 1273 and 1323 K. Air cooling at about 250 K/min was used for all specimens except for the 1323 K heat treatment. In the latter case, furnace cooling at about 60 K/min was used. The copper materials remained in the steel cans during the entire heating cycle. Diffusion of Fe into the alloy resulted in the formation of

a Cr-Fe rich diffusion zone near the can/alloy interface [53]. The diffusion zone appeared to be limited to a few hundred nanometers at most. During machining the diffusion zone was completely removed. Microscopic examinations of the aged samples were undertaken in regions close to the center of the samples to avoid the effects of the diffusion zone.

2.2.2. Pre-Alloyed Cu-Cr-Nb: Mechanical Milling and Hot Pressing

Mechanical milling of starting pre-alloyed as-atomized Cu-Cr-Nb (8/4 and 4/2) powders (<106 μm) was performed while at the Rockwell Science Center using a SPEX 8000 mill, shown in Figure 5, for times of ½, 1, 2, 4 and 8 hours. Ten-gram batches of powder and 50 grams of 440C stainless steel and WC balls, a ball-to-powder charge ratio of 5:1, were loaded into hardened steel vials under an argon atmosphere (< 1.5 ppm oxygen). The breakdown of the four ball sizes used was as follows: 3, ½-in.; 2, 5/16-in. (WC); 8, ¼-in.; and 20, 3/16-in. balls. Cook and Courtney showed that the net welding and fracture rates were approximately doubled when using differently sized ball combinations [54], which was, in part, the reason for use of different ball sizes here. Initially, hexane was also added as a process control agent (PCA) to mitigate the strong welding/agglomeration and sticking tendencies of Cu powder. For the preliminary work on Cu-8/4, external fan cooling was also used to reduce sticking and increases in temperature, but powder yield was still ~50% after MM for 2 hr. This yield was not considered sufficient, therefore, an alternate organic liquid and cooling method were sought for milling of Cu-4 Cr-2 Nb.

Thus, for Cu-4/2, an approach of applying external liquid nitrogen (LN2) cooling concurrently with a PCA was used to reduce heating and cold welding and promote fracturing. LN2 was allowed to drip continuously over the vial during processing. Two-hour trials were run using methanol and toluene as PCA's. Use of toluene resulted in the

highest yield (~90%), thus, it was used henceforth. For comparison purposes, a set of milling experiments was also carried out using WC balls and vial – with fan cooling and no LN2 cooling or PCA. The number and size of WC balls used were 4, 7/16-in. and 3, 5/16-in. It was presumed that a dry WC media would cause little sticking.

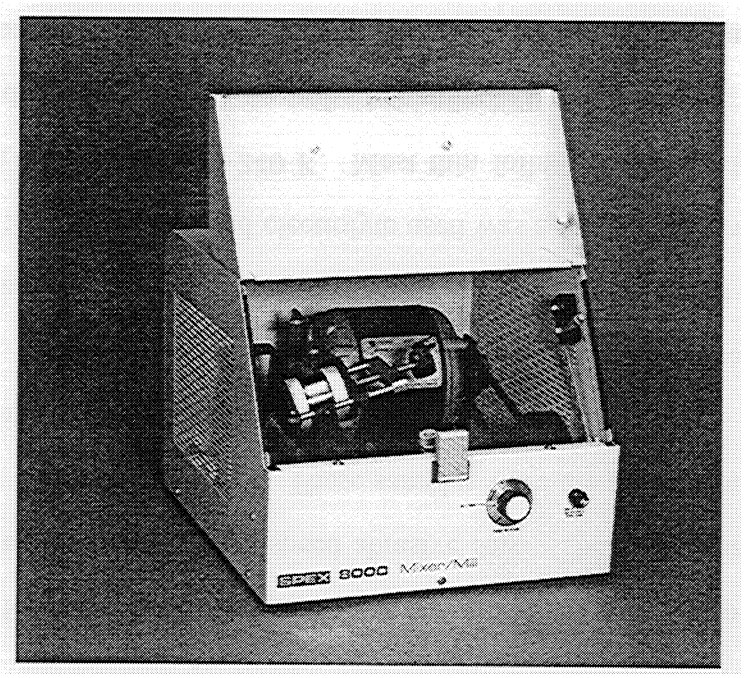

Figure 5. SPEX 8000 Mixer/Mill used in the high-energy ball milling of Cu-Cr-Nb alloys.

The powders were consolidated while at the Rockwell Science Center. Powders were densified by uniaxial hot pressing at ~810°C and 100 MPa for 3 hours. An Instron 1125 load frame with an attached vacuum furnace was utilized. Pressures of ~1-5 × 10^{-6} Torr were typically achieved. (Heat-up and cool-down times were usually ~12 min. and ~1.5 hr, respectively.) A high-temperature Ni-base superalloy punch and die fixture was used. The ends of the punches and interior die walls were coated with BN spray as a lubricant and release agent. The dimensions of the punch and die were specified so as to produce ~1.35 cm diameter buttons. The buttons typically had a thickness of about 4.5 ± 1 mm.

2.3. Specimen Preparation and Analytical Techniques

2.3.1. As Atomized and Extruded Cu-Cr-Nb

As-atomized powders, as-extruded, and extruded and heat treated specimens were mounted and prepared by standard metallographic techniques for optical and/or scanning electron microscopy. The cold-mounted (powder) and hot-mounted (extruded bar sectioned transverse to extrusion direction) samples were first ground with 240, 320, 400, and 600 grit SiC paper. This was followed by polishing on nylon cloth with 6-μm diamond polishing compound. Lastly, 0.05-μm alumina colloidal suspension was used on a napped cloth for the final polishing step. A solution of 25 ml de-ionized water (DI H_2O), 25 ml ammonium hydroxide (NH_4OH), 20 ml 3% hydrogen peroxide (H_2O_2) and four pellets of sodium hydroxide (NaOH) at room temperature was used for etching [11].

Samples for transmission electron microscopy (TEM) were cut perpendicular to the extrusion direction using a high-speed abrasive saw. The sliced material was thin enough to punch 3 mm disc samples. These samples were then mechanically thinned to ~125 μm – starting with 400 and finishing with 2000 grit SiC paper – using a Gatan lapping fixture. Such prepared specimens were finally electrolytically thinned to perforation utilizing a Struers Tenupol-II Dual-jet Polisher operated at an applied potential of 10-15 V. The preferred electrolyte used was a methanol-20 vol% nitric acid bath chilled to a temperature of ~240 K. Most thin foils revealed oxide and/or debris formation and redeposition during electrolytic thinning. These foils were further cleaned in a Gatan 600 or VCR XLA/2000 Ion Mill using 4-5 keV argon ions and a current of ~0.5 mA.

For TEM analysis a Philips EM400T electron microscope (NASA-Lewis) operated at 120 kV and a Philips EM400 electron microscope (U. C. Davis) operated at 100 kV were used. The Philips EM-400T TEM was equipped with a Kevex ultrathin

window energy dispersive spectrometer (EDS) system. The precipitates were characterized using convergent beam electron diffraction (CBED) analysis, selected area diffraction (SAD) patterns and XEDS spectra. Finally, for scanning electron microscopy (SEM), a JEOL 6100 SEM (NASA-Lewis) was used, typically at 15 kV.

2.3.2. As-Atomized, Mechanical Milled and Hot Pressed Cu-Cr-Nb

As-atomized and as-milled powders were cold-mounted and the as-atomized/hot pressed and as-milled/hot pressed buttons were cross-sectioned (into semi-circular discs) and hot-mounted with rectangular cross-section exposed for metallography. Metallography was performed in a similar manner as the extruded material (above), except a final 1200 grit SiC paper was used, followed by 15 then 3 μm diamond slurry. The etchant used was a solution of 25 ml DI H_2O, 25 ml NH_4OH and 15-20 ml 3% H_2O_2.

Specimens for TEM examination were sliced – parallel to initial cross-sectional cut – from the halved hot pressed buttons with a slow-speed diamond saw. These rectangular slices were thin enough to punch 3 mm disc samples. These samples were then mechanically thinned to 100-150 μm – starting with 400 and finishing with 2000 grit SiC paper – using a Gatan lapping fixture. Such prepared specimens were finally electrolytically thinned to perforation utilizing a Struers Tenupol-3 Dual-jet Polisher operated at an applied potential of ~15 V. The remainder of preparation was basically the same as for the above extruded Cu-Cr-Nb. Finally, as-milled (2 and 8 hr) Cu-8 Cr-4 Nb powders were prepared for TEM. This was accomplished by incorporating the powder into a Gatan G-1 epoxy matrix, which was first blended with a mixture of 70% graphite (by volume) and 30% Al_2O_3 powders. (The graphite provided adequate conductivity, the alumina ensured extra strength.) The overall blend was inserted into and allowed to cure in a 3.175 mm inner-diameter plastic tube. Thin slices were cut and center dimpled to

about 20 μm. They were then ion milled to perforation in a Gatan 600 Ion-mill, at a gun voltage of 5 kV, a current of 1 mA and an angle of ~10°.

For TEM analysis of the above prepared representative specimens, a Philips CM30 electron microscope (Rockwell Science Center) was utilized with an accelerating voltage of 300 kV. The second-phase particles were, again, characterized using CBED and SAD analysis. SEM was carried out with a Philips XL30 FEG field emission microscope operated at 15 keV with a Gatan digital imaging system. X-ray diffraction (XRD) was also done, in part, for particle-phase determination. Details of XRD parameters used are given in section **2.5.2**.

2.4. PHYSICAL PROPERTY ASSESSMENT

2.4.1. As Atomized and Extruded Cu-Cr-Nb

NASA-Lewis Research Center provided tensile testing support. The extruded bars and selected aged specimens were cut and machined into tensile samples for testing at room and elevated temperatures. At NASA, tensile testing was conducted under vacuum in an Instron frame at an engineering strain rate of 6.7×10^{-3}/min. The pressure in the chamber for the elevated temperature tensile tests was less than 1.33×10^{-4} MPa. The maximum time excursion for heating specimens was less than 1 hr. A minimum of two tests was conducted at each temperature. In addition, Vickers microhardness (HV) with 100 g load and Rockwell B hardness measurements were taken at room temperature. The penetration depth for microhardness at 100 g was ~7.1 μm, significantly larger than the Bilby layer, such that the surface hardening effects due to prior mechanical polishing were negligible. The 100 g microhardness indentations produced diagonals of approximately 35 μm. The maximum grain size is ~5 μm and that of particle size is on the order of 1 μm, such that a sufficient number of grains and particles were incorporated in the indent, i.e. the microhardness values effectively averaged out the mechanical strength of the

alloy. Usually 10 measurements were taken and analyzed using standard statistical procedures.

2.4.2. As-Atomized, Mechanically Milled and Hot Pressed Cu-Cr-Nb

2.4.2.1. Mechanical (Hardness) Testing

Mechanical testing of consolidated mechanically milled/alloyed Cu-Cr-Nb specimens was carried out mainly by Rockwell B hardness measurements using Wilson and Buehler Macromet Rockwell Hardness Testers. Microhardness testing was also performed on as-milled powders and consolidated material to assess any changes in strength as a result of high temperature exposure during consolidation. This should give a good idea of stability of processed material. For such measurements, Vickers microhardness (HV) testing with 100 g load was performed with Leica and Page-Wilson Tukon Microhardness Testers. Powder hardness measurements were accomplished by testing the powders already cold mounted and metallographically prepared. Powder particle cross-sections chosen for testing had sufficiently large diameters, e.g., at least 3-5 times the indentation, so as to virtually eliminate effects of surrounding mounting material. For powder of each milling condition, most indentation sizes (and hardnesses) were consistent in value, and those that varied widely, i.e. were in obvious error, were not included in any statistical analysis. This also mitigated any mounting matrix effects.

2.4.2.2. Conductivity Measurements and Chemical Analysis

Electrical conductivity measurements were carried out with a Magnaflux Model FM-120 Conductivity Meter at Rocketdyne, a division of Boeing. For these measurements, an approximately ½ in. probe was placed on a reference annealed pure copper "standard block" for calibration. The needle gage, of arbitrary units from 1 to 100, was set to "100" for the pure copper reference. Then, the hot pressed Cu-Cr-Nb buttons (and as-extruded samples) were tested in a similar way with the needle indicating the

conductivity relative to the reference standard, i.e. percentage of the International Annealed Copper Standard, %IACS. Finally, chemical analyses (for impurity elements, etc.) were carried out on starting powders, as-atomized/hot pressed and as-milled/hot pressed (half-buttons) by LUVAK, Inc., a service provider of materials analysis in Boylston, MA.

2.5. Quantitative Characterization of Microstructural Features

2.5.1. As Atomized and Extruded Cu-Cr-Nb

2.5.1.1. Strengthening Phase Particle Size Analysis

For extruded material, particle size measurements were performed using TEM for small particles and SEM for large particles. At least 200 particles per specimen were counted while paying careful attention that only Cr_2Nb particles were selected. Particle measurements of TEM and SEM images were done using a Leica Quantimet 500 Image Analysis System. To minimize error in particle counting in TEM bright field, dislocation contrast was kept low and various diffraction conditions in the same area were used to ensure the clear distinction of particle boundaries.

2.5.2.2. Grain/Subgrain Size Analysis

Grains and subgrains were measured by a combination of direct ruler measurements and lineal analysis on TEM micrographs. The ruler method was applied mainly for Cu-8 Cr-4 Nb, for certain aging conditions, with about 50-100 grains measured. For grains size measurements performed using the lineal analysis method – primarily for Cu-4 Cr-2 Nb, the following formula was used for the mean linear intercept:

$$\bar{L}_L = \frac{L_t}{N_L M}. \qquad (14)$$

Here, L_t is the total line length, N_L is the total number of grain boundary intercepts counted and M is (for this work) the TEM magnification. The grain size was actually

taken as $D = 3/2\,\bar{L}_L$, to account for the fact that $\bar{L}_L$ is more directly related to the grain-boundary area per unit volume than to actual grain size [55]. This method was more conducive to measuring 200-300 grains.

2.5.2. As-Atomized, Mechanically Milled and Hot Pressed Cu-Cr-Nb

2.5.2.1. Strengthening Phase Particle Size Analysis

For material in powder and hot pressed form, dispersoid sizes were measured directly from SEM and TEM images for large (>0.2 μm) and small (<0.2 μm) particles/precipitates, respectively. The effects of milling (time) on large particle size was determined by lineal analysis performed on SEM prints of starting and as-milled powders. This was possible by multiplying Eq. (14) by the volume fraction of the primary particles considered for measurement. For selected milling times of hot pressed Cu-4 Cr-2 Nb, as many particles as possible were chosen (~200) and measured directly off TEM negatives via image analysis (e.g. NIH Image software).

2.5.2.2. Grain/Subgrain Size Analysis - XRD Line Broadening vs. Lineal Intercept Method

For phase identification and crystallite/subgrain/grain-size analyses, X-ray diffraction (XRD) was carried out. The equipment used was a Scintag XDS-2000 X-Ray Diffractometer operated in step scan mode with Cu K_α radiation (average λ = 1.54184 Å), at 45 kV and 40 mA. The incremental step size was typically 0.02° 2θ, with a 10-sec. collection time per step. The x-rays were collected using a 0.2 mm receiving reference slit. The Warren-Averback method was used for substructure characterization via analysis of (111)/(222) and (200)/(400) Cu peaks. Instrument contribution to peak/line broadening was corrected for using data obtained with a LaB_6 standard. Material analyzed included hot pressed samples, plus one example of as-milled powder.

Also, for selected milling times, lineal analysis using Eq. (14) was done for comparative purposes vis-a-vis XRD/Warren-Averback results. TEM images were used in such cases.

III. RESULTS

The present study of Cu-Cr-Nb alloys generally followed a two-stage approach, as spelled out in section **1.2** and the Experimental part. That is, it began with an investigation into mechanical property and microstructural effects of high-temperature aging treatments on Cu-8 Cr-4 Nb to assess stability of extruded microstructures and correlate them with properties for different thermal treatment time/temperature conditions. The results of this study, in large part, justified the second stage of this current approach. The second set of results center on this second part pertaining to the design of new microstructures via mechanical milling, with emphasis on Cu-4/2. This portion includes processing and characterization, i.e. as-milled and hot pressed hardness values, milled/hot pressed conductivities, amount of impurity elements as functions of milling time, and corresponding microstructures.

3.1. MICROSTRUCTURE/PROPERTY BEHAVIOR OF EXTRUDED Cu-Cr-Nb

The first phase of this collective study of Cu-Cr-Nb alloys deals mainly with strengthening phase and copper grain morphology characterization as a function of elevated temperature exposure – correlated to strength – in the as-extruded form.

3.1.1. Precipitate Identification, Structure and Morphology

Figure 6 includes an SEM image and TEM images of the microstructure for as-extruded Cu-8 Cr-4 Nb alloy. Also included, as Figure 7, are TEM images of as-extruded Cu-4 Cr-2 Nb alloy. Additional optical micrographs of both as-extruded alloys are presented as Appendix A. A bimodal precipitate distribution was observed in all studied specimens. The largest particles are formed congruently from the melt and are therefore considered "primary" particles ('A' in Figures 6 and 7(b)). Many of these primary particles are observed at grain boundaries and triple points and are usually ovoid or

irregularly shaped. The secondary particles ('B' in Figures 6(b and c) and 7) are those which precipitate from solid solution during cooling subsequent to solidification. Consequently they are usually up to an order of magnitude smaller than primary particles and exhibit a roughly spherical shape. Based on such electron microscopy observations, TEM, e.g., Figures 6(b), 6(c) and 7, typically reveals the smaller of the primary particles, i.e. the 'A' particles; whereas, SEM and optical microscopy reveal the largest Cr_2Nb particles, e.g., Fig. 6(a).) Finally, diffraction contrast experiments via specimen tilting in the TEM, performed as part of particle identification, have proven both primary and secondary precipitates as incoherent.

The particles were specifically identified - in the TEM via electron diffraction (see Figures 8-10) - as the cubic C15 ($MgCu_2$-type, FCC) Cr_2Nb structure, which is the stable form of the Cr_2Nb Laves phase at low temperatures [14]. Figure 8 is a relatively low magnification TEM image of as-extruded Cu-8 Cr-4 Nb, with a corresponding SAD pattern reflecting only Cu and FCC Cr_2Nb rings. This C15 phase is also confirmed at

Figure 6 – (a) Typical SEM of as-extruded Cu-8 Cr-4 Nb alloy microstructure.

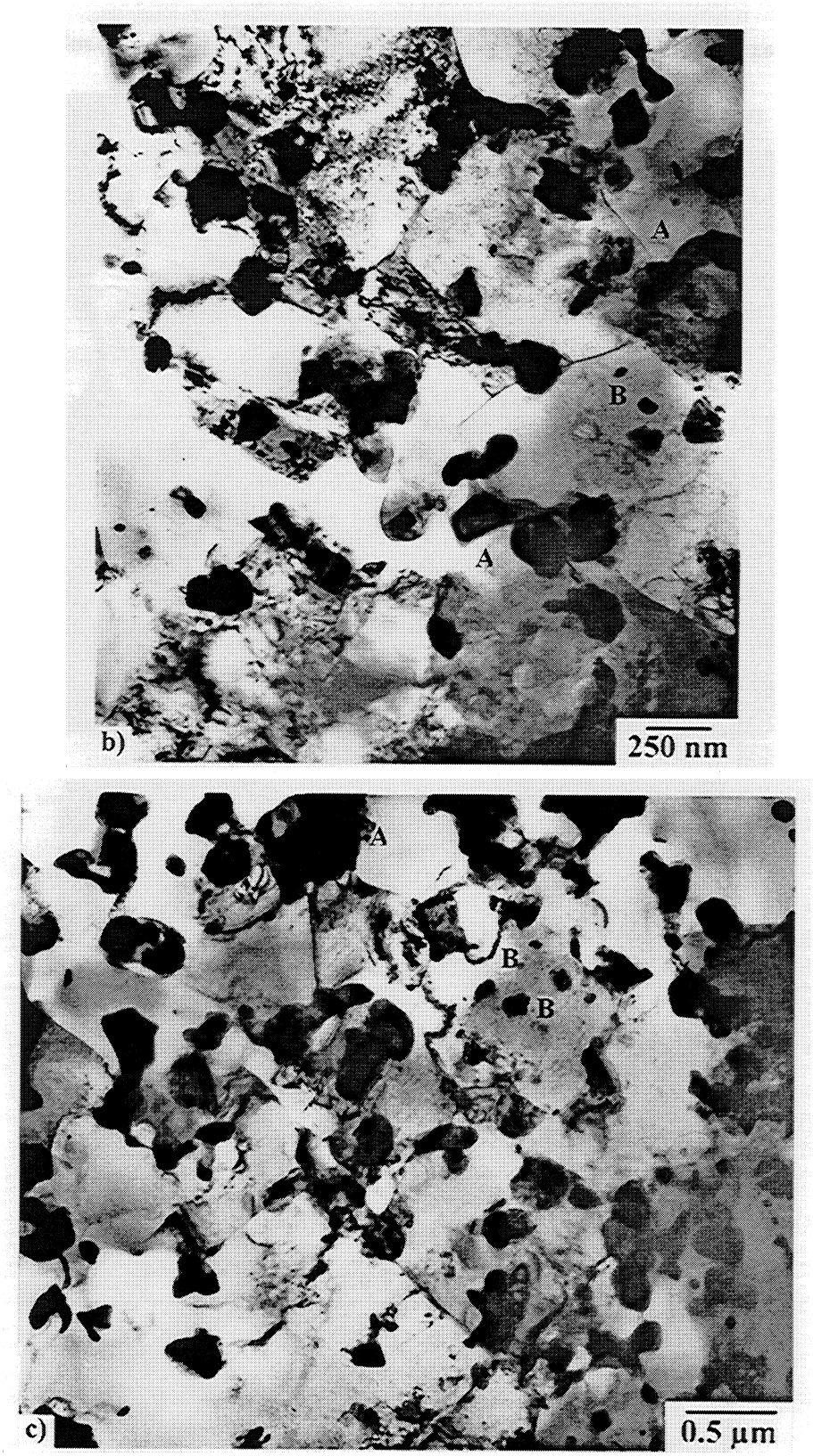

Figure 6 – (b) and (c) TEM of as-extruded Cu-8 Cr-4 Nb alloy microstructure.

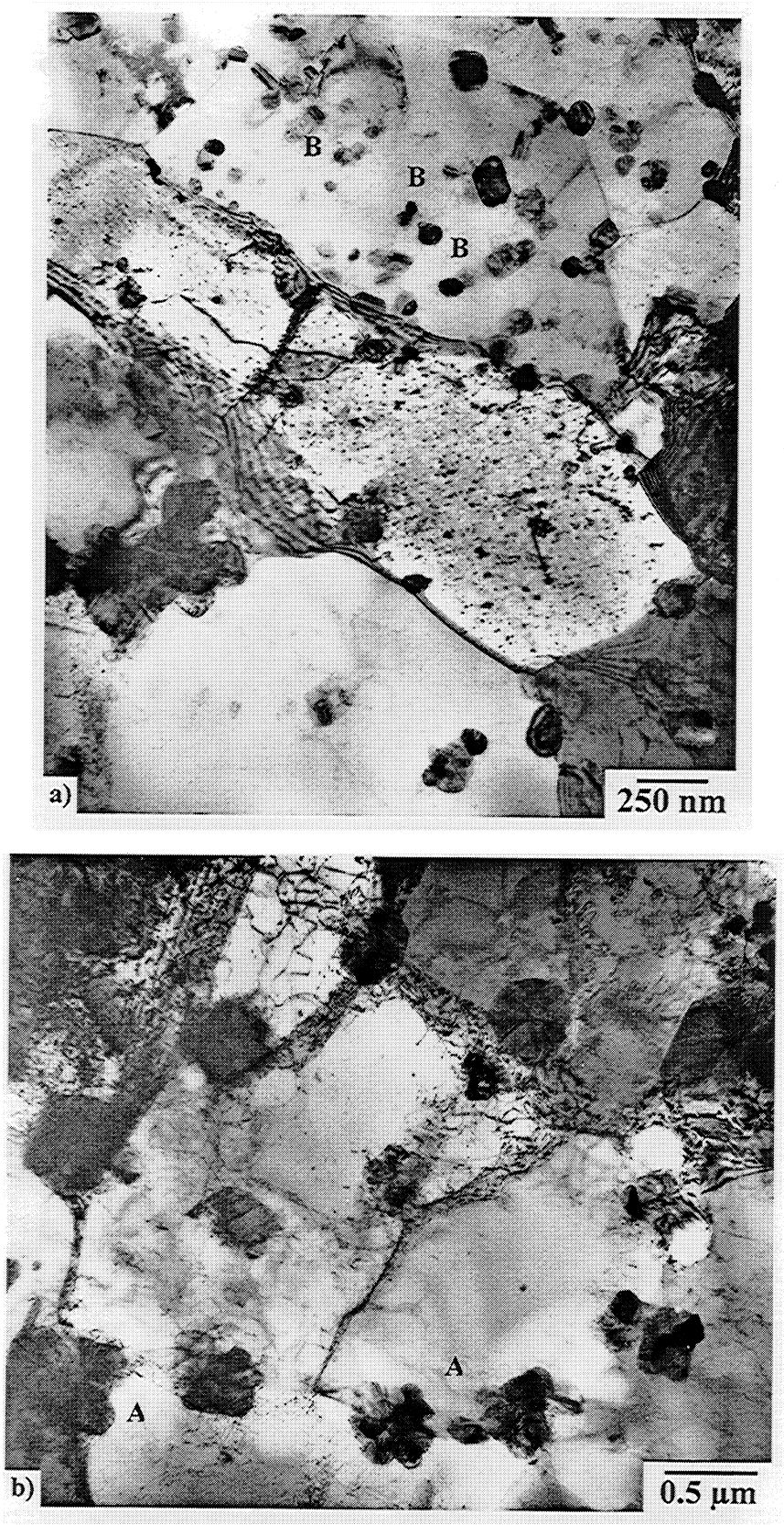

Figure 7 – TEM of as-extruded Cu-4 Cr-2 Nb alloy microstructure.

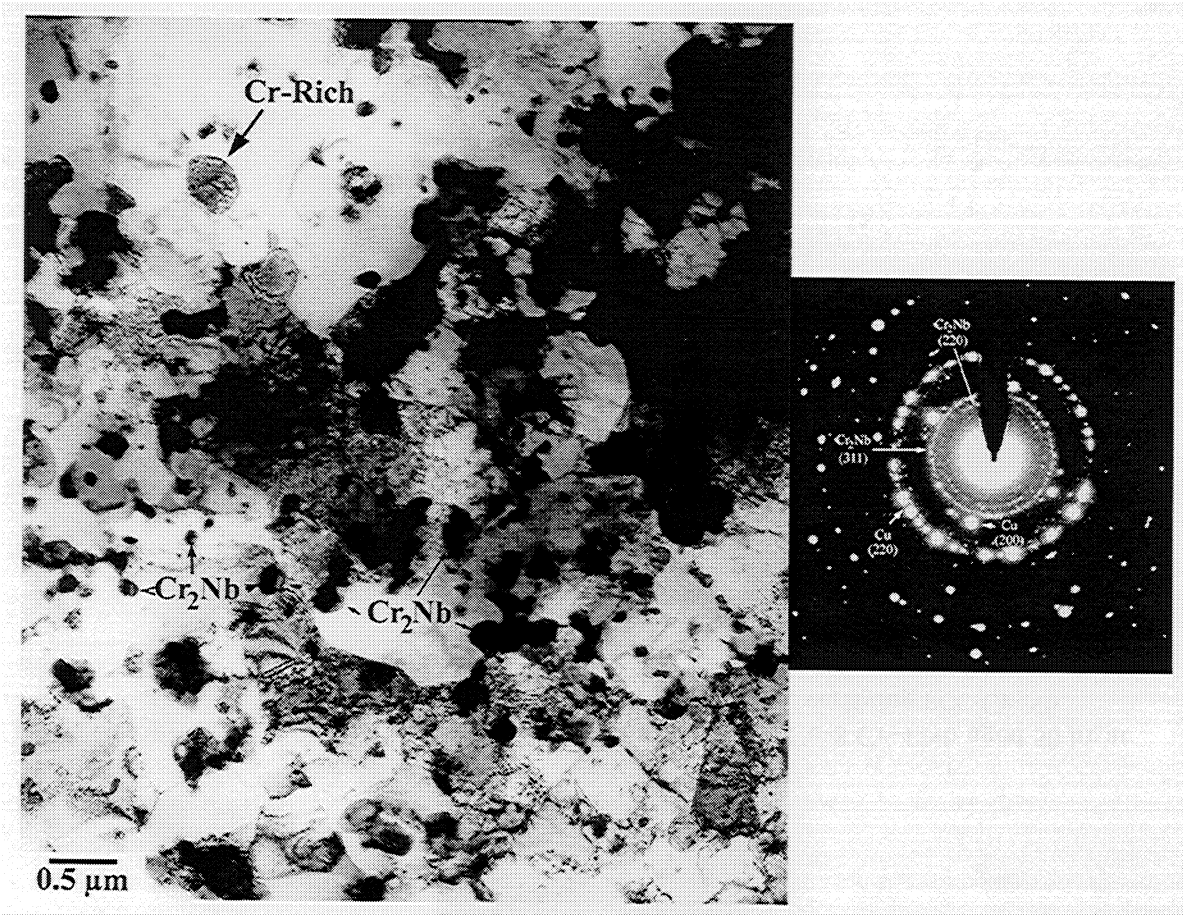

Figure 8 – TEM micrograph of as-extruded Cu-8 Cr-4 Nb with corresponding SAD ring pattern revealing FCC Cr_2Nb.

higher magnification, i.e. at the particle level, e.g., Figures 9 and 10. Figure 9 focuses on primary particles, while Fig. 10 focuses on secondary particles. The frequently observed faults of the Cr_2Nb particles were identified as twins on the {111} planes [56]. Two specific examples of such faults, among many, are identified in the TEM image of Figure 11. These faults are crystallographically-aligned and very closely resemble the twin faults proposed by Thoma and Perepezko [14]. They consider these faults typical for the polytype Laves phases. For the majority of the Cr_2Nb precipitates, the Cr:Nb ratio of 2:1

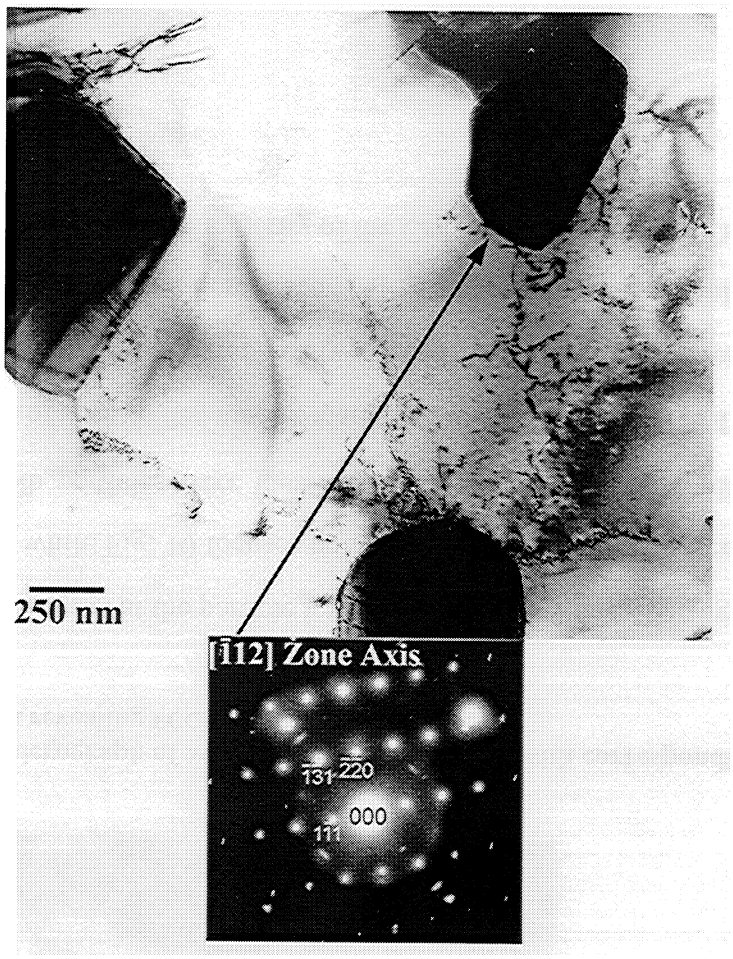

Figure 9 – Primary precipitates at triple points/boundaries in Cu-8 Cr-4 Nb aged 50 hr at 1323 K. The SAD pattern is of one such precipitate, verifying FCC Cr_2Nb.

was confirmed by XEDS measurements. Small FCC particles were also found to exhibit a Cr:Nb ratio of 1:1, but these were rare (<1%). Preliminary XEDS analysis indicated these particles also contain oxygen. More work is necessary to identify these compounds and structures.

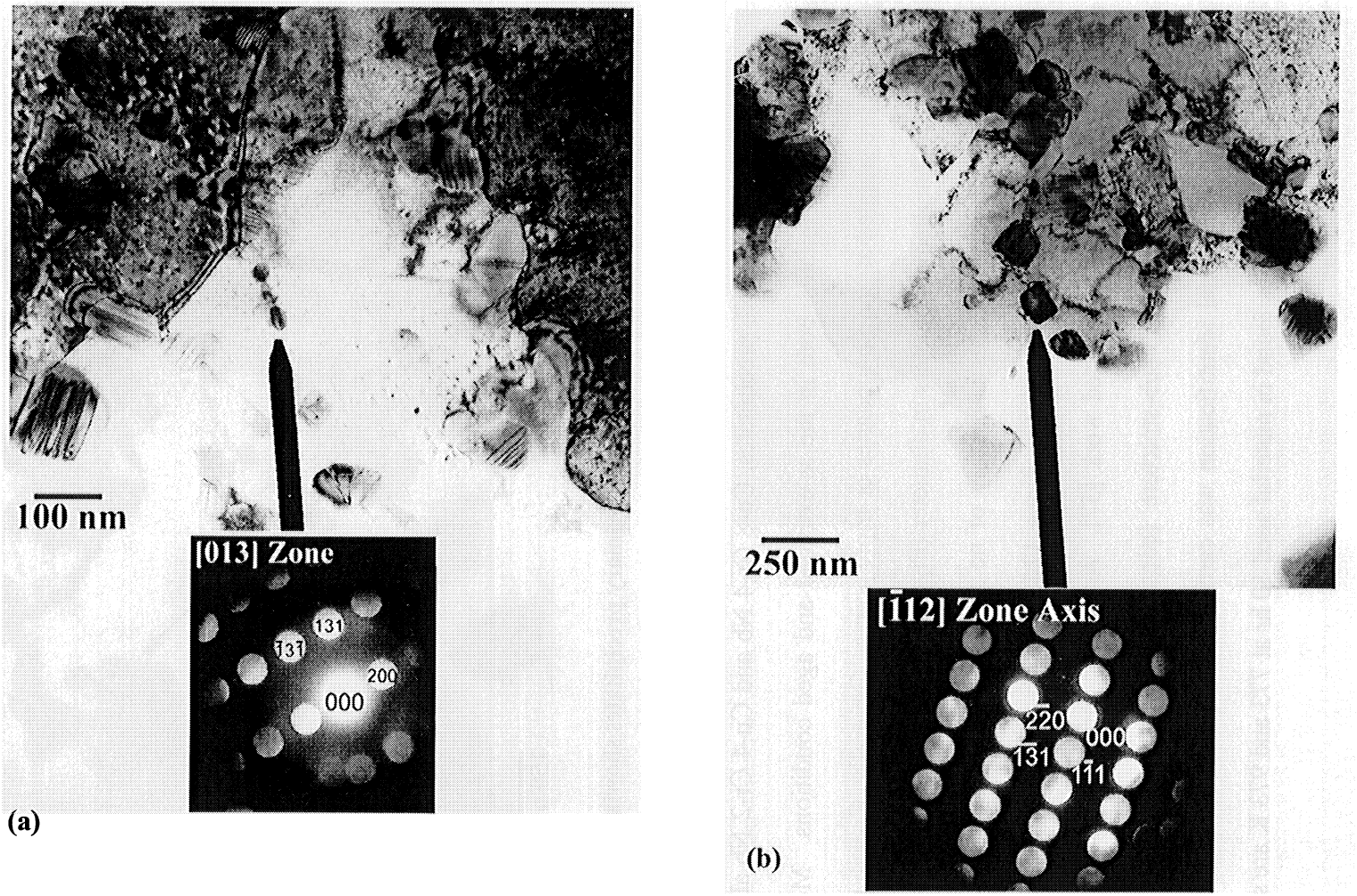

Figure 10 – Secondary precipitates in Cu-8 Cr-4 Nb aged 10 hr at 773 K. The Convergent Beam (CBED) Patterns of two particles reflect FCC (a) a [013] Zone Pattern and (b) a [$\bar{1}$12] Zone Pattern, confirming FCC-Cr_2Nb.

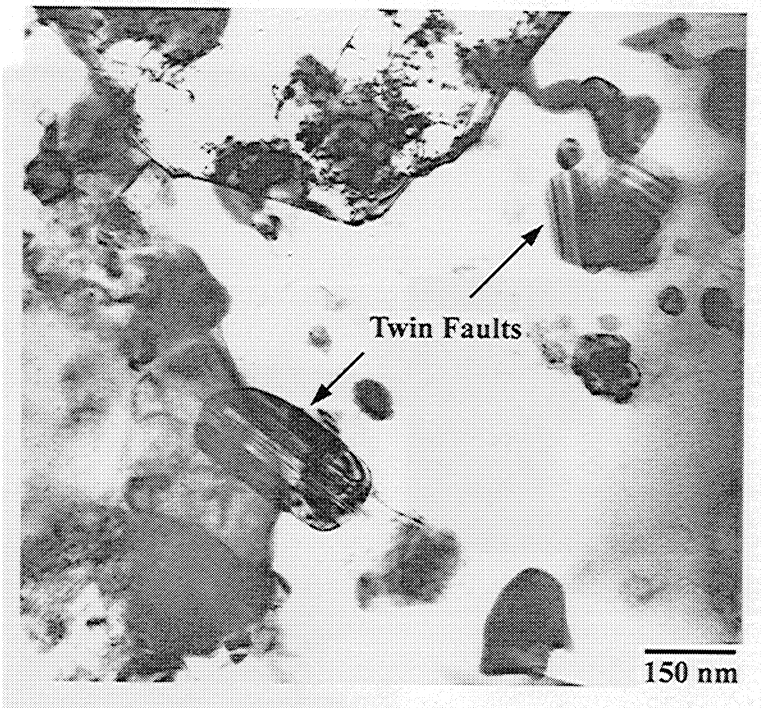

Figure 11 – As-extruded Cu-8 Cr-4 Nb with primary precipitates showing typical twin faults.

In addition to Cr_2Nb precipitates, Cu-8 Cr-4 Nb and Cu-4 Cr-2 Nb alloys feature some Cr-rich precipitates, both in the as-extruded and aged conditions. Most of these particles are situated at grain boundaries or triple points. Generally, Cr-rich particles are at least a few hundred nanometers in diameter (Figures 8, 12 and 13). Also, but to even a lesser extent, Nb-rich particles invariably of no more than 100 nm in size have been found mostly in material heat treated above 1200 K. Nb-rich particles were covered more in depth in already reported work [57]. As seen in Fig. 13, Cr-rich particles are characterized by a 'grainy' sub-structure (contrast) that was used for their initial identification. Additional identification was carried out via XEDS. XEDS spectra of "typical" Cr-rich particles found in material aged 10 hr at 773 and 973 K are shown in

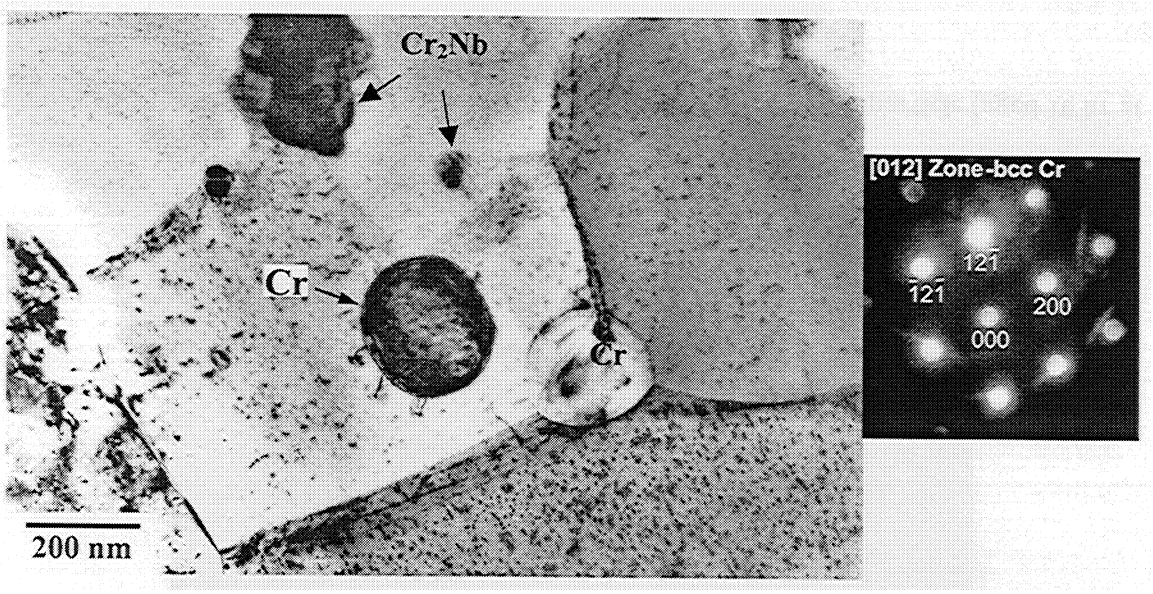

Figure 12 – A Cr precipitate found in Cu-8 Cr-4 Nb aged 10 hr at 773 K. The SAD Pattern is a [012] zone pattern of such a BCC Cr particle.

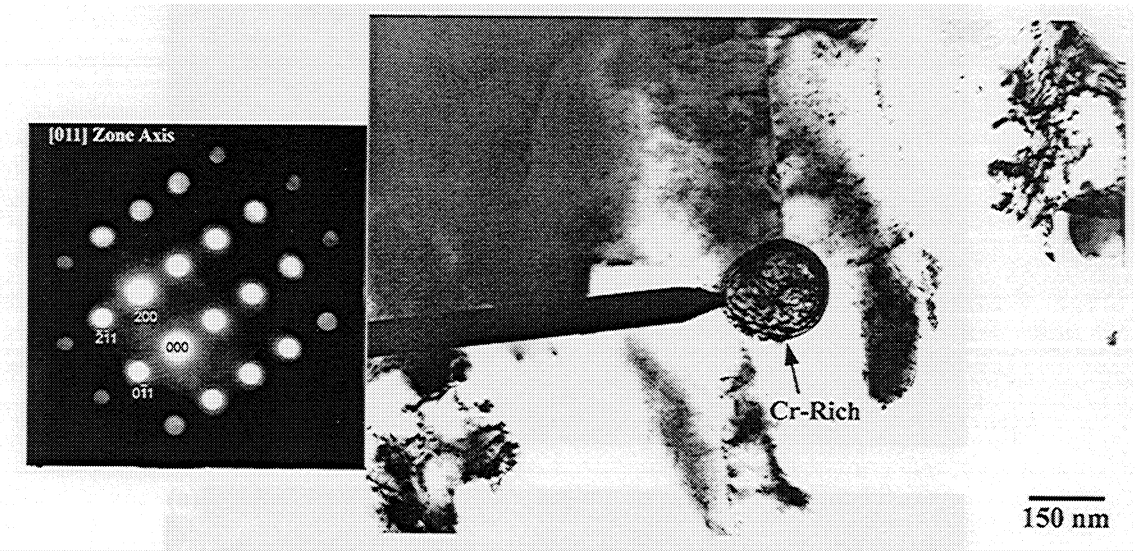

Figure 13 – A Cr-rich precipitate found in Cu-8 Cr-4 Nb aged 10 hr at 973 K. The CBED Pattern is a [011] zone pattern of such a particle.

Figure 14(b) & (c), respectively. For comparison, Fig. 14(a) shows a typical spectrum for stoichiometric Cr_2Nb. Based on the chemistry of the alloy which was intentionally Cr-rich to react all the Nb, elemental Cr precipitates were expected. XEDS analysis

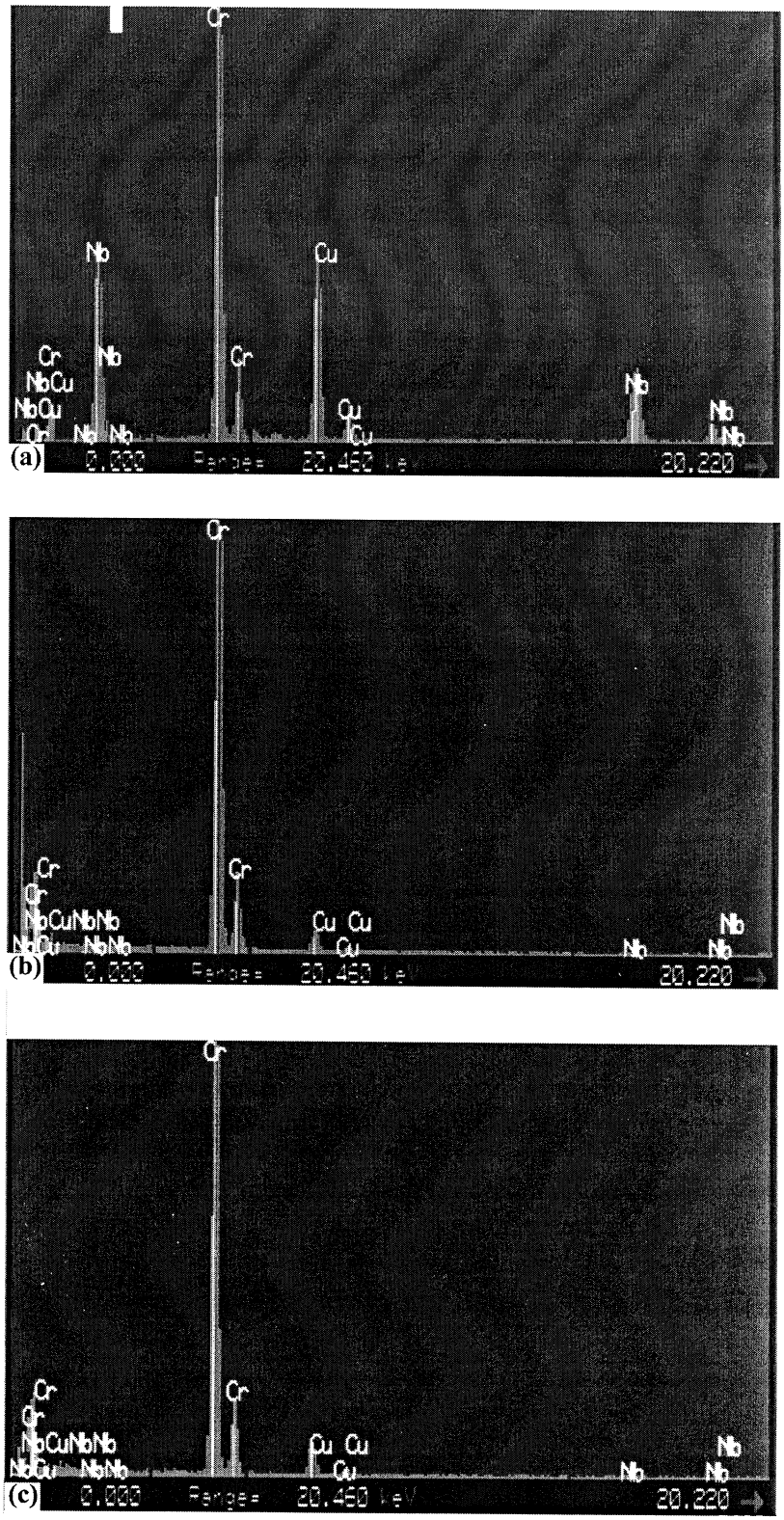

Figure 14 – EDS Spectra of (a) typical Cr_2Nb Precipitate; (b) Cr-rich particle (aged 10 hr at 773 K; and (c) Cr-rich particle (aged 10 hr at 973 K).

indicated that the Cr-rich precipitates contain more than 96 at.% Cr (Figures 13 & 14(c)) and frequently 98-99.5 at.% Cr (e.g., Figures 12 & 14(b)). Convergent beam analysis of the Cr particle of Fig. 12 confirmed the presence of BCC Cr with a lattice parameter, a, of 0.2884 nm. The same analysis of the Cr-rich particle in Fig. 13 shows a BCC pattern with $a = 0.276$ nm. (Such Cr-rich particles will also show up in hot pressed Cu-4 Cr-2 Nb, as pointed out later.)

Finally, for Cu-8 Cr-4 Nb the volume fractions of small and large precipitates, calculated using a point count (area fraction) method, are 2.17 ± 0.3 % and 10.86 ± 1.9 %, respectively [58]. Within the experimental error, the total volume fraction (13.03 ± 2.2 %) is close to the value of 14.0 %, which was calculated based on the alloy chemistry (and the assumption that virtually all Cr and Nb form C15 Cr_2Nb). Given this overall volume fraction of Cr_2Nb, and taking the density of pure copper and Cr_2Nb as 8.94 g/cm^3 and 7.66 g/cm^3, respectively, gives an overall alloy density of ~8.76 g/cm^3. The particle volume fraction in the Cu-4 Cr-2 Nb alloy was calculated in a similar manner and found to be ~7.1 %, which is basically ½ that for Cu-8/4. This gives a calculated density of ~8.85 g/cm^3 for Cu-4/2. The table below summarizes these data, including measured densities, based on Archimedes principle. The measured values are about 1% lower than theoretical values. This can be accounted for, at least in part, on the composition range of Cr_2Nb (see Fig. 1) and the existence of Cr-rich particles (7.19 g/cm^3), like those just presented.

Table II -
Densities of Cu-Cr-Nb Alloys

Copper Alloy	**Cr_2Nb** Vol. Fract., f (calc.)	**Density (Theoret./Calc.)** (g/cm^3)	**Density (Measured)** (g/cm^3)
Cu-8 Cr-4 Nb	0.14	8.756	8.646 ± 0.03
Cu-4 Cr-2 Nb	0.07	8.846	8.752 ± 0.02
Pure Cu	- -	8.94	- -

3.1.1.1. Cr_2Nb Particle Sizes in As-Extruded Cu-8 Cr-4 Nb

In order to assess the effects of aging on particle size, and more importantly, Orowan contributions to overall strength, particle sizes were determined for Cu-8 Cr-4 Nb in the as-extruded and aged conditions. Figure 15 shows the particle-size histograms for small precipitates (up to 300 nm) and large precipitates (>300 nm) for as-extruded bars. More specifically, the particle-size spectra depicted in Fig. 15(a) and Fig. 15(b) comprise such particles as the 'B' and 'A' precipitates, respectively, seen in Figure 6.

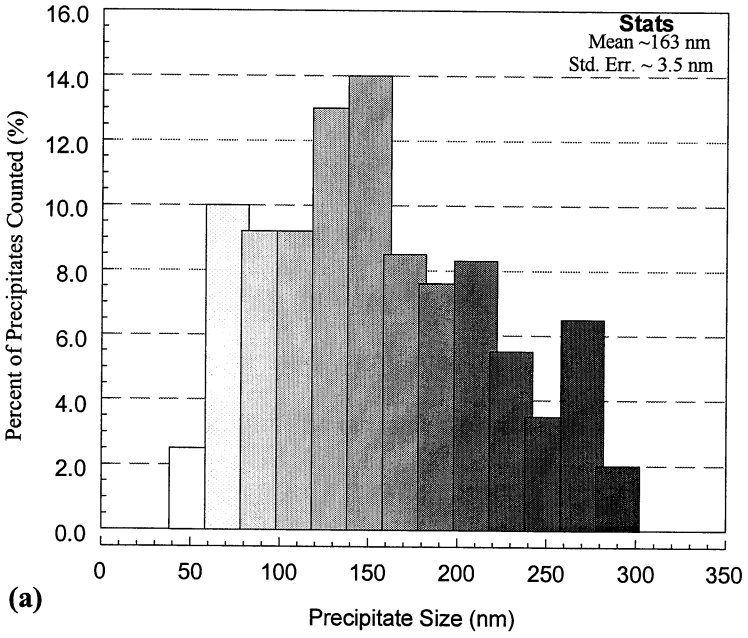

Figure 15 – Histogram of particle size distribution (PSD) for (a) small, secondary and (b) large, primary precipitates in as-extruded Cu-8 Cr-4 Nb alloy.

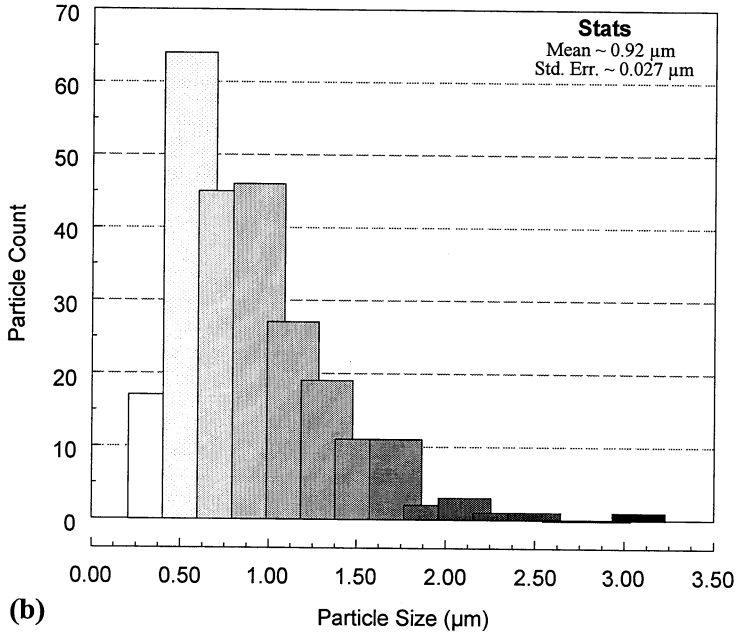

Figure 15 (Cont'd) – Histogram of particle size distribution (PSD) for (a) small, secondary and (b) large, primary precipitates in as-extruded Cu-8 Cr-4 Nb alloy.

3.1.1.2. Cr_2Nb Particle Sizes in Extruded/Aged Cu-8 Cr-4 Nb

Figures 16-18 represent resultant histograms from particle measurements and representative microstructures (TEM and SEM) for selected material aging conditions. Figure 16 represents such particle size distributions (PSD's) for secondary particulate sizes of extruded Cu-8 Cr-4 Nb in the 773 K- and 973 K-1 hr aged conditions. The average particle size is indicated for each aging condition. Aging at 773 and 973 K resulted in a decrease in the average secondary precipitate size compared to the particle-size distribution for the as-extruded condition. In this case, the decrease was due to precipitation of, in effect, second-generation fine secondary precipitates from the supersaturated solid solution formed during extrusion at 1133 K. These fine precipitates of about 20-30 nm, as depicted in Figure 17, which do not coarsen much following precipitation, shift the particle size distributions towards finer sizes and decrease the average size of the secondary precipitates. TEM observations of extruded Cu-8/4 thermally treated at 773 and 973 K for longer exposure times are illustrated in Figure 18.

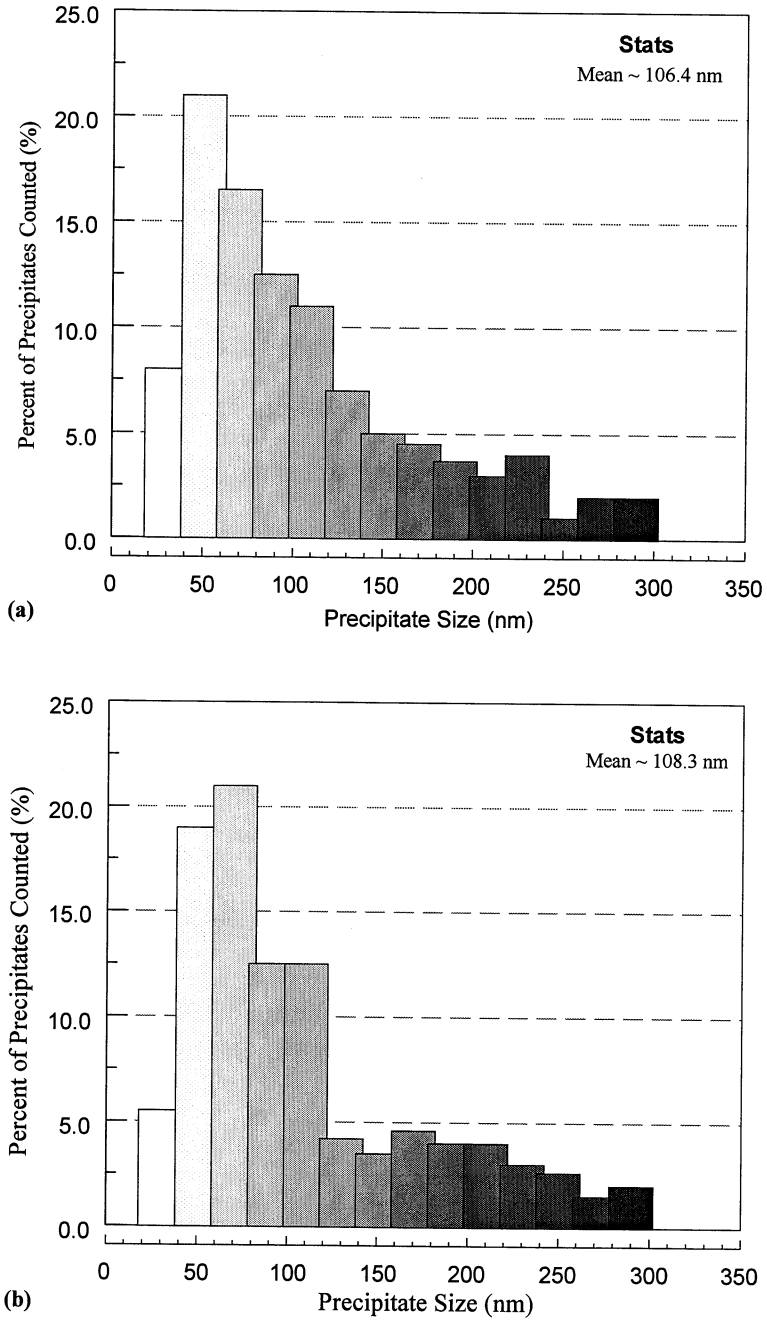

Figure 16 – Histogram of PSDs for small, secondary precipitates in extruded Cu-8 Cr-4 Nb alloy aged for 1 hr at (a) 773 K and (b) 973 K.

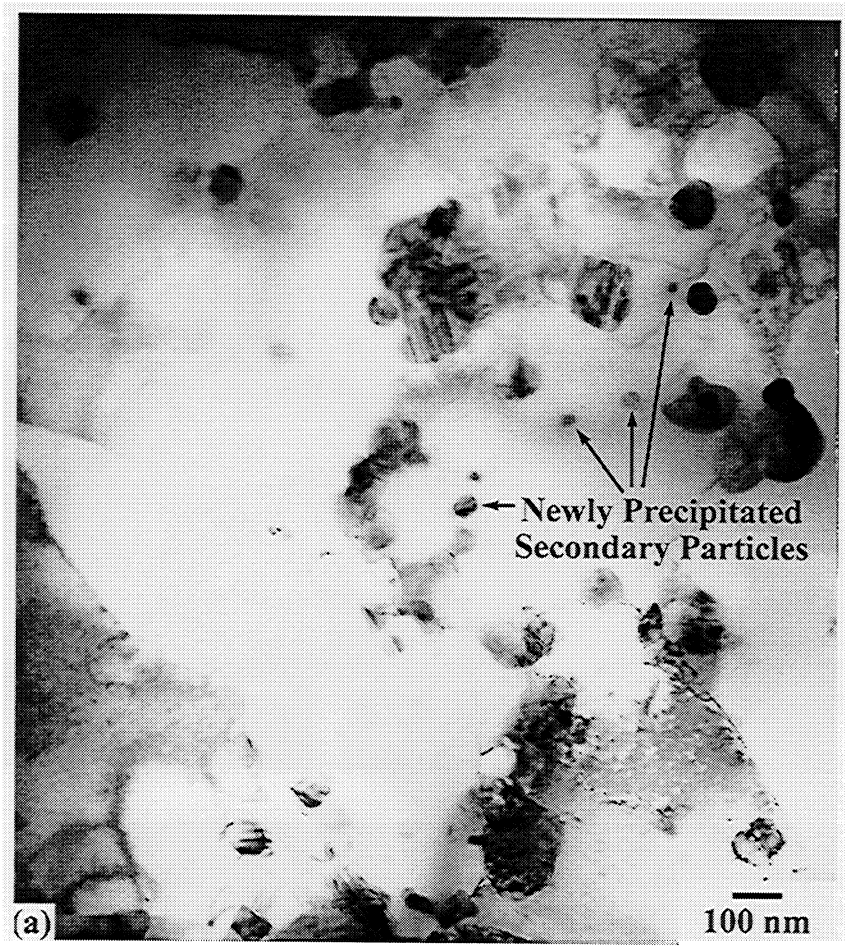

Figure 17 – (a) TEM images emphasizing secondary precipitates in extruded Cu-8 Cr-4 Nb alloy aged for 1 hr at 773 K.

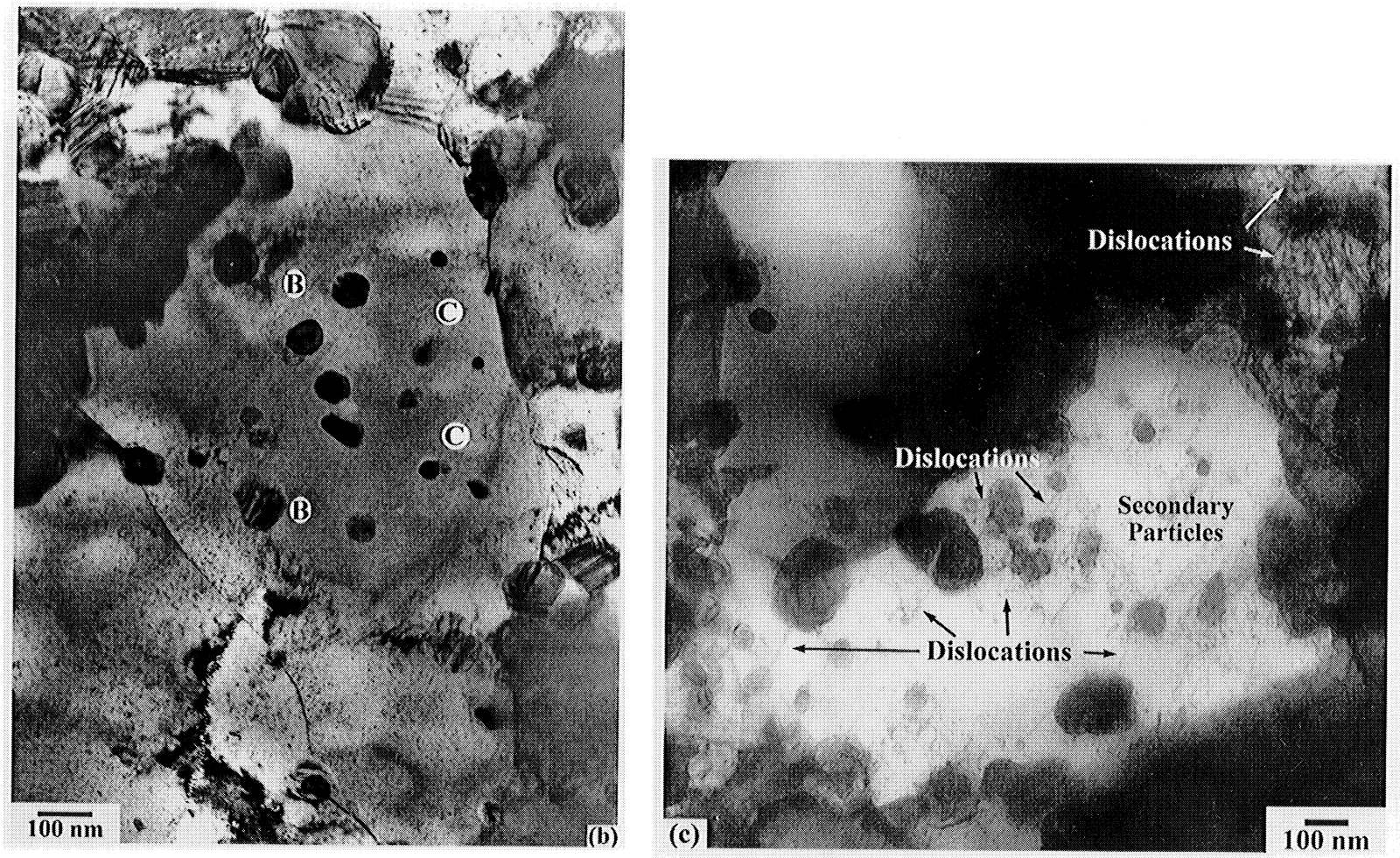

Figure 17 – (b) and (c) TEM images emphasizing secondary precipitates in extruded Cu-8 Cr-4 Nb alloy aged for 1 hr at 973 K. 'B' represents secondary Cr_2Nb particles and 'C' represents second-generation-type secondary particles. Dislocations are observed associated with small particles in (c), as shown by arrows.

Figure 18 – (a) TEM observations of microstructures in extruded Cu-8 Cr-4 Nb alloy aged at 773 K for 100 hr.

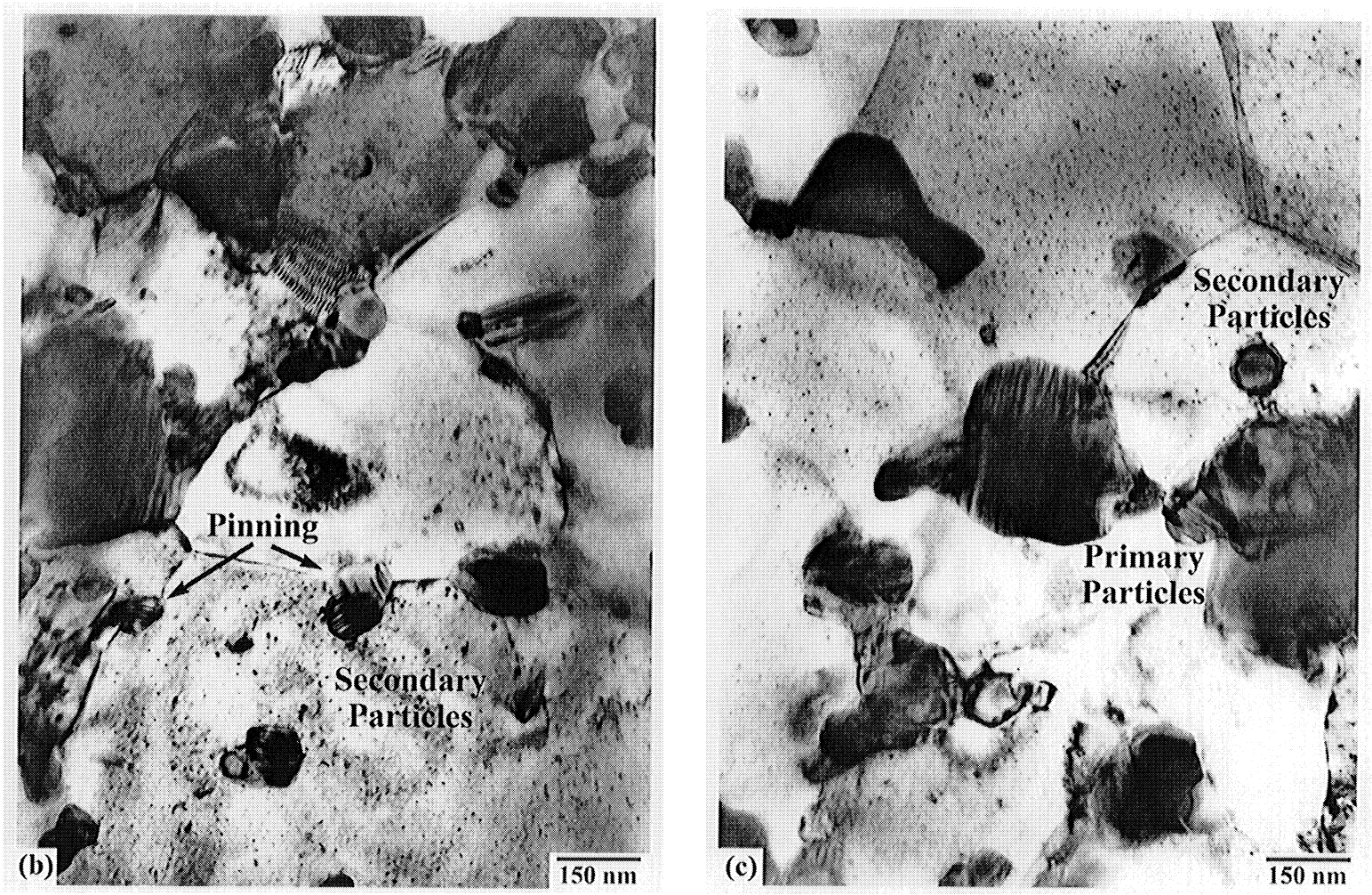

Figure 18, – (b) and (c) TEM observations of microstructures in extruded Cu-8 Cr-4 Nb alloy aged at 973 K for 50 hr.

Figure 19 presents similar histograms for secondary particle sizes after aging the alloy at 1173 K for 1 and 10 hours. At 1173 K, after aging 1 and 10 hr the average Cr_2Nb size also decreased below, but then increased to about the same as that for as-extruded

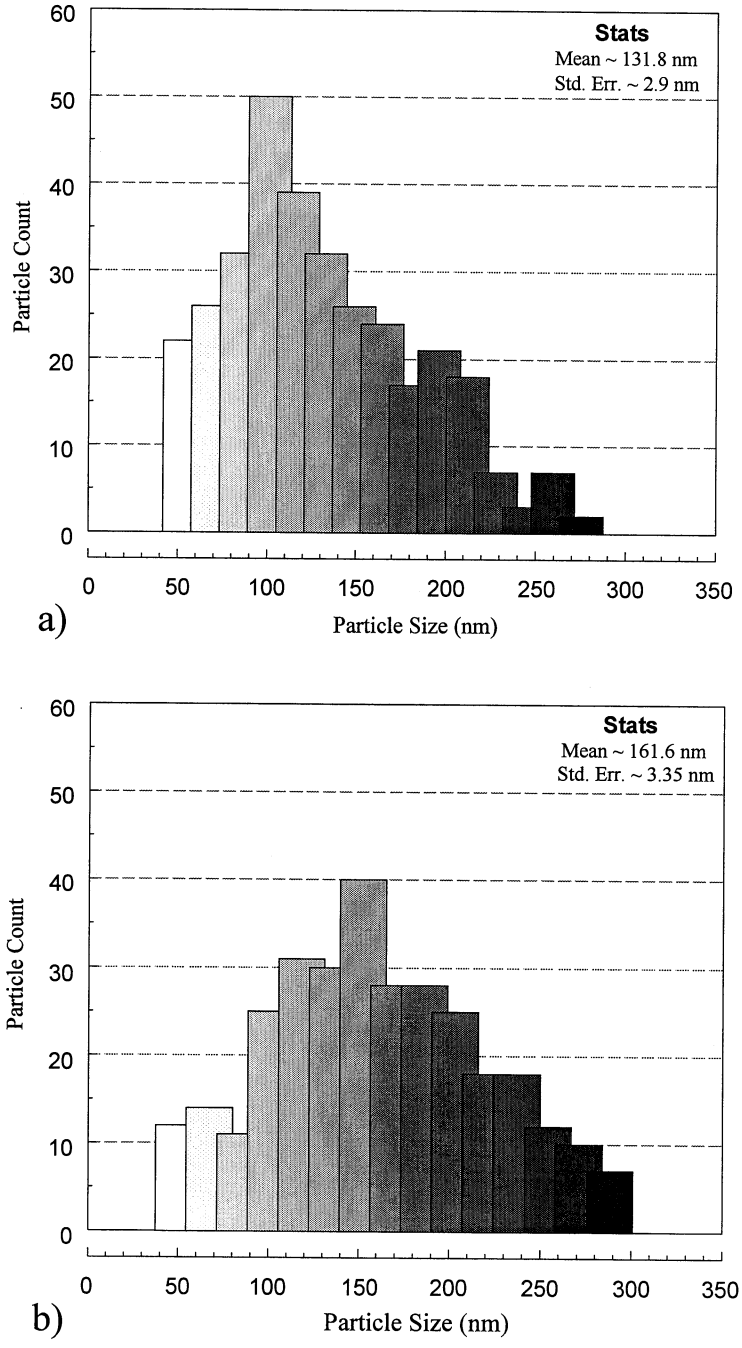

Figure 19 – Histogram of PSDs for small, secondary precipitates in extruded Cu-8 Cr-4 Nb alloy aged at 1173 K for (a) 1 hr and (b) 10 hr.

material [58]. Figure 20 is a TEM image of extruded Cu-8 Cr-4 Nb aged at 1173 K for 1 hr. The magnification is such that the majority of particles seen are secondary precipitates, which have sizes about the average given in Fig. 19(a).

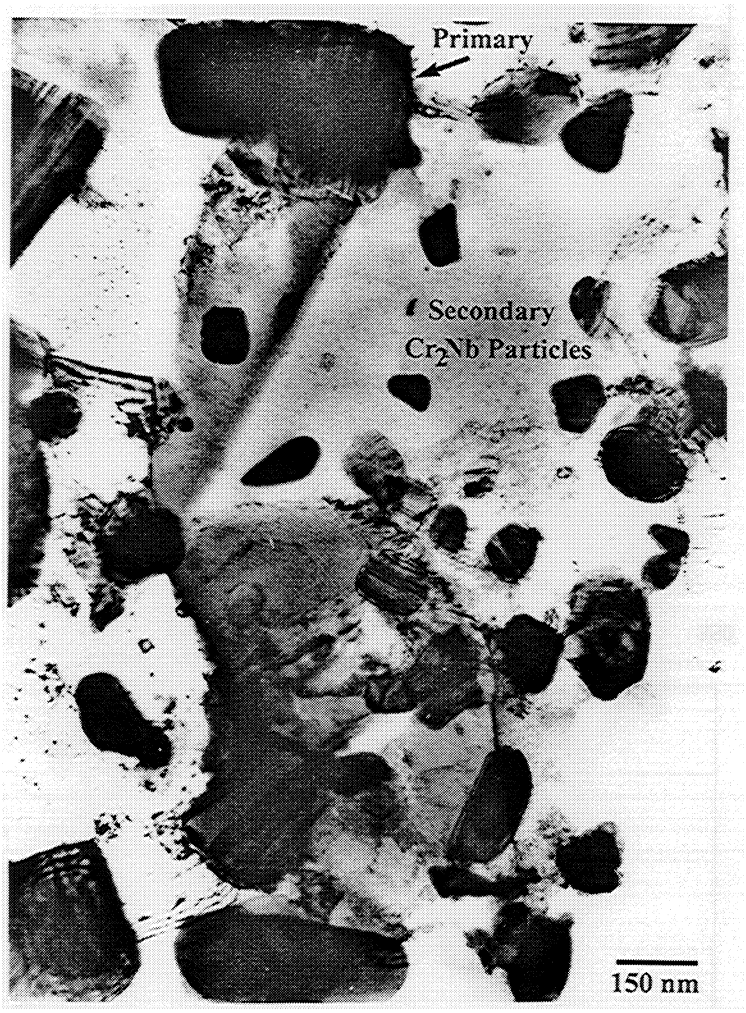

Figure 20 – High-magnification TEM of extruded Cu-8 Cr-4 Nb aged at 1173 K for 1 hr.

The histograms of the secondary and primary particle size after annealing at 1323 K for 50 hr are shown in Figure 21. The mean particle sizes for several aging temperatures and times are presented in Table III. The mean primary particle size gradually increases with annealing time as shown in Table III. SEM images revealing primary particles in Cu-8/4 aged at 1323 K for 1 and 50 hr are given in Figure 22. Results from aging at 973 K presented in Table III show that after 50 hr of coarsening the

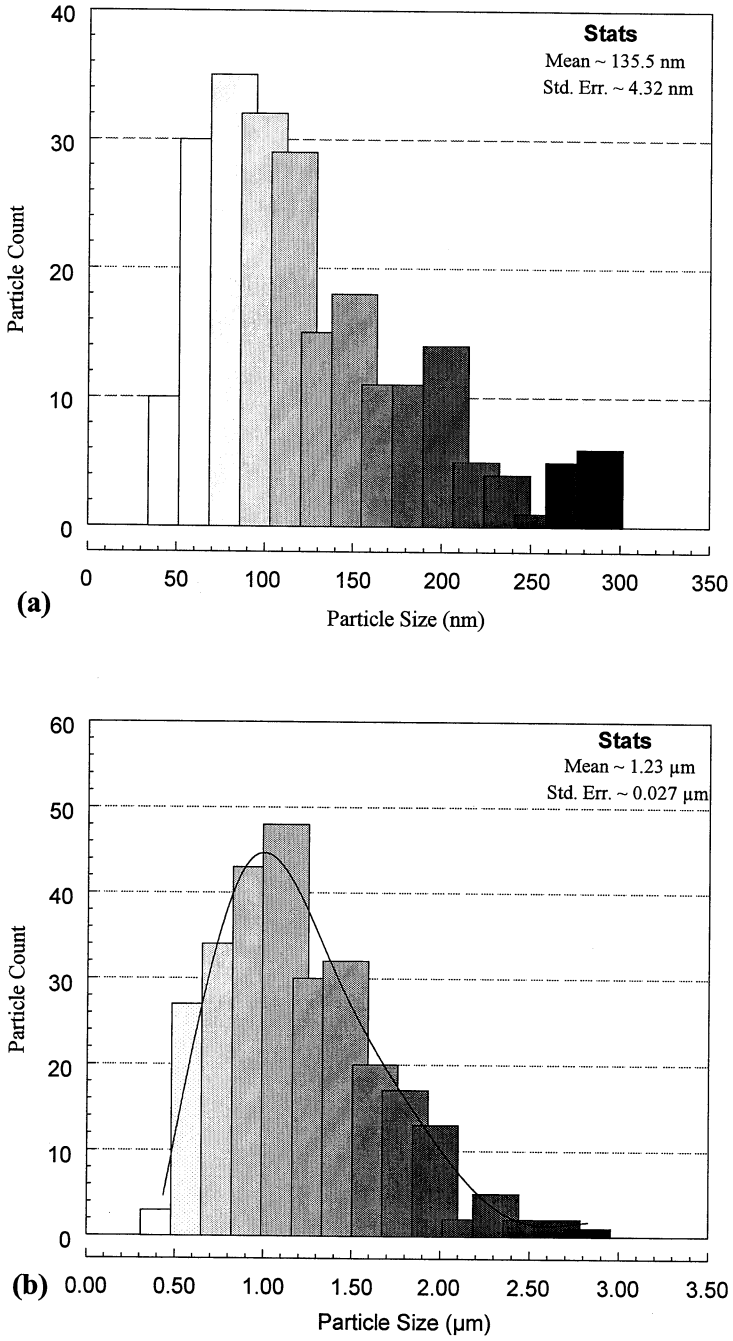

Figure 21 – Histogram of PSDs for (a) small, secondary and (b) large, primary precipitates from extruded Cu-8 Cr-4 Nb alloy aged at 1323 K for 50 hr.

primary particle size is not significantly different for aging temperatures of 973 K and 1323 K. Again, notice that the secondary precipitates actually experience a slight decrease in size for essentially all temperatures for 1 hr, and even for 1323 K for 50 hr, compared to as-extruded results. Figure 23 is a TEM image typifying this coexistence of

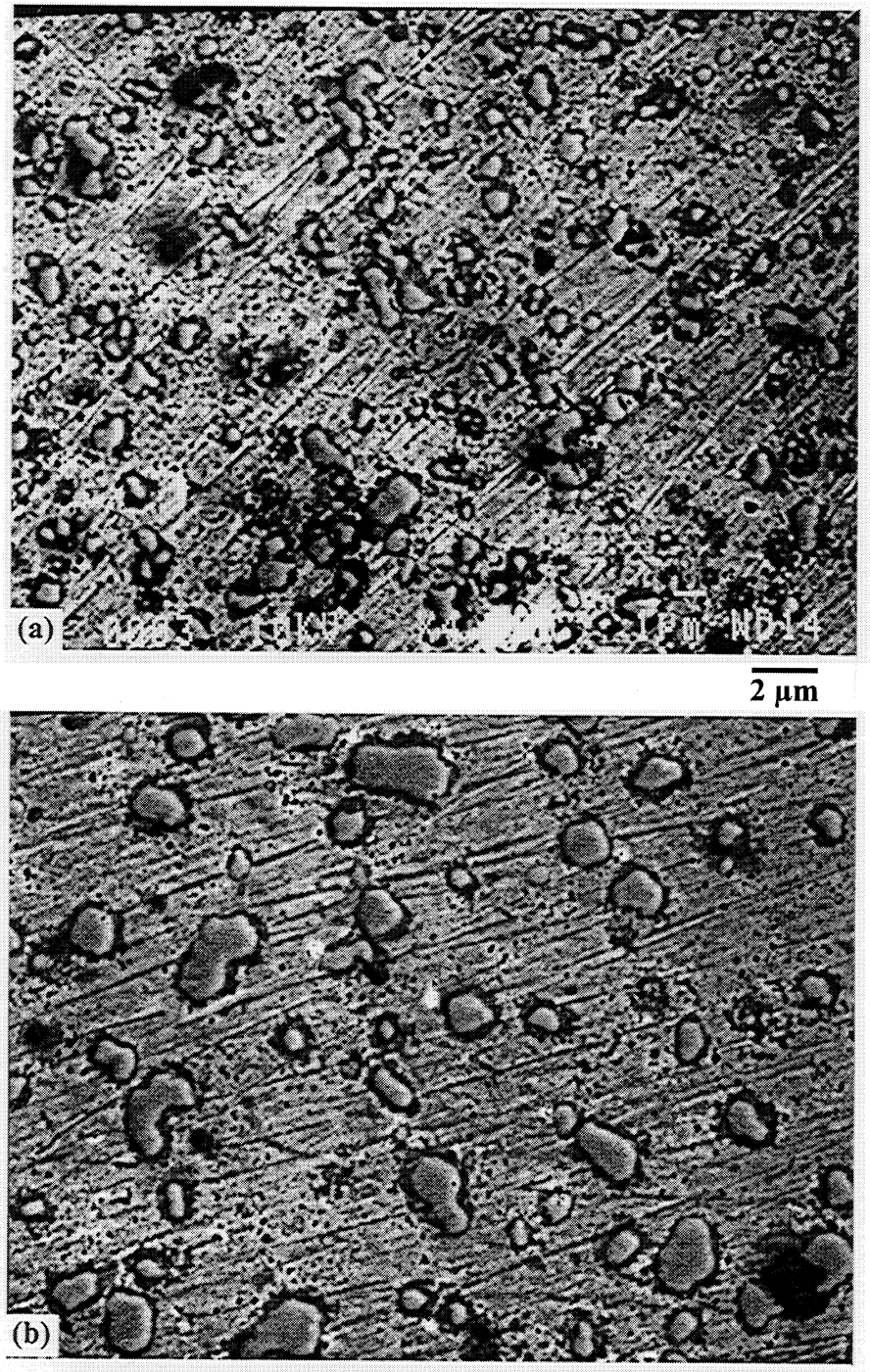

Figure 22 – SEM micrographs showing size distribution of large, primary precipitates for extruded Cu-8 Cr-4 Nb alloy aged at 1323 K for (a) 1 hr and (b) 50 hr.

both first-generation ('B') and smaller, second-generation ('C') secondary precipitates that results in a reduced overall average size. This is expanded on later in the Discussion.

Finally, it is of a statistical interest to note how a majority of the particle size distributions tend to follow a log-normal distribution; a log-normal curve fit is explicitly drawn in Fig. 21 (b).

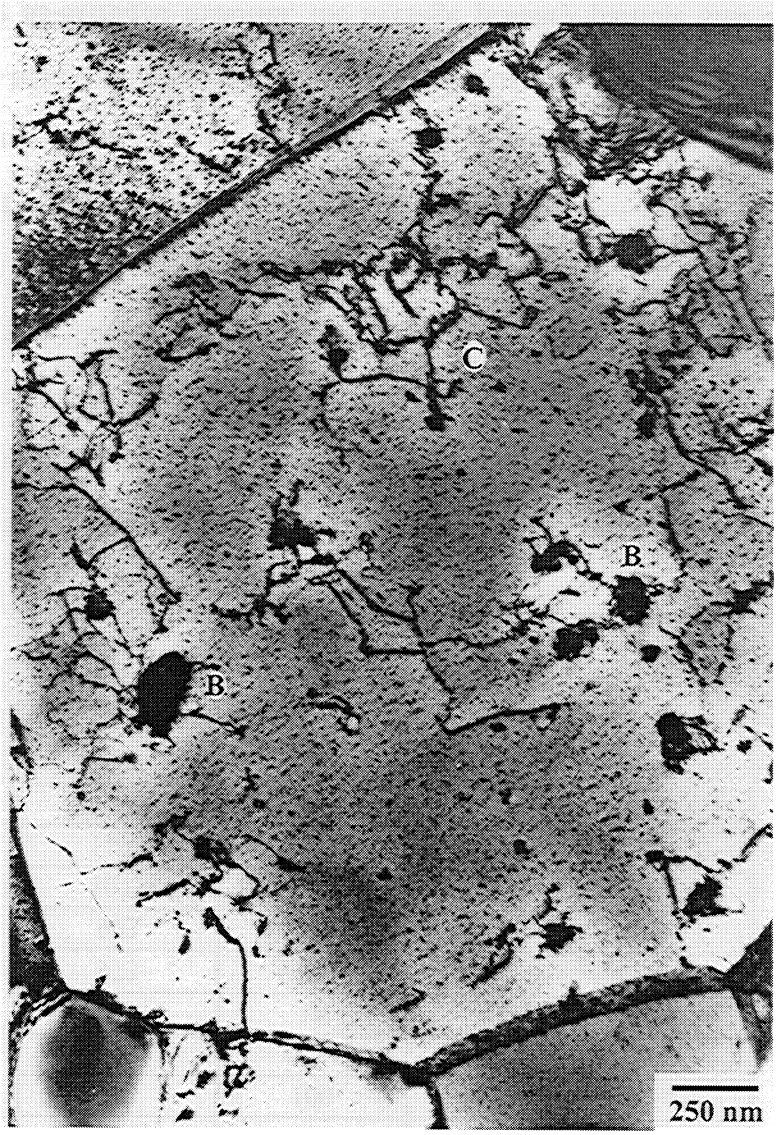

Figure 23 – TEM micrograph showing first-generation ('B') and second-generation ('C') secondary particles for extruded Cu-8 Cr-4 Nb alloy aged at 1323 K for 50 hr.

Table III –
Effect Of Aging On Cr_2Nb Precipitate Mean Size

Aging Temperature (K)	Aging Time (h)	Mean Precipitate Diameter	
		Primary (μm)	Secondary (nm)
As-Extruded		0.92 ±0.03	163 ± 7
773	1	- -	106.4
773	100	- -	156.5
973	1		108.3
973	10	- -	~130
973	50	0.93 ±0.06	132.4
973	100	- -	148 ± 6
1073	100	- -	169 ± 17
1173	1	- -	132 ± 6
1173	10	- -	162 ± 6.7
1323	1	0.61 ±0.01	185.9 ± 8.8
1323	10	- -	155.4 ± 9
1323	50	1.23 ±0.03	135.5 ± 8.6
1323	100	1.35 ±0.03	- -

As seen in Table III, the secondary particles do shift towards larger sizes with increasing aging time for up to 1173 K. For 1073 K, only 100 hr aging was looked at, which has an average secondary-particle size of 169 ± 17 nm. As expected, this value compares well with that for as-extruded particle size since the total thermal excursion of the two specimens may be considered equivalent [58]. The secondary-particle sizes for Cu-8 Cr-4 Nb as-extruded material subjected to 100 hr at temperatures up to 1073 K remain in the same range as for 773 K. Furthermore, this emphasizes again the sluggish coarsening kinetics in this temperature range. Although some coarsening occurs when compared to as-atomized or as-extruded material, the average primary particle size after 100 hr at 1323 K also remains on the same order of magnitude. This result illustrates the sluggish coarsening process of the primary Cr_2Nb precipitates. Due to this slow coarsening of both the primary and secondary particles, a sufficient size difference between primary and secondary particles still exists even after prolonged exposures at very high

temperatures. This current observation confirms a previous arbitrary experimental cut-off value of 300 nm that was considered for the difference between primary and secondary particles [58]. Finally, from Table III and the micrographs, the primary particle sizes range from ~3-10 times the secondary particles sizes.

3.1.2. Matrix Grain Structure

In Cu-8 Cr-4 Nb the copper matrix displays a recrystallized equiaxed grain structure in the plane perpendicular to the extrusion direction at all temperatures used in the present study, e.g., Figure 24. Optical metallography of the bars in the longitudinal

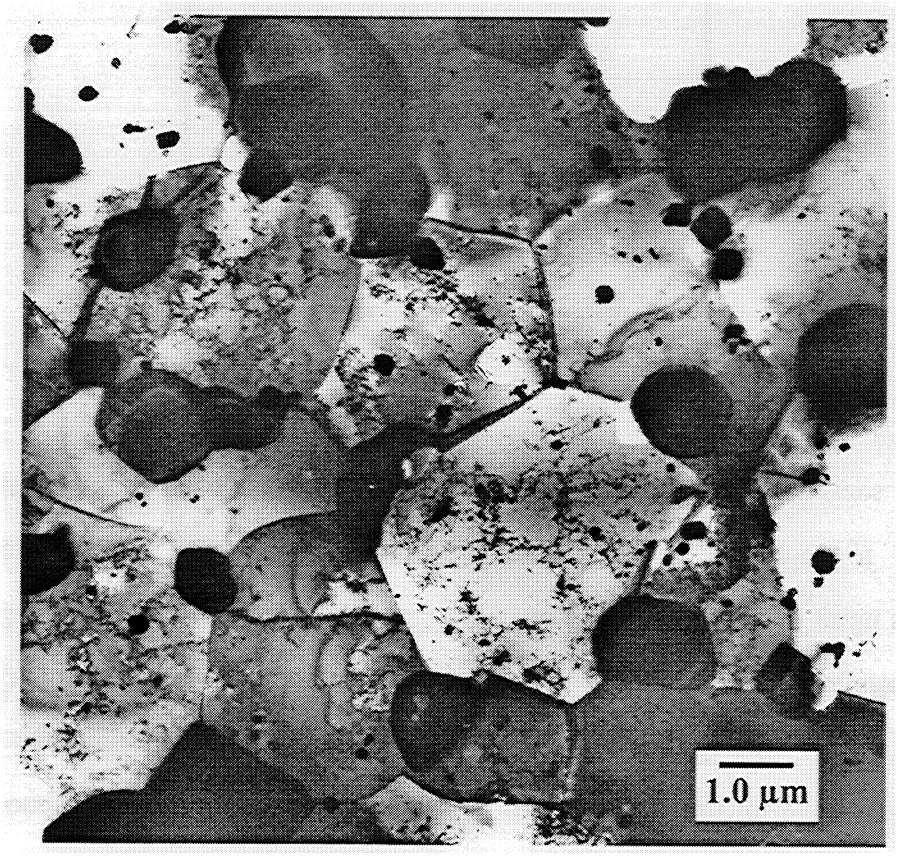

Figure 24 – Matrix grain structure in Cu-8 Cr-4 Nb alloy (transverse to extrusion direction) after aging for 100 hr at 1323 K.

direction did indicate elongation of the copper grains in the extrusion direction. The aspect ratio of the grains in the longitudinal direction was ~4.0. The grain size ranges from ~0.2 to 2.6 μm in the plane perpendicular to the extrusion direction for the as-extruded condition, with the average being ~0.9 μm and 1.53 μm for Cu-8 Cr-4 Nb and Cu-4 Cr-2 Nb, respectively. Aging up to 973 K did not significantly change the value for Cu-8 Cr-4 Nb [58]. The average grain size increased slightly to 1.6 μm after 10 hr at 1173 and 2.7 μm after 50 and 100 hr at 1323 K. The maximum value of grain size in the latter specimens was ~4 μm. (Figures 23 and 24 give examples of grains of approximately average size.) Table IV contains the aforementioned grain sizes.

Table IV - Average Grain Size of As-Extruded Cu-Cr-Nb and Aged Cu-8 Cr-4 Nb

Condition	Size (μm)
As-Extruded 8/4	0.9
As-Extruded 4/2	1.53
773 K – 100 hr	0.9
1073 K – 100 hr	2.6
1173 K – 10 hr	1.6
1323 K – 100 hr	2.7 (max 3.8)

Heat treatment also resulted in grains containing only few free dislocations and straight boundaries often at equilibrium 120° angles. These are evident in Figures 24-26. Also evident in Fig. 25 are the aforementioned twin faults typically found in Cr_2Nb. Figures 24-26 also reveal primary and less frequently secondary particles residing at grain boundaries and triple points. These precipitates appear to provide effective grain-boundary pinning, as explicitly evinced in Fig. 26. Finally, Figures 17(c), 23 and 26 also show dislocations trapped by or interacting with small intragranular precipitates, even after 50 hr at 1323 K.

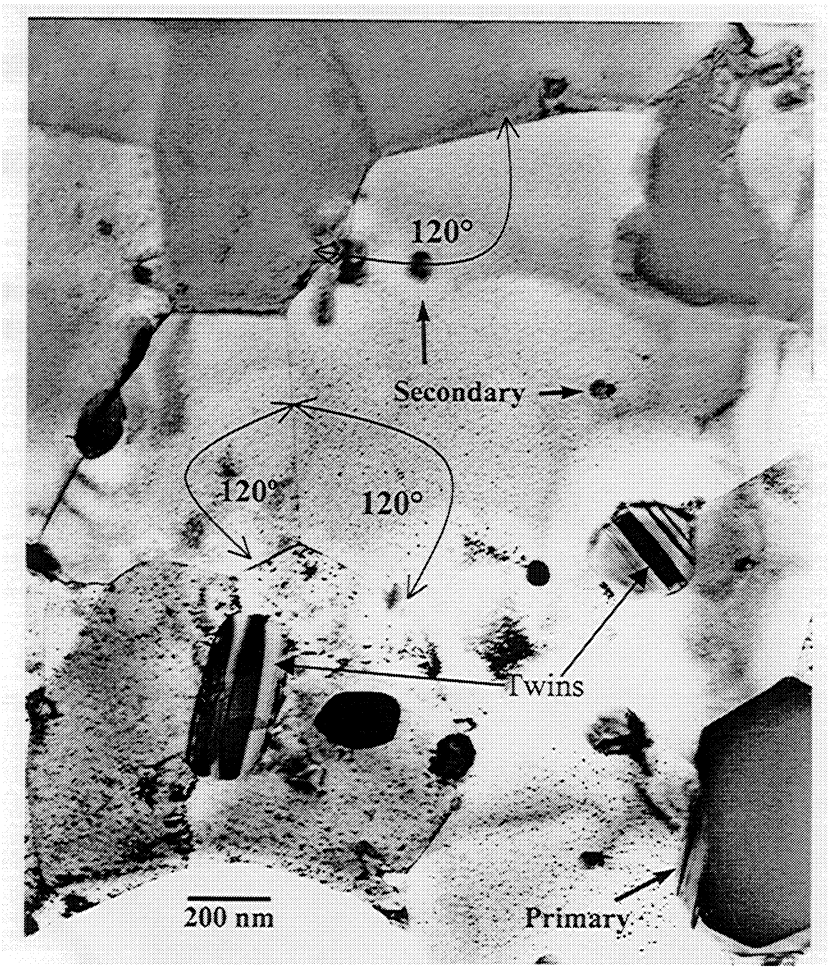

Figure 25 – Matrix and precipitate structure in Cu-8 Cr-4 Nb aged 10 hr at 1173 K. Note the equilibrium grain boundaries typically at 120° angles. Also, twins in the precipitates are, again, pointed out.

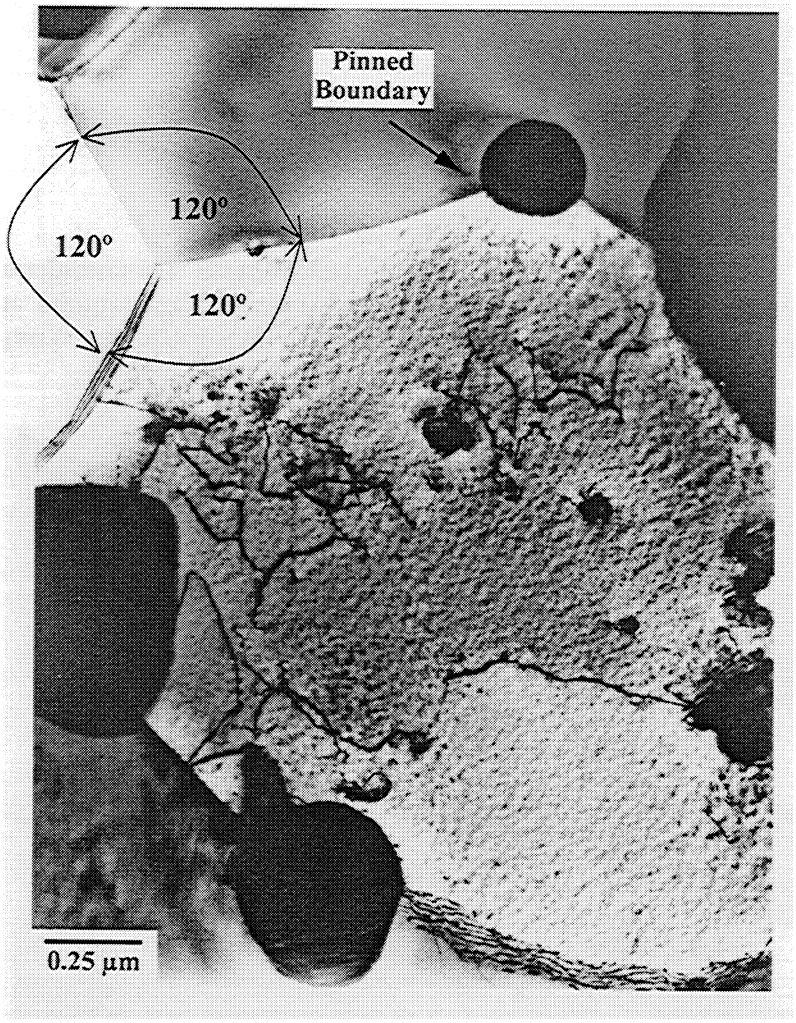

Figure 26 – Matrix and precipitate structure in Cu-8 Cr-4 Nb aged 10 hr at 1323 K. Note the pinned boundary and trapped dislocations.

3.1.3. Mechanical Properties

To begin with, relevant mechanical property data for initial as-extruded Cu-8 Cr-4 Nb and Cu-4 Cr-2 Nb material are presented in Table V.

Table V -
RT Mechanical Properties of Cu and As-Extruded Cu-Cr-Nb Alloys

Copper Alloy	Young's Modulus (GPa)	0.2% Yield Stress σ_y (MPa)	Hardness (HV)	Hardness (HRB)
Cu-8 Cr-4 Nb	120[a]	240-280[c]	132[e]	69[e]
Cu-4 Cr-2 Nb	120[a]	206[d]	117[e]	57[e]
Pure Cu (g.s. ~50 μm)	117[b]	48[b]	~50[f]	40 (HRF)[g]

[a][59], [b][60], [c][13, 53, 58, 61], [d][61], [e]Present Work Measurements, [f][62, 63], [g][64]

The effects of high temperature exposure at 1073, 1173, 1273 and 1323 K on room temperature tensile and yield strength (YS) of Cu-8 Cr-4 Nb alloys are shown in Figure 27. (These supporting results were obtained by NASA-Lewis and are presented here to augment and facilitate mechanical property correlation with microstructure, which, again, is the overall emphasis of this present study.) Ultimate tensile strength (UTS) values remain high even after holding at extremely high temperatures. For instance, the ultimate tensile strength decreases by only 90 MPa from the as-extruded value of 410 MPa after 10 hr exposure at 1323 K. The specimen aged at 1173 K for 100 hours suffered a loss of only 70 MPa from its original yield strength of ~240 MPa. A final observation of Fig. 27 is the interesting strength behavior exhibited by Cu-8 Cr-4 Nb when thermally treated at 1323 K. The actual yield strength increases after aging 10 and 50 hr relative to 1 hr and the ultimate tensile strength increase after aging 50 hr relative to 1 hr can be explained on a microstructural basis when noticing in Table III that the secondary particles actually decrease in size with such heat treatment.

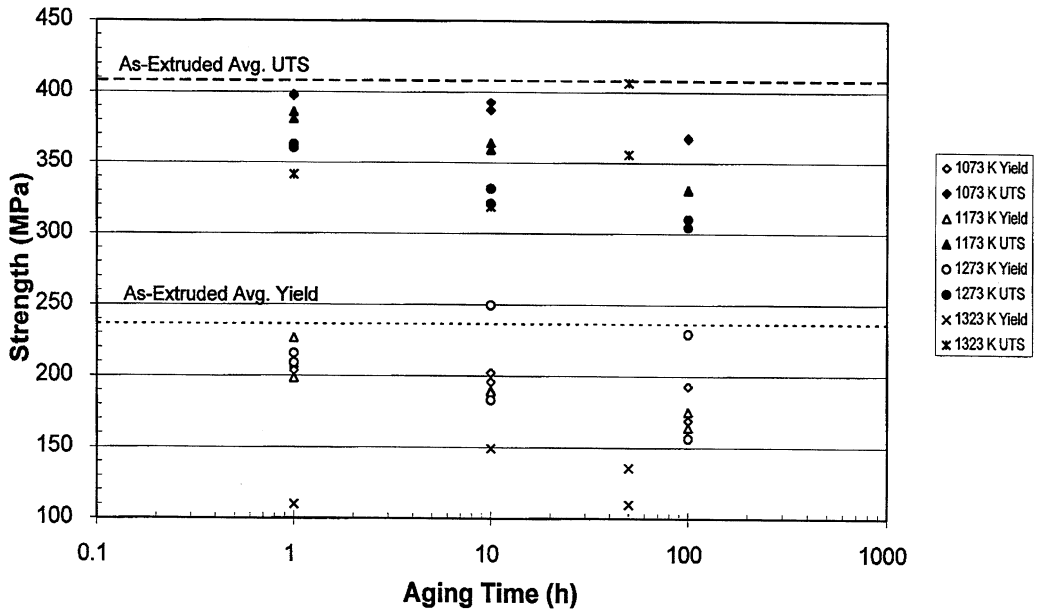

Figure 27 – Room Temperature Strength of Cu-8 Cr-4 Nb alloy following high-temperature aging (as taken from Ref. [53]).

Aging at lower temperatures (773 and 973 K) for 1 hour resulted in strengthening produced by the new and small-size secondary particles, as manifested in Figure 28. In contrast, at temperatures close to or above the extrusion temperature (1073 K and above), no strengthening effect is observed after the first hour exposure. A final observation to be made from Fig. 28 is that even after exposures to temperatures of 773 and 973 K for 50 and 100 hrs, the hardness remains in the same vicinity as as-extruded values.

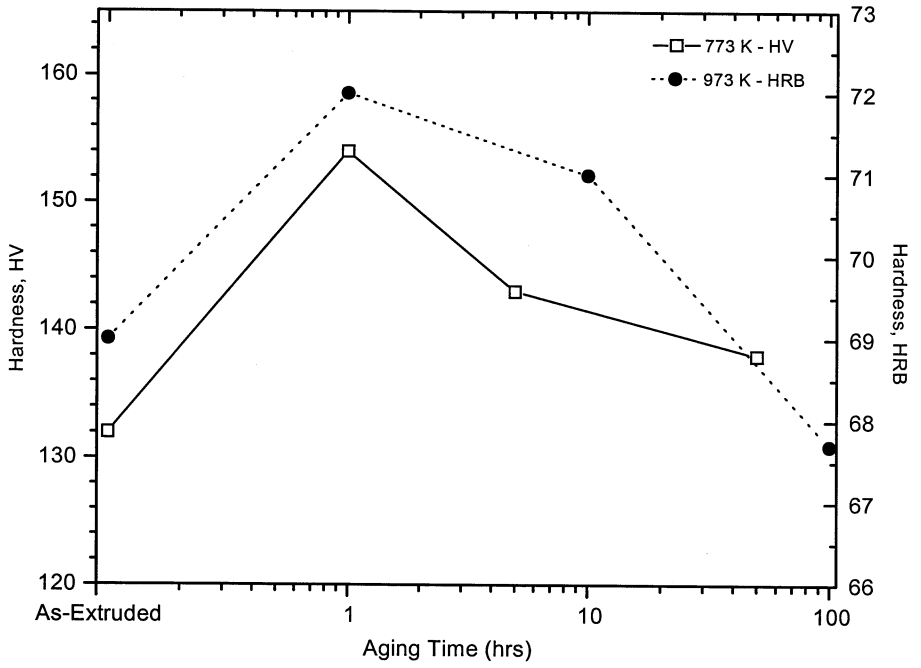

Figure 28 – Room Temperature Hardness of Cu-8 Cr-4 Nb alloy following aging at 773 and 973 K up to 100 hr.

Figure 29 shows the microhardness (HV) variation as a function of temperature for 100 hour anneal. Even after extreme high temperature exposure, e.g., after 100 hr at 1323 K, the hardness reduces by only 38 HV from the as-extruded value of 132 HV. All these results indicate the good thermal stability of this alloy. Despite the decrease with aging temperature, the retained mechanical property values are notably superior to traditional alloys such as NARloy-Z [53,58].

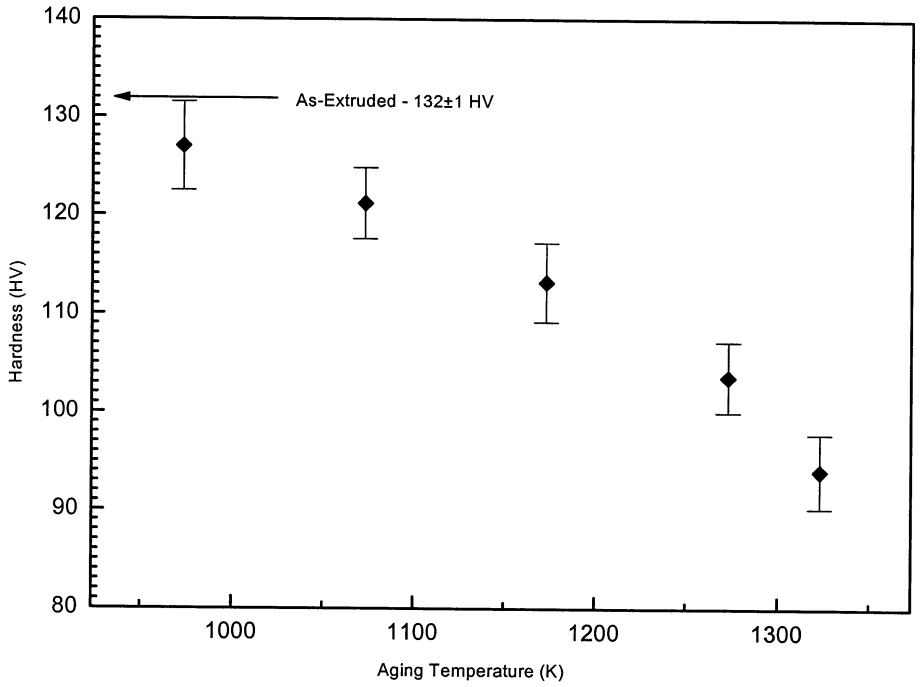

Figure 29 – Room Temperature Hardness of Cu-8 Cr-4 Nb alloy following high-temperature aging for 100 hrs.

At this point, it is also worth presenting strengths of Cu-8 Cr-4 Nb and Cu-4 Cr-2 Nb as functions of temperature. The behavior of elevated temperature yield and ultimate tensile strengths is illustrated in Figures 30 and 31, respectively, for Cu-8/4 and Cu-4/2. For comparison, curves for NARloy-Z are also included. Similarly included are such mechanical property trends for a commercially available DS Cu alloy containing dispersed Al_2O_3 particles [65], namely GlidCop Al-15 (with 0.7 vol% Al_2O_3). Although not plotted, it is worth mentioning another GlidCop alloy, Al-25 (1.2 vol% Al_2O_3), which has demonstrated a UTS range of 390 to 60 MPa for 298 to 1073 K [67]. The most important revelation from Figure 30 is how both Cu-Cr-Nb alloys out perform the alloy (NARloy-Z) currently used in the Space Shuttle main engines. As also revealed in Fig. 30, the yield strengths of Cu-8 Cr-4 Nb exceed the YS of GlidCop Al-15 for temperatures above 650 K and the yield strengths of Cu-4 Cr-2 Nb are above the YS of GlidCop Al-15 above 750 K. The UTS of Cu-Cr-Nb alloys transcend the UTS of the other alloys at temperatures above ~775 K, as seen in Fig. 31. Moreover, the UTS of Cu-8 Cr-4 Nb is

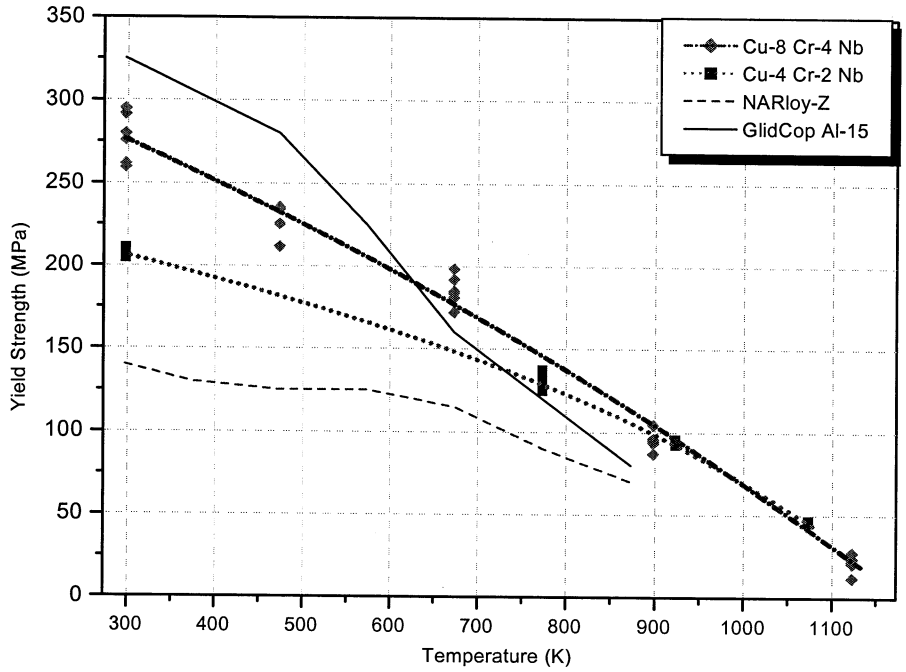

Figure 30 – Yield Strengths as a function of temperature for Cu-8 Cr-4 Nb, Cu-4 Cr-2 Nb, NARloy-Z and GlidCop Al-15 alloys. (Cu-Cr-Nb data from refs. [61]; NARloy-Z data taken from ref. [58]; and GlidCop Al-15 data taken from ref. [66].)

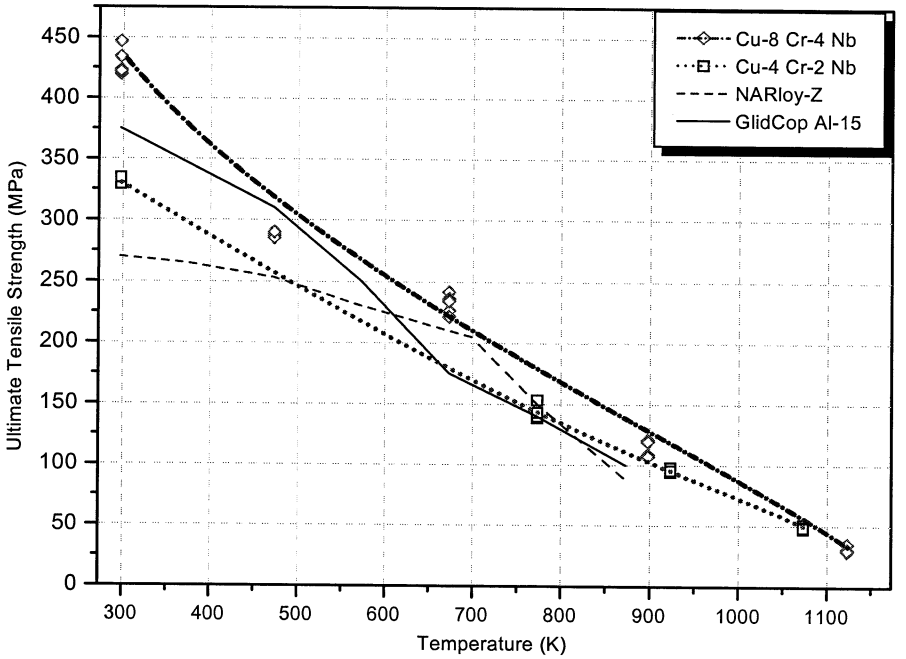

Figure 31 – Ultimate Tensile Strengths as a function of temperature for Cu-8 Cr-4 Nb, Cu-4 Cr-2 Nb, NARloy-Z and GlidCop Al-15 alloys. (Cu-Cr-Nb data from refs. [61]; NARloy-Z data taken from ref. [58]; and GlidCop Al-15 data taken from ref. [66].)

superior for virtually all test temperatures. These characteristics suggest that Cu-Cr-Nb alloys are prime candidates for next-generation particle-strengthened Cu alloys for advanced applications. Finally, for an additional aspect of mechanical property behavior, temperature-dependent compressive yield strengths of Cu-8/4 and Cu-4/2 (generated by NASA) are given graphically in Figure 32. One obvious interesting facet this plot highlights is that beyond 450 K the strength data for both basically coincide.

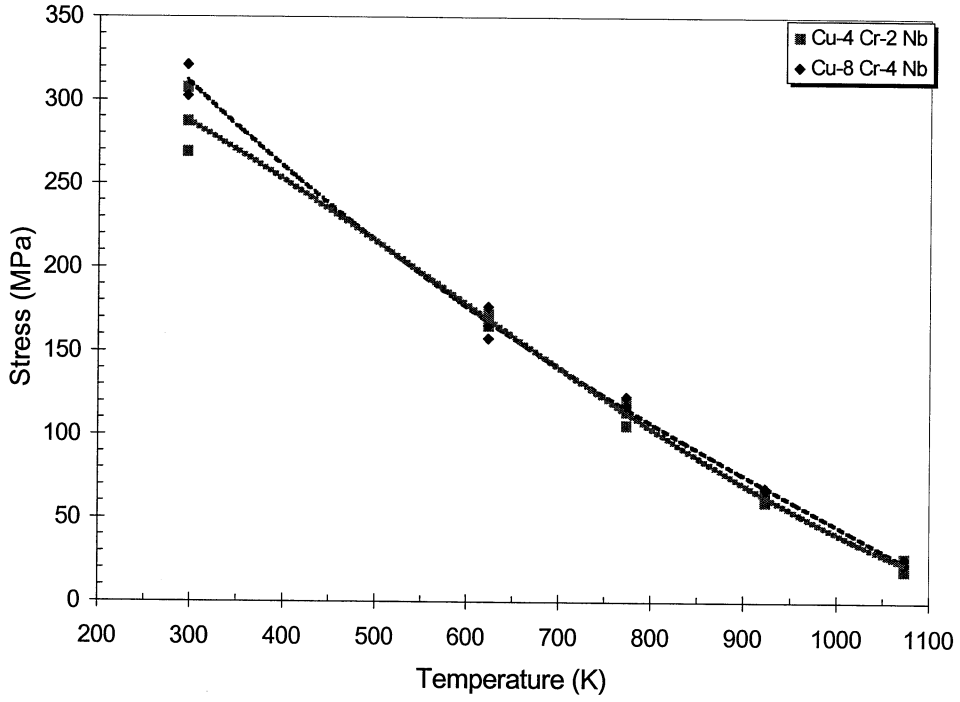

Figure 32 – Compressive Yield Strengths of Cu-8 Cr-4 Nb and Cu-4 Cr-2 Nb as a function of temperature [68].

All evidence from work thus far on Cu-8 Cr-4 Nb points to a DS Cu alloy with exceptional thermal/microstructural stability and low- and high-temperature strength. High thermal stability is manifested by 1) Cr_2Nb and Cu grain sizes remaining in their initial size ranges (Tables III and IV); and 2) Hardness and yield strength dropping only ~30% (Figures 27-29) – when thermally aged up to ~0.93 T_m. Mechanical testing performed up to 1143 K (870°C, 0.85 T_m) indicate unusually good high-temperature strength and thermal stability – see Figures 30-32. These results are remarkable in

comparison with other particle-strengthened Cu alloys (e.g., GlidCop Al-15 [7], NARloy-Z, Cu-Cr [29], Cu-Zr [30]) in which particle coarsening or dissolution occurs causing excessive grain growth that compromises the mechanical properties above ~0.75 T_m. These and other detailed examples of microstructure and property behavior and relations which substantiate the observed enhanced thermal and mechanical property stability up to 1323 K have been recently published and/or reported [53,57,58,69].

3.1.4. Thermal and Electrical Conductivity Properties

The thermal conductivity has been previously experimentally determined for as-extruded Cu-8 Cr-4 Nb and Cu-4 Cr-2 Nb – by the Thermophysical Properties Research Laboratory (TPRL) at Purdue University. TPRL determined thermal diffusivity (α_d) using the laser flash diffusivity method and measured specific heat (C_p) using DSC (with sapphire as the reference material) [70] – then calculated thermal conductivity (κ) using Eq. (10). Figure 33 graphically gives the κ results for a range of temperatures (298-1073 K). These data can be used as a means to back calculate the material specific, effective Lorentz number, L, intrinsic to Cu-Cr-Nb in any form (extruded, hot pressed, etc.). As gleaned from Fig. 33, the room temperature (298 K) values are roughly 285 W/m-K and 345 W/m-K for Cu-8 Cr-4 Nb and Cu-4 Cr-2 Nb, respectively. These specific values are the basis for the calculation of the RT L value(s) below. This L, as compared to L for pure Cu, allows a better and more accurate evaluation of thermal conductivities from the Wiedemann-Franz law for the present and future work on Cu-Cr-Nb. A final, salient observation to highlight from Fig. 33 is how the relative κ values for Cu-Cr-Nb actually increase with temperature. For example, Cu-4 Cr-2 Nb values increase to ~93% IACS at 873 K. This phenomenon is most likely due to Cr_2Nb effects on alloy heat capacity, or of dampening Cu-lattice vibrations. But, more work on this aspect is needed to reach any definite conclusions.

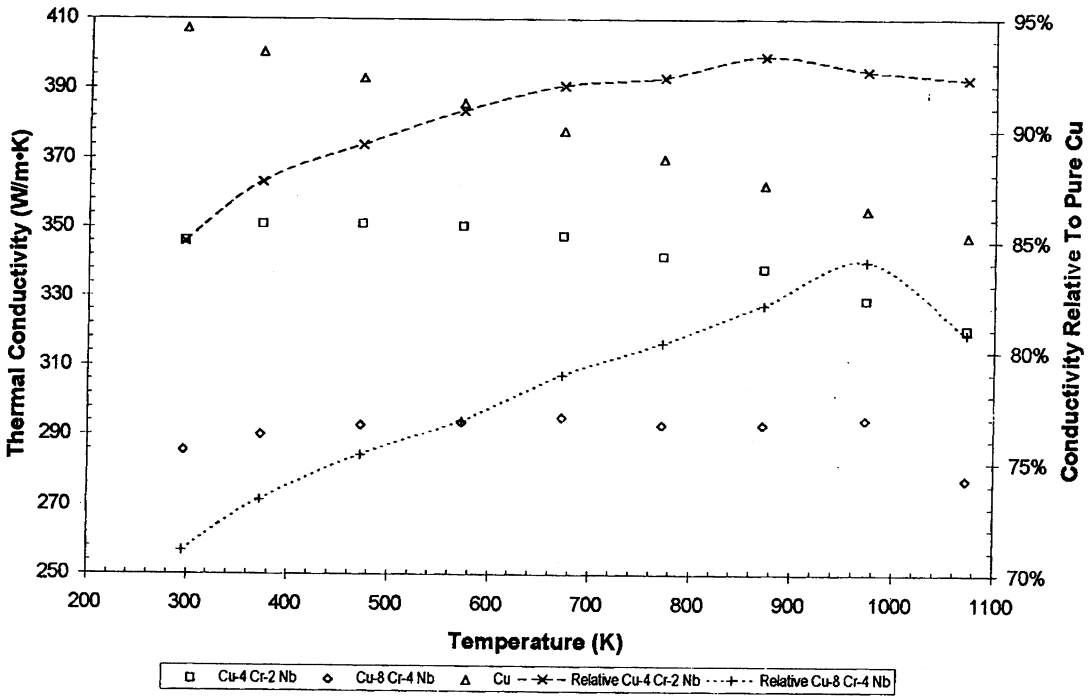

Figure 33 – Comparison of measured Thermal Conductivities of two Cu-Cr-Nb alloys (adapted from ref. [71]).

Electrical resistivity and thermal conductivity data have been compiled from the literature for copper and are summarized in Table VI. Based on Table VI, for this study, the values taken for electrical resistivity and thermal conductivity for pure copper are 1.70 μΩ-cm and 398 W/m-K, respectively. Using this resistivity value for pure Cu and the measured %IACS values, electrical conductivity values were calculated and, along with the experimental thermal conductivity data, are summarized in Table VII. Again, with metals, the Wiedemann-Franz law allows direct relation of electrical to thermal conductivity. Such a relation is employed next to the electrical and thermal conductivity data in Table VII.

Table VI -
Room Temperature Electrical and Thermal Conductivities of OFHC (Annealed/Pure) Copper

Electrical Resistivity, ρ (μΩ-cm)	ρ Refs.	Electrical Conductivity × 10^4(Ω-cm)$^{-1}$	Thermal Conductivity, κ, W/m-K	κ Refs.
1.694	[72]	59.9	398	[76]
1.67	[73]	58.0	399	[72]
1.724	[74]	59.0	397	[72]
1.71	[75]	58.5	390	[77]
			406	[70]
Avg.: 1.70		**58.84**	**398**	

Table VII -
Conductivity Properties of Cu and As-Extruded Cu-Cr-Nb Alloys

Copper Alloy	Electrical (%IACS)	Electrical, σ_{el} × 10^4(Ω-cm)$^{-1}$	Thermal[1] (W/m-K)	Thermal[2] (W/m-K)
Cu-8 Cr-4 Nb	68[a] (54[b])	40.01	285	280
Cu-4 Cr-2 Nb	82[a] (74[b])	48.25	346	339
Pure Cu (g.s. ~50 μm)	100	58.84	406	398

[a]Previous accepted and used values [78]; [b]Present Measurements; [1]Measured;
[2]Calculated based on an average κ of 398 W/m-K for pure Cu from literature.

Normalizing the thermal conductivity values in Fig. 33 to 398 W/m-K for pure Cu gives ~339 and 280 W/m-K for as-extruded Cu-4 Cr-2 Nb and Cu-8 Cr-4 Nb, respectively. Substituting each of these thermal values and the absolute electrical conductivity values in Table VII (converted to absolute electrical conductivities, taking σ_e for pure Cu as 58.84×10^4 Ω-cm)$^{-1}$) into Eq. (9) yields the effective Lorentz number for each alloy. At room temperature, an $L \approx 2.36\times10^{-8}$ W-Ω/K^2 was obtained for both Cu-8 Cr-2 Nb and Cu-4 Cr-2 Nb. This value shall be used for any subsequent thermal conductivity calculations for Cu-Cr-Nb alloys when electrical conductivity is known. (At this juncture, it is worth commenting on the two different %IACS values given in Table VII. The present measured values are low due to the incorporation of iron from the steel

can used to extrude the material. The previous electrical values (in Table VII) and the thermal values presented in Fig. 33 were determined for extruded Cu-Cr-Nb with steps taken to avoid any iron contamination from the steel can.)

3.2. PROCESSED (MM/MA) Cu-Cr-Nb

In toto, Section **3.1** strongly indicates that Cu-Cr-Nb alloys, with an emphasis on Cu-8 Cr-4 Nb, possess both high strength and high conductivity at low and high temperatures relative to Cu and other DS Cu. Moreover, they are shown to be inherently thermally stable in terms of their microstructures, and even more importantly, mechanical properties. The high strength and stability are essentially due to a combination of small and large, stable Cr_2Nb particles, which effectively impede Cu grain growth. Now for "part two" of this present study, as annunciated in the Objectives (**1.2.2**), mechanical milling (MM) is applied to alloy powder material as a technique to build on the demonstrated strength and stability behavior. At this point, it is relevant to mention again that, since as-extruded Cu-4 Cr-2 Nb has a higher conductivity than as-extruded Cu-8 Cr-4 Nb, emphasis is placed on P/M Cu-4 Cr-2 Nb throughout the MM phase of the present study. Densified MM Cu-Cr-Nb is expected to have finer Cu grains and a more uniform size and distribution of finer Cr_2Nb particles compared to as-extruded material. Again, the goal is to apply MM in order to refine the initial microstructure to a level that ultimately improves the strength of, particularly, Cu-4 Cr-2 Nb – relative to as-extruded Cu-8 Cr-4 Nb. In addition to size refinement, it is also expected that MM can effectively bring average primary and secondary particle sizes closer together, i.e. develop a single particle size distribution, which should further enhance thermal stability.

MM at incrementally longer times makes following the progression of microstructures and properties, and their optimization, possible. The utility of microscopy for thermally processed extruded material equally applies to MM material.

Microscopy allows direct observation, interrogation and quantitative analyses of expected grain- and Cr_2Nb particle-size reduction during material processing and control involving the severe plastic deformation from MM. Direct observations of atomized powder and primary precipitate breakdown are made relatively easy with optical microscopy and SEM. Again, the structural evolution is correlated with the strength and conductivity behavior evolution. Thusly, what follows next is a presentation of the results for mechanically milled Cu-Cr-Nb powder and dense material. Microstructural evolution (e.g., assessment of dispersoids present, dispersoid size, grain size, etc., using TEM, SEM and XRD) is dealt with first, followed by property behavior (e.g., hardness and electrical conductivity) as a function of milling duration, or severe plastic deformation.

3.2.1. Second-Phase Evolution in Mechanically Milled Cu-Cr-Nb

3.2.1.1. Starting and Milled Powder Particles: SEM/Optical

The morphologies of starting Cu-4 Cr-2 Nb and Cu-8 Cr-4 Nb powders are shown in Figures 34 and 35, respectively. These confirm that the starting powders are less than about 106 μm, i.e. -150 mesh. Figure 36 shows the evolution of shape and size of the powder particles with milling time for Cu-8/4. After 1 hr milling, the size increases due to micro-welding and the shape remains somewhat equiaxed. Milling 2 then 4 hr leads to a flaky morphology, but an overall reduction in size due to micro-fracture. Formation of spheres and then more flattened, flaky particles is expected due to copper's ductility and workability, especially when warmed. Similar morphology also occurred in the milling of pure copper [79], Cu-15% Nb [80] and Al-Ti [81]. Milling Cu-4/2 with a PCA and LN2 cooling produces a different effect, as seen in Figure 37. Visual and optical inspection of the milled powder particles indicate only slightly flattened, albeit irregularly shaped particles, with very few obvious flakes.

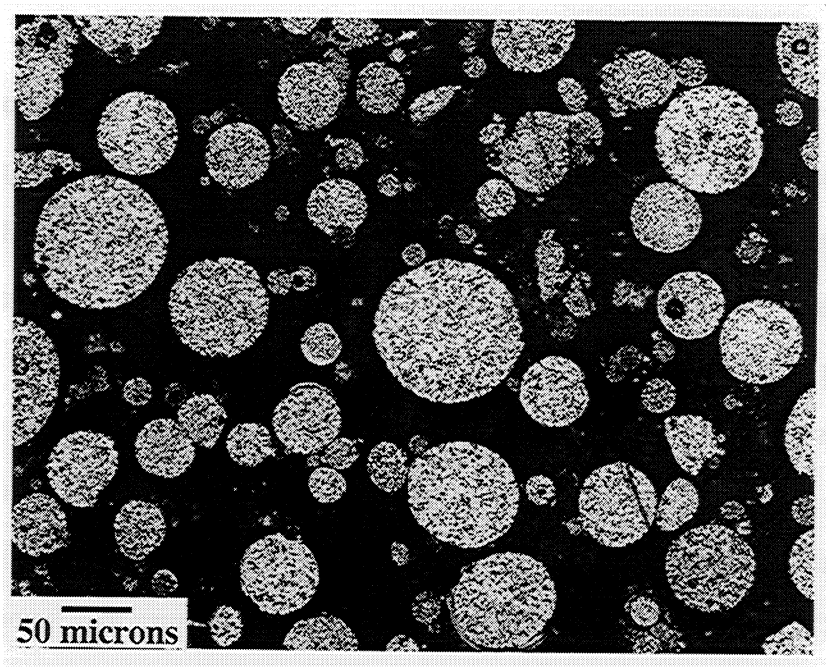

Figure 34 – Optical micrograph of as-atomized Cu-4 Cr-2 Nb powder.

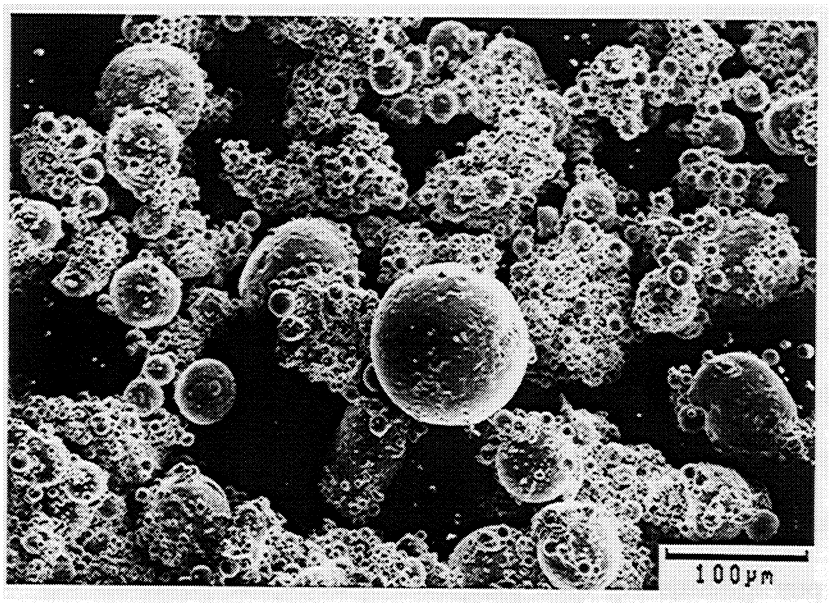

Figure 35 – SEM micrograph of as-atomized Cu-8 Cr-4 Nb powder.

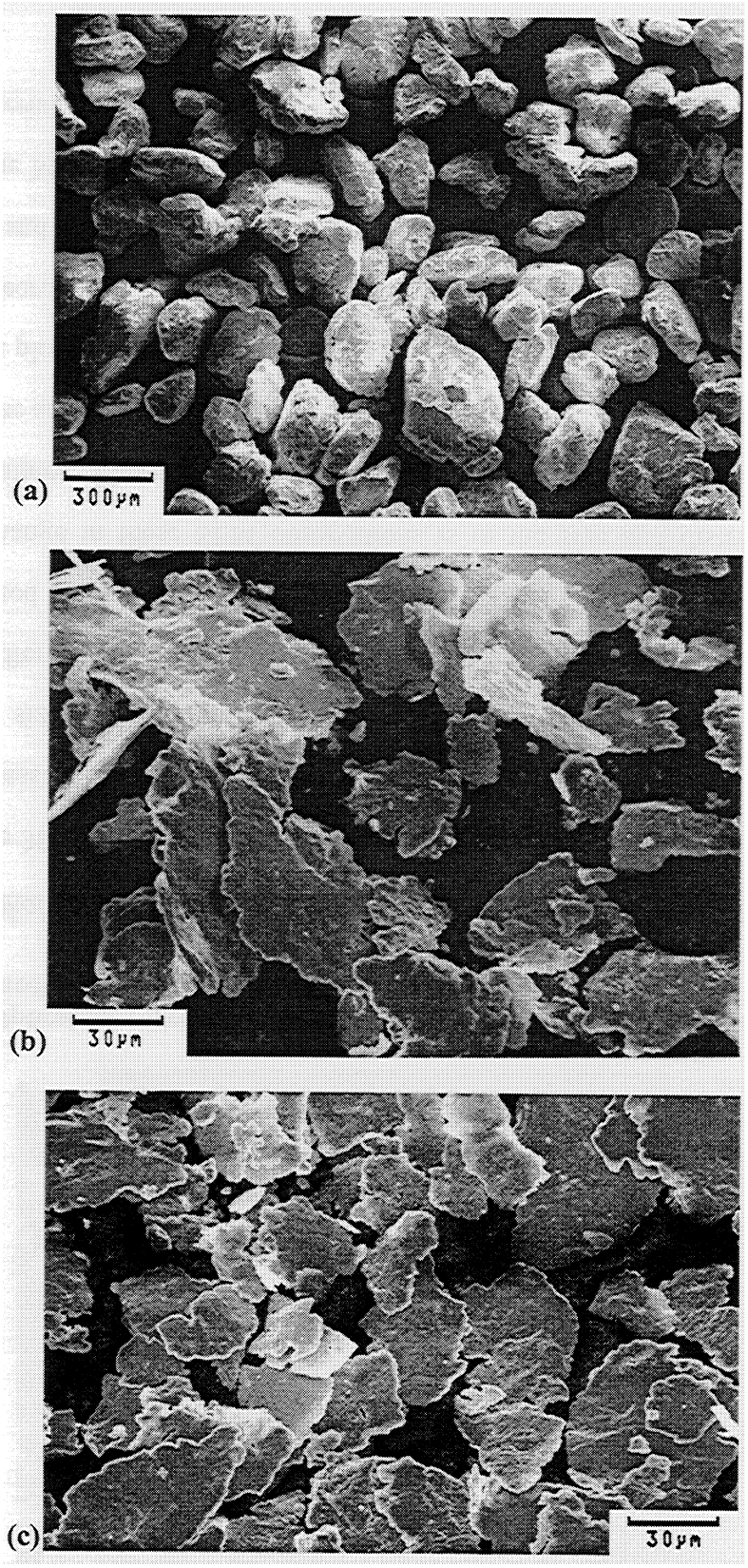

Figure 36 – SEM micrographs of Cu-8 Cr-4 Nb powder mechanically milled (a) 1 hr; (b) 2 hr; and (c) 4 hr.

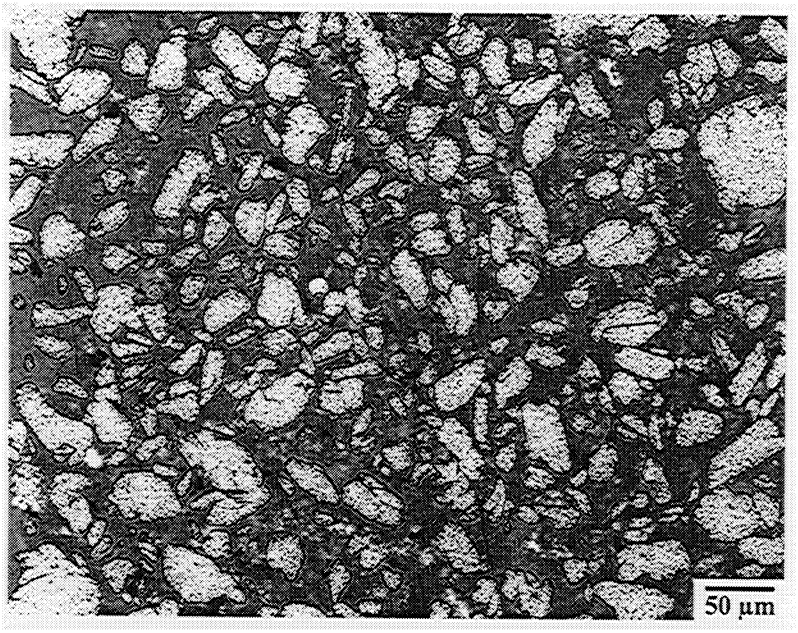

Figure 37 – Optical micrograph of Cu-4 Cr-2 Nb powder mechanically milled 4 hr with steel vial and ball media, PCA and LN2 cooling.

3.2.1.2. Morphological Evolution of Primary Cr_2Nb: SEM

Figure 38(a) and (b) are SEM micrographs depicting the two extreme conditions of P/M processed Cu-8 Cr-4 Nb, i.e. as-atomized and MM-8 hr. Note the drastic reduction in size, a more uniform size and a more even distribution of the large precipitates after milling. Figure 39 shows similar SEM micrographs of Cu-4 Cr-2 Nb in the as-atomized (a) and mechanically milled (½ - 8 hr) conditions (b - f). The most noticeable change in these SEM observations is in the size and distribution of large Cr_2Nb precipitates. There exists an appreciable trend of size refinement and increasingly more even size and spatial distribution of precipitates with increased milling time. Figure 40 contains a plot of mean primary particle size as a function of milling time. The large Cr_2Nb size decreases from ~0.78 μm to ~0.18 μm in MM Cu-4 Cr-2 Nb. (Note that the as-atomized and MM-4 hr size are slightly less than that for Cu-8 Cr-4 Nb.) When comparing the MM-8 hr size to the average secondary particle size of ~0.16 μm for as-extruded material, the aim of merging the two sizes has been mostly achieved.

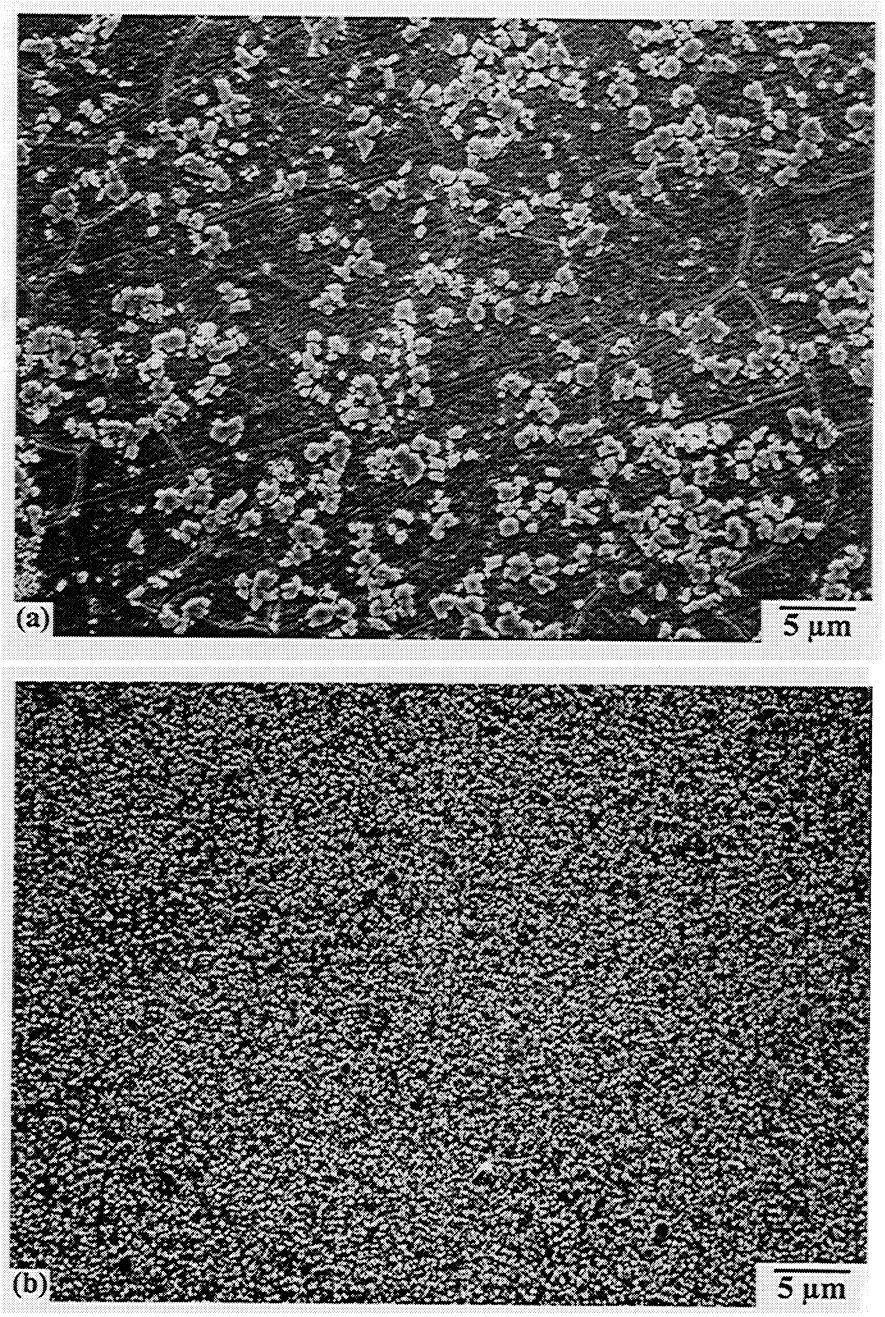

Figure 38 – Cu-8 Cr-4 Nb Powder (a) As-Atomized and (b) mechanically milled 8 hr.

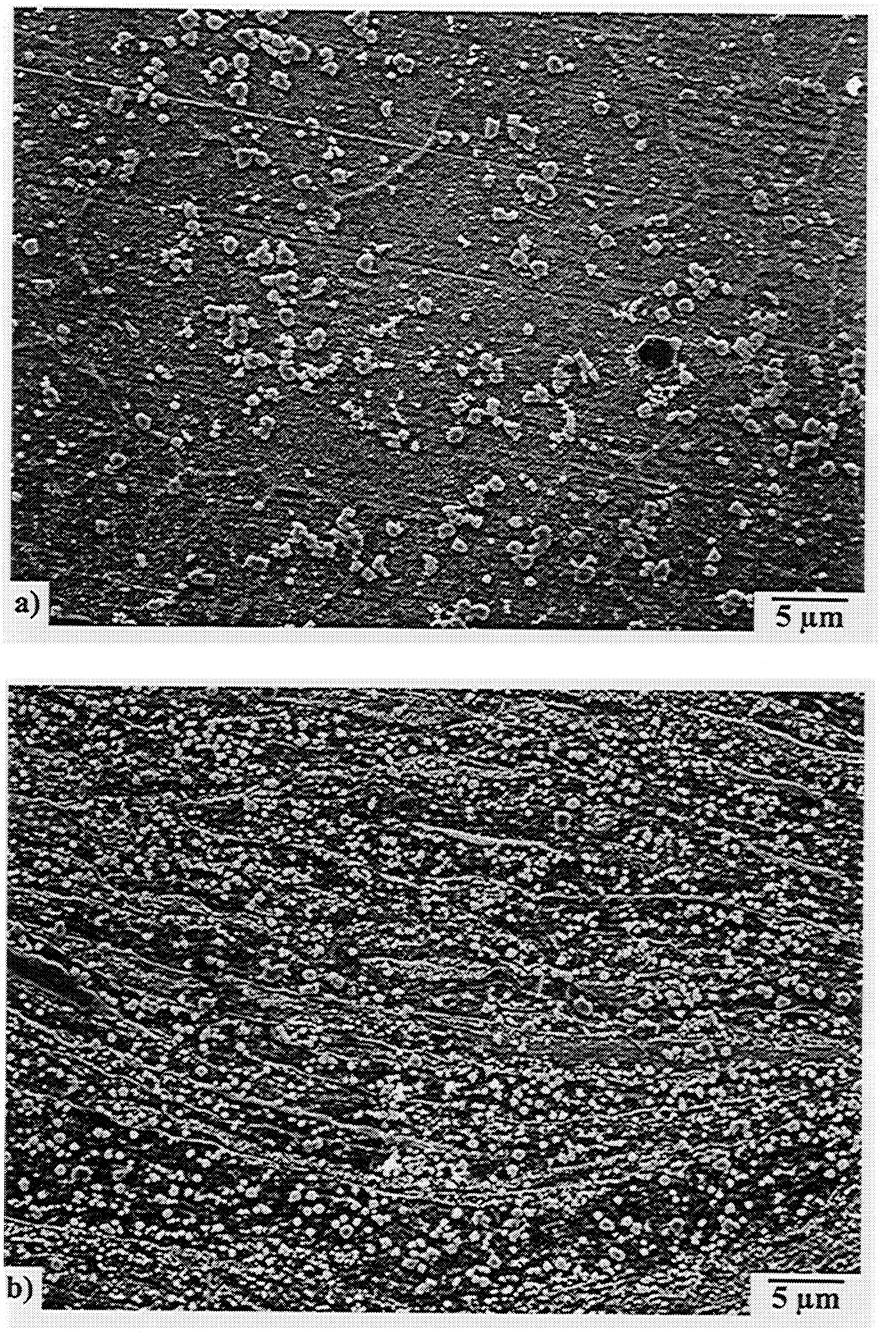

Figure 39 – Cu-4 Cr-2 Nb Powder (a) As-Atomized and (b) mechanically milled ½ hr.

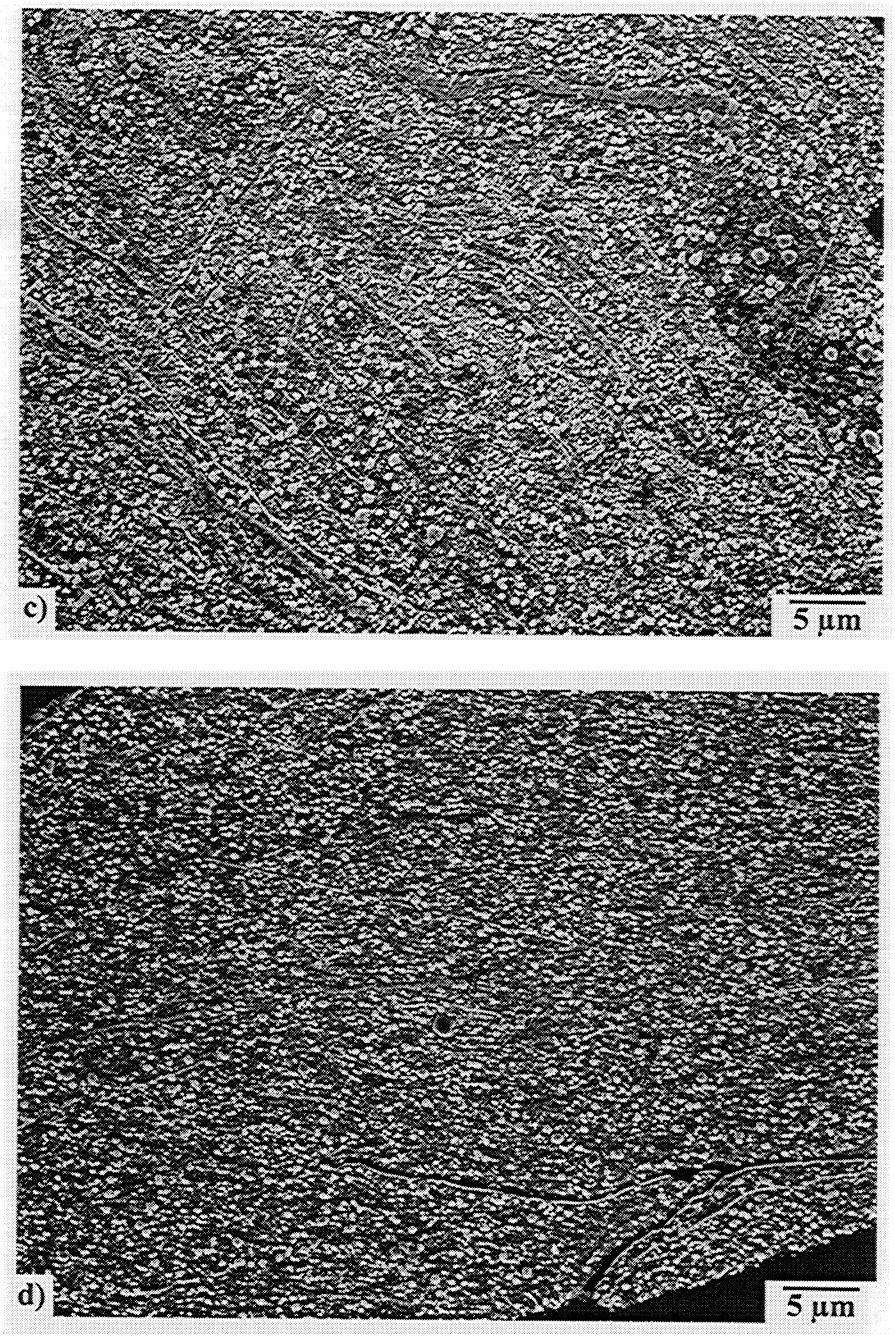

Figure 39 – Cu-4 Cr-2 Nb Powder mechanically milled (c) 1 hr and (d) 2 hr.

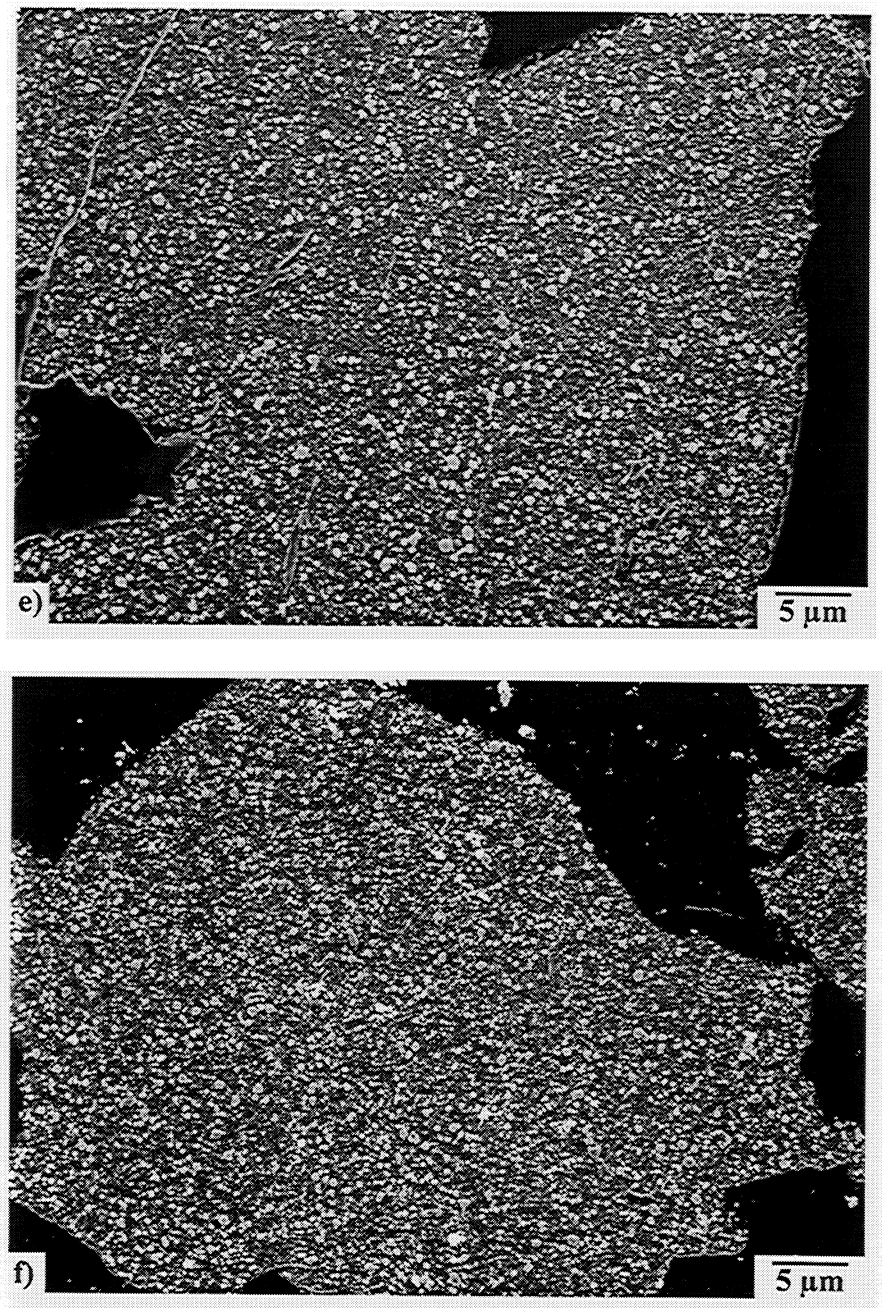

Figure 39 – Cu-4 Cr-2 Nb Powder mechanically milled (e) 4 hr and (f) 8 hr.

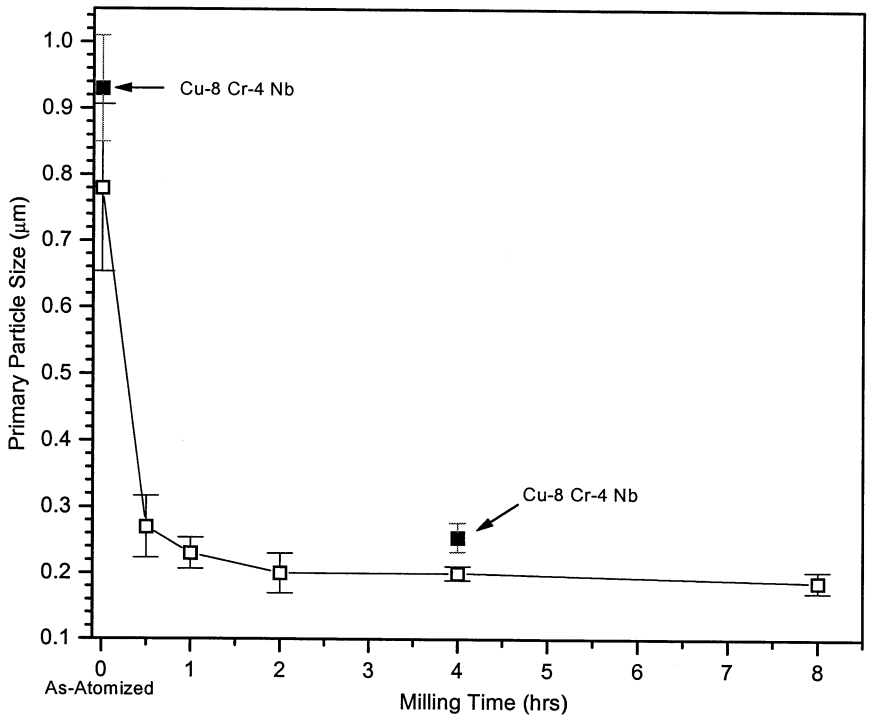

Figure 40 – Mean size of Primary Cr_2Nb particles in Cu-4 Cr-2 Nb as a function of milling time, including two representative points for MM Cu-8 Cr-4 Nb.

The most drastic microstructural change occurs for material MM-½ hr (Fig. 39(b)), when compared to as-received material (Fig. 39(a)) as seen in Fig. 40. Note the prevalent convoluted layered, or lamellar structure for ½ hr-milled powder, typical for such processing as represented in Figure 4(a). These microscopy results of milled Cu-Cr-Nb alloys evidently prove that the twofold objective of attaining a more homogeneous distribution of refined large Cr_2Nb particles and transforming a bimodal into a single particle size distribution is not only possible, but also has been met. In light of this achieved objective, the concept and efficacy of MM as applied to Cu-Cr-Nb alloys have been validated with respect to primary Cr_2Nb particles. For completeness, Figure 41 contains SEM micrographs of the microstructural progression with milling time of MM and hot pressed Cu-4 Cr-2 Nb. It is clearly seen that obvious large particles gradually disappear. Also apparent is the as-milled, "wavy" structure is retained even after 3-hr hot pressing at 810°C. Beyond these observations, what is also now required is the

interrogation and confirmation of the composition of second phases present prior to and after high-temperature consolidation for selected milling times, which is addressed next.

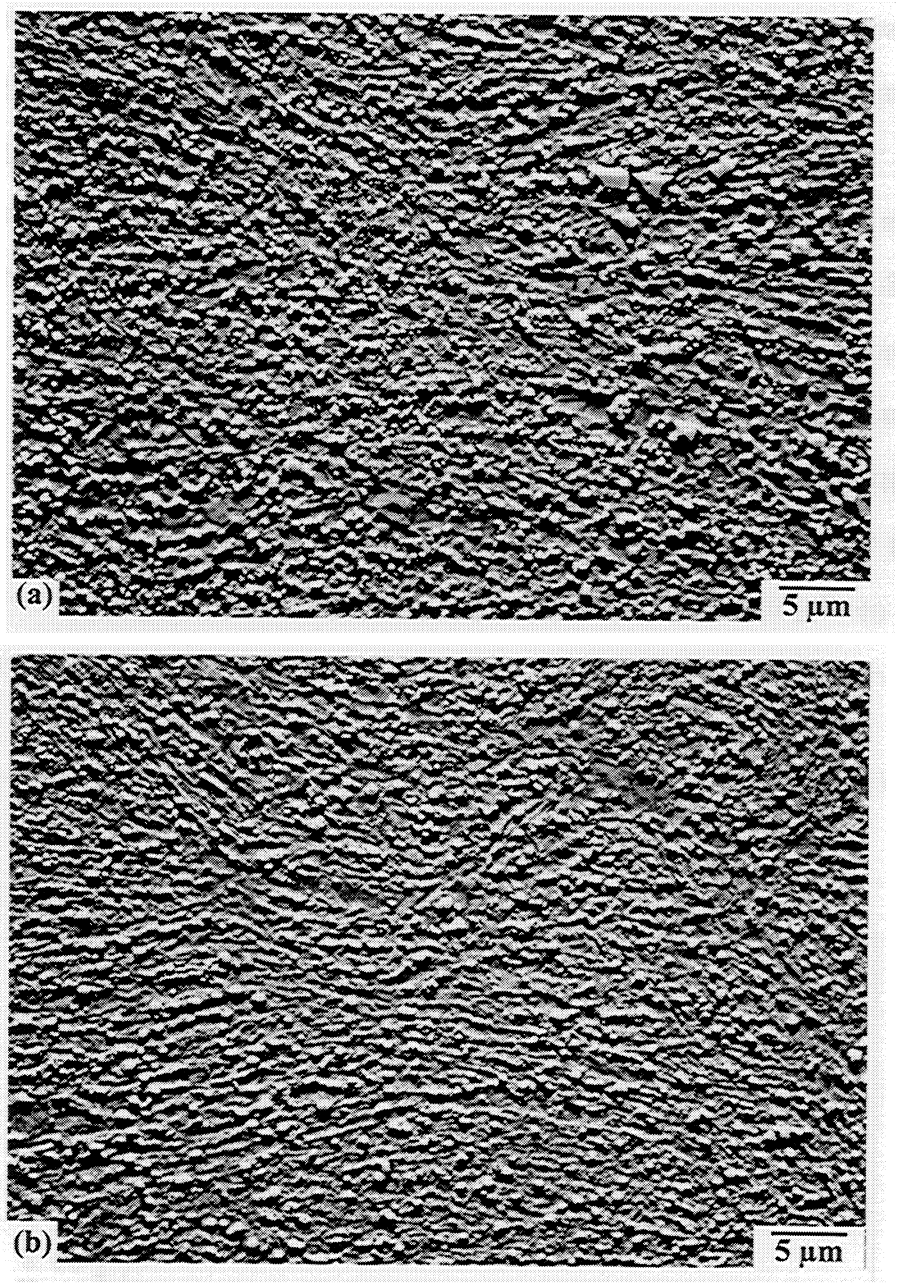

Figure 41 – Hot pressed Cu-4 Cr-2 Nb powder mechanically milled (a) ½ hr and (b) 1 hr.

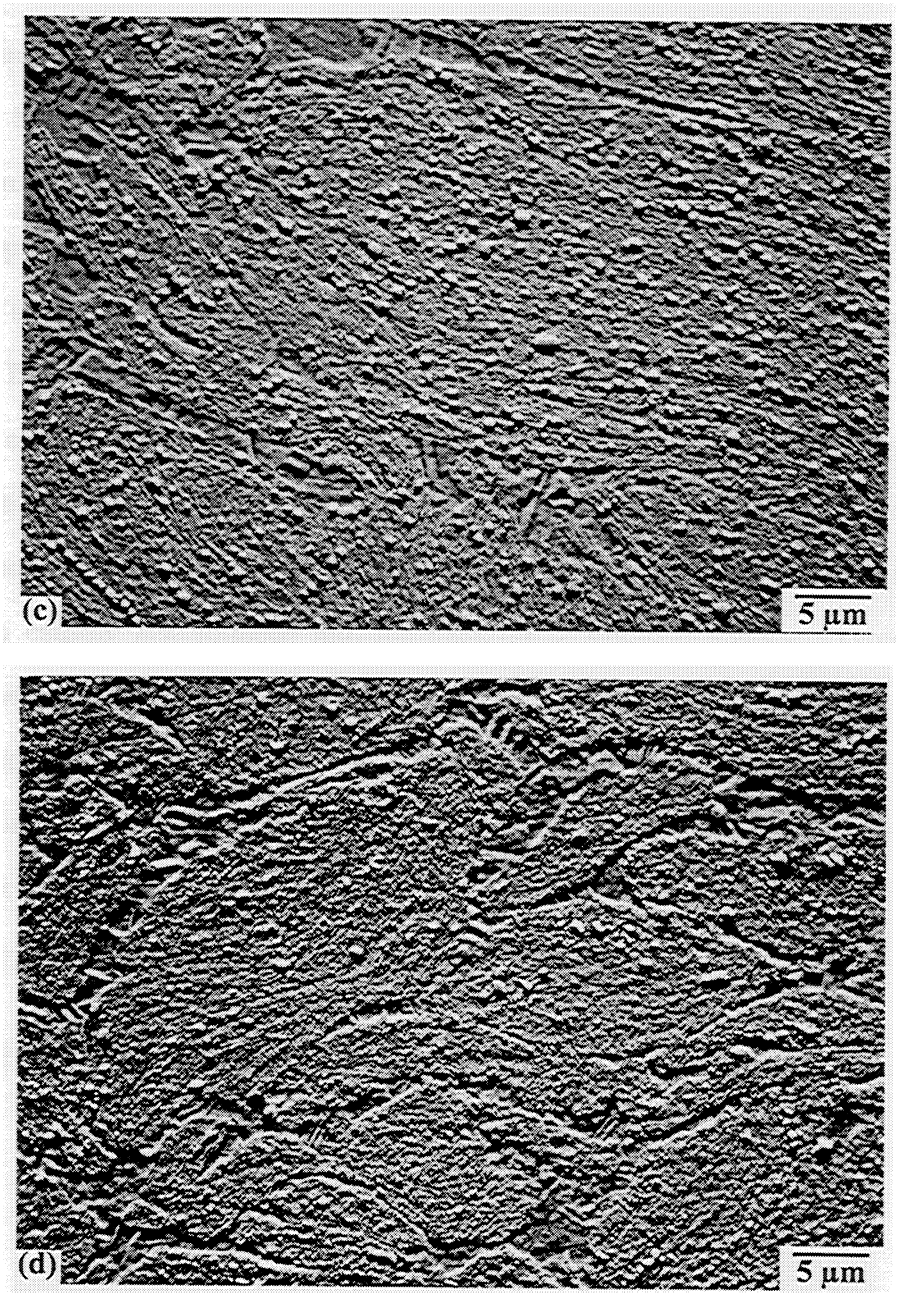

Figure 41 – Hot pressed Cu-4 Cr-2 Nb powder mechanically milled (c) 2 hr and (d) 4 hr.

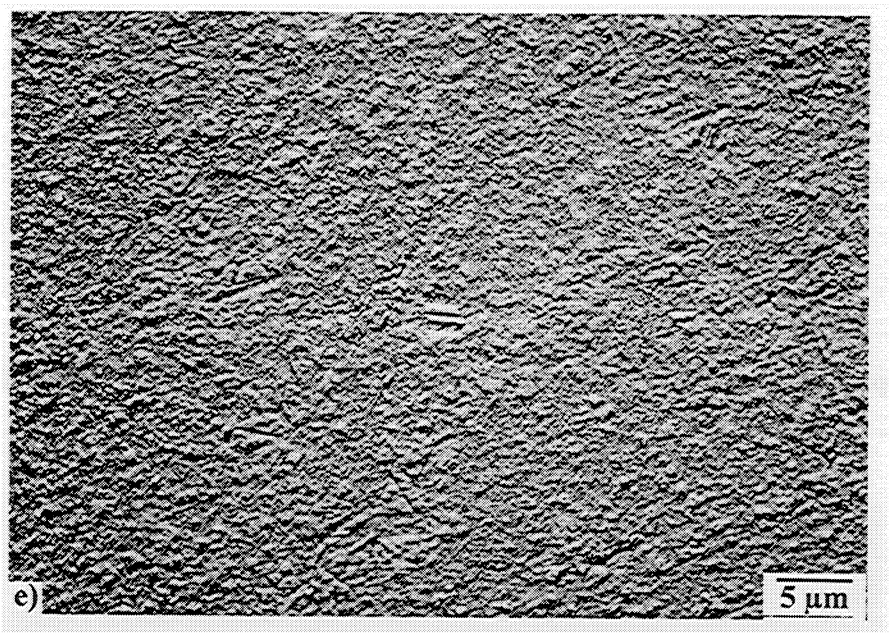

Figure 41 – (e) Hot Pressed Cu-4 Cr-2 Nb Powder mechanically milled 8 hr.

3.2.1.3. Phase and Particle Identification, Structure and Morphology: XRD Analysis

The addition of the carbon-containing PCA and milling with steel media resulted in occlusion of carbon and iron into the powder during milling. Figure 42 below shows the amount of these elements (plus oxygen), in wt. ppm, incorporated into the powder during processing (MM and/or hot pressing steps). What is even more important than how much carbon, was induced into the material is where it resides. Tables VIII-X contain the pertinent crystallographic, d-spacing and 2-theta values for Cu and all possible second-phase dispersoids. X-ray diffraction (XRD) of as-milled powder shows Cr_2Nb, as expected. A portion of the XRD spectrum obtained from as-4 hr milled Cu-4/2 powder is given as Figure 43. Based on Tables IX and X, this 2-theta range is sufficient to contain at least one peak from the various possible particle compounds. This, indeed, confirms that Cr_2Nb phase still remains, which is revealed by SEM (Fig. 39(e)). Scrutiny of the entire scanned spectrum (2-theta from 35 to 120 degrees) revealed no noticeable additional phases. This would suggest that any degree of carbon content would be in solid solution.

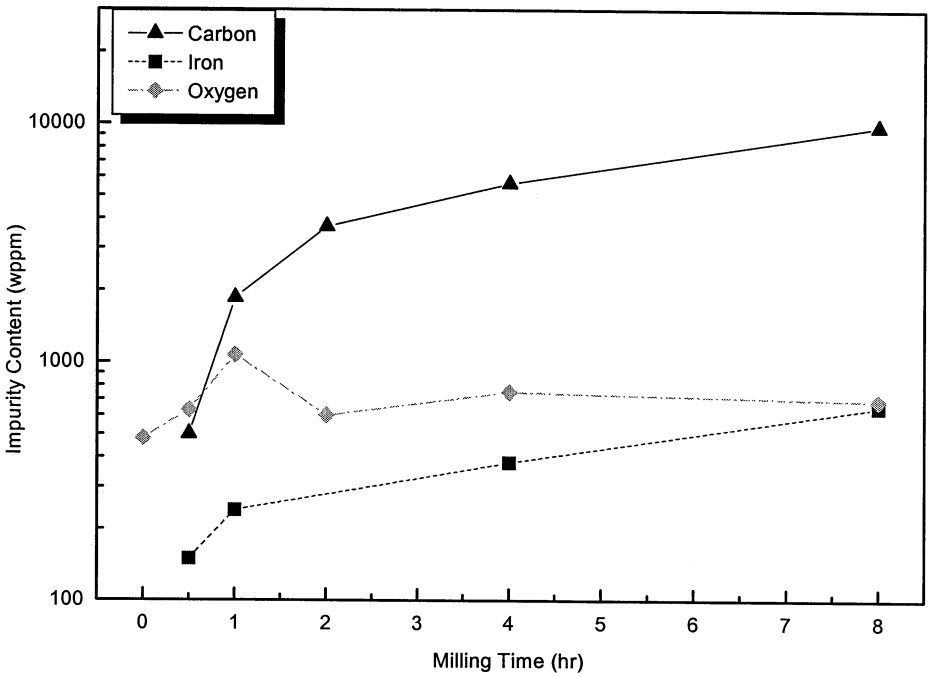

Figure 42 – Effects of milling time on C, Fe, and O content in Cu-4 Cr-2 Nb.

Table VIII -
Crystallographic Data of Probable/Relevant Phases

Phase/ Compound	Crystal Structure	Lattice Parameter, Å		Atoms Per Unit Cell
		a	*c*	
Cu	cubic, FCC	3.615	- -	4
Cr	cubic, BCC	2.884	- -	2
Nb	cubic, BCC	3.307	- -	2
Cr_2Nb[a]	cubic, FCC (C15)	6.97 - 7.02	- -	24
ε-Cr_2Nb[a]	HCP (C14)	4.87	7.94	12
NbC_{1-x}	FCC, NaCl	4.41 - 4.47	- -	8
$Cr_{23}C_6$	FCC	10.65	- -	116
Ref.	[82,83[a]]	[82, 84]		[82,83[a]]

Table IX -
d_{hkl}-Spacing and 2θ* Values for Cr_2Nb (C15), Cr_2Nb (C14), NbC and $Cr_{23}C_6$

hkl	Cr_2Nb (C15) d (Å)	2θ (deg)	NbC d (Å)	2θ (deg)	$Cr_{23}C_6$ d (Å)	2θ (deg)	*hkil*	Cr_2Nb (C14) d (Å)	2θ (deg)
110							$\bar{1}100$	4.218	21.05
111	4.033	22.02	2.558	35.06	6.151	14.39	0002	3.970	22.38
200	3.493	25.48	2.215	40.70	5.327	16.63	$\bar{1}101$	3.725	23.87
211							$01\bar{1}1$	3.725	23.87
220	2.470	36.35	1.566	58.92	3.767	23.60	$10\bar{1}2$	2.891	30.91
310							$\bar{1}102$	2.891	30.91
311	2.106	42.91	1.336	70.44	3.212	27.75	$11\bar{2}0$	2.435	36.88
222	2.016	44.92	1.279	74.08	3.076	29.01	$\bar{2}111$	2.328	38.65
321							$10\bar{1}3$	2.242	40.19
400	1.746	52.35	1.108	88.14	2.664	33.62	$\bar{1}103$	2.242	40.19
331	1.602	57.46	1.016	98.57	2.444	36.74	$20\bar{2}0$	2.109	42.85
411							$\bar{1}2\bar{1}2$	2.076	43.57
420	1.562	59.10	0.991	102.09	2.382	37.73	$11\bar{2}2$	2.076	43.57
422	1.426	65.40	0.904	116.83	2.175	41.49	$02\bar{2}1$	2.038	44.41
511	1.344	69.92	0.853	129.25	2.050	44.13	0004	1.985	45.67

*Using $n\lambda = 2d\sin\theta$, taking $\lambda_{Cuk\alpha} = 1.54184$ Å

Table X -
Interplanar Spacing and 2θ* Values for Cu, Cr and Nb

hkl	Cu d (Å)	2θ (deg)	Cr d (Å)	2θ (deg)	Nb d (Å)	2θ (deg)
110			2.039	44.39	2.338	38.47
111	2.087	43.35				
200	1.808	50.49	1.442	64.58	1.654	55.53
211			1.177	81.73	1.350	69.58
220	1.278	74.15	1.020	98.13	1.169	82.42
310			0.912	115.26	1.046	94.88
311	1.090	90.03				
222	1.044	95.14	0.833	135.41	0.955	107.59
321			0.771	175.95	0.884	121.28
400	0.904	116.93	0.721		0.827	137.41
331	0.829	136.49	0.680		0.779	162.41
411						
420	0.808	144.70	0.645		0.739	
422	0.738					
511	0.696					

*Using $n\lambda = 2d\sin\theta$, taking $\lambda_{Cuk\alpha} = 1.54184$ Å

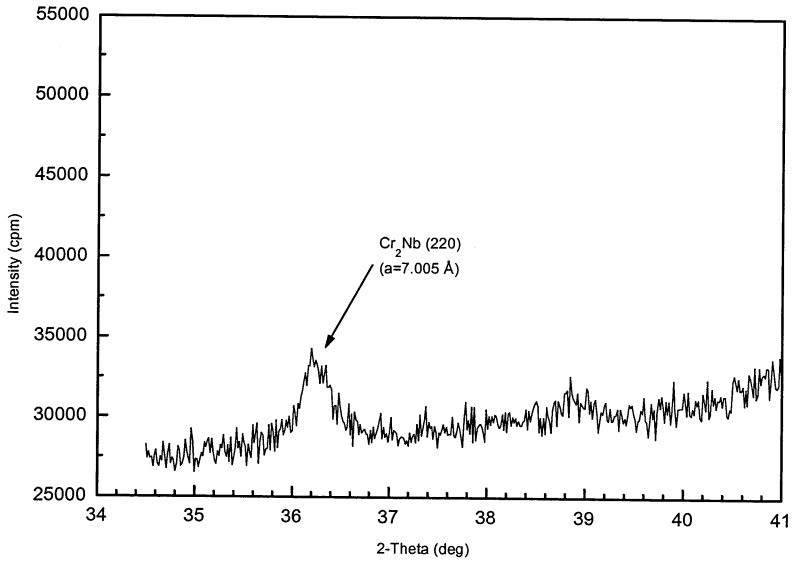

Figure 43 – XRD Spectrum showing the (220) peak for C15 Cr_2Nb in as-4 hr-milled Cu-4 Cr-2 Nb.

At this point, providing an illustration of one subtle indication of carbon (and other impurities) in solid solution is warranted. Figure 44 contains two XRD spectra of specific Cu 2θ peaks for: 1) as-4 hr milled.Cu-4/2 powder and 2) 4 hr milled/hot pressed Cu-4/2. The peaks from as-4 hr milled material are shifted slightly towards lower 2θ relative to the hot pressed peak, which indicates a slight increase in the lattice parameter of Cu. From the 2θ values for the (111) and (200) Cu peaks of hot pressed Cu-4/2, a lattice parameter of 3.616 ± 0.0005 Å is calculated, which is essentially that of pure copper. The same 2θ peak values for the as-milled material give a Cu lattice constant of ~3.624 ± 0.001 Å. Even this slight increase is strong evidence that carbon (interstitial), and most likely Fe, Cr and Nb (substitutional), were mechanically driven into metastable supersaturated solid solution. The hot pressed peaks are sharper, indicating a larger crystallite size and/or lower internal strain, probably more the latter, as is shown below. In addition, determining what form C takes when it comes out of supersaturated solid solution during hot pressing, vis-a-vis Cr_2Nb, is essential.

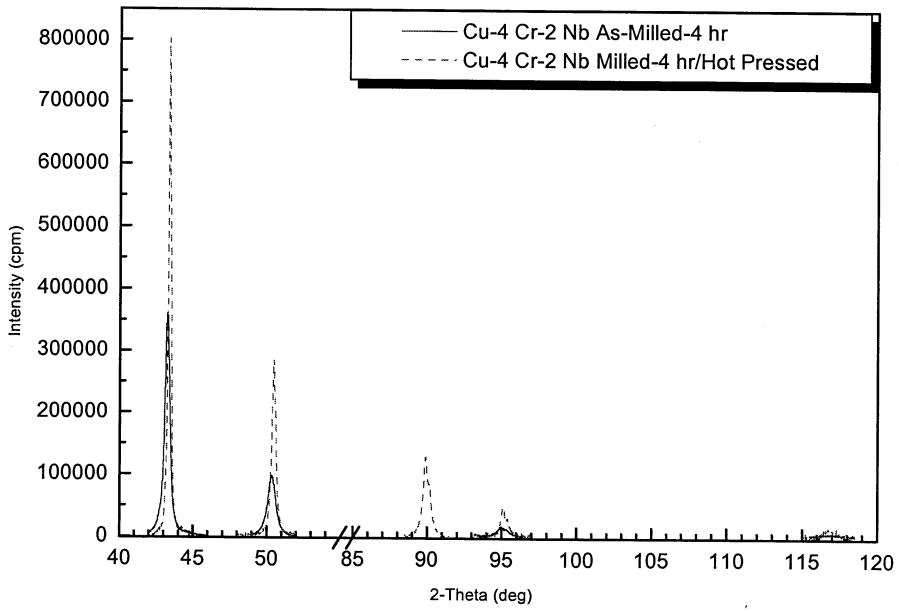

Figure 44 – Overlay of XRD spectra of Cu peaks from As-4 hr-milled and MM-4 hr/hot pressed Cu-4 Cr-2 Nb.

Further XRD of hot pressed milled powder does, indeed, strongly indicate C-Nb and possible C-Cr reactions, as shown by formation of such carbide peaks, with a simultaneous intensity loss in Cr_2Nb peaks. The relative amounts (peak intensities) of the carbides increase with milling time, as the spectra in Figure 45 indicate. When comparing Figures 43 and 45, it is obvious that upon hot pressing at 810°C for 3 hrs, C reacts with Cr_2Nb to form NbC. Thus, it turns out that the carbon pick-up ultimately leads to formation of carbide phases upon milled-powder consolidation. More detail of this reaction and the disposition of Cr is offered later in the Discussion. Weight percent and peak position values shown in Figures 42 and 43 were used to estimate the progression in volume fraction of Cr_2Nb, NbC (and Cr) with milling time. A table of such values is also presented in the Discussion.

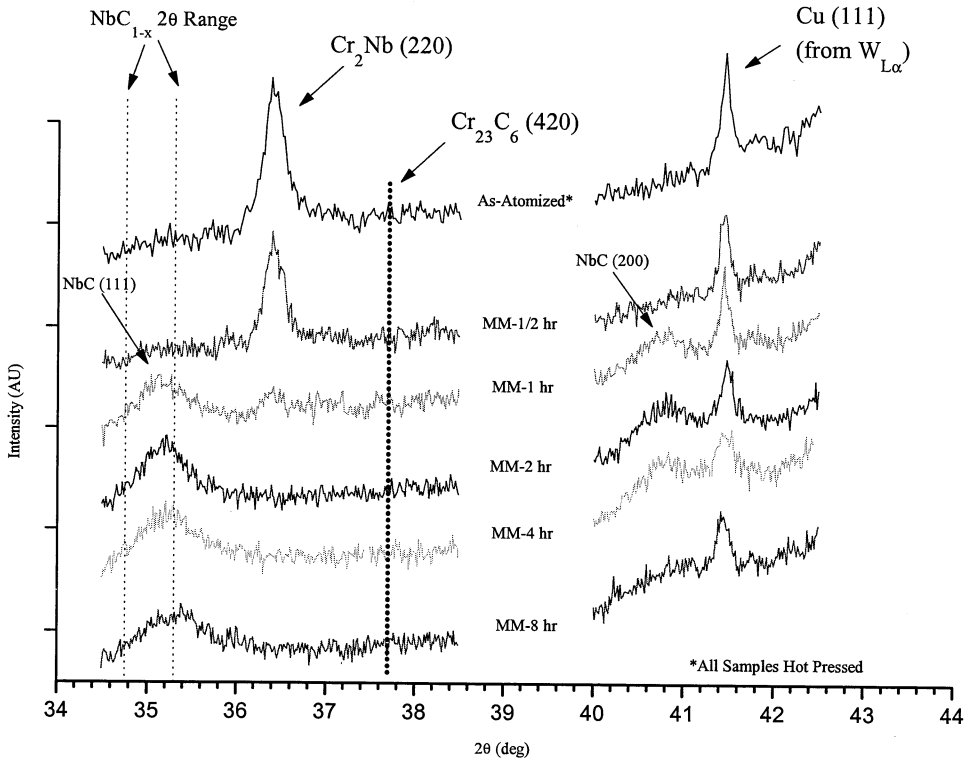

Figure 45 – XRD spectra of mechanically milled/hot pressed Cu-4 Cr-2 Nb showing the formation of NbC with the loss of Cr_2Nb due to introduction of carbon (in PCA).

Finally, additional XRD, convergent beam and selected area electron diffraction (CBED and SAD) pattern analyses are presented later, which confirm that C does react with Cr_2Nb to form NbC and, to a lesser extent, $Cr_{23}C_6$. Table XI below gives the physical properties of the strengthening particles present in MM'd material before and/or after consolidation. Based on the above results, a "new" DS Cu alloy has been inadvertently created. However, this addition of carbides to the Cu at the expense of Cr_2Nb should manifest itself as providing comparable, if not better, properties than Cr_2Nb alone. This contention is based, in part, on the fact that these carbides have relatively high negative free energies of formation and elastic moduli (see Table XI below) and the elements have low diffusivities and solubilities in Cu – especially Nb and C (see Table I). Therefore, the carbides should presumably remain stable at high temperatures and provide at least equivalent Orowan strengthening and Hall-Petch effects as do Cr_2Nb precipitates. In other words, when compared to Cr_2Nb, NbC is a viable alternative

dispersoid, making its formation fortuitous. Thus, at this point, based on this assertion, it should be indicated that the formation of carbides is obviously considered, but not necessarily emphasized, per se, especially with regard to remaining strengthening analysis.

Table XI -
Physical Properties of Strengthening Particles Present

Strengthening Phase	Density[a] (g/cm^3)	Melting Temperature[b] (K)	Heat of Formation, $-\Delta H_f$ (at 298 K, kJ/mol)	Young's Modulus, E (GPa)	Micro-Hardness (GPa)
Cr_2Nb	7.66	2043	20.9[c]	~214-268[d]	8.5-9.5[g]
Cr	7.19	2136	- -	249[e]	--
NbC_{1-x}	7.80	3873	140.8*	~450[f]	20-24[h]
$Cr_{23}C_6$	6.953	1807-1850	54.7*	- -	16.5[i]

*in kJ/mol C [85] [a][84], [b][82,83], [c][86], [d][87-89], [e][88], [f][90], [g][87,91,92], [h][90,93], [i][90,93].

3.2.2. Microstructural (and Phase) Evolution in MM/Hot Pressed Material (TEM)

The effect of MM on grain structure was assessed primarily with TEM. As an initial look at non-milled and as-milled microstructures for comparison purposes, Figure 46 gives TEM images of as-atomized and as-8 hr-milled (with fan cooling) Cu-8 Cr-4 Nb powder particles. The grain and Cr_2Nb structures that existed prior to milling have been transformed into fragmented, granular structures, induced from the severe plastic deformation of repeated micro- fracturing and welding. The overall grain/fragment size is less than about 100 nm. The virtually continuous ring pattern inset also provides direct evidence of fine grains and that the boundaries are at large-angle misorientations. Again, from this TEM examination of the pre-milled powder, containing the bulky primary Cr_2Nb and larger Cu grains; and the milled powder, containing a more refined and homogeneous microstructure, MM has, again, proven effective for its stated purposes.

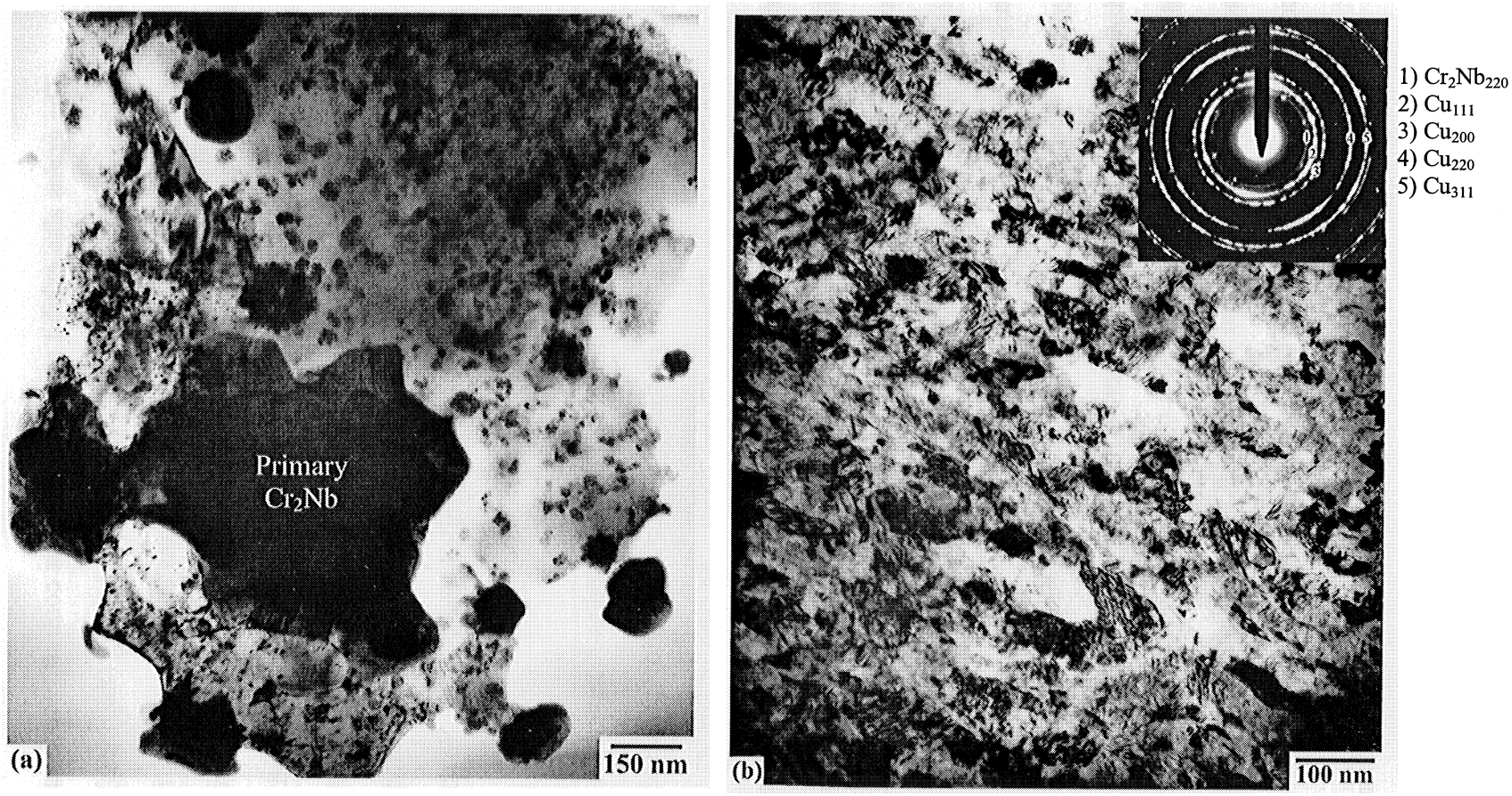

Figure 46 – (a) TEM micrograph of an as-atomized Cu-8 Cr-4 Nb alloy powder particle; (b) TEM observation of an as-8 hr-milled Cu-8 Cr-4 Nb alloy powder particle. (b) exhibits a relatively complex, internal strain contrast. Large granular misorientations are also evinced by the virtually *continuous* SAD ring pattern, which also reveals presence of Cr_2Nb.

The grains also exhibit a mottled, complex contrast, which indicates a high level of internal strains [94-95]. The slight azimuthal spreading (fuzziness) of the rings in Fig. 46(b) is also indicative of internal strains, analogous to XRD internal strain peak broadening. Based on these present observations and prior work on heavily deformed (equal channel angular processed) Cu by Valiev [96], the grains and boundaries are in a non-equilibrium state. Finally, notice the presence of Cr_2Nb in the as-milled powder – by its reflection pointed out in the SAD ring pattern inset. This, along with such Cr_2Nb detection in Fig. 43 in similar as-4 hr-milled Cu-4 Cr-2 Nb take on even more significance when considering hot pressed MM powder.

Figure 47 shows TEM images of consolidated as-received Cu-4 Cr-2 Nb. Similar to as-extruded, the initial hot pressed Cu-4 Cr-2 Nb alloy possesses grain sizes in the range of 0.25 - 2.5 μm (Figures 47 and 39(a)). As seen in Fig. 47, the as-atomized/hot pressed Cu-4 Cr-2 Nb alloy contains a very similar grain and bimodal precipitate size distribution as the extruded material. The average grain size of hot pressed Cu-4/2 (~1.42 μm) is very comparable to that for as-extruded Cu-4/2 (1.53 μm), and again, ≈50% larger than that of as-extruded Cu-8/4 alloys. As in extruded Cu-8/4 and Cu-4/2, most larger particles range from 0.5 – 2 μm in size – best seen in Fig. 39(a) – while the smaller type are typically less than 300 nm (a majority of precipitates in Fig. 47). Again, as the data in Fig. 40 indicate, the average primary particle size for Cu-4/2 (~0.78 μm) is slightly less than that for Cu-8/4 (~0.93 μm), but within the margins of error. Finally, notice the remaining original powder-particle boundary for the as-atomized/hot pressed condition (arrows in Figure 47(a)).

TEM micrographs of hot pressed powders after one-half and 4 hr milling are shown in Figures 48/49 and 50/51, respectively. After ½ hr milling, the microstructure reveals deformed layered regions, or a textured structure of elongated grains (Fig. 48(a)), along with areas with evidently little deformation (Fig. 49(b)). That is, the microstructure

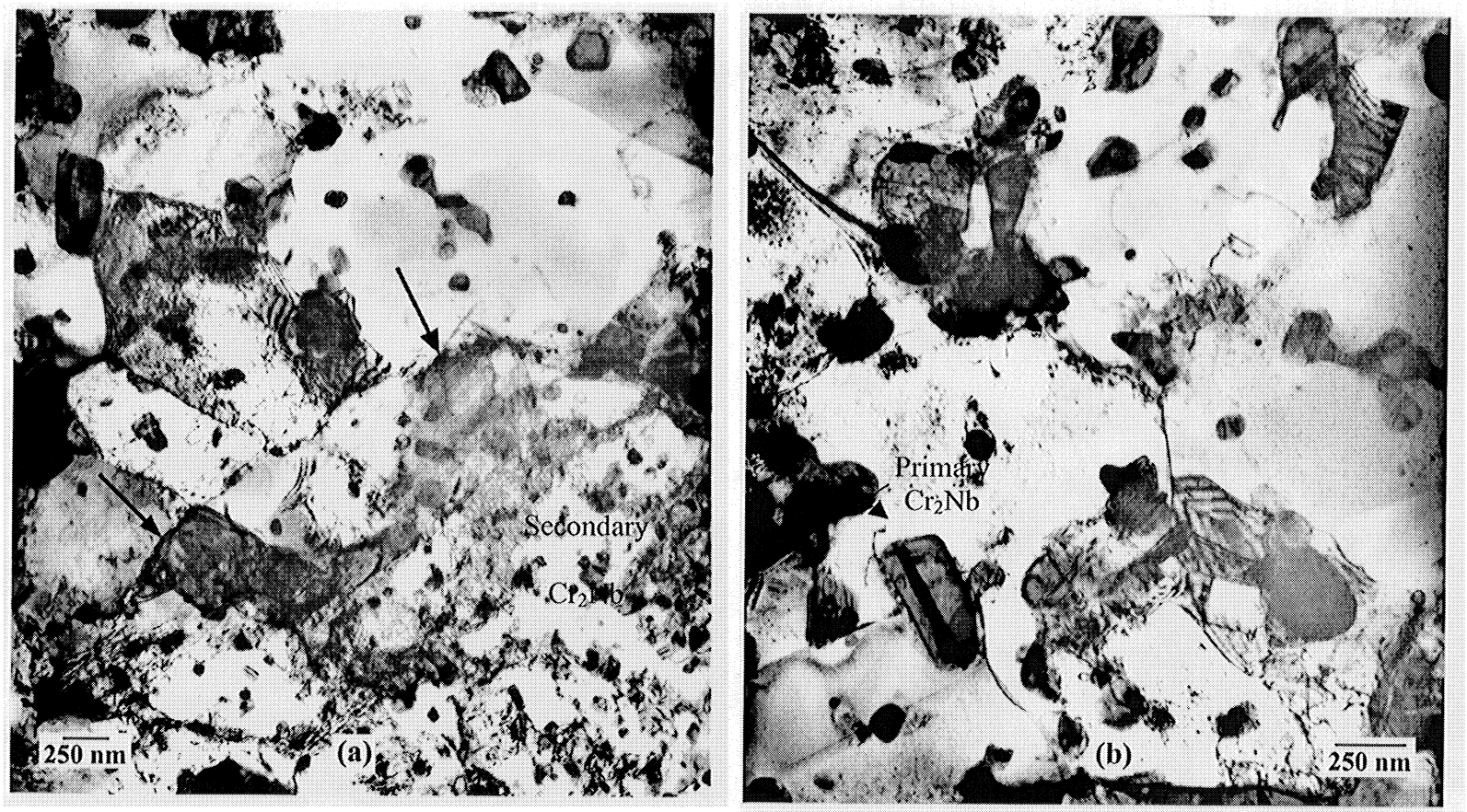

Figure 47 – TEM micrographs of as-atomized/hot pressed Cu-4 Cr-2 Nb alloy: (a) and (b) both show quite a variation in initial Cu grain and Cr_2Nb precipitate size (even for those under ≈300 nm); a remaining prior powder particle boundary can also be seen in (a).

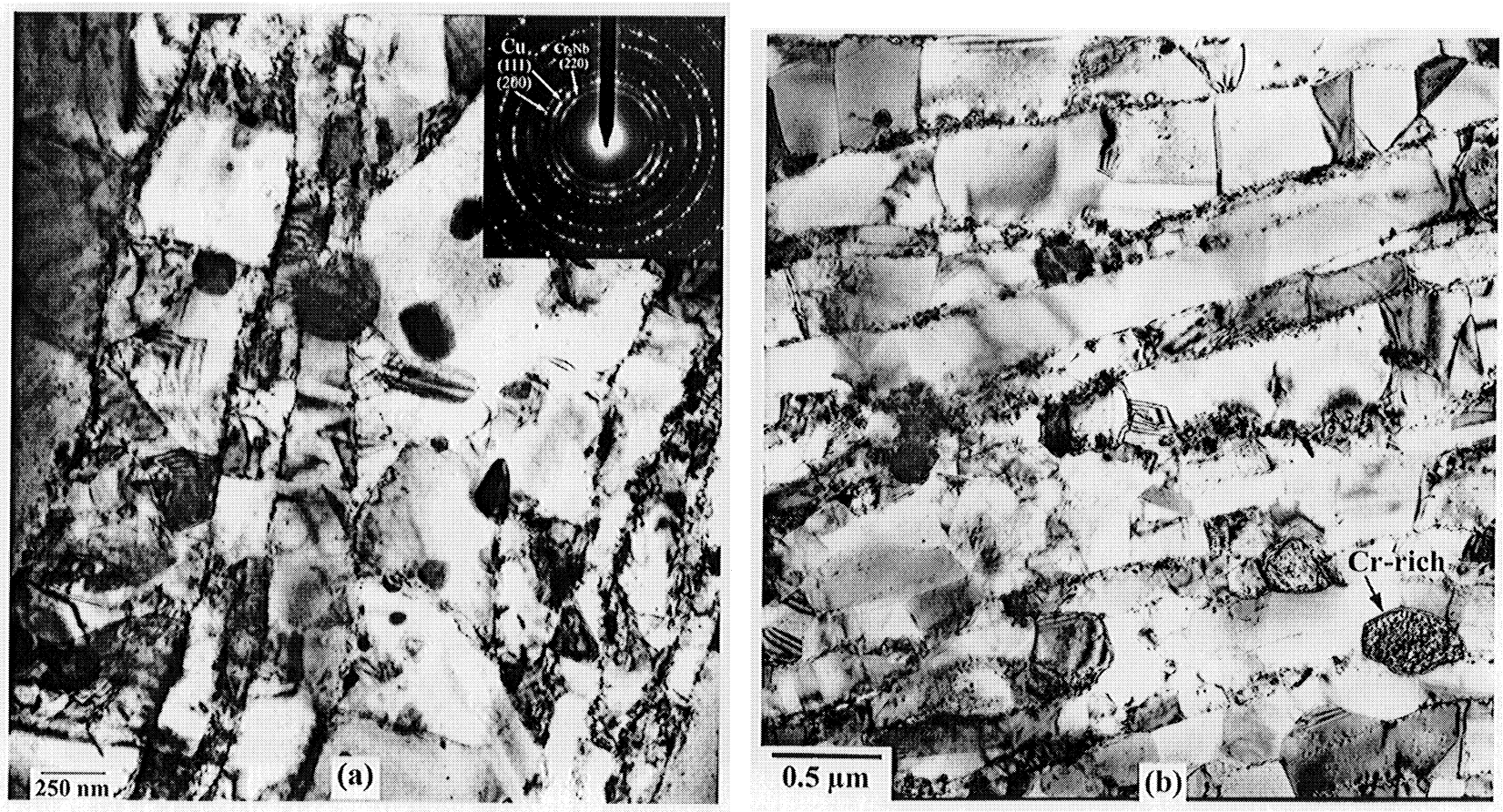

Figure 48 – Images of hot pressed Cu-4 Cr-2 Nb alloy powder MM-½ hr as also seen by TEM; both (a) and (b) reveal an essentially layered structure, depicting extensive plastic deformation; (Also, notice the *discontinuous* SAD ring pattern inset in (a) and the sheared Cr-rich dispersoid in (b).)

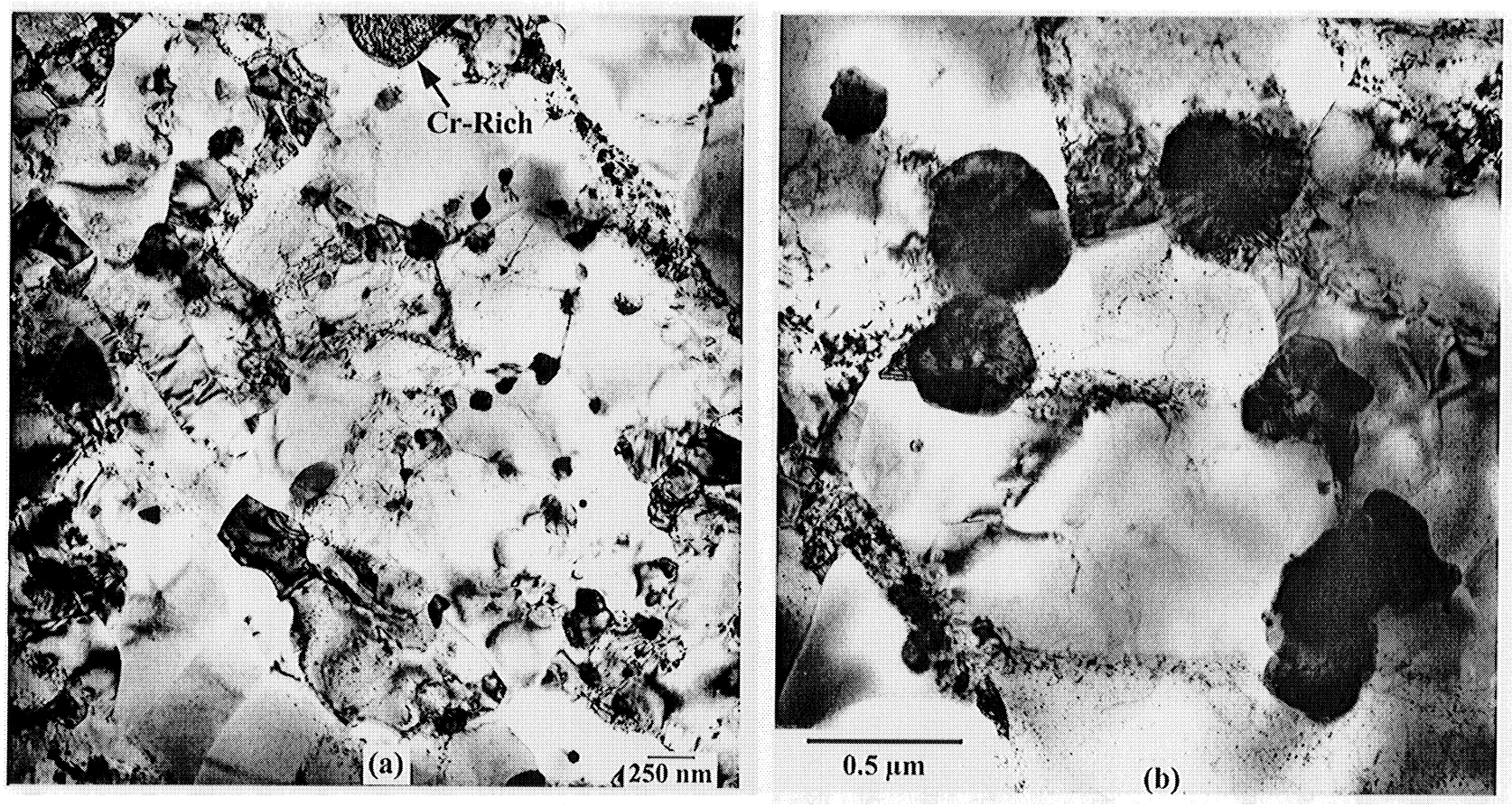

Figure 49 – Images of hot pressed Cu-4 Cr-2 Nb alloy powder MM-½ hr as also seen in TEM. In this case both (a) and (b) show regions of relatively little deformation, i.e. lacking such previously shown elongated grains. This indicates non-uniform cold-working, i.e. non-steady-state, incomplete milling. (Also, notice again a Cr-rich precipitate in (a).)

is non-uniform, with varying degrees of elongation, which suggests the MM process is incomplete, which is typical for short milling times. Figure 48 represents the same condition as shown in Fig. 39(b). The discontinuous SAD ring pattern inset in Fig. 48(a) further indicates a textured, non-uniform microstructure. In addition, a non-uniform distribution of precipitates may be noticed, which also suggests the milling time is not long enough, e.g., the primary Cr_2Nb is still at "original" grain boundaries in Fig. 49. However, Figure 48 does definitely reveal an initial overall grain size refinement and flattening due to the severe plastic deformation. In addition, the ring pattern inset verifies the XRD results (Fig. 45) regarding the presence of the Cr_2Nb phase.

Finally, after milling for 4 hr, the microstructure is much more refined and uniform compared to consolidated as-atomized and MM-½ hr material. For example, Figures 50 and 51(a) reveal a generally equiaxed and fine grain structure, with virtually all grain and precipitate sizes being less than about 150 nm. This drastically refined grain structure to ultrafine, sub-micron size is, again, further evinced by the continuous Cu SAD rings in the SAD pattern inset in Figure 50. These reflections arranged in such continuous circles is evidence of appreciable misorientations remaining across boundaries, i.e. high-angle boundaries still remain after hot pressing. Such grain-size results not only signify that the objective of Cu grain refinement has been largely met, but also that the concept and efficacy of MM as applied to Cu-4 Cr-2 Nb is further validated with respect to Cu structure.

Now, comparing these microstructures to that for 8-hr milled Cu-8 Cr-4 Nb (Figure 46(b)) directly illustrates the relatively minor change in overall microstructure before and after high temperature densification. The grains and boundaries in Fig. 50 are slightly more relaxed than those in Fig. 46(b), as also indicated by slightly sharper diffraction rings, but the contrast still remains fairly complex. All of this points to a

mechanically refined two-phase microstructure that remains relatively stable even after exposure at 810°C for 3 hrs.

Figure 50 – TEM observation of hot pressed Cu-4 Cr-2 Nb alloy powder MM-4 hr. As opposed to the previous (TEM) microstructures, this exhibits a relatively uniform, equiaxed and ultra-fine grain structure with high-angle boundaries. This is also evinced by the *continuous* SAD ring pattern inset.

Due to their refinement, it is difficult to distinguish between Cu grains and second-phase(s) in bright field. Therefore, Figure 51(b) is a dark-field TEM image showing the significantly refined second-phase particles with an essentially uniform distribution, analogous to Figures 39(f) and 41(e). They are also seen at grain boundaries. These dispersoids are identified in the SAD ring pattern as NbC; Cr_2Nb is

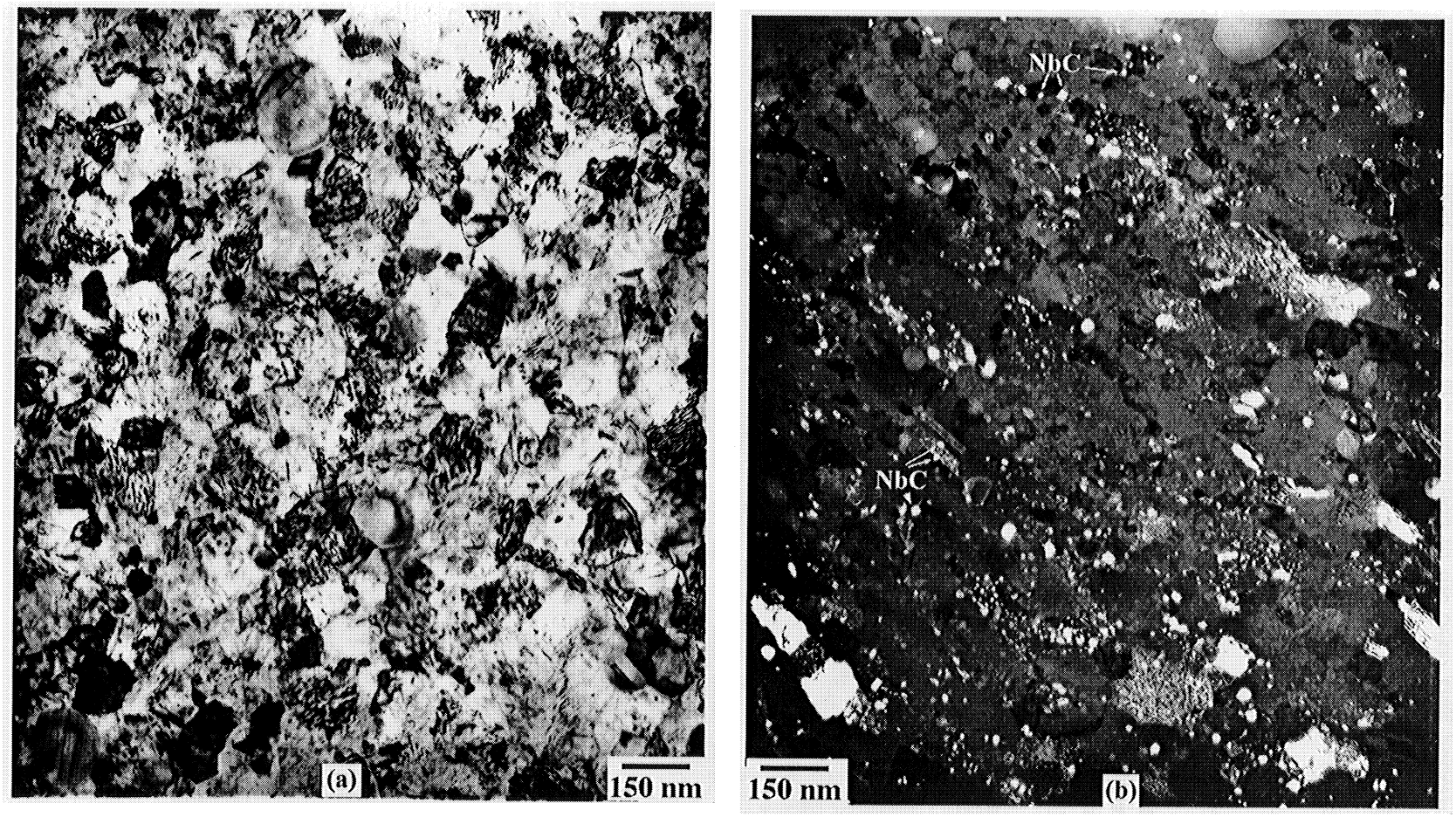

Figure 51 – TEM observation of hot pressed Cu-4 Cr-2 Nb alloy powder MM-4 hr: (a) Bright-field TEM showing refined, equiaxed grain/subgrain structure; (b) Dark-field TEM image showing fine dispersoids, which are identified as NbC in the SAD ring pattern of Fig. 50.

not apparent. This, again, verifies the XRD trace for 4-hr milled/hot pressed Cu-4 Cr-2 Nb in Fig. 45. What is not detected thus far is Cr and its form. Chromium is fortuitously detected in the XRD spectra collected primarily for Cu (reflections), which is forthcoming in Section **3.2.4**.

Once again, the initial bimodal precipitate-size distribution can be seen to have effectively disappeared, as intended with the application of MM, regardless of dispersoid type. It is shown next how, as a result of this microstructural evolution, a steady state condition with a basically steady peak hardness is achieved. More thorough quantitative measurements of grain and particle size and distributions, and evaluation and application of the relative contributions of Hall-Petch and Orowan strengthening to this final mechanical strength are important aspects of this study and are detailed later.

3.2.3. Mechanical and Electrical/Thermal Properities vs. Milling Time

3.2.3.1. Rockwell Hardness and Electrical Conductivity vs. Milling Time for Cu-4 Cr-2 Nb

Figure 52 shows the variation of hardness and electrical conductivity as a function of milling time when either steel balls and vial (a) or WC balls and vial were used (b). Note that the hardness values plotted are based on Rockwell B scale, i.e. HRB. Also, the electrical conductivity reported here is in %IACS. (These are also converted to actual conductivity values $[\text{ohm-cm}]^{-1}$ when necessary in calculations.) The steepest incremental increase in hardness results from the initial half-hour milling regardless of the milling media used. This is actually in good correlation to the grain size refinement along with precipitate size and distribution change noticed by TEM (Fig. 48) and SEM (Fig. 39(b)).

Beyond one-half hour, the increase in hardness becomes less and less precipitous and effectively levels off after four hours of milling. Conversely, electrical conductivity

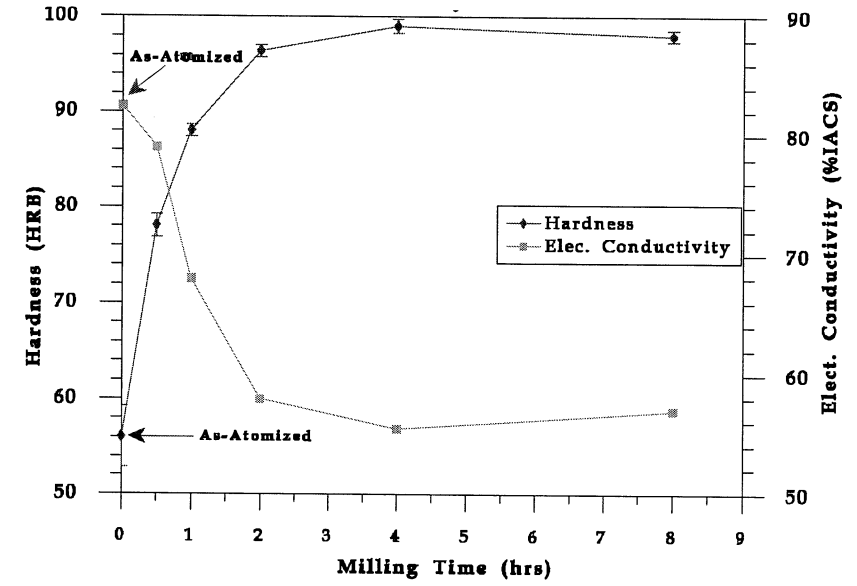

(a) * Milled with Steel Vial/Balls - PCA/LN2 Cooling

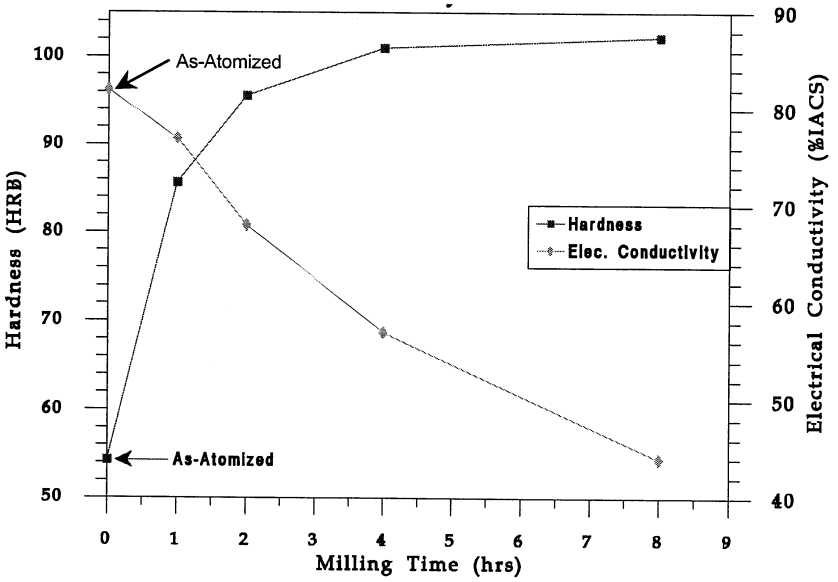

(b) * All data correspond to Hot Pressed Material. Milling done with WC Vial/Balls - Fan Cooled

Figure 52 – Effects of milling time on hardness and electrical conductivity of hot pressed Cu-4 Cr-2 Nb after a) milling with steel vial/balls – with PCA and LN2 cooling; and b) milling with WC vial/balls - with no PCA and fan cooling.

decreases sharply after two-hour milling using steel media, and essentially levels off beyond this time at about 56% IACS. In other words, the hardness increased exponentially with time, whereas conductivity decreased exponentially with time. In contrast, when milling was performed using WC, electrical conductivity did not drop as

sharply for up to two hour milling, but shows an overall steady, almost linear decrease with milling time. A conductivity of 44% IACS was measured after 8 hr milling. The profile for steel media suggests a more explicit correlation of conductivity with hardness (i.e., they both "saturate"), while that for WC media indicates that conductivity would continue to decrease with milling time, effectively independent of hardness. Finally, the apparent steady peak hardness and corresponding microstructures (Figures 39(e-f), 41(d-e), 50 and 51) suggests a steady state condition has been achieved. The following Vickers microhardness study reveals a very similar trend.

The eventually steady conductivity for material milled with steel media is most likely due to roughly constant volume fractions of particles forming as carbides (with C coming out of solid solution) – for 4 and 8 hr milling. However, when using the WC media, with no PCA, WC and cobalt wear debris contaminated the powder in a gradually increasing manner. Figure 53 shows SEM observations of Cu-4 Cr-2 Nb powder after milling 4 and 8 hr with WC vial and balls. The media did show spalling and pitting, and as Fig. 53 reveals, the worn media was incorporated into the powder charge. There is an obvious qualitative increase in WC content from 4 to 8 hr. (A quantitative value of W, C and Co content for 4 hr is given shortly in Table XIII.) Thus, as the volume fraction of WC increases, the conductivity decreases accordingly. This outcome, unfortunately, made WC a nonviable option for milling media, since avoiding Fe and a PCA is preferred. WC vial and balls were initially used to avoid Fe and PCA contamination, since WC is relatively hard and inert compared to steel, and sticking and agglomeration of Cu alloy powder is relatively minor.

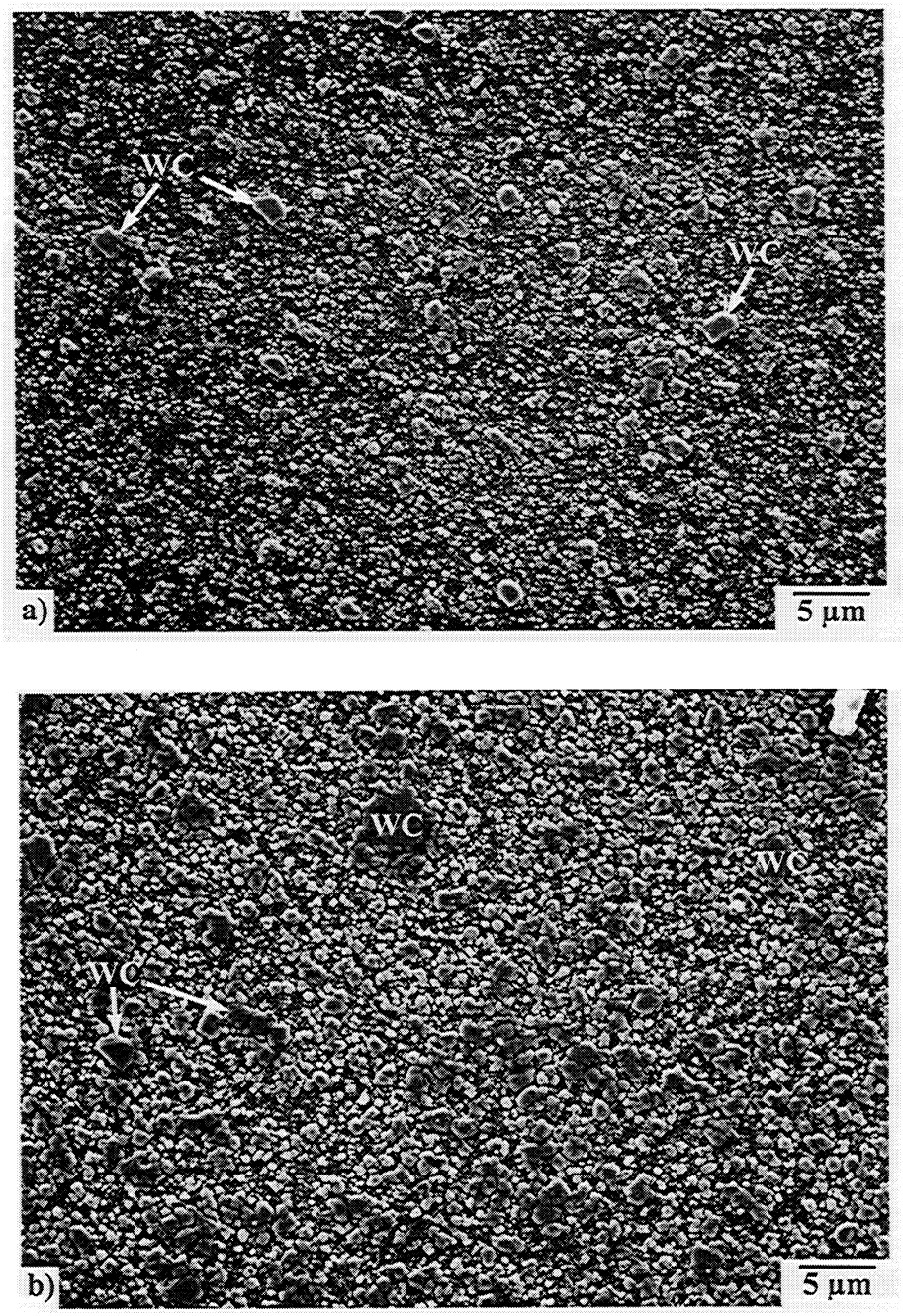

Figure 53 – Cu-4 Cr-2 Nb mechanically milled with WC media and fan cooling for (a) 4 hr and (b) 8 hr.

3.2.3.2. Vickers Hardness and Equivalent Yield Strength vs. Milling Time for Cu-4 Cr-2 Nb

Figures 54 and 55 represent microhardness (HV) variation of as-milled and as-milled/hot pressed Cu-4 Cr-2 Nb powder with milling time. Both profiles exhibit a similar hardening/strengthening trend: early rapid increase, followed by a leveling-off (saturation/steady-state condition). For diamond pyramid indenters, like the Vickers indenter used in this study, hardness can be empirically related to cold-worked yield stress of polycrystalline metals by the relation HV $\approx 3\sigma_y$ (in [MPa]) [63, 97]. In other words, such a relation can be applied for materials that exhibit little work hardening, e.g., already-deformed (pre-hardened) and nanocrystalline materials [63, 98]. Two relevant instances where this correlation has been established involve DS Cu alloys. Morris and Morris [99] found such a relation for their less ductile, rapidly solidified Cu-Cr alloys. From their work on mechanically alloyed Cu-(10-28) vol% Nb, Benghalem and Morris [100] also found this 1/3 relation (to hold) for material having 140-300 nm grain sizes.

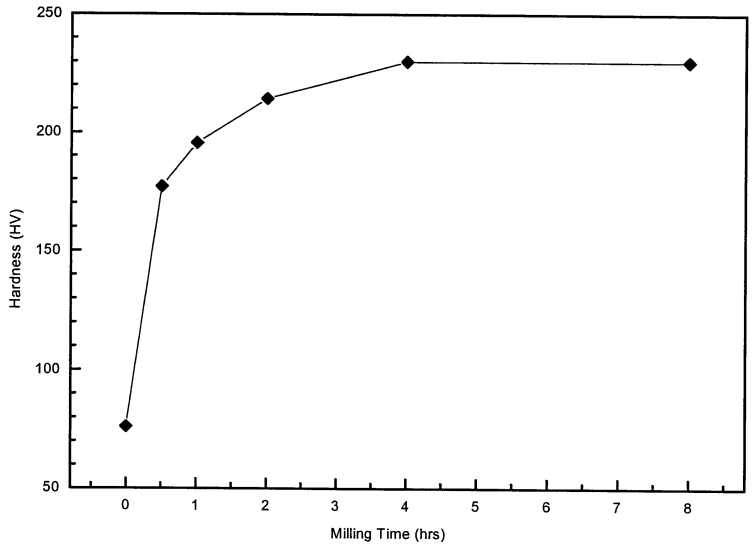

Figure 54 - Effects of milling time on Vickers Hardness of as-milled Cu-4 Cr-2 Nb. (Milling condition: Steel vial/balls - with PCA and LN2 cooling).

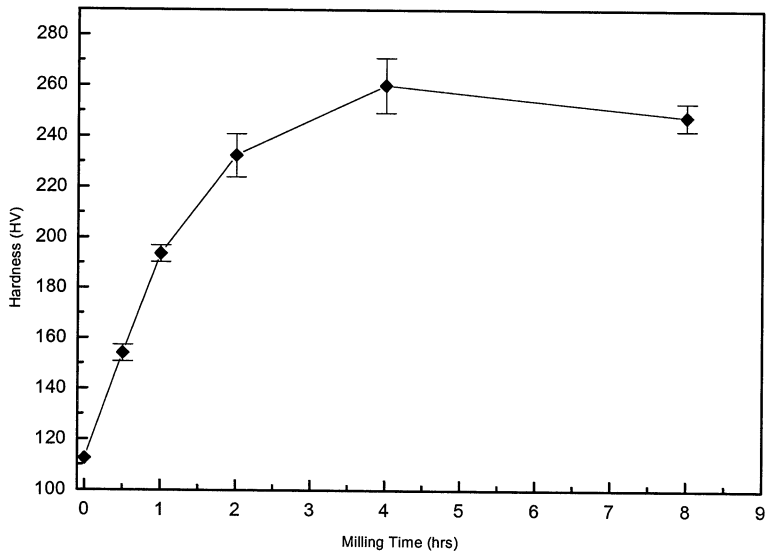

Figure 55 - Effects of milling time on Vickers Hardness of as-milled/hot pressed Cu-4 Cr-2 Nb. (Milling condition: Steel vial/balls - with PCA and LN2 cooling).

Based on the above findings, the HV $\approx 3\sigma_y$ relation was applied to the above hot pressed hardness data and taken as approximate equivalent yield stresses, which are plotted in Figure 56. The maximum yield stress is ≈850 MPa. The most valid values are most likely those for milling times ≥ 2 hrs, since significant hardening has occurred for 2 hr milling and beyond – with only modest additional hardening taking place beyond 2 hr. For example, the as-received/hot pressed, prehardened value of ~365 MPa is 77% higher that the measured 206 MPa, as expected. Finally, the hardness data in Figures 52 and 55 prove the efficacy of MM at improving the strength of Cu-4 Cr-2 Nb to above that of extruded Cu-8 Cr-4 Nb (Fig. 28), thereby fully satisfying the MM objectives set forth.

(As an aside, it can be noted here that additional analysis of hardness data has been done. Appendix B is a plot of Vickers hardness as a function Rockwell B hardness; it is essentially a compilation of all hardness data acquired in this work on Cu-8 Cr-4 Nb and Cu-4 Cr-2 Nb alloys in the starting powder, extruded, hot pressed, as-milled powder, milled powder/hot pressed and aged conditions. For the higher hardness values, as indicated on the plot, HV can be estimated for Cu-Cr-Nb alloys from knowing HRB, which can, in turn, be converted to an approximate equivalent yield strength.)

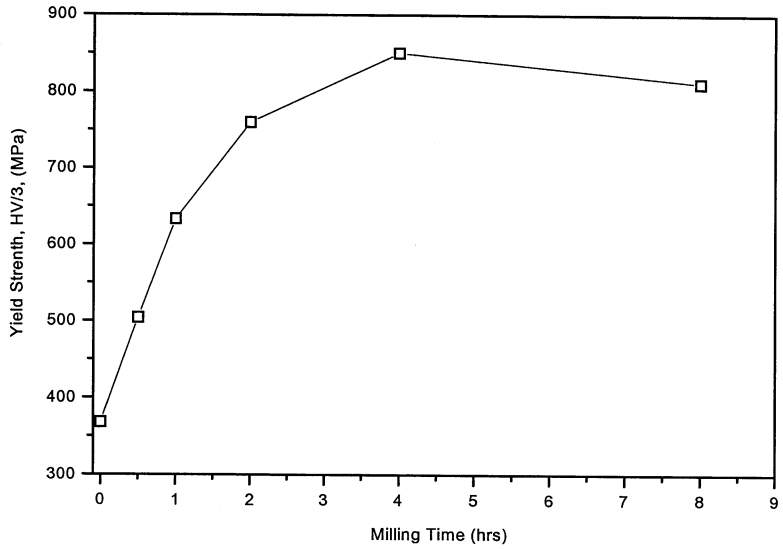

Figure 56 - Effects of milling time on hardness equivalent yield strength of as-milled/hot pressed Cu-4 Cr-2 Nb.

3.2.3.3. Rockwell Hardness and Electrical Conductivity of Four Mechanically Milled DS Cu Alloys

Hardness and electrical conductivity values and impurity content for hot pressed as-atomized and 4 hr milled powders are shown in Tables XII and XIII, respectively. For comparison, the same results for MM of Cu-8 Cr-4 Nb alloy, a DS Cu-Al_2O_3 alloy (GlidCop Al-15) and precipitation strengthened NARloy-Z alloy (Cu-3 wt.% Ag-0.5 wt.% Zr) are also shown. Again, the latter is the copper alloy currently used in aerospace applications. Figure 57 is a graphical representation of the relevant hardness data of Tables XII and XIII. Note that the as-atomized/hot pressed values for Cu-Cr-Nb in Table XII are comparable to those for as-extruded material.

Table XII -
Initial Properties of As-Atomized/
Hot Pressed DS Copper Alloys

Material	Oxygen Content (wppm)	Hardness (HRB)	Electrical Conductivity (%IACS)
Cu-4 Cr-2 Nb	480	~57	82
Cu-8 Cr-4 Nb	450	69	71
NARloy-Z	680	48	82
GlidCop Al-15	- -	66	92

Table XIII -
Impurity Content, Hardness and Electrical Conductivity of Mechanically Milled/Hot Pressed DS Cu Alloys

Material: Impurity (wppm)	**Cu-4Cr-2Nb** MM-4hr (Stl/PCA/Fan)	**Cu-4Cr-2Nb** MM-4hr (WC/Fan)	**Cu-8Cr-4Nb** MM-4hr (Stl/PCA/Fan)	**GlidCop Al-15** MM-4hr (Stl/PCA/LN2)	**NARloy-Z** MM-4hr (Stl/PCA/LN2)
Oxygen	630	1320	1770	- -	1000
Carbon	5870	2500	2640	4960	4080
Iron	790	- -	460	380	150
Tungsten	- -	25400	- -	- -	- -
Cobalt	- -	1800	- -	- -	- -
Hardness (HRB)	**99.6** **97***	**101**	**101.4** **99***	**91** **72***	**96.5** **94.5***
Elect. Conduct. (%IACS)	**55** **57.5***	**57** **- -**	**51** **53***	**71** **67***	**69** **69***

* Hardness and Electrical Conductivity after Simulated Braze Cycle at 1210 K-1 hr/Furnace Cooled

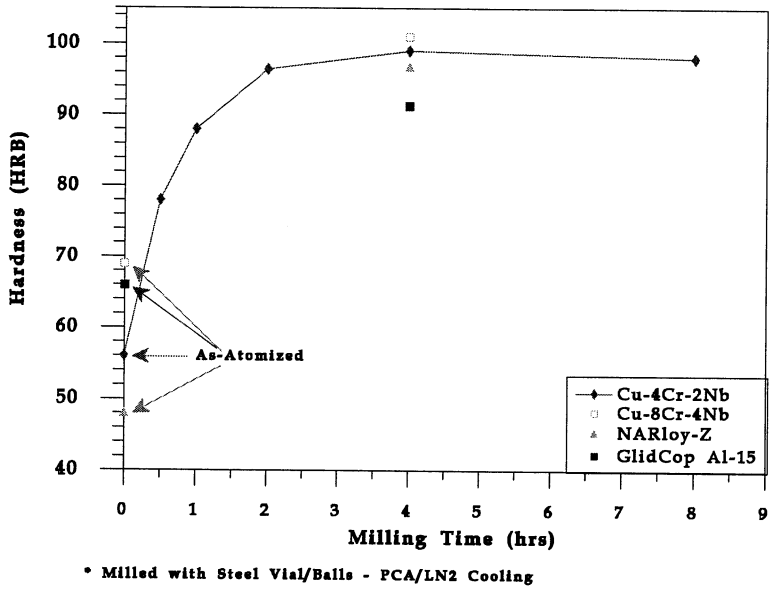

Figure 57 - Effect of milling time on hardness of hot pressed Cu-4 Cr-2 Nb when milled with steel vial/balls - and PCA, specifically comparing with three other 4-hr milled/hot pressed Particle/Dispersion-Strengthened Cu alloys.

It is interesting to note how two of the other three 4 hr hardness values fall within ± 3 HRB of the Cu-4 Cr-2 Nb HRB data point. Also, despite their difference in particle volume fractions, Cu-8/4 and Cu-4/2 are remarkably close. Taken together, this suggest that these 4-hr hardnesses are more related to Cu grain size effects than to amount and type of dispersed particle.

3.2.3.4. Electrical and Thermal Conductivity of Mechanically Milled Cu-4 Cr-2 Nb

In order to address thermal conductivity of processed Cu-Cr-Nb, electrical conductivity data in $(\Omega\text{-cm})^{-1}$ are first required. Such data for MM'd Cu-4/2 have been calculated using the measured electrical conductivity, in %IACS, and the 58.84×10^4 $(\Omega\text{-cm})^{-1}$ value for pure copper, and are tabulated in Table XIV. Also listed in Table XIV are corresponding calculated thermal conductivities. Again, with metals, the Wiedemann-Franz law allows direct conversion of electrical to thermal conductivity, although direct measurement of thermal conductivity would be most preferred. The thermal conductivities are calculated using the established L value of $\mathbf{2.36 \times 10^{-8}}$ W-Ω/K^2 with the electrical conductivities given in column 3. Figure 58 is a graphical representation of such thermal conductivities given in Table VIV. (Lacking another L value – except for pure Cu – the above L value is used for consistency, even though Cr_2Nb is gradually replaced by carbides during milling with PCA.) Finally, it noteworthy that the RT percent-of-pure-copper values for thermal conductivity in Fig. 33 are close to the electrical %IACS values in Table XII. In other words, the as-extruded conductivity values can be taken as essentially those for hot pressed Cu-Cr-Nb.

Table XIV -
Room Temperature Electrical and Thermal Conductivities of Mechanically Milled Cu-4 Cr-2 Nb

Milling Time	Electrical Conductivity[1]	Electrical Conductivity[2]	Electrical Resistivity[3]	Thermal Conductivity[4]
hr	%IACS	$\times 10^4(\Omega\text{-cm})^{-1}$	(μΩ-cm)	W/m-K
0	82	48.5	2.07	339.0
½	79	46.6	2.15	324.6
1	68	40.1	2.50	279.4
2	58	34.2	2.93	238.3
4	55.5	32.7	3.06	228.0
8	57	33.6	2.98	234.2

[1]Measured values
[2]Calculated based on σ_e of 58.84×10^4 $(\Omega\text{-cm})^{-1}$ for pure, annealed Cu (see Table VI).
[3]Calculated as the inverse of electrical conductivity
[4]Calculated from Wiedemann-Franz, taking K_{Cu} = 398 W/m-K and L=2.36×10^{-8} W-Ω/K^2

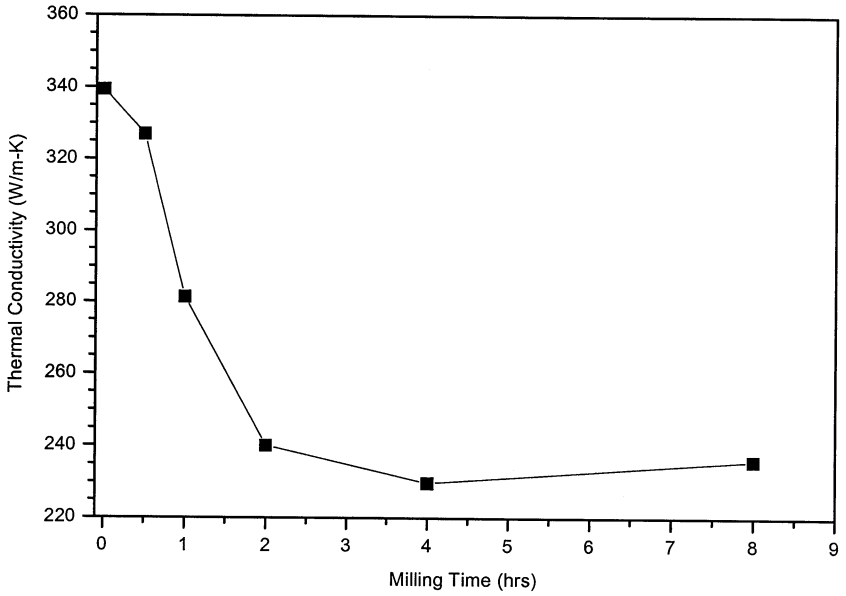

Figure 58 – Calculated Thermal Conductivity for Cu-4 Cr-2 Nb as a function of Milling time (of Hot Pressed material).

3.2.3.5. Effects of Heat Treatment on Hardness and Electrical Conductivity of Mechanically Milled (and Extruded) Cu-Cr-Nb Alloys

To better assess the effects of microstructure, e.g., grain and particle size, on the hardness and conductivity of as-extruded and mechanically milled/hot pressed Cu-4 Cr-2 Nb, such materials were aged for 50 hours at 1000°C (1273 K). In addition to actual hardness and electrical conductivity values, Table XV below also includes the change in these values after this heat treatment. Notice that the percent reduction in hardness is less for the milled material than for the non-milled/extruded material. This suggests that milling not only provides strengthening to Cu-4 Cr-2 Nb, but also enhanced thermal stability, which were the objectives of this "part-two" study of Cu-Cr-Nb. (For the as-extruded Cu-8/4 and 4/2, high-temperature annealing has much greater effect on the hardness than conductivity.) For comparison, similarly processed NARloy-Z was considered and results given. Notice how the hardness of NARloy-Z is basically halved from the high-temperature anneal and the conductivity actually dropped. The hardening precipitates formed from Cu-Zr-Ag and Ag were solutionized and did not fully re-

precipitate upon furnace cooling, which led to extensive grain growth, thus proving much less stable with respect to its solutionizing and related grain growth.

Table XV -
Effect of High-Temperature Anneal on Properties of Milled and Non-Milled Cu-Cr-Nb and Milled NARloy-Z

Cu Alloy	Cu Alloy Condition	Hardness, HRB	Elect. Cond., %IACS	ΔHRB, %	ΔIACS, %
Cu-4 Cr-2 Nb	As-Extruded	57	74	- -	- -
	+ 1000°C-50 hr Ann.	30	76	-47	+2.7
	MM-4 hr; Hot Pressed	~100	~55.5	- -	- -
	+ 1000°C-50 hr Ann.	~78	~72.5	-22	+30
Cu-8 Cr-4 Nb	As-Extruded	69	53.5	- -	- -
	+ 1000°C-50 hr Age	48.6	54	-30	+1.0
	MM-4 hr; Hot Pressed	~101	~51.5	- -	- -
	+ 1000°C-50 hr Ann.	~84.3	~53.5	-17	+4.0
NARloy-Z	MM-4 hr; Hot Pressed	~97	~69	- -	- -
	+ 1000°C-50 hr Ann.	~48.5	~60	-50	-13.0

Figure 59(a) and (b) are TEM micrographs of the milled/hot pressed, then annealed Cu-4/2 which does show obvious microstructural coarsening when compared to just milled/hot pressed material (Figures 50 and 51). But, the Cu grains and NbC do remain under ~0.6 μm and 100 nm, respectively, as also reflected by the fairly continuous Cu rings diffracting in the associated SAD pattern. This stability is obviously a manifestation of stable dispersoids pinning the boundaries, as is very evident in Fig. 59(b). And, by showing less complex contrast (sharp rings) and thickness fringes, the grains and grain boundaries are considered at or near equilibrium, unlike those in Figures 50 and 51. Finally, the relatively significant increase in conductivity of the milled Cu-4/2 after annealing does indicate that coarsening and Cu grain relaxation have a more direct effect on conductivity than they do on hardness.

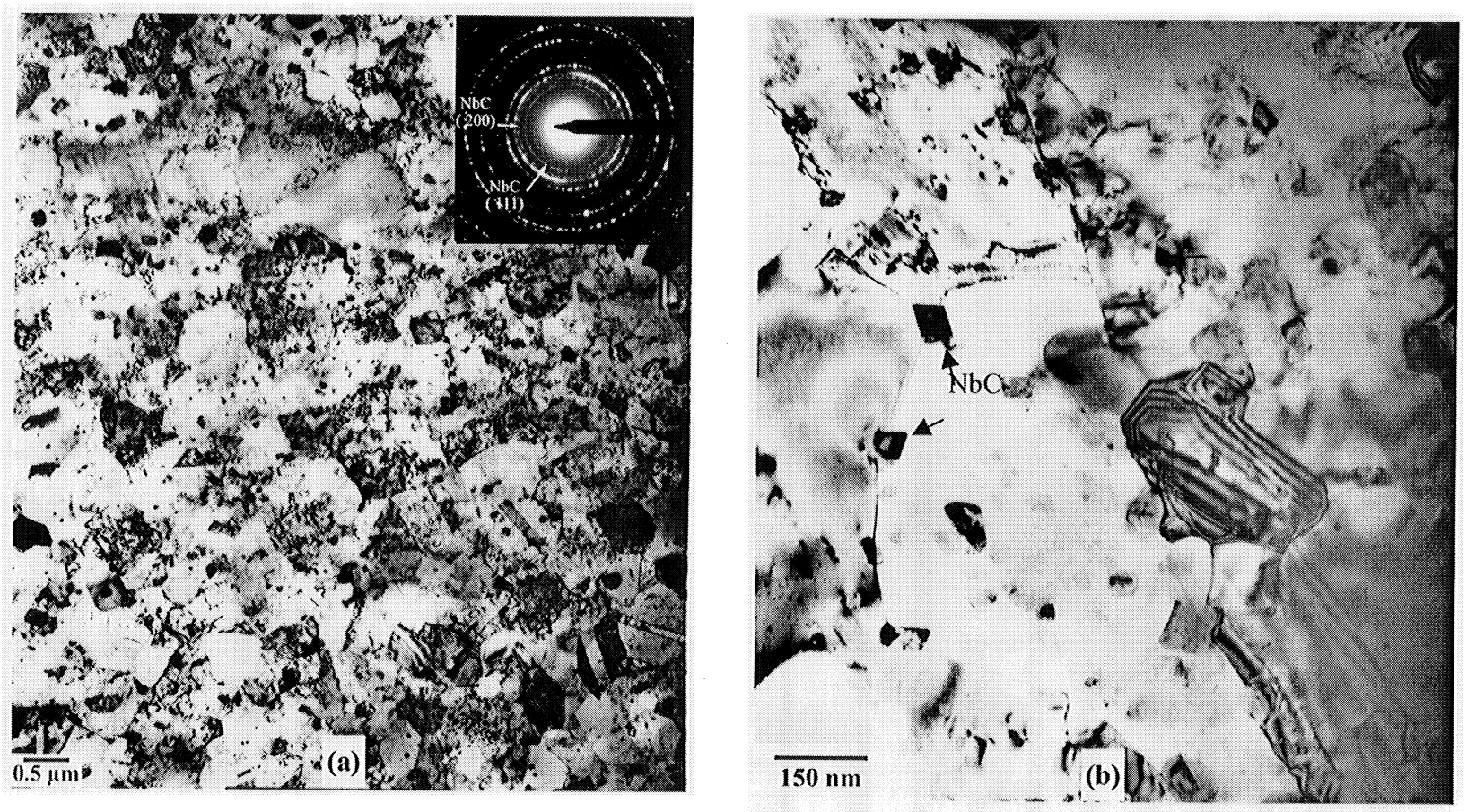

Figure 59 – Cu-4 Cr-2 Nb MM-4 hr/Hot Pressed/Annealed at 1273 K for 50 hr. (a) and (b) The grains are stabilized still at the sub-micron scale; (a) SAD ring pattern still showing fairly continuous Cu rings and (b) showing obviously well defined equilibrium grain boundaries pinned by dispersoids.

Figure 60 is an XRD spectrum taken from the MM-4 hr Cu-4 Cr-2 Nb after the 1273 K-50 hr heat treatment. When comparing to Fig. 45, it is apparent from the narrower peak in Fig. 60 that NbC coarsens and the distinct $Cr_{23}C_6$ peak materializing indicates it has a larger size and, to a lesser extent, volume fraction than before heat treatment. In fact, coarser NbC and $Cr_{23}C_6$ have been revealed in bright-field TEM, e.g., Figures 59 and 61. Figures 61 and 62 show specifically identified coarsened carbide particles. Note that $Cr_{23}C_6$ carbides were not identified, either visually in TEM or through electron and x-ray diffraction, for the non-annealed material. NbC particles are smaller than $Cr_{23}C_6$, thereby showing sluggish coarsening compared to $Cr_{23}C_6$. This is expected based on Eq. (2) and considering 1) niobium and chromium are the respective rate controlling species for coarsening, since they both have lower diffusivities (D) than carbon (Table I); 2) Nb has a lower diffusivity in Cu than does Cr (Table I); and 3) the molar volume (V_m) of $Cr_{23}C_6$ (182.4 cm^3/mol) is much larger than that of NbC (13.2 cm^3/mol).

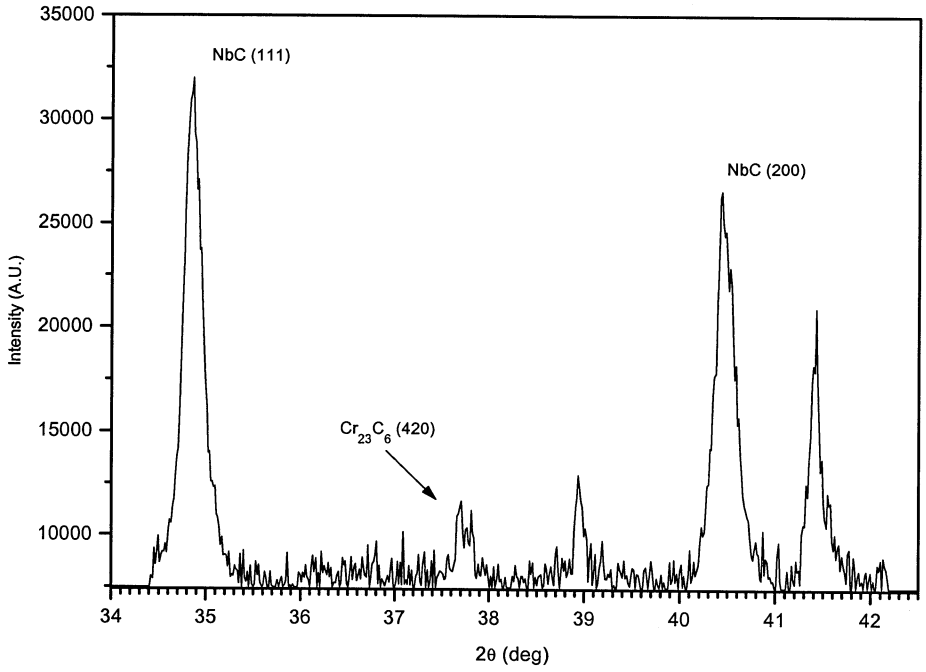

Figure 60 – XRD Spectrum showing two relatively distinct, intense NbC peaks and one smaller $Cr_{23}C_6$ peak from Cu-4Cr-2Nb, which was MM'd 4 hrs and Hot Pressed, then followed by an anneal at 1273 K for 50 hrs.

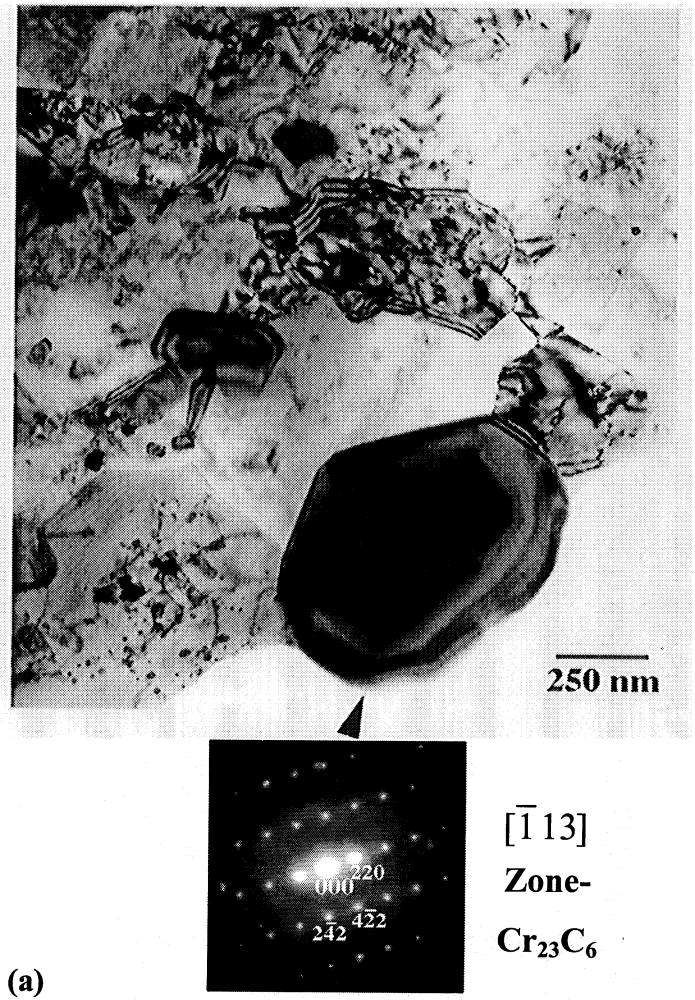

Figure 61 – Cu-4 Cr-2 Nb MM-4 hr/Hot Pressed/Annealed at 1273 K for 50 hr, showing relatively large $Cr_{23}C_6$ particles. (a) is an SAD pattern of an FCC-type Zone; (b) is an SAD of an FCC-type [011] Zone.

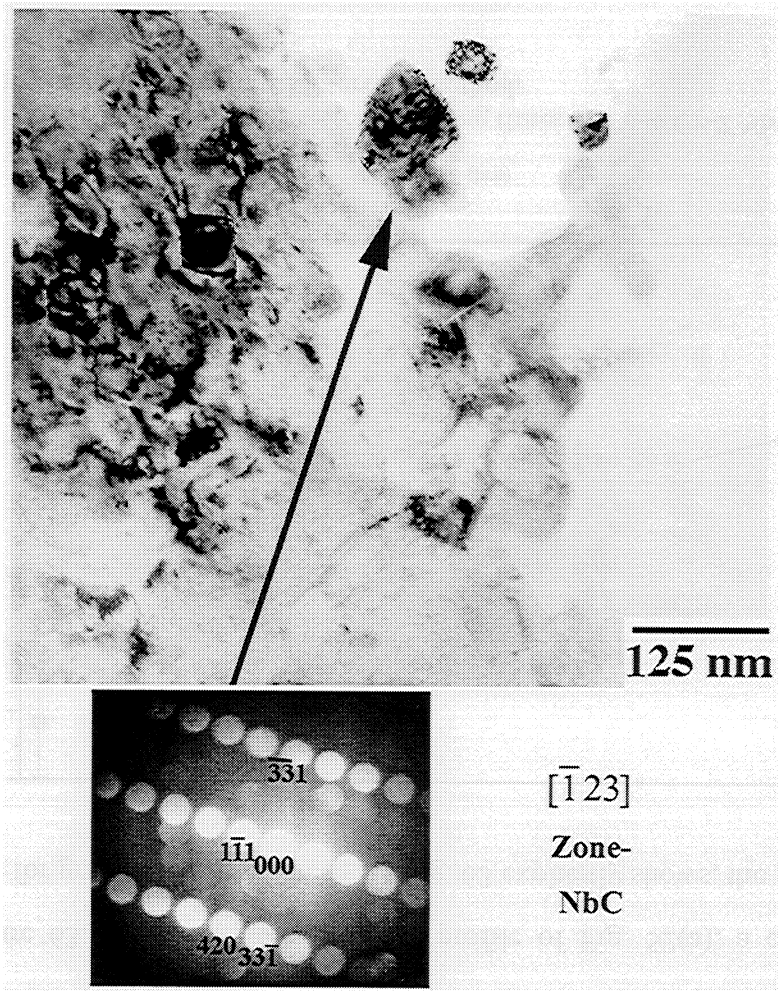

Figure 62 – Cu-4 Cr-2 Nb MM-4 hr/Hot Pressed/Annealed at 1273 K for 50 hr, with CBED pattern of an $NbC_{\sim 0.92}$ particle.

The following section presents selected grain and particle size data that will help elucidate how microstructural changes affect the properties in Table XV.

3.2.4. Particle/Grain Size Analysis

Since microstructural properties dictate mechanical and conductivity properties, image analyses of representative microstructures (e.g., TEM negatives) and XRD analyses for quantitative precipitate and grain size measurements, respectively, were carried out. This also allowed for graphical representations of grain and particle sizes as related to milling time. Relation of such graphs to Figures 52 and 54-56 would show

evidence of which microstructural feature is controlling the overall strength increase and conductivity decrease with milling time.

Grain/subgrain/crystallite sizes for mechanically milled material were estimated using lineal intercept analysis (Eq. (14)), and these were supplemented with Warren-Averbach values obtained using XRD. Average grain sizes obtained by the "direct" linear measurement method for hot pressed Cu-8/4 and 4/2 are ~1.0 μm and 1.43 μm, respectively (essentially the same as for as-extruded material, which is in agreement with their similar hardnesses). Lineal analysis of TEM-level microstructures of MM-4 hr/hot pressed Cu-4 Cr-2 Nb produced a D of ≈110 nm, one order of magnitude lower. The same processed material with a subsequent 1273 K-50 hr anneal has an average grain size of ~550 nm. These values, along with the result for MM-½ hr/hot pressed material are plotted in Figure 63. Based on the hardness profile of Fig. 52(a), a corresponding, inverted profile for grain size is predicted. As Fig. 63 explicitly shows, the grain size

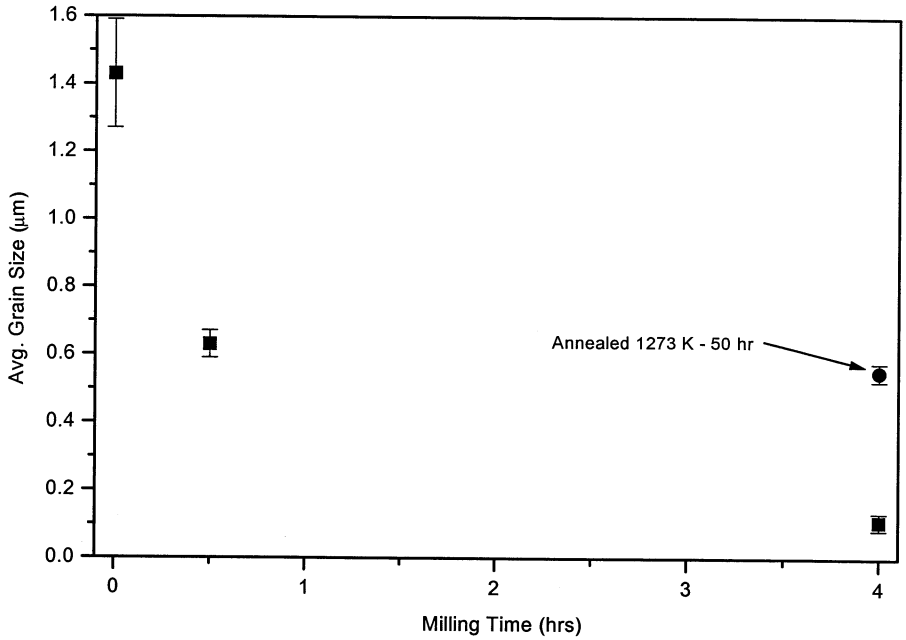

Figure 63 – Hot pressed grain sizes for selected milling times of Cu-4 Cr-2 Nb – determined using the lineal intercept method.

reduction does, indeed, correlate well to the corresponding hardness increase. In other words, the plot in Fig. 63 basically mirrors the hardness trace in Fig. 52(a) about the x-axis. It is interesting and telling how the hardness values (of about 78 HRB) and grain sizes for MM-½ hr/hot pressed and MM-4 hr/hot pressed/annealed are comparable.

Figure 64 represents $Cu_{(111)}$, $Cu_{(200)}$, $Cu_{(222)}$, and $Cu_{(400)}$ XRD peaks as they progress with milling time. These particular peaks were used for Warren-Averbach analyses as an additional technique to generate grain/crystallite sizes. Figure 65 is a plot

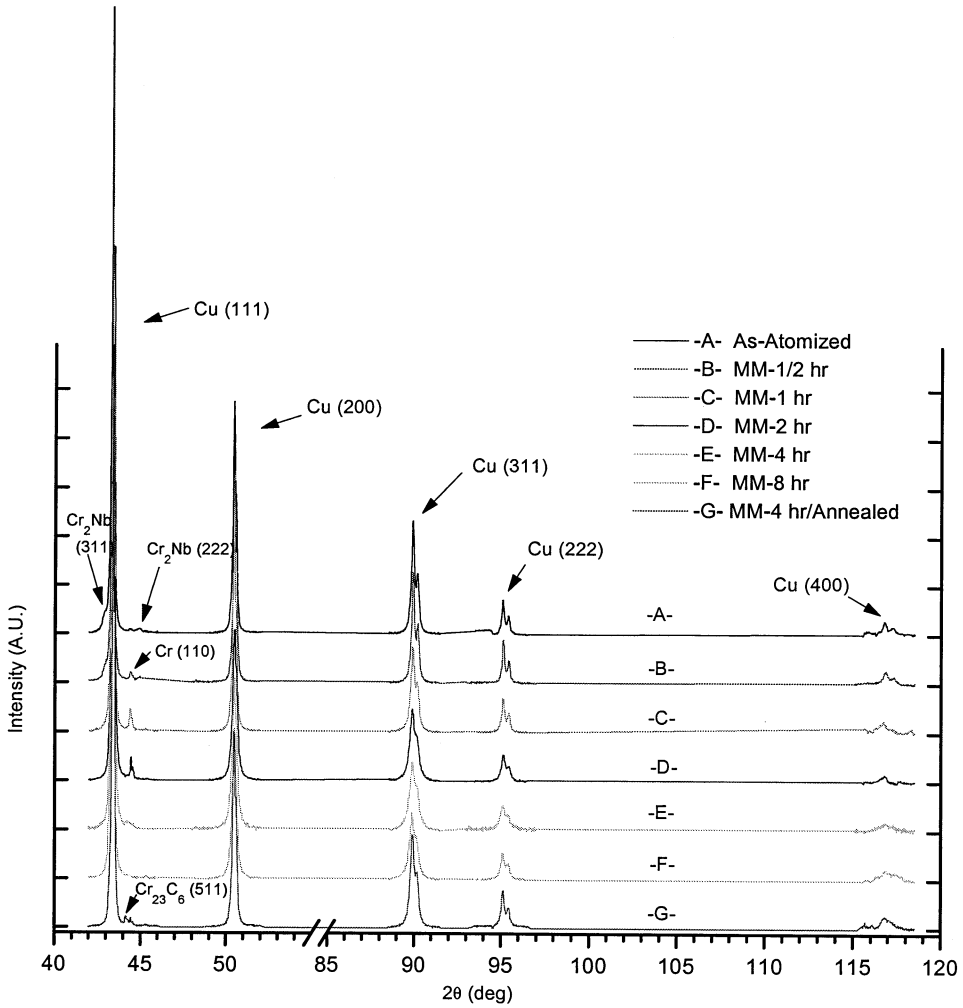

Figure 64 – Progression of Relevant Cu Peaks with Milling Time in Cu-4 Cr-2 Nb. (Note existence of other phase, as identified by arrows: Cr_2Nb, Cr and $Cr_{23}C_6$.)

of crystallite size as a function of milling time. It should be pointed out here that the crystallite sizes derived from Warren-Averbach are in error, i.e. are much lower values than those taken from TEM images, as clearly evident when comparing values of Fig.63 to those in Fig. 65. (A general description of Warren-Averbach crystallite sizes versus TEM-measured grain sizes is presented in the Discussion.) Thus, more attention should be given to the relative trend of values than the absolute values when considering data plotted in Fig. 65. Despite the differences in absolute values, the trend with milling time depicted in both plots do parallel. Such profiles of rapid grain-size reduction followed by a minimization (Figures 63 and 65), again, confirm the predicted trend. But, what is more striking is how closely the profile for this particular microstructural feature – grain size – inversely follows the hardness profile and directly parallels the conductivity profile of Figures 52 and 54-55, and Figures 52(a) and 58, respectively.

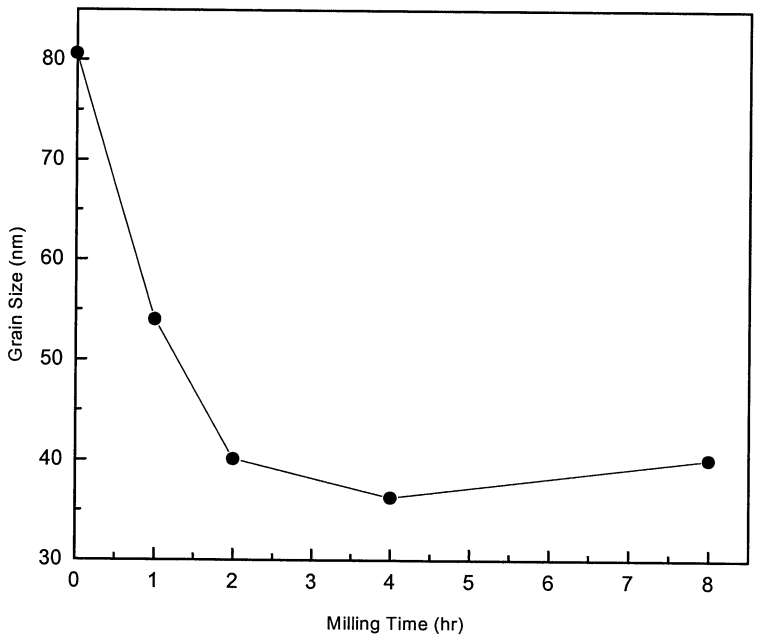

Figure 65 – Progression of grain/crystallite size of Cu Matrix with Milling Time in Cu-4 Cr-2 Nb – determined using XRD/Warren-Averback analysis.

3.2.5. Strength and Conductivity Related to Particle/Grain Size

Inherent in this present study is to take grain/crystallite and particle/precipitate sizes and interpret them through graphical analyses involving strength (hardness) and conductivity values. For example, correlating data from Figures 42, 52, 54-56 and 58 with corresponding data from Figures 40, 63 and 65 would give a good indication of which microstructural features are controlling which properties, etc. Such analysis is left to the Discussion, Section **4.2.2**.

Overall, from the results of Section **3.2** it can be stated that mechanical milling of Cu-4 Cr-2 Nb has drastically refined large Cr_2Nb and grain sizes (Figures 40 and 64) and, thusly, improved strength relative to as-extruded Cu-8 Cr-4 Nb (e.g., Fig. 57). However, the main measured drawback thus far is an adverse effect of MM on conductivity.

IV. DISCUSSION

4.1. EXTRUDED Cu-Cr-Nb

4.1.1. Microstructural Feature Evolution upon Aging

4.1.1.1. Secondary Cr_2Nb Phase

Michal [101] has carried out thermodynamic modeling of the Cu-Cr-Nb system, which allowed a pseudo-binary Cu-Cr_2Nb phase diagram to be calculated (see Appendix C). From this phase diagram and prior experimental observations by Ellis [11], it has been theoretically and empirically determined that the Cr_2Nb phase precipitates directly out of the liquid at the hypereutectic composition of the present alloys. In the rapidly solidified powders, the initial Cr_2Nb particles formed by solidification of the liquid presumably grow very fast and in any direction before the matrix structure is solidified. The resultant microstructure contains large *primary* particles, usually at grain boundaries that may have a very irregular morphology, as observed in Fig. 6. The solubility range in the solid copper matrix is expected to be higher than the equilibrium value due to rapid cooling rates. Therefore, precipitation of smaller *secondary* Cr_2Nb particles from the supersaturated copper solid solution occurs during subsequent cooling (below the solvus temperature) of the atomized powder. Size calculations of these *secondary* particles obtained during atomization with cooling rates of 10^2 -10^3 K/s were previously carried out [57]. This was based on 1) assumed atom fluxes, 2) local diffusion distances (Nb taken as rate-controlling), 3) FCC crystal structure of secondary Cr_2Nb precipitates; 4) considering an undercooling of about 100 K below the solidus, and 5) 773 K as the lower temperature bound for significant diffusion [102]. The results indicate that the size of the Cr_2Nb particles formed from supersaturated solid solution upon solidification and subsequent cooling ranges between 16 and 50 nm.

The calculated size values for particles formed within a solid matrix seem in reasonable agreement with the previous assumption (based solely on microstructural features) that particles on the order of tens of nanometers are *secondary* particles [58]. From the above calculation, it is also clear that the large particles around 1 μm could not form by precipitation from solid solution and therefore are primary particles. Thus, the combination of solidification (fast growth from liquid solution) and solid state precipitation processes (with substantial diffusion restriction) gives the rapidly solidified powders an initial bimodal Cr_2Nb particle distribution with larger primary and smaller secondary particles, as can be seen in Figures 6-8 and 15. As noted in Section **2.5.2**, such particles have been established as incoherent.

Finally, the existence of faults in the precipitates (see Fig. 11) sheds light onto another aspect regarding primary particle phase formation. Such faults, as observed in Figures 11, 18(c) and 25, strongly indicate that the primary precipitates solidified initially as the C14 ($MgZn_2$-type, HCP) phase - at around 2040 K - and then underwent a C14→C15 structure transformation starting in the vicinity of 1860 K upon subsequent cooling. Such a transformation, even in the present Cu-Cr_2Nb case, can be explained based on the studies by several investigators of solidification, solid-state precipitation and related microstructures of Cr_2Nb/Laves phases, where such faulting behavior was consistently observed and proven as twinning of the {111}<112> type [14,56,103-107]. Pirouz and Hazzledine [104] have proposed a synchro-shear Shockley partial dislocation model that explains how such a polytype transformation could proceed by a shear mechanism and convert a C14 structure into a twinned C15 structure. Finally, faulting is also observed in smaller, secondary particles, which are most likely deformation twins induced by thermal and lattice mismatch stresses [103].

The solubilities of Cr and Nb in copper exhibit a dramatic increase at temperatures above 1100 K. Therefore, the extrusion step at 1133 K leads some of the

fine particles in the initial rapidly solidified material to dissolve back into the copper matrix. Similar to the atomized material, secondary Cr_2Nb particles precipitate out of this supersaturated solid solution upon subsequent aging. In fact, a subsequent precipitation of particles from this supersaturated solid solution was documented in a previous paper [58]. This precipitation process is shown by comparing the particle size distribution diagrams for the as-extruded and 1 hour aged alloys at 773 and 973 K that clearly indicates the formation of new, small, secondary precipitates (Figures 15 and 16). Again, such second-generation precipitates can be seen in Figure 17(a and b); they are labeled 'C' in (b). This assumption is consistent with previous measurements done by Ellis which indicated that the resistivity changes related to the precipitation process in the solid solution in Cu-8 Cr-4 Nb alloy were completed after 1 hour aging at 773 K [11].

The extrusion process which is performed at temperatures higher than the Cu-Cr_2Nb solvus line has a sufficiently fast cooling rate to form a supersaturated solid solution. Aging at temperatures below the solvus (773 and 973 K) gives rise to a normal precipitation behavior with nucleation and growth of new secondary particles giving subsequent strengthening after short holding times. As already mentioned, this precipitation process explains the typical bimodal particle microstructure observed in aged materials.

At temperatures comparable to or higher than the extrusion temperature, processes more complex than precipitate nucleation and growth take place. While still limited at very high temperatures, such as 1173 and 1323 K, Ostwald ripening of larger secondary particles leads to their growth (in the order of hundreds of nanometers) at the expense of smaller ones, which dissolve. At the same time, since 1323 K is well above the solvus line, these smaller precipitates also shrink due to going back into solution, i.e. reversion. Upon furnace cooling from 1323 K, a new generation of very fine secondary Cr_2Nb particles precipitate out of this supersaturated solid solution, resulting in a trimodal

particle distribution as seen in Figures 23, 24 and 26. This explains the secondary particle size behavior in Table III.

4.1.1.2. Copper-Matrix Grains

The extruded material generally has an equiaxed grain structure, when observed transverse to the extrusion direct, e.g., Fig. 24. The matrix structure of thermally treated extruded Cu-8 Cr-4 Nb also contains numerous straight boundaries, which are tied to 120° equilibrium triple points, as recognized in Figures 18(c), 25 and 26. As given in Table IV, the average copper grain size of Cu-8 Cr-4 Nb ranges from 0.9 μm for as-extruded condition to 2.7 μm for 1323 K-100 hr aged condition. This relatively limited grain coarsening is a consequence of a stabilization stemming from the Cr_2Nb strengthening/pinning phase. These sizes and the as-extruded Cu-4 Cr-2 Nb average grain size of 1.53 μm are actually significant in regards to material strengthening. Such grain structures and their strengthening and stability effects are critical to achieving and maintaining high mechanical strengths, and are discussed later.

4.1.2. Thermal Stability

4.1.2.1. Second-Phase Cr_2Nb Particulates

The retention of strength at elevated temperature is highly dependent on thermal stability of the microstructure. It is well known that a system with particles of different sizes is thermodynamically unstable due to large surface energy effects. Larger particles having lower overall interfacial area tend to grow at the expense of smaller precipitates, which tend to dissolve and shrink, thus giving an overall lower system free energy. Alloy stability is enhanced by slowing this coarsening process. Out of all the Cr_2Nb precipitate size data obtained, the only consistent data that can be reasonably analyzed in terms of coarsening kinetics are the secondary and primary particle size results for the 773 K and

1323 K aging conditions, respectively. The coarsening data for primary and secondary particles at these temperatures were analyzed to determine the governing process assuming no real change in volume fraction occurs. Since the solid solubilities are miniscule, especially at 773 K, and primary particles form from liquid and only limited dissolution has been observed, the assumption that the volume fraction remains roughly constant seems reasonable. Previous measurements of small and large particle volume fractions after aging at 973 K appear to confirm this assumption [58].

Figure 66 is a plot of secondary precipitate size data for 773 K taken from Table III. Actually plotted are precipitate radii cubed versus aging time. As seen from this plot, this volume diffusion controlled, LSW-type (linear regression) analysis of radii data gives a very good correlation. This outcome can be explained, at least in part, by the fact that most secondary precipitates are within grains, which would make volume diffusion the likely primary transport mechanism for the rate-controlling species. (In this case, Nb

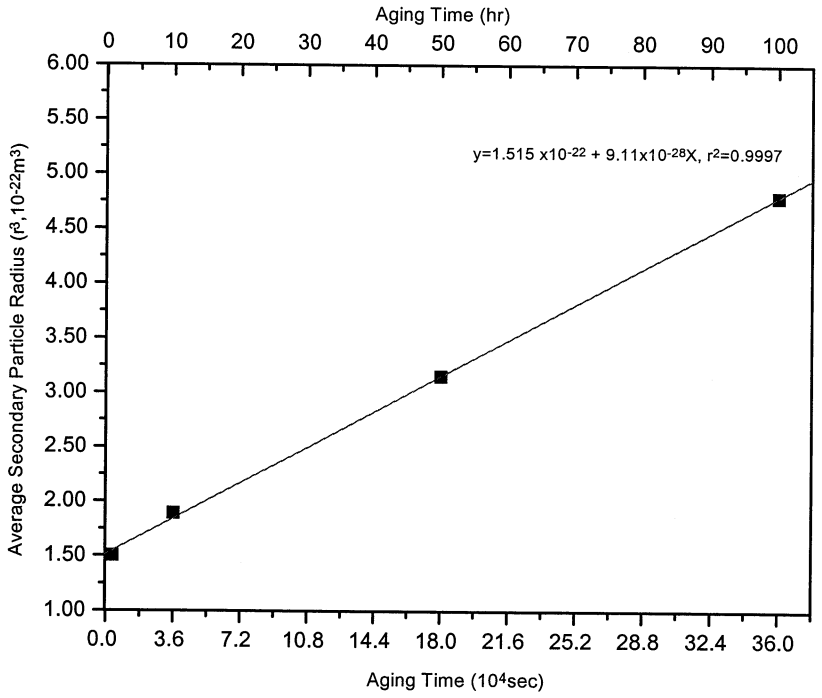

Figure 66 – LSW treatment of average secondary Cr_2Nb size in extruded Cu-8 Cr-4 Nb after aging 1, 10, 50 and 100 hr at 773 K.

is the rate-controlling species, since its diffusivity in Cu is lower than that of Cr (Table I).) This analysis resulted in a slope of 9.11×10^{-28} m^3/s, which can be considered the empirical LSW rate constant, k. The k calculated using Eq. (2) at a temperature of 773 K, at which $D_{Nb} \approx 2.13 \times 10^{-17}$ m^2/s and $C_{Nb} \approx 0.0001$, and taking $V_m \approx 2.57 \times 10^{-5}$ m^3/mol and the interfacial energy value as 0.7 J/m^2, typical for incoherent precipitates [108], is substantially lower: $\approx 5.3 \times 10^{-34}$ m^3/s. This difference of roughly 6 orders of magnitude is most likely due to additional mass transport mechanisms, namely grain/subgrain boundary and dislocation pipe diffusion, actually operating simultaneously with volume diffusion, as well as, in part, particle-size measurement error.

These short-circuit solute diffusion paths are known to become significant, even surpassing lattice diffusion, at temperatures below 0.5-0.75 T_m, where T_m is the equilibrium melting temperature in degree Kelvin. Also, the activation energy, Q, for grain boundary and dislocation pipe diffusion are typically ~½ and ¾ that for lattice diffusion, respectively [109-111]. Since 773 is about 0.57 T_m and secondary precipitates are associated with dislocations and even grain/subgrain boundaries (e.g., Figures 17(c), 18(b), 23 and 26) it is expected that the effective, or apparent diffusion coefficient (activation energy for diffusion) should, indeed, factor in and reflect such short-circuit effects. In fact, the empirically effective D was back-calculated from the experimental k value, using the above C_{Nb}, V_m and γ values, and found to be 3.66×10^{-15} m^2/s, which is obviously higher than the assumed D of 2.13×10^{-17} m^2/s. With this, and taking D_o as that for lattice diffusion of Nb in Cu (Table I), a Q of ~159 kJ/mol was calculated for Nb diffusion. This activation energy is about 2/3 that of lattice diffusion of Nb in Cu (~251 kJ/mol); thus, it is reasonable to attribute the disparities in experimental and calculated k values, large part, to simultaneous short-circuit diffusion mechanisms.

The microstructural investigations and mechanical tests presented indicate the high degree of thermal stability of the particles in Cu-Cr-Nb alloys up to 973 K. 973 K is an

arbitrary value but it is considered the upper bound of service temperatures for many new applications of high strength high conductivity copper alloys. Although the above LSW-analysis of secondary particle coarsening and, for example, the secondary particle morphologies exhibited in Figures 17(a) and 18(a), show direct evidence of coarsening, they also indicate that the rate and extent of coarsening are very slow and minor, respectively – at the lower aging temperatures used in this study. The slight variation of hardness values with time (see Fig. 28) at these aging temperatures confirm the microstructural results of secondary particle coarsening. As already shown, the slow coarsening kinetics are consistent with the low diffusivity of Nb and low solubilities of Cr and Nb in copper up to 973 K. But, by imposing even higher aging temperatures and evaluating the Cr_2Nb ripening response, the functionality, or "window of stability" for Cu-Cr_2Nb alloys can be widened further - with greater confidence in the elevated-temperature performance of Cu-Cr_2Nb. Hence, effects of aging on precipitates for material aged at 1073 K, 1173 K and 1323 K was considered.

Figure 67 shows a plot of $\bar{r}^2$, $\bar{r}^3$, and $\bar{r}^4$ versus time at 1323 K, where $\bar{r}$ is the average radius of the primary precipitates. The $\bar{r}$ values were measured from SEM images like those in Fig. 22. It is apparent from such SEM observations that the primary particles barely double in size from 1 to 50 hr exposure even at 1323 K, with actual sizes given in Table III. A linear relationship was assumed, and a straight line was fit to the data using a least squares linear regression. The data fit both volume and grain-boundary diffusion controlled (VDC/$\bar{r}^3$ and GBDC/$\bar{r}^4$) coarsening kinetics. The grain boundary ripening is in accordance with the preferred distribution of the large precipitates at grain boundaries and/or triple points (e.g., Figures 6, 9, 24 and 26). A comparison of the experimental value of the coarsening rate constant (k'=5.6 × 10^{-31} m^4/s) with a calculated value for GBDC is not possible since no precise grain boundary data (e.g., diffusivities, solubilities, thickness, etc.) are available for the present system.

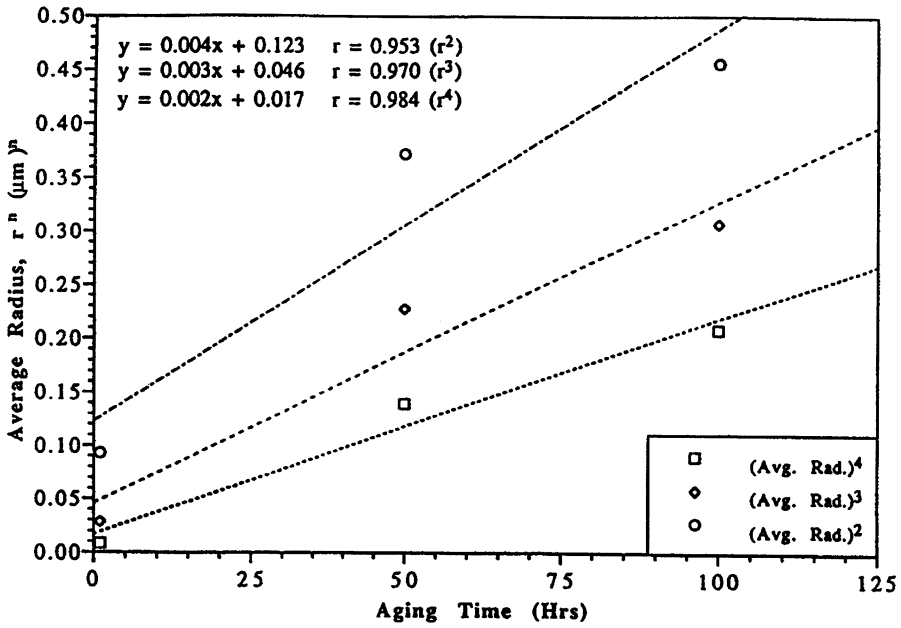

Figure 67 - Average large Cr_2Nb particle radius, $\bar{r}$, vs. aging time at 1323 K for Cu-8 Cr-4 Nb alloy. (Plot of $\bar{r}$ raised to power 2, 3, and 4 where slopes give corresponding rate constants, k, for possible rate controlling processes: interface controlled, volume diffusion controlled, and grain boundary controlled, respectively.) (As given in ref. [57].)

Analogous to the secondary particle coarsening analysis, such a comparison of VDC k values is possible, thus relevant. VDC calculations, again, were made taking niobium, the slower diffusing element, as the rate-controlling element at 1323 K. (At 1323 K, $D_{Nb} \approx 2.44\times10^{-14}$ m^2/s and $C_{Nb} \approx 0.002$.) The calculated value of the reaction constant (k=7.1 × 10^{-26} m^3/s) for VDC is about one order of magnitude smaller than the experimental value for VDC growth (k=7.78 × 10^{-25} m^3/s). Modifications of the coarsening kinetics given by LSW theory for such effects as overlapping strain and diffusion fields, finite volume fractions and non-steady state processes give kinetics factor variations of 1 to ~5, depending on particular modification [112]. For instance, an increase in particle volume fraction from 0.19 to 0.32 caused only doubling of the coarsening rate constant [16]. Therefore, the one order of magnitude difference likely reflects, at least in part, an increase in the coarsening kinetics caused by the main grain boundary diffusion contribution and, partially, experimental error.

Thus, it appears most probable that Ostwald ripening involving both grain boundary and bulk diffusion is the process operating to coarsen the Cr_2Nb precipitates. This is supported to some extent by the fact that some primary precipitates do exist within grains (e.g., Figures 8 and 24). In addition, secondary particles, found mostly inside grains (e.g., Figures 6 and 10), most likely interact with neighboring primaries, thereby also contributing to primary particle coarsening through Gibbs-Thomson diffusion gradients. Although any exchange of Nb and Cr between secondary and primary particles (during thermal exposure) may cause some inherent uncertainty in the preceding independent coarsening analysis of the individual particle types, such analyses is still considered acceptable.

In contrast to aging below 1200 K, the secondary particles show a continuous decrease in average size during aging at 1323 K as given in Table III. As alluded to earlier, this is most likely due to the additional dissolution of particles back into the matrix when the aging temperature is above the solvus line on the pseudo-binary Cu-Cr_2Nb phase diagram [101]. The experimental observation of a solvus line between 1200 and 1323 K is in agreement with the solvus line calculation by Michal. Thus, the smallest *secondary* precipitates not only dissolve due to larger ones coarsening, but also shrink by the thermodynamic process of reversion at temperatures above 1200 K.

Despite this evident dissolution of smaller secondary precipitates, they remain in sufficient number even at these high aging temperatures to give significant strengthening. At 1323 K, the new secondary precipitates formed during subsequent cooling are shown associated with dislocations in Figures 23 and 26. In addition, preexisting Cr-rich particles, as identified in Figures 8 and 12-14, (and relatively few Nb-rich particles that materialize with aging [57]) have sizes comparable to the secondary particles. Compared to secondary precipitates, larger primary particles are less thermodynamically affected, i.e. more stable, due to much lower capillarity effects or reduced overall specific surface

area (energy). Therefore, primary precipitates exhibit slow net coarsening (coarsening exceeding any resolution) that becomes evident at temperatures above 1100 K. The results and analysis together show that Cr_2Nb intermetallic particles should provide stability to a Cu matrix during high temperature exposure in service.

4.1.2.2. Copper-Matrix Grains

The observed changes in matrix and precipitate microstructures can be used to explain the good thermal stability of Cu-8 Cr-4 Nb alloys. Cr_2Nb precipitates strengthen the alloy by grain boundary Zener-pinning effects (primary) and by providing Orowan-type dislocation obstacles (secondary). Experimental results indicate that grain sizes remain in the micron range for all aging treatments. Even after 100 hr at 1073 K the grain size does not become larger than an average of 2.6 μm. This clearly indicates the pinning effect of precipitates, which is addressed again, shortly. Calculations of the maximum grain size according to the Hillert-Gladman expression, i.e. Eq. (6), were made to further distinguish between the pinning effect of small versus large particles. The calculated grain size - for the most extreme aging condition - considering small particles (d_{calc} = 3.9 to 4.9 μm) was in better agreement with the observed maximum values of 4 μm than the calculated value of ~8 μm for the larger (primary) particles. This suggests that secondary particles are more effective at pinning the grain boundaries than are the primary particles. This, of course, is contrary to expectation since primary precipitates are almost entirely found at grain boundaries as opposed to secondary particles, which are found at grain boundaries and more in grain interiors. This may be explained by experimental error in initial volume fraction measurements and/or the applicability of the given Hillert-Gladman expression to the present system.

According to Humphreys *et al.* [113] particles of diameter greater than about 1 μm will stimulate nucleation of recrystallization upon annealing of deformed DS

material. It is proposed that such large, prior-formed primary Cr_2Nb particles also serve as heterogeneous nucleation sites for liquid copper solidification. Grains pinned by such large particles will have sizes corresponding to one grain per particle and described by

$$D_N = \frac{d}{f_v^{1/3}} \tag{15}$$

where d is the particle diameter and f_v is the volume fraction. As revealed in Figure 24, and again in Figure 68 below, one Cu grain associated with one entire primary particle is common. When taking the volume fraction of primary precipitates as ~0.11 and the

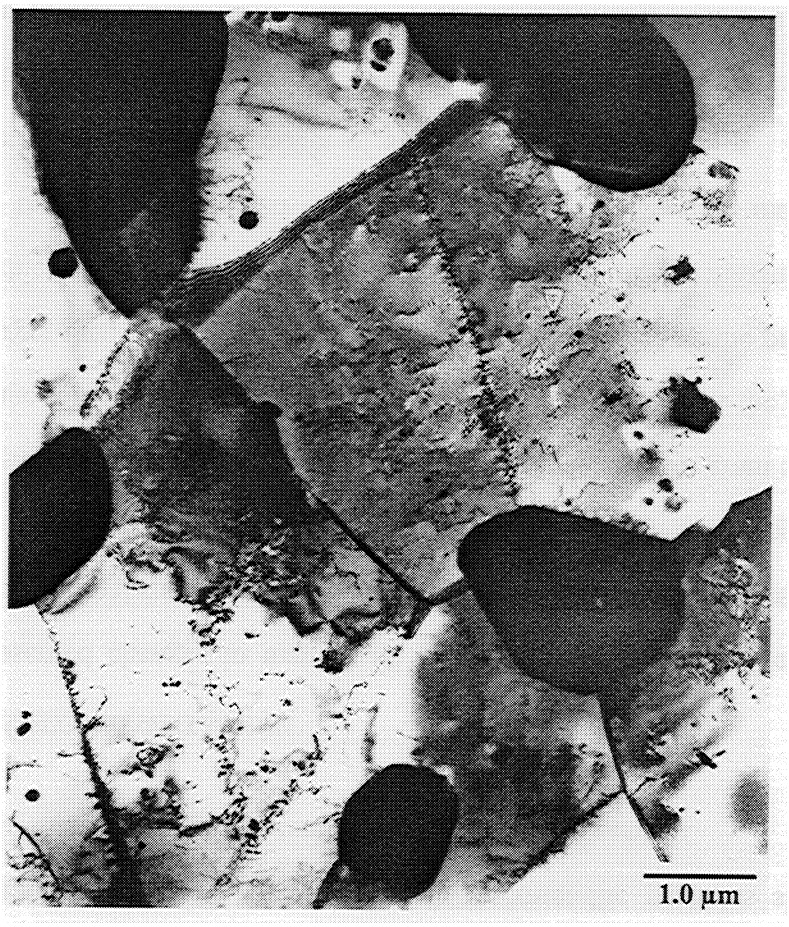

Figure 68 – TEM observation of matrix grains and Primary Cr_2Nb Precipitates in extruded Cu-8 Cr-4 Nb aged 100 hr at 1323 K.

average diameter as 1.35 μm for, again, the 1323 K-100 hr aged sample, a calculated grain size of about 2.8 μm is obtained from Eq. (15). Note how close this is to the average measured diameter of 2.7 μm. However, this analysis neglects any Zener-pinning effects of the secondary particles, which can be seen pinning boundaries in Figures 17(b) and 18(b); thus, another model is sought. Elst *et al.* [114] have essentially put forth modified Hillert-Gladman models for cases of a bimodal distribution of incoherent equiaxed particles and precipitates preferentially located at grain boundaries.

A slight simplification of what they have done for the bimodal case would be to put Eq. (6) in such a form as to incorporate both particle sizes and volume fractions, that is:

$$d_{\text{calc}} = \frac{4}{3}\left[\frac{f(\text{P})}{r(\text{P})} + \frac{f(\text{S})}{r(\text{S})}\right]^{-1}. \tag{16}$$

Here, P and S designate (P)rimary and (S)econdary precipitates. A slightly simplified rendition of the grain boundary precipitate model given by Elst *et al.* can be given next as:

$$d_{\text{calc}} = 2.265\frac{r}{f_{\text{vg}}^{1/2}}. \tag{17}$$

Here, f_{vg} is the volume fraction of grain boundary particles, and r their average radius. When the appropriate radii and volume fractions (e.g., f (S) ~ 0.022, f (P) = f_{vg} ~ 0.11) for, again, Cu-8 Cr-4 Nb aged at 1323 K are substituted into Eqs. (16) and (17), grain size values of ~2.74 μm and 4.6 μm are calculated, respectively. It is interesting, but not necessarily unexpected, that the bimodal model gives a closer value to experimental results. Equation (17), by neglecting the secondary particles, predicts a larger (than measured) grain size. This strongly suggests that secondary particles must also mitigate grain coarsening to a certain extent. From the above analysis, it can be stated that both

primary and secondary precipitates contribute to Zener-drag, thereby retarding grain growth. Secondary particles have been observed at grain/subgrain boundaries, and in Figure 18(b) and 26, apparent secondary-size (<300 nm) Cr_2Nb particle are obviously pinning the boundaries during thermal exposure at 973 and 1323 K, respectively.

4.1.3. Mechanical Properties

The two main contributions to strengthening in Cu-Cr-Nb are the Orowan and Hall-Petch strengthening mechanisms. Orowan strengthening due to fine particles was calculated using the Orowan-Ashby formula, Eq. (3). Table XVI contains secondary particle size data for selected aging conditions. Also given are corresponding amounts of Orowan strengthening contribution derived from such secondary precipitates (see Appendix D for details of calculations). The results of $\Delta\sigma_{OR}$ calculations for fine particles from about 106 to 170 nm in size range from ~51 to 72 MPa. In these calculations, it was assumed that the volume fraction of small particles was the same as in previously

TABLE XVI -
Selected Secondary Particle Size, Spacing and Orowan Strengthening Contribution

Cu-8 Cr-4 Nb Condition	Secondary Particle Size, *d* (nm)	Particle Spacing, λ^* (nm)	Orowan $\Delta\sigma_{OR}$, MPa
As-extruded	163 ± 7	800	50.6
Aged 1 h at 773K	106.4	519	71.8
Aged 100 h at 773K	156.5	764	52.4
Aged 1 h at 973K	108.3	529	70.8
Aged 10 h at 973K	~130	634	61.0
Aged 100 h at 973K	148 ± 7	722	54.8
Aged 100 h at 1073K	169 ± 17	829	48.9
Aged 1 h at 1173K	132 ± 6	644	60.2
Aged 10 h at 1173K	162 ± 6.7	790	51.0
Aged 50 h at 1323 K	135.5 ± 8.6	664	58.8

*Based on Eq. (3) and f of 0.022.

measured specimens aged up to 973 K [58]. As expected, the contribution to Orowan strengthening of the large precipitates with an average size of 1 μm is less than half that provided by small particles. Furthermore, this lower contribution becomes even more negligible when considering the much lower volume fraction of large particles within grains relative to grain boundaries. Therefore, unlike small particles, large precipitates provide essentially no Orowan strengthening effect. In considering the proposed resolution or dissolution theory, any strength loss after high-temperature exposure can be attributed, in part, to redissolving the smallest particles into the solid solution. The experimental results indicate that more strength is lost from the decreased volume fraction than is gained by any solid solution strengthening.

In comparing the strength behavior for 773 and 973 K in Figure 28 with the corresponding data in Table XVI, the changes in relative strength are comparable. The increase in hardness after 1-hr aging correlates with the smaller average secondary particle sizes. Furthermore, when small particles coarsen from 130 nm to 148 nm after 100 hr aging, the calculated (10%) and experimentally observed (about 11% from Fig. 28) resultant decreases in strength are effectively equivalent. A similar trend is also noticed for 773 K aging. The Cu grains show minimal coarsening in this temperature range, stabilized largely by primary particles, which provide little direct strengthening. Therefore, such evolution of strength with thermal processing can be attributed to slight coarsening of small, secondary Cr_2Nb particles, which slightly reduces the Orowan effect derived from them. These calculated percentage drops in hardness and Orowan strengthening due to secondary-particle coarsening are in good agreement with mechanical test results. The yield strength after heat treating 100 hr at 973 K remains at 88.6% of the yield strength for 10 hr at 973 K [58]. Finally, as mentioned earlier, 973 K can be considered on the high side for service temperatures for DS copper applications.

For example, the inner wall of the actively cooled combustion chamber liner in the Space Shuttle Main Engines (SSME's) typically experiences temperatures of 840 - 920 K [78].

To calculate the grain boundary strengthening contribution, the Hall-Petch relationship, Eq. (5) was used, where $\sigma_0 = 26$ MPa, $k_y = 0.16$ MPa$\sqrt{m}$ [115], and a pure copper matrix was assumed. The average grain sizes in Table XVII were substituted into Eq. (5). The calculated grain boundary strengthening for the as-extruded condition is ~195 and 155 MPa for the Cu-8 Cr-4 Nb and Cu-4 Cr-2 Nb alloy, respectively. This and other aged condition values are given Table XVII. Upon examination of yield strength data based on Figure 27, also included in Table XVII, it is apparent that the sums of the calculated Orowan and Hall-Petch contributions tabulated in Table XVII are commensurate with the experimentally determined values for yield strengths of Cu-Cr-Nb alloys, especially for as-extruded material. (The volume fraction of secondary particles used for the Orowan calculations was taken as 0.022 for both as-extruded alloys.) It is worth pointing out here that the larger grain size, hence, lower Hall-Petch and yield strength, for as-extruded Cu-4 Cr-2 Nb compared to Cu-8 Cr-4 Nb is due to the former having fewer primary particles for Cu grains to nucleate and/or impinge upon during alloy solidification during atomization.

Table XVII -
Average Grain Size and Calculated and Measured Strengths
for **As-Extruded Cu-Cr-Nb and Aged Cu-8 Cr-4 Nb**

Condition	**Grain Size** (μm)	**Hall-Petch,** $\sigma_{H\text{-}P}$ (MPa)	$\sigma_{H\text{-}P} + \Delta\sigma_{OR}$ (MPa)	Yield Strength (MPa)*
As-Extruded 8/4	0.9	194.7	245.3	240-280
As-Extruded 4/2	1.53	155.4	206	~206
773 K – 100 hr	0.9	194.7	247.1	- -
1073 K – 100 hr	2.6	125.2	174.1	~180
1173 K – 10 hr	1.6	152.5	203	~190
1323 K – 100 hr	2.7 (max 3.8)	123.4	182	- -

*Based on Data Presented in Figures 27 and 30.

Another salient outcome of the above analyses of the microstructural contributions to alloy strength is that a comparison of the calculated strengthening effects given in Tables XVI and XVII for as-extruded material and specimens aged from 773 K - 1323 K up to 100 hr directly indicates that the predominant contribution in all cases is grain boundary strengthening. This is supported by essentially the same micrometer grain-size range that was experimentally observed even after 100 hr at 1323 K. As described previously, this clearly demonstrates the effective drag force particles exert on grain boundaries, which does not markedly diminish when these particles grow in the size range encountered in these alloys. In general, the Hall-Petch effect contributes about 2/3 of the overall strength of as-extruded and aged Cu-Cr-Nb, while the Orowan effect provide the balance of strength. In fact, an initially unexpected outcome of this present work involves the analysis of microstructural data in terms of pertinent strengthening mechanisms for extruded Cu-8 Cr-4 Nb. This analysis reveals that particles provide more (indirect) strengthening effects via dislocation interactions with pinned grain boundaries (Hall-Petch) than due to direct particle/dislocation interactions (Orowan effect). This, again, supports the premise of Hazzledine for such second-phase particulate strength contributions [49]. Again, Morris and Morris [4] contend that for dispersoid-containing alloys, the Orowan process should dominate.

When a ratio of change in strength from the Hall-Petch effect ($\Delta\sigma_{H\text{-}P} = \sigma_{H\text{-}P}\text{-}\sigma_o$) to added strength from the Orowan effect ($\Delta\sigma_{OR}$) is considered over a dispersoid size range of up to 1 μm, the above finding is reinforced. Figure 69 is a graphical representation of such a ratio. The grain sizes used in the Hall-Petch contribution calculations are assumed to be governed by dispersoid size and volume fraction, i.e. they are taken as the Zener-pinned sizes (Eq. (6)). Figure 69 indeed illustrates that for second- phase particles greater that ~30 nm in size, Hall-Petch strengthening predominates. Even the secondary precipitates have average sizes at least 4 times this for all cases. From this analysis, it

turns out that the present findings of Hall-Petch (grain size based on Zener pinning) strengthening dominating for extruded Cu-8 Cr-4 Nb should be, in fact, expected. All of the experimental and predicted results for the Cu-Cr-Nb system(s) support Hazzledine's contention of Hall-Petch dominance when second-phase particles can induce and/or maintain a small grain size. In contrast, for the DS Cu alloy GlidcopAl-15 with 0.007 volume fraction of ~15-20 nm-size Al_2O_3 dispersoids [51-52], the Orowan effect plays a larger role in alloy strength, as expected based on Fig. 69, and substantial and discontinuous grain growth is observed when it is thermally treated [7].

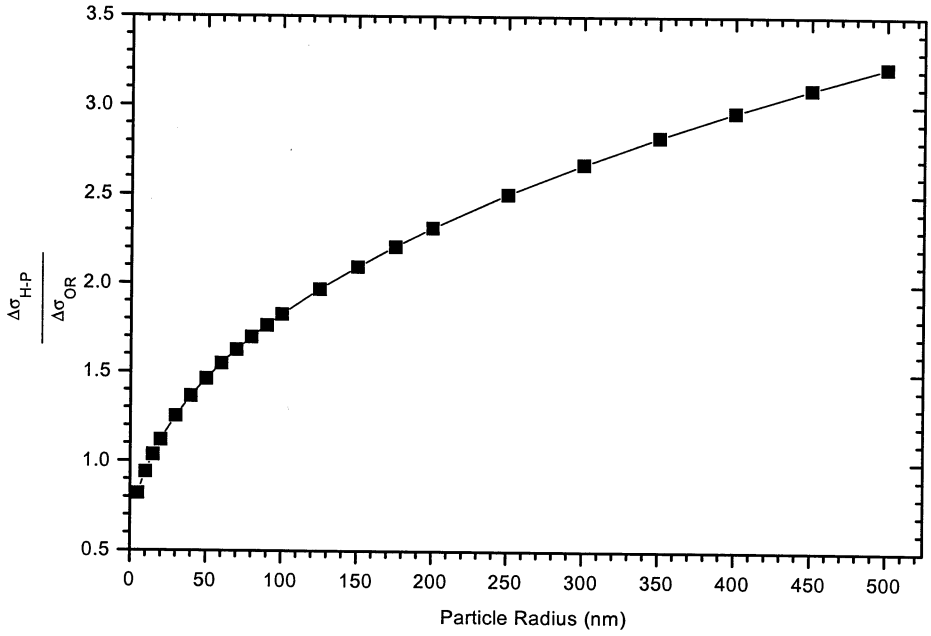

Figure 69 – Ratio of indirect particle strengthening (grain-size contribution) to direct particle strengthening (particle-size contribution) for dispersoid sizes up to 1 μm.

Finally, as Figures 30 and 31 show, Cu-Cr-Nb alloys have superior high-temperature mechanical strengths compared to NARloy-Z, again, the currently used Cu alloy for high-temperature aerospace applications. The high-temperature behavior is most likely governed by the primary, grain-boundary Cr_2Nb particles. Such particles necessarily inhibit grain boundary sliding, a deformation mode above ~0.5 T_m, thus, enhance high-temperature strength. In contrast, both NARloy-Z and GlidCop lack an

abundance of grain boundary particles, especially GlidCop Al-15 – having only a total dispersoid volume fraction of 0.007.

This investigation has proven that the overall strength of Cu-Cr-Nb alloys is derived from a low volume fraction of smaller Cr_2Nb particles, which imparts direct Orowan strengthening, and a larger volume fraction of larger particles, which provides even higher and relatively constant indirect grain boundary, or Hall-Petch strengthening. Moreover, the sluggish coarsening behavior of both types of Cr_2Nb particles gives rise to a stable microstructure. Microstructural analysis supports the experimentally observed stability of mechanical strength of particularly Cu-8 Cr-4 Nb alloys even after exposure to temperatures very close to their melting point. This is especially true for the Cu-8 Cr-4 Nb alloy thermally treated at 973 K up to 100 hr. Since such aging does not cause a substantial increase in grain and particle size the decrement in mechanical strength is minimal. The increase in strength and stability of Cu derived from a given overall volume fraction of such Cr_2Nb particles has been established, but what is also required is consideration of any opposite effects of such particles on copper conductivity.

4.1.4. Thermal and Electrical Conductivity of Extruded Cu-Cr-Nb

As a means to model the first order effects of volume fraction and conductivity of mostly-spherical particles on copper conductivity, plots of Eq. (12) were made for different hypothetical particulate conductivities, and are shown in Figure 70. As expected, such plots based on Eq. (12) give a linear dependence of conductivity on particulate volume fraction. In order to assess where, or if, they fit within these lines the experimental thermal conductivity data for pure Cu and extruded Cu-8 Cr-4 Nb and Cu-4 Cr-2 Nb - taken from Figure 33 - are also plotted. As interpreted from the experimental data falling below all predictive data, decreases in conductivity (increases in resistivity) are not adequately calculated by Eqs. (11) and (12). Even taking $\kappa_p \approx 0$, i.e. Cr_2Nb as a

pore phase, use of such formulas suggests a conductivity of roughly 90% IACS based on a volume fraction of about 0.07 in Cu-4 Cr-2 Nb, since they do not take into account impurity, grain and dispersoid size; and other defect effects.

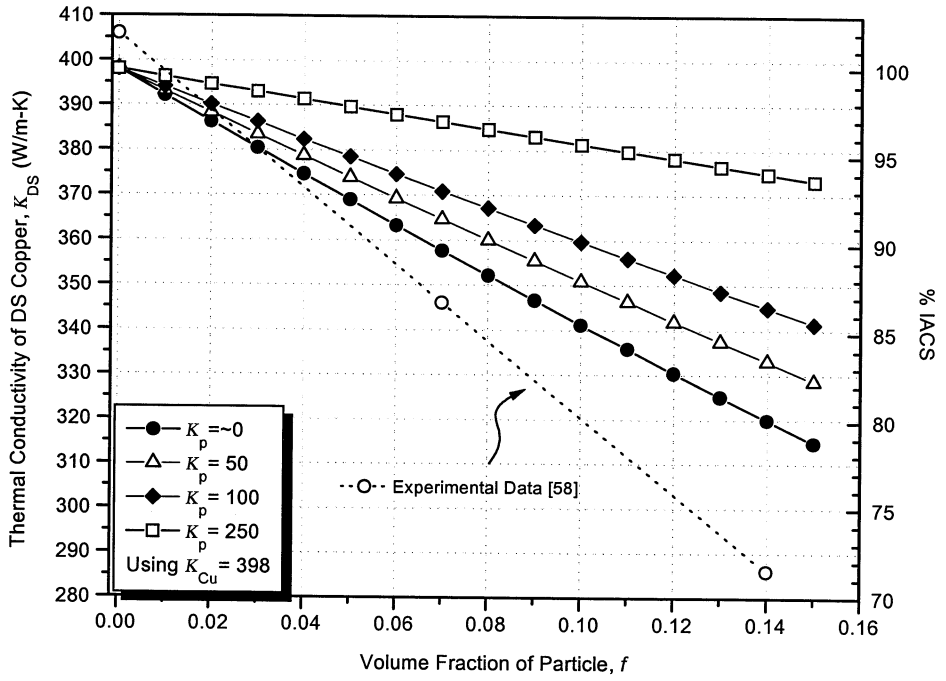

Figure 70 – Predicted thermal conductivities of DS Cu based on Maxwell's/Schroder's formulas, which are essentially only rule of mixtures, and, therefore, limited.

A modified Maxwell formula has been derived by Hasselman and Johnson [116] to account for interfacial and second-phase size effects on conductivity. Such formula, as used by Geiger, Hasselman, Donaldson and Welch for an Al-SiC system [117, 118] can be presented in the following form:

$$\kappa_{\text{mix}} = \kappa_m \frac{\frac{\kappa_p}{\kappa_m}(1+2V_p) + 2\left[\frac{\kappa_p}{h_c a}+1\right](1-V_p)}{\frac{\kappa_p}{\kappa_m}(1-V_p) + \left[\frac{\kappa_p}{h_c a}+1\right](2+V_p)}. \qquad (18)$$

Here, $1/h_c$ is an interfacial resistance factor, with h_c being the interfacial heat transfer coefficient, or thermal conductance and a is the average radius of spherical strengthening

particles. Two plots of Eq. (18) are displayed in Figure 71. Both were calculated by taking κ_m = 398 W/m-K, κ_p = 100 W/m-K, $a \approx 0.4$ μm (based on the weighted average of as-extruded secondary and primary precipitate sizes) and $h_c \approx 0$ for one and $h_c \approx 7\times10^8$ W/m^2-K [117] for the other. Due to incoherent interfaces, an $h_c \approx 0$ is reasonable, i.e. electrons are scattered at the interface and little energy is transferred to and by the dispersoids. This contention is also supported by such intermetallic dispersoids having very few free electrons for heat and electrical energy transfer, giving them a pore effect with respect to conductivity. Even though both lines fall below the Maxwell line, they still poorly predict the empirical data. Since, again, solute/impurity atom scattering is not accounted for in Eq. (18). This most likely is the other main resistivity contribution responsible for this remaining disparity.

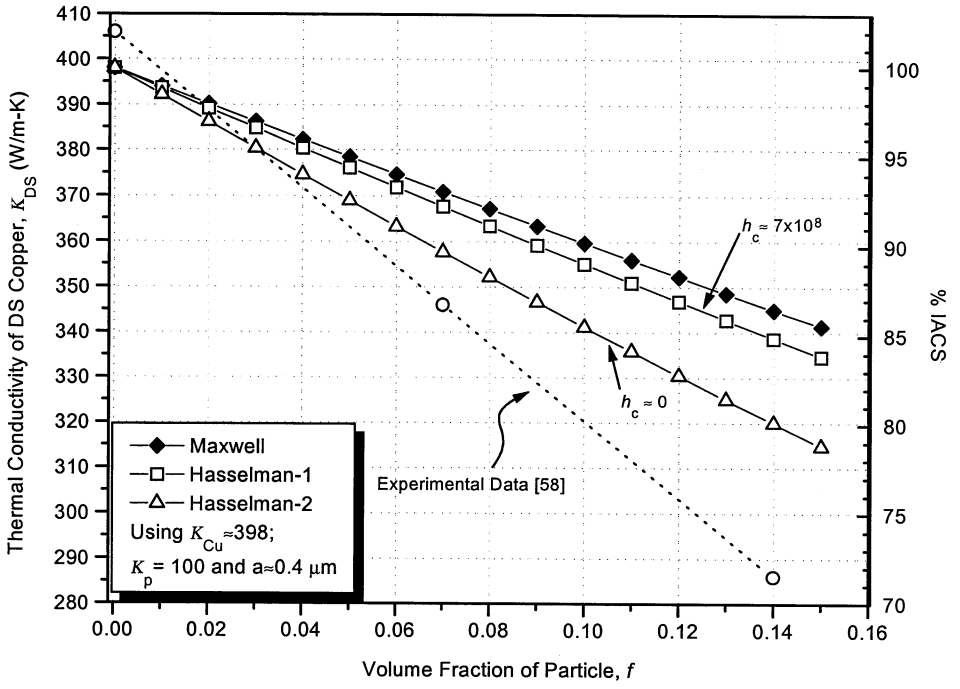

Figure 71 – Comparison of Maxwell and Hasselman predictions of DS Cu alloy thermal conductivity based on dispersoid volume fraction and conductivity.

The electrical resistivity corresponding to the thermal conductivity based on $h_c \approx 0$ corresponds to about 2.2 and 1.97 μΩ-cm for Cu-8 Cr-4 Nb and Cu-4 Cr-2 Nb,

respectively. The measured resistivities are ~2.5 and 2.07 μΩ-cm. Comparison of these values also indicates that alloying elements still add a component to total resistivity. A relevant graphical representation of the effects of solute (impurity) atoms on the resistivity of pure copper is given in Figure 72. As seen from this graph, Cr falls about in the middle of other solutes in its effect on Cu resistivity. Cr contributions to Cu receptivity would need to be in the range of 0.1-0.3 μΩ-cm to account for the above

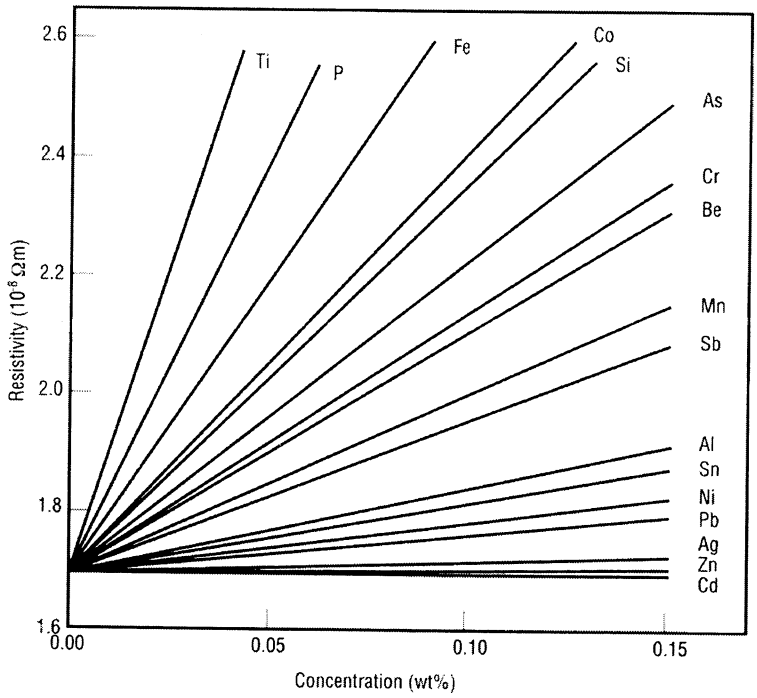

Figure 72 – Effect of alloying elements on the resistivity of Copper (as taken from [119]).

disparities. Based on Fig. 72, this corresponds to a Cr level of about 0.02-0.05 wt.%, which is possible, considering the extrusion temperature of 1133 K, but the exact solute Cr content is not known. Nb should have less effect due to its much lower solubility. Verhoeven, *et al.* [120] found an increase of ~0.1 μΩ-cm due to solute Nb in drawn Cu-Nb. Taken together, it is reasonable to attribute the remaining 0.1-0.3 μΩ-cm to solute Cr and Nb. An established expression relating resistivity to solute concentration is the well-known Nordheim's rule, which is given as:

$$\rho = \rho_0 + AC(1 - BC), \tag{19}$$

where ρ_0 is the electrical resistivity of the pure solvent C is the solute concentration and A and B are empirical constants [119, 121-122]. Even though the expression for Nordheim's rule describes an inverted parabola, for dilute alloys ($\lesssim$ 0.2 wt% solute) a linear relation is described, e.g., Fig. 72.

For particle-strengthened alloys, the level of a given solute in solution is not necessarily the expected equilibrium value. Miyake and Fine [123] have correlated particle size and yield stress with resistivity in their aging studies of a particular precipitation-hardened Cu-based alloy (Cu-Ni_5P_2). One interesting aspect of their analysis involves a resistivity dependence on solute solubility related to particle size, i.e. a Gibbs-Thomson effect on alloy resistivity. They essentially combined Nordheim's rule (Eq. (19)) with the Gibbs-Thomson formula (Eq.(1)) to produce the following expression:

$$\frac{\rho_r - \rho_o}{\rho_{eq} - \rho_o} = \exp\left(\frac{2\sigma V_m}{\bar{r}RT}\right) \tag{20}$$

where ρ_r is the resistivity of the matrix having enhanced solute solubility due to second-phase particles of finite radii; and ρ_{eq} is the resistivity of the matrix having an equilibrium level of solute in solution (infinite particle radius). Figure 2 shows a solute solubility in a matrix based on the Gibbs-Thomson effect for an averaged particle radius (size).

A plot of Eq. (20) is presented as Figure 73. It reveals that particles of less than about 100 nm in size can greatly add to alloy resistivity through their effect of increasing solute solubility. Based on Figure 73, the overall average Cr_2Nb size in as-extruded Cu-8 Cr-4 Nb (0.75 μm) would increase solute solubility by a factor of about 4%. A caveat of Eq. (20) is that it does not consider particle volume fraction, which would also seem to play a role. Maybe a combination of Eq. (20) with Eq. (18) – with Eq. (18) converted to

resistivity – would provide a more complete and accurate model; but, this will be left to future work. Miyake and Fine also analyzed a strength dependence on particle size (involving Orowan and LSW relations). In fact, Miyake, *et al.* [119] apply this approach in describing a basis for rational alloy design and optimization of high conductivity-high strength alloys.

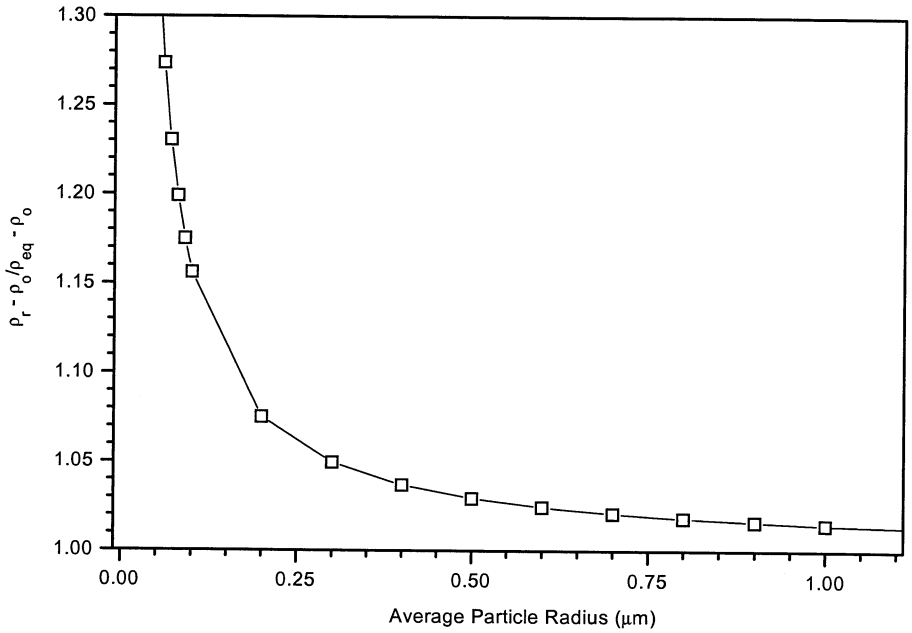

Figure 73 – Effect of particle size on parent matrix resistivity (Eq. (20)).

What is discussed next are correlations of already-established relevant strengthening mechanism contributions to the processed (MM) microstructures. Again, the milling objective was to refine the microstructure described above and uniformly distribute the dispersed phase with a single, narrow(er) size distribution. As shown and described in the first part of this study, the initial powders of Cu-8/4 and Cu-4/2 have a bimodal precipitate size distribution; the large particles being $\gtrsim$0.5-1 μm. As mentioned earlier, such particles would provide only minor Orowan strengthening, e.g., at most ~20 MPa for 5-10 vol%. To highlight an example for comparison, refining these particles down to ~100 nm (via MM), would increase the Orowan effect almost seven times (to ~134 MPa).

4.2. Analyses of P/M Processed Cu-Cr-Nb

4.2.1. Evolution of Second-Phase(s) with Milling Time

4.2.1.1. Post-Milling/Pre-Consolidation

Again, as SEM analysis revealed, mechanical milling of Cu-Cr-Nb was very effective at breaking down the large, primary Cr_2Nb, as illustrated in Figures 38-40. As expected, Figures 43 and 46(b) confirm that the second-phase still present in 4 hr-milled Cu-4 Cr-2 Nb and 8 hr-milled Cu-8 Cr-4 Nb is Cr_2Nb. And, as Fig. 40 shows, the size of primary Cr_2Nb particles dropped from averages of ~0.78 μm (4/2) and 0.93 μm (8/4) for as-atomized powder to ~0.2 μm (4/2) and 0.25 μm (8/4) for 4 hr-milled powder. MM most likely had only relatively little effect on secondary Cr_2Nb particles. The size refinement and the more uniform distribution of primary Cr_2Nb is quite noticeable in Figures 38-39. On the contrary, it is difficult to discern the exact location of these particles in Figures 38-39. However, given the nature of MM, the refined Cr_2Nb presumably ended up at grain and/or prior-particle boundaries – after milling times of $\gtrsim$2 hr. Finally, along with size and distribution evolution, the effects of MM with a carbon-rich PCA include the transformation of *Cr_2Nb* particles into different second-phase particles upon powder densification, especially for longer milling times.

4.2.1.2. Post-Consolidation

With the extent of carbon pick up during milling, as revealed in the chemical analysis results of Fig. 42, and the preexisting Cr and Nb, carbide formation upon consolidation at ~810°C was virtually inevitable. The great affinity of transition metals for carbon is well established and explained [85]. Given this characteristic of Nb and Cr and comparing the heats of formation of the identified particles in Table XI, the product of NbC_{1-x} and $Cr_{23}C_6$ (and Cr) from a reaction of C with Cr_2Nb, as well as Nb and Cr – in extended solid solution from MM, is thermodynamically favored, thus, expected. Based

on estimated lattice parameters from x-ray and electron diffraction patterns (e.g., Figures 45, 50 and 59) and data from ref. [124], the stoichiometry of NbC_{1-x} was estimated. Also detected in Fig. 64 is BCC-Cr, and, again, Cr-rich particles were identified in Figures 48 and 49. Based on the carbon contents read from Figure 42, NbC stoichiometries, densities and molar masses of dispersoids, etc., content of likely dispersoids were calculated. Below is a table giving the approximated Cr_2Nb, Cr, NbC_{1-x} (with estimated

Table XVIII - Calculated Volume Percents and Stoichiometry of Dispersoids in Mechanically Milled/ Hot Pressed Cu-4 Cr-2 Nb

Milling Time (hr)	Dispersoids	Volume Percent	Total Volume Percent
0	Cr_2Nb Cr	7.00 ~0.16	7.16
0.5	Cr_2Nb Cr $NbC_{.80}$	5.95 0.67 0.61	7.23
1	Cr_2Nb Cr $NbC_{.75}$ $Cr_{23}C_6$	2.40 2.63 2.36 < 1	~8.0
2	Cr_2Nb Cr $NbC_{.72}$ $Cr_{23}C_6$	0.72 2.65 3.57 1.44	8.47
4	Cr_2Nb Cr $NbC_{.707}$ $Cr_{23}C_6$	0.55 1.33 3.60 2.89	8.42
8	Cr_2Nb Cr $NbC_{.688}$ $Cr_{23}C_6$	0.37 1.36 3.56 2.96	8.27
4 + 1273 K-50 hr Anneal	Cr_2Nb Cr $NbC_{.92\pm.07}$ $Cr_{23}C_6$	0.36 1.31 3.62 2.91	8.2

1-x values) and $Cr_{23}C_6$ volume percents with milling time. (From the oxygen content in Figure 42, volume percents of Cu_2O were also estimated, and found to be about 0.5 vol% on average for almost all milling times.)

As the results indicate, the total particle volume percent increases to about 8.39 ± 0.1% due to the C addition – in the 2-8 hr milling time range. The comparable particle volume levels for 2-8 hr milling partly explain the comparable conductivities (Fig. 52(a)). The calculated volume fractions for Cr-phase particles correspond well to their XRD peak levels in Fig. 64. For milling 2 hr and beyond, there is enough C to react with all Nb, which leaves the excess Cr (particles). The calculated amounts of NbC and Cr_2Nb in Table XVIII also correlate well with their diffraction peaks in Fig. 45. Based on its calculated presence, it is both interesting and peculiar that $Cr_{23}C_6$ is neither detected by XRD and SAD, nor readily identifiable, e.g., in Figures 50 and 51. This is presumably due to its small size and particular diffracting characteristics, i.e. it may not diffract strongly, especially for their sizes in MM-4 hr/hot pressed Cu-4 Cr-2 Nb. Its initial size can be reasonably assumed small considering its complex lattice structure (a = 10.65 Å and 116 atoms/unit cell) and related sluggish reaction/formation kinetics. Note that $Cr_{23}C_6$ was distinctly observed and identified (in Figures 60 and 61) after the 1273-50 hr anneal, for which condition noticeable coarsening occurred and the calculated volume percent is comparable to that for the preannealed material. Finally, the C that reacted with existing Cr_2Nb particles, as seen in Fig. 39, during hot pressing formed carbides (mainly NbC_{1-x}) which inherited a spatial distribution essentially the same as that of the as-milled Cr_2Nb particles. This is somewhat evident from Fig. 51(b).

4.2.2. Mechanical Property and Corresponding Microstructure Behavior

4.2.2.1. Hardness and Microstructural Trends: Comparison and Analysis

As revealed by Figure 52, the electrical conductivity and hardness of Cu-4 Cr-2 Nb level off after about 4 hour milling for all specimens, particularly when milled with steel media. The maximum hardness actually corresponds to the 4 hr milling condition. This saturation indicates the MM process has reached a steady-state, or a balance of work hardening and work softening (dynamic recovery) has been achieved; i.e. dislocation generation and annihilation are in near equilibrium. This saturation of strength, measured as hardness, necessarily correlates to a constancy in (sub)structure, i.e. a steady-state cell/grain and particle size distribution and dislocation density. An additional point to state here is that from this "saturation" phenomenon, processing may be considered effectively complete in the 4-8 hr range of milling. In other words, if strengthening has reached a "limit," it can be safely deduced that *microstructural refinement* has reached a corresponding limit - for the particular current set of milling conditions used. Based on the time to saturation, 4 hr was chosen as an appropriate, convenient milling time for which to compare milled properties of additional particle-strengthened Cu alloys.

First, from Table XIII and Fig. 57, it is noteworthy that the hardness value for Cu-4 Cr-2 Nb are comparable with those of Cu-8 Cr-4 Nb after 4 hr milling (~100 HRB), which exceeds expectation when considering initial hardness values in Table XII. This is presumably due to a comparable microstructural refinement of the two Cu-Cr-Nb alloys by mechanical milling. Moreover, this suggests that the hardness is related more to grain and precipitate size refinement than to precipitate volume fraction. This behavior gave more compelling reason to pursue the lower alloyed Cu-4 Cr-2 Nb in its investigation and use. Finally, Cu-Cr-Nb alloys generally reach higher hardness values than GlidCop Al-15 and NARloy-Z, although these latter alloys retain a higher electrical conductivity after

milling. The (saturated) hardness values for the latter Cu alloys are close enough to those for Cu-Cr-Nb to affirm that it is extent of deformation of Cu that largely determines the hardness level. However, the type and size of strengthening phase are the critical factors determining ultimate low- and high-temperature strength and stability.

Actually, a similar saturation behavior was observed for attritor-milled Cu-10% Mo as reported by Schroth and Franetovic [5]. Figure 74 below shows their plot of Vickers hardness of milled powder as a function of attritor milling time. Note that for attritor milling at 250 rpm, saturation ensues after about 10 hrs. Also worth noting, when comparing Figures 74 and 54, the profiles as well as the maximum hardness reached are comparable. (As expected, the required milling times are longer for the less energetic attritor.)

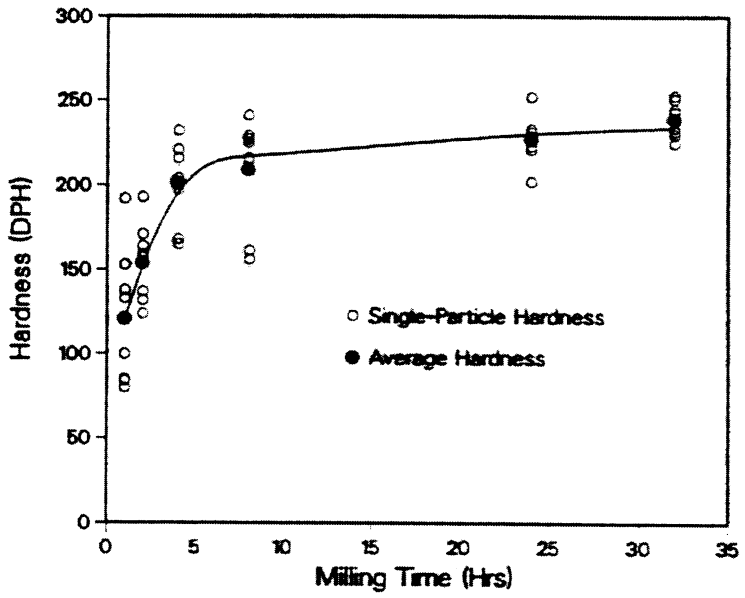

Figure 74 – Particle hardnesses for mechanically alloyed Cu-10% Mo – attritor milled at 250 rpm. (The solid circles are the average values.)

At this juncture, it is fitting to mention another example of such a hardness saturation. In their work on FCC-based Al-Fe-Ce powder, Öveçoglu and Nix also observed a saturation in Vickers microhardness (to ~160 HV) after about 3-4 hr SPEX

milling [125]. In their case they characterized this hardness saturation as signifying the completion of mechanical alloying.

In their study of the physics of mechanical alloying (and milling), which included the SPEX shaker mill, Maurice and Courtney [126] indicate that when MM/MA is used to produce a fine microstructure, i.e. a *microstructural refinement* criterion is used for process completion, an "accumulated true strain of 3 to 5 is needed for process completion." With the milling times employed in this investigation, such strains were likely achieved, especially considering the following.

Based on work on heavily deformed/drawn Cu-X composites (X = Nb, Fe, Ta, Cr), this predicted true strain range is deemed reasonable. Investigators such as Jerman, Spitzig, Verhoeven, Downing, Chumbley, etc. [43,120,127,128-130] have also demonstrated that Cu undergoes dynamic recovery (and eventually recrystallization [stage IV deformation]) when deformed to total true strain ($\ln\{A_o/A\}$) values greater than ≈3-4. Such strain levels lead to a constant dislocation density (10^{10}–10^{11} cm^{-2}) and grain size (~0.2 μm-0.5 μm), which result in strength saturation [127]. That is, they experimentally established strains in the "3 to 5" range are needed to reach strength saturation, especially when strength is strictly related to Cu grain size. From these observations and examination of Figure 52, it can be concluded that the Cu matrix in Cu-Cr-Nb alloys has undergone an accumulated true strain of most likely around 4 for (SPEX) milling times ≳4 hrs. Indeed, during the later stages of the MM process, the Cu matrix undergoes a dynamic process of deformation→recovery→(limited) recrystallization, which, again, is indicated by the hardness saturation of Fig. 52. Finally, the constancy of dislocation density has implications to resistivity when considering the dislocation contribution.

As a comparison, the above rapid saturation phenomenon, especially for MM, has also been evident for pure copper. Previous work on heavily deformed copper – drawn [62, 127], *mechanically milled* [79,131,132] and torsion strained [133,134] – where true (logarithmic) strains, ε_t, of ~3-10 were produced, has shown that the copper grain/subgrain sizes reach a minimum of 150-300 nm and reach microhardnesses of ~115-125 HV. Huang, *et al.* [79] also report an estimated dislocation density on the order of 10^{10} cm^{-2} for pure Cu ball-milled 20 hr. Based on their results of MM of pure Cu powders, Le Brun *et al.* [131] contend that dynamic recovery and enhanced ductility govern the behavior of milled Cu. That is, they also found a "saturation" in hardness in their mechanical milling of pure Cu, and attributed this to copper's relative ease of recovery and cold welding (see Figure 75). This behavior of (pure) copper effectively prevents a reduction in grain/subgrain size below a certain level (~0.3 μm in their case), regardless of milling time, under a given set of milling conditions (i.e. temperature, ball-to-powder ratio, milling device/energy, etc.). Le Brun *et al.*, in fact, emphasized that this saturation behavior for Cu seen in Fig. 75 was not affected by longer milling duration.

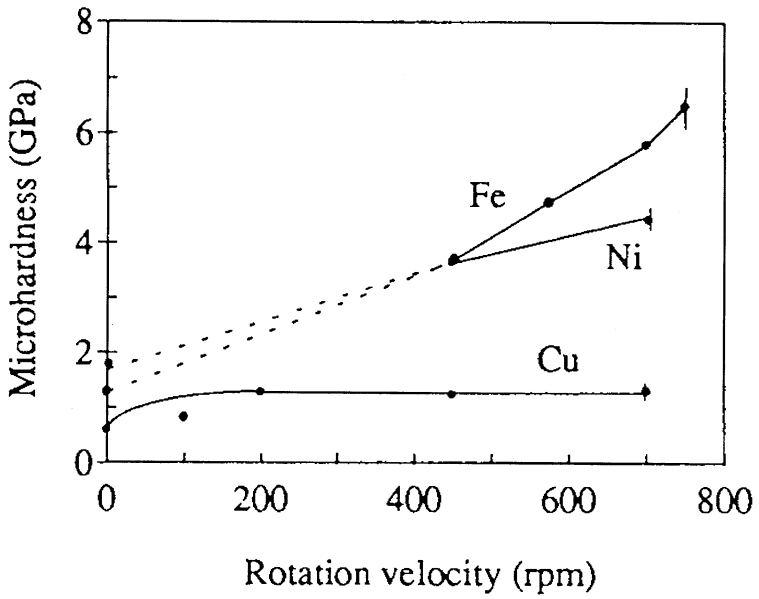

Figure 75 – Microhardness of as-milled Cu (and Fe and Ni) powder as a function of milling velocity (as taken from ref. [126]).

Finally, mechanically milled Cu-Cr-Nb saturating at twice its initial hardness evidently comes from the even more refined grain size and the 7-14 vol% of a dispersed second phase. It is very interesting and germane to point out that pure Cu would have to be synthesized with a grain size in the 6-20 nm range in order to achieve hardnesses approaching that of fully milled Cu-Cr-Nb. Investigators of nanocrystalline Cu synthesized by inert-gas condensation have reported hardnesses of 230-250 HV for the above grain size range [63, 135]. Of course, annealing the above severely plastically deformed and nano-grained pure Cu at ~0.5 T_m would induce extensive grain growth and hardness drops in such material without grain boundary pinners. If fact, in one particular case of the former, Cu grain size increased by 1.5 orders of magnitude (0.2→3.2 μm) after just 1 hr at 533 K [133]. For the latter case, such Cu having grain sizes in the tens of nanometers would be highly unstable and out of equilibrium. More specifically, grain growth has occurred even at room temperature (see Refs. 1 & 2 in [134]), making nanocrystalline Cu useless (for high strength) above ~100°C. To emphasize again the relative stability of Cu-Cr_2Nb alloys, aging mechanically processed Cu-4 Cr-2 Nb at 1273 K for 50 hr resulted in only a 5.5 times increase in grain size (0.1→0.55 μm).

Along the same lines, having only particles in a matrix (with no grain refinement) gives no significant strengthening. For example, using the compocasting process, Ichikawa and Achikita [136] added 0.5 to 30 vol% of ~0.7 - 2 μm-size MC particles (M = Nb, W, Ta, Ti and V) to Cu. Over this vol.% range, the hardness increased from ~58 HV to only ~125 HV. This finding plainly demonstrates the importance of obtaining a fine-grained structure that can then be sustained through dispersed-particle stabilization. Thus, having a finite volume fraction of *fine dispersoids* in a *fine-grained* matrix is imperative in maintaining high-temperature *stability* and, moreover, low and high temperature strength in Cu-based alloys. (The 1-3 μm grain size of heat treated extruded Cu-Cr-Nb is actually considered already relatively fine.)

4.2.2.2. Hardness and Microstructure: Stability Analysis and Comparisons

An additional, more interesting, stability aspect specific to milled Cu-4 Cr-2 Nb is revealed when comparing microstructure and hardness of as-milled powders to those for hot pressed milled powder. Inspection of Figure 46(b) – TEM image of as-8 hr-milled Cu-8 Cr-4 Nb powder – and Figure 51(a) – TEM image of 4-hr milled and hot pressed Cu-4 Cr-2 Nb – gives direct evidence of only marginal grain growth during hot pressing at 810°C and 100 MPa for 3 hrs. The grain sizes are maintained in the order of 100 nm. (Based on the comparable hardness values for 4 and 8 hr milling times (Fig. 52), it is reasonable to compare these two microstructures.). Finally, as similarly found for attritor-milled/hot pressed Cu-15at.% Nb [80], this apparent limited grain growth behavior indicates that the present hot pressing conditions necessarily fall within a "window" of temperature and pressure that virtually maintains the as-milled ultrafine structure while attaining full density [137]. This is direct evidence that even at the hot pressing temperature and pressure used, the second-phase particles hinder any real, global recrystallization and growth of grains, as also evinced by sustained hardness.

The hardness actually increases from ~230 HV for as-4 hr-milled powder to ~260 HV when this material is hot pressed (see Figures 54 and 55). This retained hardness is due largely to the stabilized grains/subgrains, as discussed above, even though additional carbide particles form from (interstitial) carbon reacting with mainly Nb (see fine NbC particles in Fig. 51(b) and their content in Table XVIII). Such milled-microstructure stability behavior is similar to that indicated in earlier mechanical alloying work of Benjamin and Schelleng [138]. In their study of Al-(0-7 wt%)Mg alloy, they found that mechanical alloying/attrition (MA) - with an oxygen and carbon containing PCA - led to just this behavior for milled and milled/consolidated material. They point out that "the [refined microstructure associated with the] large amount of internal energy imparted to the powder by the MA processing is pinned by the dispersoid and is retained to a large

degree during the consolidation ... and is a major source of the strength of the material." As first mentioned in the Results, the milled and milled/hot pressed material also have similar substructures in terms of the apparent complex internal strain contrast. From this and the above discussion, the phenomenon as described by Benjamin and Schelleng evidently applies to milled Cu-Cr-Nb alloys.

Taking this point one step further, annealing the MM-4 hr/hot pressed Cu-Cr-Nb at 1273 K for 50 hr provided more compelling proof of their enhanced stability, especially when compared to non-milled/extruded Cu-Cr-Nb and NARloy-Z. Consider the data in Table XV to compare various pre- and post-anneal hardness and conductivity values. It should be reemphasized that the MM Cu-8 Cr-4 Nb and Cu-4 Cr-2 Nb not only possess much higher and more similar starting *hardness* values as compared to the as-atomized/extruded Cu-Cr-Nb alloys (~100 HRB compared to 57 and 69 HRB), but also more comparable responses to the anneal (22 and 17% compared to 47 and 30% ΔHRB). Again, this demonstrates the benefits of a *refined* grain and dispersed-particle size and a more uniform size and spatial distribution of particles – all achieved by MM. Finally, NARloy-Z suffered the greatest loss in both hardness and conductivity. Such a relative lack of high-temperature thermal stability suggests that MM NARloy-Z alloy is inferior to even as-extruded Cu-8 Cr-4 Nb, at least in this one respect.

4.2.2.3. Grain Size and Hall-Petch Correlations

Relevant to this processing-microstructure-property approach in characterizing MM Cu-Cr-Nb alloys is estimating to what extent strength and conductivity are dependent on grain size as well as particle size and spacing. To this end, interpretation of the data may include analysis of the slopes and intercepts of plots of strength vs. $1/d^{1/2}$ (Hall-Petch), 1/d and $\{\ln(r/\mathbf{b})\}/(\lambda\text{-}2r)$. Once again, Morris and Morris [4] have deemed the Hall-Petch relation invalid as for its application to the mechanically alloyed DS copper systems they

investigated. Such a judgement was based on graphical analysis of strength vs. $1/d^{½}$, which showed a negative y-intercept. From this, Morris and Morris contend that, opposite to dispersed particles, grain boundaries contribute essentially little or nothing to the strength of milled DS Cu alloys, or any (non-milled) DS alloy. This is contrary to the findings of Hall-Petch and Orowan strengthening analyses of extruded Cu-Cr_2Nb (Section **4.1.3**) and, again, to Hazzledine's conclusion [49]. Such inconsistencies only add to the importance of and purpose for Hall-Petch analysis involving mechanically milled Cu-Cr-Nb. In fact, the mechanical milling strength and grain-size data (Figures 55/56 and Figures 63/65, respectively) are well suited for systematic Hall-Petch analyses.

But before analyzing present mechanical property data vis-a-vis grain (and dispersoid) sizes, a brief description of how grain-size analysis techniques compare is warranted. Again, this includes the use of TEM versus XRD.

Grain/crystallite size measurements are commonly carried out by X-ray diffraction (XRD) and electron microscopy techniques (TEM or high resolution SEM). From TEM and SEM images, grain sizes are measured directly, from which grain size distributions can be generated. In contrast, XRD techniques provide only an average grain size. These techniques make use of the grain-size dependence of Bragg peak broadening. Corrections for instrumental broadening must be made. Scherrer analysis is straightforward, but only considers that the broadening of X-ray peaks is due to small crystallite sizes. The Warren-Averbach (WA) method is more sophisticated by taking into account broadening caused by internal stresses, as well. Furthermore, WA analysis may distinguish between broadening due to grain size and to intrinsic faults and twins. Therefore, measurable differences may be found between Scherrer (larger values) and WA (smaller values) results and between results from different X-ray peaks for grain size estimation. The Scherrer method yields a volume-weighted average while the WA yields an area-weighted average grain size. Typically, these two averages differ by a factor of 2 [139]. Nieman *et*

al. report a smaller error (10-25%) in grain size determination by the WA method for grain sizes up to 25 nm but the error may be up to 100% when the grain size exceeds 50 nm [140].

Generally, average TEM grain sizes and X-ray results are in good agreement, particularly for the WA analysis with strain and fault corrections [139]. As expected, the best agreement is found when the grain size distribution is narrow (e. g., [141]). When the grain size distribution is large, the TEM method is preferable. Only in a few cases, large discrepancies are reported between microscope and XRD measured grain size [142,143]. For instance, Hahn *et al.* reported SEM grain sizes to be 4 times larger than XRD line broadening data [142]. However, in this case, the SEM size was found to be that of agglomerates rather than that of individual nanoparticles.

From the above discussion, it was expected, *a priori*, that W-A analysis would give drastically lower grain/subgrain sizes than TEM analysis, but was carried out to provide relative changes in size with milling time. As seen in Fig. 65, XRD analysis produced a result of ~81 nm for as-atomized/hot pressed Cu-4 Cr-2 Nb. Again, the TEM measured value was about 1.43 μm. For the 4-hr milled/hot pressed sample, W-A gives a value of 38 nm, while lineal analysis from TEM images gives about 110 nm. Such disparities are, again, assumed to be from the observed sizes being substantially higher than 50 nm, especially for the as-atomized/hot pressed case. (Note that the extent of disparity decreases with grain size, as expected.) Notwithstanding, the sizes and trend traced in Fig. 65 are in line with such XRD analysis results for other mechanically milled/alloyed material systems, e.g., as reported in refs. [144 and 145]. Therefore, the information revealed in Fig. 65 is considered representative and relevant. This is also substantiated in the following analysis.

Indeed, when hardness is plotted against $1/d^{½}$ and $1/d$, where d is taken as the Warren-Averbach crystallite size, a linear relationship is produced, as represented in Figures 76 and 77. As regression analysis in Fig. 76 indicates, the linear fit line does

have a negative y-intercept. However, there is a positive y-intercept in Fig. 77. Again, Morris and Morris contend a negative intercept renders the usual Hall-Petch analysis ($1/d^{1/2}$) invalid. Nevertheless, it is interesting that the fit is actually slightly better for the $1/d^{1/2}$ plot. This may also be related to the fact that, for milled material with dispersoids, $d \approx \lambda_p$. Finally, the slope of the $1/d$ plot, found via linear regression, proves to be about 93.5, which is close to the value of 92 for yield stress versus $1/d$ reported by Morris and Morris [4]. This value from Morris and Morris was taken from linear regression through data points of eight different MM DS and other copper alloys. That is, Cu-Cr_2Nb(-NbC) appears to behave consistently with other (DS) copper alloys, which gives credence and validity to the present data and analyses.

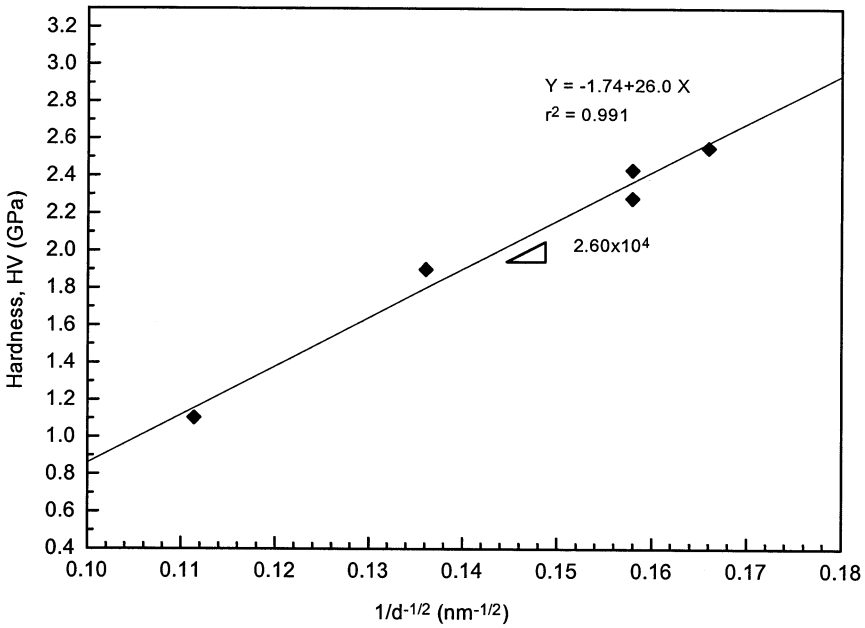

Figure 76 – Hall-Petch relation for hardness and W-A crystallite size for milled/hot pressed Cu-4 Cr-2 Nb.

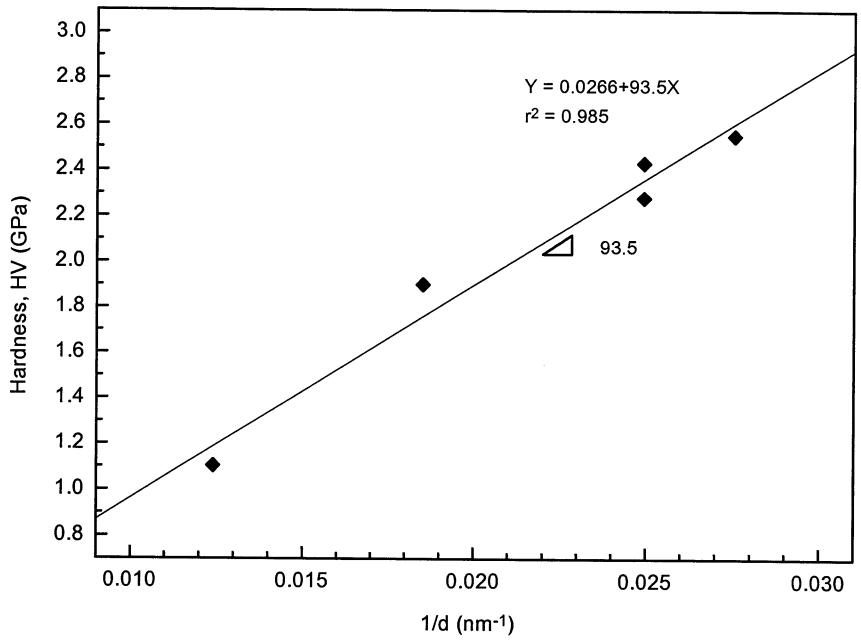

Figure 77 – Hardness dependence on inverse grain size for milled/hot pressed Cu-4 Cr-2 Nb.

However, when hardness is plotted against $1/d^{1/2}$, where d is grain size from lineal analysis (Fig. 63), a positive y-intercept and an even slightly better fit are found, as depicted in Figure 78. Thus, when considering more realistic, actual grain sizes, the Hall-Petch ($1/d^{1/2}$) analysis appears (more) valid. This would corroborate the work on extruded Cu-Cr-Nb, which showed a reasonably consistent correlation between yield stress and grain size. All of this also supports Hazzledine's aforementioned argument. The role of the Hall-Petch effect is also demonstrated in Fig. 78 upon noticing how the comparable measured grains sizes of Cu-4 Cr-2 Nb MM-1/2 hr/hot pressed and MM-4 hr/hot pressed/ annealed at 1273 K – 50 hr give comparable hardness values.

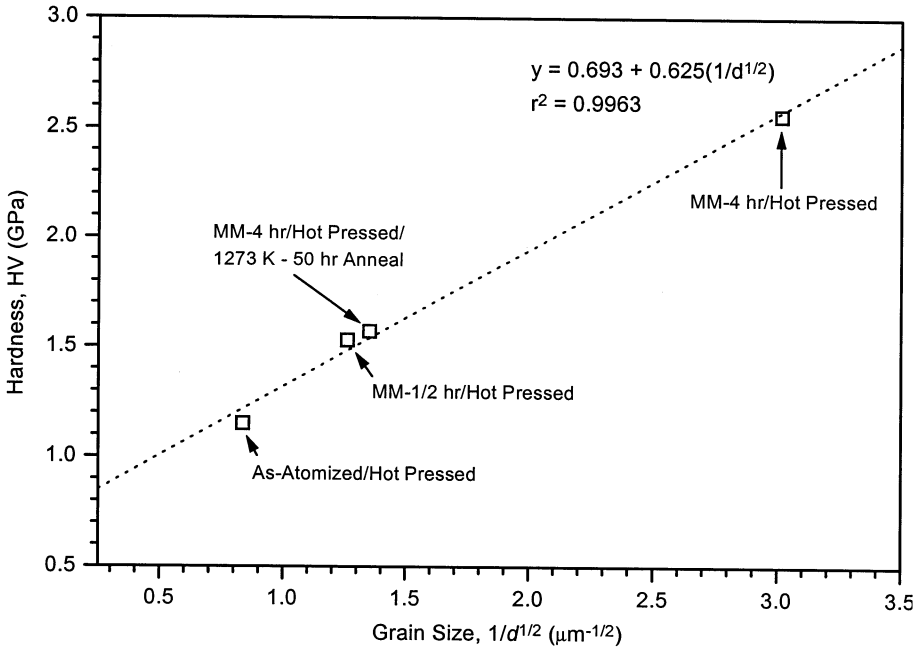

Figure 78 – Hall-Petch relation for hardness and lineal intercept grain size for milled/hot pressed Cu-4 Cr-2 Nb.

Finally, as given in Fig. 56, the calculated equivalent yield stress is about 850 MPa for MM-4 hr/hot pressed Cu-4 Cr-2 Nb. The calculated Hall-Petch contribution (Eq. (5)) for the average grain size of 110 nm is about 508 MPa. Assuming the calculated equivalent yield stress as reasonably close to the actual material yield stress, the Hall-Petch represents about 60% of the overall yield strength. Again, such a majority strength contribution is consistent with the (~66% for) as-extruded Cu-Cr-Nb. The slightly higher remaining Orowan strengthening contribution (40%) is reasonable when considering such small (<50 nm) NbC particles revealed in the DF TEM of Fig. 51(b). The refined as-milled Cr_2Nb particles act, in effect, as "seeds" for heterogeneous carbide (and excess Cr) phase formation/nucleation. That is, the smaller the post-milled Cr_2Nb (and the more Cr, Nb and C in extended solution) the smaller the carbides (NbC) formed during hot pressing. This gives the relatively higher Orowan strengthening contribution.

Expressions for gains in flow stress (e.g., microhardness/yield strength) derived from such microstructural features have been presented and analyzed, but what is also now needed are analogous expressions for conductivity/resistivity and analyses thereof.

4.2.3. Electrical/Thermal Conductivity-Microstructure Analyses

4.2.3.1. Survey of Potential Microstructural Effects on Conductivity

The empirical %IACS values for Cu-7vol% Cr_2Nb in Figures 52 and 33 are substantially lower than those predicted (Figures 70 and 71), especially for longer milled material. This discrepancy lends itself to the need to consider various resistivity contributions expressed in Eq. (13). Again, the Cu-4 Cr-2 Nb milled above 1 hr has an improved hardness relative to as-extruded Cu-8 Cr-4 Nb and as-atomized/hot pressed Cu-4 Cr-2 Nb, but a reduced conductivity. Therefore, it is necessary to account for each contribution to this fairly extensive drop in conductivity as a function of milling/processing time. Such analysis to establish the various relative contributions is done along similar lines as the analysis by Verhoeven, *et al.* [120] of heavily deformed Cu-X alloys. That is, it includes post-consolidation annealing experiments, plotting resistivity, or conductivity (ρ in $\mu\Omega$-cm, σ_e in %IACS) vs. grain size for various milling times – for linear regression analysis.

Thus, an additional goal of microstructural analysis is to shed light on the direct correlation of strength and conductivity particular to Cu-Cr_2Nb alloys, including micro-effects on each (e.g., impurities, dislocations, grain and dispersoid size, etc.). At first look, the conductivity decrease in Cu-Cr-Nb alloy with milling time would seem to be related more to the impurity content and type than to degree of deformation. This is indicated by the difference and similarity in the conductivity and hardness profiles, respectively, for steel and WC milling media (Fig. 52). From the similarity of the hardness profiles, it is reasonable to assume that the extent of deformation, i.e. work

hardening/softening of Cu as well as grain- and second-phase particle-size refinement, is roughly equal for both milling media. Therefore, any likely drop in conductivity from a deformed Cu substructure and increased grain boundary and precipitate/matrix interfaces should be virtually the same. However, use of the steel vial and balls, and the required PCA, was shown to have introduced Fe and C into the milled powder. These impurities evidently had more of an adverse effect on conductivity than did impurities from the WC, at least up to 4 hrs. However, for longer milling times, the relatively severe oxygen contamination, as well as WC and Co contamination from the WC milling media (values given in Table XIII), appear to eventually cause more loss of conductivity than does C and Fe contamination, as previously reported [146].

To further distinguish the specific effect of these impurities coming from the steel milling media and PCA, Figure 79 presents conductivity and impurity content as functions of milling time on the same axes. As presented in the Results and Table XVIII, the carbon is mainly tied up as carbides. The Fe content taken from Figure 79 ranges from 0.015 wt.% (MM-½ hr) to 0.065 wt.% (MM-8 hr). Base on the work on Cu-Fe alloys of Boltax [147] and Spitzig *et al.* [148], and the Cu-Fe phase diagram used, such Fe levels should be completely soluble in Cu at the sintering temperature of 810°C, but virtually insoluble at 25°C. However, such investigators found that the kinetics of Fe precipitation is slow such that Fe dissolved in Cu at high temperatures (~675°C) is not precipitated out during furnace cooling or during a 2 hr hold at 400°C. Thus, the worse case scenario for the MM Cu-4 Cr-2 Nb is that virtually all Fe remains in solution.

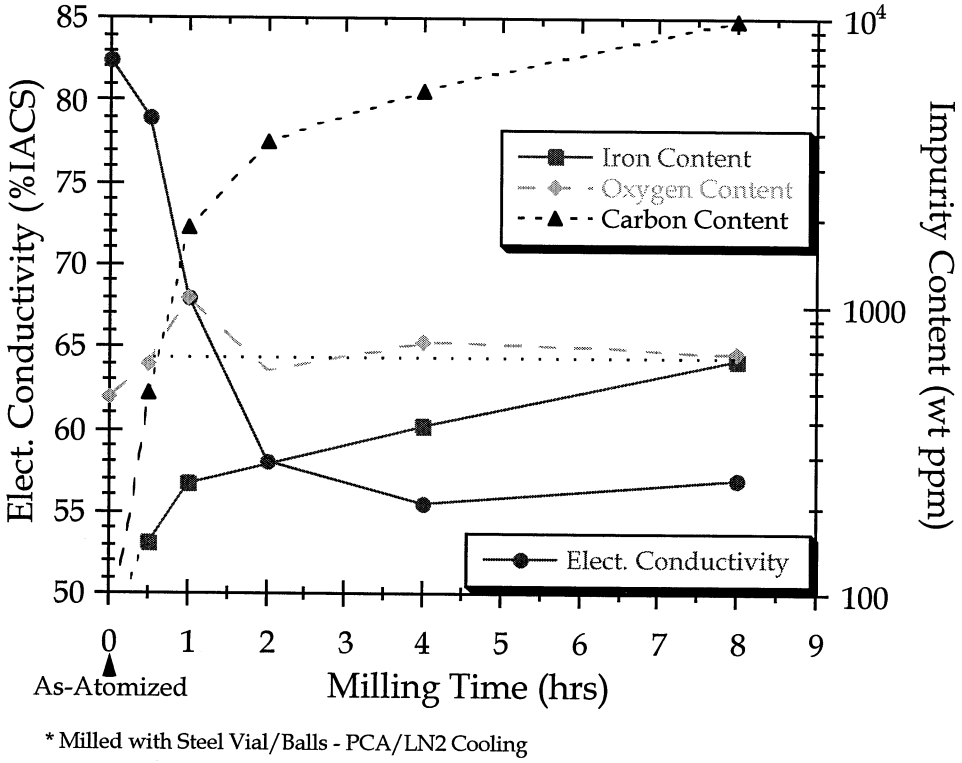

* Milled with Steel Vial/Balls - PCA/LN2 Cooling

Figure 79 – Electrical conductivity and impurity content related to milling time for hot pressed Cu-4 Cr-2 Nb.

As seen from Fig. 72, the above range of Fe in solution corresponds to an increase in Cu resistivity from ~0.14 to 0.6 μΩ-cm (or a drop of 5% IACS and 18% IACS in as-atomized/hot pressed Cu-4 Cr-2 Nb conductivity, respectively). The actual drop in conductivity due to Fe is most likely less than this since the MM material provides ample internal (point, line and planar) defects for heterogeneous Fe segregation/clustering during sintering and actual precipitation during furnace cooling. However, the actual degree of Fe precipitation is uncertain at this point. The slight increase in conductivity after 8 hr milling may be due to such Fe precipitation and/or reactions of excess C with Cr and Fe in extended solid solution to form $Cr_{23}C_6$ and Fe_3C, respectively, even though none have been identified. Finally, although also never identified, O most likely ended up as essentially very low volume fractions (~0.5 vol%) of fine Cu_2O particles, as mentioned earlier. This assertion can be made when considering 1) the samples were exposed to 810°C for 3 hrs then furnace cooled, 2) O have low solubility in Cu at low(er)

temperatures, and 3) as Fig. 79 shows, the conductivity actually slightly increases while oxygen remains basically constant.

Figure 80 is a plot of Eq. (20) with an emphasis on smaller particles. This indicates that for particles with an overall average size less than about 100 nm, the solute solubility, and more importantly, the associated relative resistivity, increase appreciably. As alluded to earlier, since Cr_2Nb particles become more fine, as well as more evenly and densely dispersed with milling, so should the carbide particles that originate from the Cr_2Nb (e.g., NbC). Thus, a large portion of any solute remaining in solution above equilibrium levels – subsequent to cooling from 810°C – is presumably thermodynamically driven into solution from the increased Gibbs-Thomson effect of small(er) particles. This, along with their reduced mean separation (e.g., see Figures 39, 40 and 51), are most likely the main effects on conductivity of all particles present for all milling times.

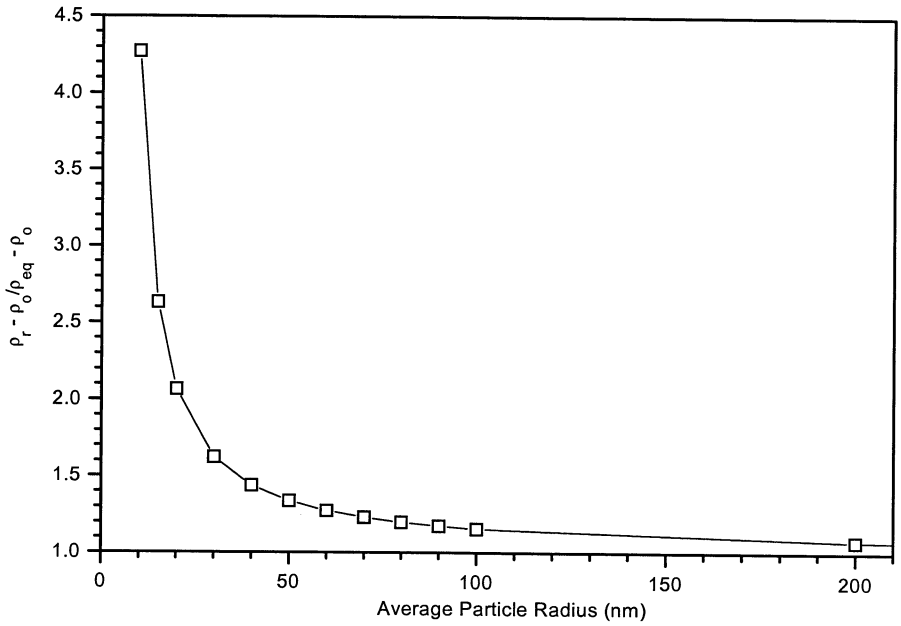

Figure 80 – Plot of Eq. (20) showing solute effects of smaller average (incoherent) particle sizes on relative alloy resistivity .

To better assess effects of crystallite size (surface area) on conductivity, the %IACS conductivity values from Fig. 52 are plotted against the corresponding crystallite sizes in Fig. 65, as shown in Figure 81. Notice that regression gives a very good linear fit. Again, when comparing, for example, Figures 63, 65 and 79 (the conductivity trace) the relation in Fig. 81 is expected, i.e. reasonable. It can be pointed out here that from the similarities in plot profiles for the grain and particles sizes, i.e. Figures 40, 63 and 65, taking particle size as the independent variable should give a result analogous to Fig. 81. Manzano-Ramirez *et al.* also found a linear relationship between resistivity and grain size for Al-based alloys [149]. And, from their studies of discontinuously reinforced aluminum (DRA), Geiger *et al.* have found that thermal conductivity is dependent on the size of reinforcement particles, of constant volume fraction, with conductivity decreasing with size – using Eq.(18) [150]. However, for the latter case, there was strong particle/matrix bonding, giving a relatively large h_c component. These findings would suggest that the drop in conductivity is largely due to the reduction in Cu grain and reinforcing particle size, i.e. an increase in electron scattering related to the increase in (Cu grain and particle/matrix) interfacial area. Altogether, with the introduction of C and Fe in a Cu system already containing Cr and Nb, and the imposed severe plastic deformation, followed by high-temperature hot pressing has made for a very complex, non-equilibrated, multi-phased system. What follows next is an analysis of which of the above described microstructural details has the greatest influence on electron mean free path, which ultimately controls conductivity in metals.

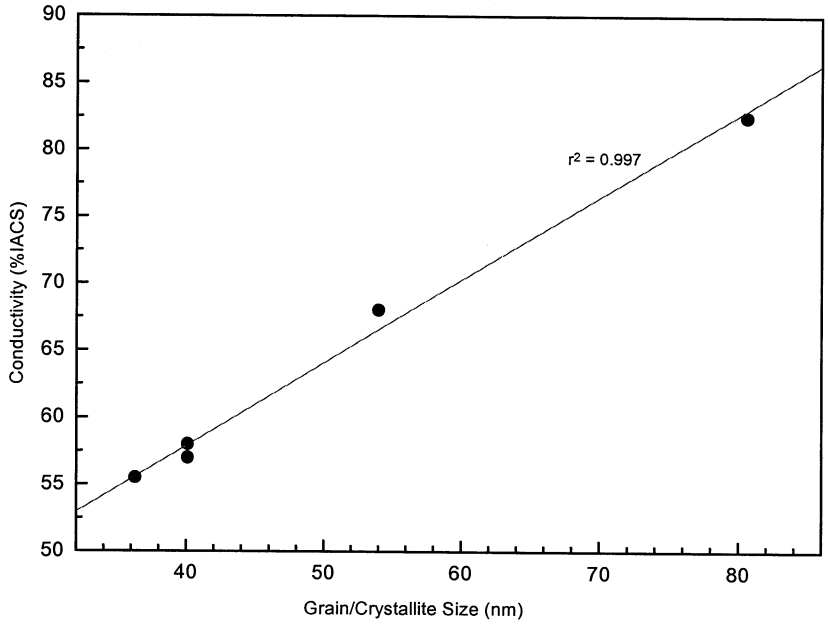

Figure 81 – Electrical conductivity as related to crystallite size for MM Cu-4 Cr-2 Nb.

4.2.3.2. Electron Mean Free Path: A Survey of Controlling Factors

From. Eqns. (7) & (8), the controlling variable is the electron mean free path (mfp), λ_{el}. Thus based on the conductivities measured for Cu-4/2 as a function of milling time, corresponding electron mfp's were calculated (see Appendix E for spreadsheet of calculations) and are presented in Table XIX. When comparing as-atomized/hot pressed Cu-4 Cr-2 Nb to copper and milled Cu-4/2 to non-milled material, the microstructural and atomic-level features described above that are appreciably responsible for the decreases in λ_{el} need to be contemplated. This should go far in narrowing down the predominant electron scattering mechanisms.

The NbC particles revealed by dark-field TEM in Fig. 51(b) are generally very small, 15-30 nm, and thus have large interfacial areas and small inter-spacings, as also seen. As Fuschillo and Gimpl [151] point out in their paper on DS Cu (Cu-ThO_2), if the interparticle spacing begins to approach the electron mfp (~39 nm), a significant fraction of the conduction electrons will "be scattered by the dispersoid surface rather than by

Table XIX - Electron Mean Free Path for Cu and Milled Cu-4 Cr-2 Nb

Milling Time (hr)	$\sigma_e \times 10^4$ $(\Omega\text{-cm})^{-1}$	ρ ($\mu\Omega$-cm)	λ_{el} (nm)
Cu	58.8	1.70	38.6
0	48.3	2.07	31.9
0.5	46.5	2.15	30.5
1	40.1	2.50	26.3
2	34.2	2.93	22.4
4	32.7	3.06	21.5
8	33.6	2.98	22.0
4 + 1273 K-50 hr Anneal	42.4	2.36	27.8

electrons and phonons in the matrix. This will augment the matrix relaxation mechanisms and diminish the effective [electron] mfp," which appears in Table XIX for each milling time. Also, the brightfield TEM of Fig. 51(a) reveals a still unrelaxed internal structure, i.e. fluctuating lattice contrast. This microstructure gives the lowest conductivity (Fig. 52(a) and Table XIX). The existence of these fine particles, the related decrease in separation distance and increase in solute solubility (Fig. 80), and the obviously perturbed matrix lattice can readily give rise to electron scattering centers occurring on average every ~22 nm, as opposed to ~39 nm for pure Cu. Furthermore, as the data in Table XV prove, the conductivity increases by 30% (in %IACS) upon annealing at 1273 K for 50 hr. The resulting microstructures shown in Figures 59(b) and 61 portray a more relaxed equilibrium grain boundary structure and larger grains (~0.5 μm) and coarsened dispersoids, especially $Cr_{23}C_6$. This can largely explain the increase in λ_{el} to ~28 nm for this case.

From the above examination and analysis, it is concluded that the decrease in conductivity as a function of milling time is attributed mainly to increased density of

electron scattering centers – lattice imperfections – in the form of 1) smaller Cu grains giving higher density of grain boundaries (ρ_{int}), 2) smaller particles having smaller spacing and larger specific interfacial areas (ρ_{int}) – giving increased Cr and Nb solubilities (ρ_{imp}), and 3) lattice-level defects, such as Fe impurities and internal strains (ρ_{imp}). The latter two almost certainly dominate. And, as found by Verhoeven *et al.* [120] and Chumbley *et al.* [152] for heavily deformed Cu-X alloys, and alluded to earlier, the dislocation contribution to resistivity (ρ_{dis}) for milling times $\gtrsim$4 hr is presumed constant and to be no more than about 0.1 μΩ-cm, i.e. ~5 and 6% drop in the conductivity relative to as-atomized/hot pressed Cu-4 Cr-2 Nb and pure Cu, respectively.

4.2.4. Strength and Conductivity: a Trade-Off and a Figure of Merit (FOM)

Verhoeven, *et al.* have investigated strength and conductivity of heavily drawn Cu-X (X = Nb, Fe, Ta, Cr filament) composites [120,129-130], Jerman *et al* [43]., studied the same properties for "deformation-processed" Cu-15 vol% Fe. An inverse correlation of strength and (electrical) conductivity measured as %IACS was shown, as in Figure 82. Data of hardness plotted against electrical conductivity (%IACS) for MM'd Cu-4 Cr-2 Nb (Fig. 83) are consistent with literature data for the dispersion-hardened Cu alloys in Fig. 82. These trends are generally expected based on the work of Shapiro and Crane [153], which showed (graphically) how strength and conductivity are in opposition and that precipitation- or particle-hardening provides the best combination. Figures 82 and 83 both demonstrate such an obvious trade-off between strength and conductivity. This trade-off definitely indicates that the primary microstructural features that provide an increase in strengthening are also responsible for a decrease in conductivity; whether they be refined grain and particle sizes, dislocation substructures, etc.

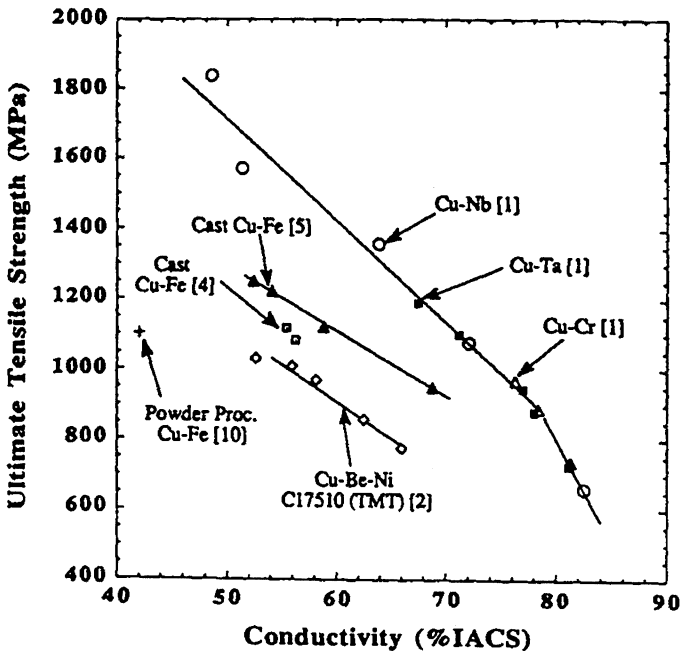

Figure 82 - Strength *vs* electrical conductivity of copper alloys [43].

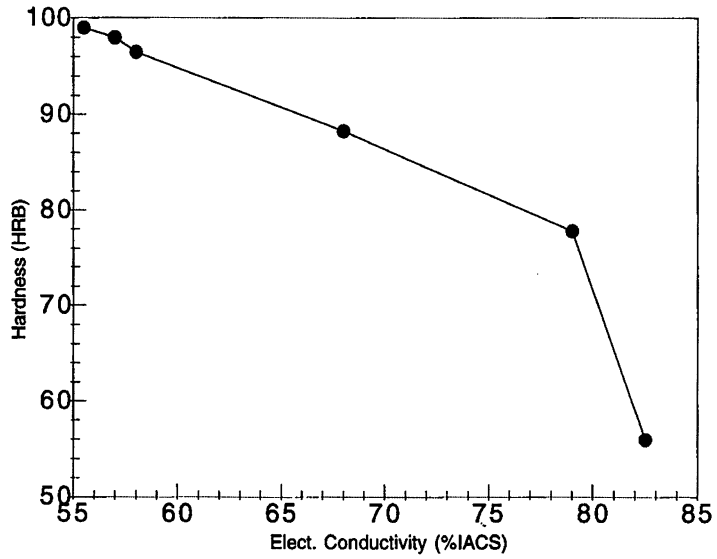

Figure 83 - Hardness-electrical conductivity relation for MM'd Cu-4 Cr-2 Nb (powders milled for 0, ½, 1, 2, 4, and 8 hrs).

Mechanical properties and then conductivity properties of processed Cu-Cr-Nb alloys were studied in depth. This revealed that as strength increased conductivity decreased. For such particle-strengthened alloys designed for high-strength high-conductivity applications, this reciprocation behavior of the two most critical properties leads to the contention that a combined-property – and its trend – be originated.

Moreover, more valuable performance information can be gained if such properties were coupled, for example, using a figure-of-merit (FOM). Such a means of combining mechanical strength and conductivity, beneficially giving the best prediction of overall performance, is achieved by the FOM, Vickers Hardness × Thermal Conductivity. Figure 84 is a plot of such an FOM. Immediately revealed in this FOM plot is an optimum combination of desired properties for a particular set of processing conditions. Also note that the FOM value MM-4 hr/hot pressed/annealed Cu-4 Cr-2 Nb is still higher than that for as-extruded Cu-8 Cr-4 Nb. For comparison, it should be noted here that such an FOM for pure Cu is about 200 HV·κ. In the end, such a mean of establishing a property-combination trend is advantageous in its utility for material application. Therefore, this final approach of introducing an FOM for processed Cu-Cr-Nb has made it possible to generate even more, salient information. Nonetheless, Fig. 84 is just one important outcome of this extensive, collective study of Cu-Cr-Nb alloys.

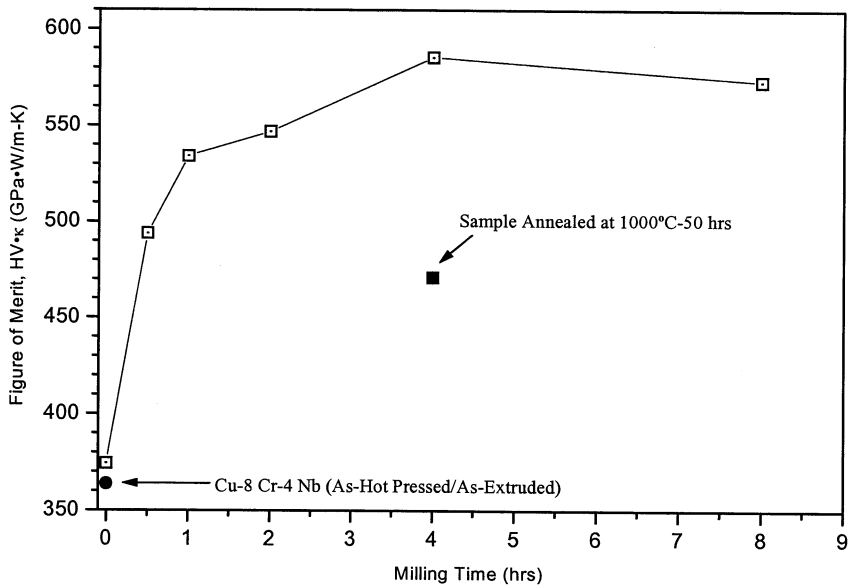

Figure 84 – Plot of 'Figure-of-Merit,' HV (GPa)·κ (W/m-K), for Mechanically Processed and Consolidated Cu-4 Cr-2 Nb Material.

V. SUMMARY AND CONCLUSIONS

An intensive investigation of Cu-Cr-Nb alloys was conducted, in part, to understand 1) the thermal stability of such alloys, particularly Cu-8 Cr-4 Nb, upon aging from 773 to 1323 K for up to 100 hr, and 2) alloy strength behavior and strengthening mechanisms. Firstly, Cu-8 Cr-4 Nb and Cu-4 Cr-2 Nb alloys exhibit a bimodal distribution of Cr_2Nb particles, namely, primary micrometer range particles formed from the liquid and secondary particles formed by precipitation from solid solution. A trimodal particle distribution with additional very fine, second-generation secondary particles is observed in extruded Cu-8 Cr-4 Nb aged 1 hr at 773 and 973 K and after slow cooling from temperatures above the extrusion temperature. Secondly, the copper matrix exhibits a fine equiaxed structure (transverse to extrusion direction) with an average grain size of 2.7 μm after exposure to 1323 K for 100 hr. No significant grain growth occurs in the studied temperature range. This is due to effective grain boundary pinning by primarily the large Cr_2Nb particles, and, in fact, grain size evidently obeys a modified Zener-pinning model.

Coarsening of the secondary and primary Cr_2Nb particles in Cu-8 Cr-4 Nb alloys was observed during aging at 773 and 973 K and 1323 K, respectively. However, both particle types remain close to their original size – 150 nm for secondary and 1 μm for primary - even after 100 hour aging. This sluggish behavior can be attributed to the low solubility and diffusivity of Nb in Cu. The extent of coarsening tended to follow LSW-type kinetics, i.e. $r^3 \propto t$ (volume diffusion) for secondary particles – at the lowest process temperature of 773 K – and $r^4 \propto t$ (grain boundary diffusion) for primary particles – at the highest process temperature of 1323 K. Deviations from LSW theory are most likely due to finite volume fraction effects and diffusion mechanisms, including dislocation pipe diffusion, operating simultaneously. Although particle coarsening occurs, the particle

distributions after long time annealing is still favorable to maintain the good mechanical properties of this alloy.

The main sources of strengthening are the Hall-Petch and Orowan mechanisms. The large particles contribute indirectly, but significantly, to alloy strength via pinning the fine grain size, i.e. the Hall-Petch effect. Hence, this grain boundary strengthening contribution is maintained after long time annealing at high temperatures and constitutes the predominant strengthening contribution in Cu-8 Cr-4 Nb alloys at room and high temperatures, specifically about two-thirds overall yield strength. The secondary particles contribute the main Orowan component, which accounts for the remaining one-third. Both experimental and calculated values of Orowan and grain boundary strengthening due to small and large particles indicate that coarsening of the precipitates results in only a minor decrease in mechanical strength after aging 100 hr at 1273 K. In sum, Cu-8 Cr-4 Nb exhibits superior microstructural and mechanical stability even after exposure to very high temperatures for extended periods of time. The stability of the alloy is directly attributable to the lack of significant coarsening of the Cr_2Nb precipitates and growth of Cu grains during thermal exposure.

The second half of this collective Cu-Cr-Nb study, which was built on the above investigative outcome of extruded material, centered on improving upon the confirmed inherent strength, stability and conductivity. Microstructural refinement of Cu-4 Cr-2 Nb, achieved via mechanical milling, and hot pressing produces a material with superior hardness and stability properties vis-a-vis as-extruded Cu-8 Cr-4 Nb. A comprehensive study of the microstructural configuration and consequent strength/conductivity behavior of Cu-Cr-Nb alloys processed/prepared via mechanical milling has been carried out. It was found that from mechanical milling Cu-Cr-Nb with a PCA, carbides (NbC and $Cr_{23}C_6$) formed upon hot pressing. Since these particles should provide similar effects as Cr_2Nb, they were treated as Cr_2Nb-like in terms of strengthening and stability. Assessing

and comparing extensive empirical data consisting of the specific microstructural effects (grain and particle size) and their relative contributions to strength and conductivity/resistivity for at least two Cu-Cr-Nb alloys provides a sufficient basis to predict if other such alloys may be even better, e.g., Cu-2 Cr-1 Nb. Also, this extensive materials characterization is critical for the reliable and eventual application of such alloys.

This research work has provided novel insight into the effects of processing and microstructure in the optimization of strength-conductivity of DS Cu alloys for high-temperature applications. Moreover, optimization via microstructural control and analysis has been achieved. Cu-4 Cr-2 Nb milled 4 hr and hot pressed showed the maximum hardness×thermal conductivity. By and large, the outset goal of assessing and verifying high-temperature microstructural and strength stability, as well as prominent strengthening mechanisms, of Cu-Cr-Nb alloys (by focussing on Cu-8 Cr-4 Nb) has been met. Also met was the subsequent goal of bettering the strength and stability performance while maintaining conductivity of the original Cu-8 Cr-4 Nb by refining the larger Cr_2Nb and Cu grain size and homogenizing size and spatial distribution of Cr_2Nb in Cu-4 Cr-2 Nb.

VI. FUTURE WORK

In its entirety, the above information presented represents a vast amount of experimental research – enabling, for the most part, the twofold objectives of this study to be met. Nonetheless, additional work would be helpful to even better address, assess and predict microstructural phenomena in and strength and conductivity behavior of Cu-Cr-Nb alloys. For example, to better predict and describe the coarsening kinetics of the large and small Cr_2Nb particles in extruded and hot pressed Cu-Cr-Nb, modified LSW expressions that more realistically account for actual phenomena taking place simultaneously, e.g., volume diffusion, grain boundary diffusion and dislocation pipe diffusion controlled ripening, require development.

For mechanically processed Cu-Cr-Nb, it would be of primary and obvious interest to mechanically mill in such a way as to avoid a PCA, i.e. carbon, to preserve processed materials as Cu-Cr_2Nb. Further work could include microprobe and/or EELS analysis, which should be used to assess extent of extended solid solubility and supersaturation of alloying elements in the mechanically-milled processed material. To better gage tensile properties, tensile tests should be carried out on mechanically milled and consolidated Cu-Cr-Nb to assess yield and ultimate tensile stresses and ductilities as functions of milling time, grain sizes, etc. Creep and fatigue tests on mechanically milled and consolidated Cu-Cr-Nb to assess creep and fatigue strengths and lives, and the effects of crystallite and particles sizes on both, would add to basic and applied knowledge of DS Cu alloy behavior and performance. In addition, performing aging studies on P/M processed Cu-Cr-Nb parallel to those done for as-extruded material may provide useful information. Much of this additional work would be necessary to establish a reliable data base that demonstrates material integrity for high-temperature applications.

Finally, it would be very interesting and instructive to mechanically mill/alloy starting Cu and Cr_2Nb powders; and Cu, Cr and Nb powders. Preliminary work involving such cases has actually been done by Axtell, *et al.* [154] and Aikin [155]. Axtell, *et al.* SPEX milled for 3 hr Cu, Cr and Nb in the atomic ratio of 70:20:10. This basically resulted in a Cu/Nb layered structure with a thin Cr_2Nb layer at the Cu/Nb interface (after heat treatment). Aikin attritor milled for 5 hr Cu + Cr_2Nb powders and Cu + Cr + Nb powders in proportions to give the same Cr_2Nb volume fraction (~0.14) as Cu-8 Cr-4 Nb. The elemental powder case produced similar results as Axtell, *et al.*, i.e. very large (10 μm) "islands" of Nb and Cr, and only relatively little actual Cr_2Nb at the interfaces (after hot extrusion). The Cu + Cr_2Nb case resulted in a non-uniform distribution of Cr_2Nb particles of up to ~5-10 μm in size.

Such preliminary findings give strong impetus in continuing this work using, for example, longer milling times to further break down the phases and extend the solid solubilities, which would favor more homogeneous, intimate alloying/mixing. The resulting microstructures and properties should be compared to such results of the present milling investigation of starting pre-alloyed Cu-4 Cr-2 Nb. For the best combination of strength and conductivity, the ultimate goal is to produce **Cu-4 Cr-2 Nb** having strictly fine Cr_2Nb particulates evenly dispersed in a virtually pure, fine-grained Cu matrix. Thus, the intellectual challenge here would be to determine which alloy synthesis provides the most uniformly distributed and finest dispersoids and the 'cleanest' Cu matrix - or best combination of strength and conductivity - and why. (But, again, NbC has proven to be similarly effective for strength and stability as Cr_2Nb, i.e. NbC is considered at least the next-best choice as a strengthening particle for Cu.)

VII. REFERENCES

1. A. V. Nadkarni, "Dispersion Strengthened Copper: Properties and Applications," *High Conductivity Copper and Aluminum Alloys,"* Ed. by E. Ling and P.W. Taubenblat, TMS/AIME, Warrendale, PA, 1984, p. 77.

2. J. J. Stephens, J. A. Romero and C. R. Hills, *Microstructural Science*, vol. **16**, Ed. by H. J. Cialoni, *et al.*, 1988, p. 245.

3. M. A. Morris and D. G. Morris, *Mater. Sci. & Eng.*, **A104**, 1988, 201.

4. M. A. Morris and D. G. Morris, *Mater. Sci. & Eng.*, **A111**, 1989, 115.

5. J. G. Schroth and V. Franetovic, *JOM*, **41**, n. 1, 1989, 37.

6. D. G. Morris and M. A. Morris, *Scripta Metall. et Mater.*, **24**, 1990, 1701.

7. J. J. Stephens and C. R. Hills, "Long Term Stability of Two Dispersion Strengthened Copper Alloys at Elevated Temperatures," Sandia National Laboratories, Albuquerque, New Mexico, (presented at the 119th Annual Meeting of TMS, Anaheim, Ca, February 18-22,) 1990.

8. N. W. Blossom and D. B. Brimhall, *Advances in Powder Metallurgy*, vol. **2**, Metal Powder Industries Federation, Princeton, N.J., 1990, p. 315.

9. D. G. Morris, M. A. Morris, A. Benghalem and C. Biselli, *Proc. of the 2nd Intern. Conf. on Struct. Applic. of Mech.Alloying,* Vancouver, British Columbia, Canada, Sept. 20-22, 1993, p. 353.

10. M. S. Nagorka, C. G. Levi and G. E. Lucus, *Metall. Trans.*, **26A**, 1995, 8594.

11. D. L. Ellis: "Precipitation Strengthened High Strength, High Conductivity Cu-Cr-Nb Alloys Produced by Chill Block Melt Spinning", PhD Thesis, Case Western Reserve University, Cleveland, Ohio, August 1989. See also NASA CR 185144, NASA Lewis Research Center, Cleveland, Ohio, Sept. 1989.

12. D. L. Ellis, G. M. Michal and N. W. Orth, *Scripta Metall.* **24**, 1990, 885.

13. D. L. Ellis and R. L. Dreshfield, "Preliminary Evaluation of a Powder Metal Copper-8 Cr-4 Nb Alloy" presented at 1992 Conference on Advanced Earth-to-Orbit Propulsion Technology, May 19-21, 1992, Marshall Space Flight Center, AL.

14. D. J. Thoma and J. H. Perepezko, *Mater. Sci. & Eng.*, **A156**, 1992, 97.

15. D. J. Chakrabati and D. E. Laughlin, *Bull. Alloy Phase Diagrams*, **2**, 1982, p. 507 and **5**, 1984, p. 59, 99.

16. M. K. Premkumar, A. Lawley, and M. J. Koczak, *Metall. Trans.*, **23A**, 1992, 3219.

17. D. A. Porter and K. E. Easterling, *Phase Transformations in Metals and Alloys*, Chapman and Hall, London, 1990, pp. 46-47.

18. G. J. Shiflet and J. A. Hawk, *Dispersion Strengthened Aluminum Alloys*, Ed. Y.-W. Kim and W. M. Griffith, The Minerals, Metals & Materials Society, 1988, p. 123.

19. I. M. Lifshitz and V. V. Slyozov, *J. Phys. Chem. Solids*, **19**, 1961, 35.

20. C. Wagner, *Z. Electochem.*, **65**, 1961, 581.

21. S. S. Kang and D. N. Yoon, *Metall. Trans.*, **13A**, 1982, 1405.

22. *Idem. ibid.*, **12A**, 1981, 65.

23. Y. Seno, Y. Tomokiyo, K. Oki, and T. Eguchi, *Trans. Jpn. Inst. Metals*, **24**, 1983, 491.

24. T. Eguchi, Y. Tomokiyo, K. Oki, and Y. Seno, *Mat. Res. Soc. Symp. Proc.*, 1984, 475.

25. R. Watanabe and Y. Masuda, *Modern Devel. Powder. Metall.*, **6**, 1974, 1.

26. R. Watanabe, K. Tada, and Y. Masuda, *Z. Metallkde*, **13**, 1976, 619.

27. J. R. Groza and J. C. Gibeling, *Mater. Sci. & Eng.*, **A171**, 1993, 115.

28. D. B. Butrymowicz, J. R. Manning, and M. E. Read, *Diffusion Rate Data and Mass Transport Phenomena for Copper Systems*, Diffusion in Metals Data Center, Metallurgy Division, Institute for Materials Research, National Bureau of Standards, Washington, D.C., (July 1977).

29. M. A. Morris and D. G. Morris, *Acta. Metall.*, **35**, 1987, 2511.

30. P. W. Taubenblat, V. J. Marina and R. Batra, "High Strength High Conductivity AMZIRC Copper & AMAX-MZC Alloy," *Wire Journal*, Sept. 1979, p.114.

31. M. Appelo and P. Fenici, *Mater. Sci. & Eng.*, **A102**, 1988, 69.

32. M. J. Tenwick and H. A. Davies, "Enhanced Strength of High Conductivity Copper Alloys," *Mater. Sci. & Eng.*, **A98**, 1988, 543.

33. U. F. Kocks, *Phil. Mag.*, **13**, 1966, 541.

34. M. F. Ashby, *Strengthening Methods in Crystals*, Ed. by A. Kelly and R. B. Nicholson, Elsevier, New York, 1971, p. 165.

35. E. O. Hall, *Proc. Phys. Soc.*, **B64**, London, 1951, 747.

36. N. J. Petch, *J. Iron & Steel Inst.*, **174**, 1953, 25.

37. M. Hillert: *Acta Metall.* **13**, 1965, 227.

38. T. Gladman: *Proc. Roy. Soc.*, **A294**, 1966, 298.

39. C. S. Smith (commun. with C. Zener), *Trans. Am. Inst. Min. Eng.*, **175**, 1948, 47.

40. R. A. Serway, C. J. Moses and C. A. Moyer, *Modern Physics*, Saunders College Publishing, New York, 1989, pp. 327-337.

41. D. R. Poirier and G. H. Geiger, *Transport Phenomena in Materials Processing*, The Minerals, Metals & Materials Society, Warrendale, PA, 1994, p. 196, 210.

42. K. Schroder, "Experimental Aspects of Electrical and Thermal Properties of Metals," *High Conductivity Copper and Aluminum Alloys*," Ed. by E. Ling and P.W. Taubenblat, TMS/AIME, Warrendale, PA, 1984, p. 1-17.

43. G. A. Jerman, I. E. Anderson and J. D. Verhoeven, *Metall. Trans.*, **24A**, 1993, 35.

44. D. R. Maurice and T. H. Courtney, *Metall. Trans.*, **21A**, 1990, 289.

45. P. S. Gilman and J. S. Benjamin, *Ann. Rev. Mater. Sci.*, **13**, 1983, 279.

46. J. S. C. Jang and C. C. Koch, *Scripta Metall,* **23**, 1989, 1805.

47. D. G. Morris and M.A. Morris, *Acta Metall.*, **39**, 1991, 1763.

48. D. G. Morris and M.A. Morris, *Mater. Sci. & Eng.*, **A134**, 1991, 1418.

49. P.M. Hazzledine, *Scripta Metall. et Mater.*, **26**, 1992, 57.

50. C. Sauer, T. Weissgaerber, W. Puesche, G. Dehm, J. Mayer and B. Kieback, *Int'l. J. Powd. Metal.,* **33**, 1997, 45.

51. S. E. Broyles, K. R. Anderson, J. R. Groza and J.C. Gibeling, *Metall. Trans.*, **27A**, 1996, 1217.

52. J. Robles, K. R. Anderson, J. R. Groza and J.C. Gibeling, *Metall. Trans.*, **25A**, 1994, 2235

53. D. L. Ellis, R. L. Dreshfield, M. J. Verrilli, and D. G. Ulmer, "Mechanical Properties of a Cu-8 Cr-4 Nb Alloy," for *Advanced Earth-to- Orbit Propulsion Technology Conf.*, NASA Marshall Space Flight Center, Huntsville, Alabama, May 17-19, 1994.

54. T. M. Cook and T. H. Courtney, *Metall. Trans.*, **26A**, 2389, 1995.

55. M. A. Meyers and K. K. Chawla, *Mechanical Behavior of Materials*, Prentice-Hall, New Jersey, 1999, p. 249-250.

56. A. Garg: NASA Lewis Research Center, Private Communication, October 1993.

57. K. R. Anderson, MS Thesis, University of California at Davis, Davis, CA, 1995; also NASA CR 198492, NASA Lewis Research Center, Cleveland, OH, June 1996.

58. K. R. Anderson, J. R. Groza, R. L. Dreshfield and D. L. Ellis, *Mat. Sci. Eng.*, **A169**, 1993, 167.

59. D. L. Ellis, NASA-John Glenn Research Center, Private Communication.

60. ***Smithells Metals Reference Book***, Seventh Edition, E. A. Brandes and G. R. Brook, Eds., Butterworth-Heinemann, Oxford, 1992, p. **22**: 28.

61. D. L. Ellis, NASA-John Glenn Research Center, Unpublished Research, July 1996.

62. A. L. Wingrove, *J. Inst. Met.*, 100, 1972, 313.

63. G. W. Nieman, J. R. Weertman, and R. W. Siegel, *J. Mater. Res.*, **6**, 1991, 1012.

64. C. R. Brooks, *Heat Treatment, Structure and Properties of Nonferrous Alloys*, American Society of Metals, Metals Park, OH, 1990, p. 283.

65. R. R. Solomon, "GlidCop® Copper Dispersion-Strengthened with Aluminum Oxide," Technical Report, SCM Metal Products, Inc., Research Triangle Park, NC, USA, 1994.

66. T. J. Miller, S. J. Zinkle and B. A. Chin, *J. Nucl. Mater.*, **179-181**, 1991, 263.

67. C. Rigollet, J. M. Gentzbittel and G. Robert, *J. de Physique IV*, Colloque C7, supplement to *J. de Physique III*, **3**, 1993, 747.

68. D. L. Ellis, NASA-John Glenn Research Center, Unpublished Results, 1996-1997.

69. K. R. Anderson, J. R. Groza, R. L. Dreshfield and D. L. Ellis, *Metall. Trans.*, **26A**, 1995, 2197.

70. R.E. Taylor, H. Groot and J. Ferrier, "Thermophysical Properties of Copper-Based Material," (A Report to NASA Lewis Research Center), TPRL 1631, Purdue University Research Park, West Lafayette, IN, January 1996.

71. D. L. Ellis and G. M. Michal, "Mechanical and Thermal Properties of Two Cu-Cr-Nb Alloys and NARloy-Z," NASA CR 198529, NASA Lewis Research Center, Cleveland, Ohio, Oct. 1996.

72. ***Smithells Metals Reference Book***, Seventh Edition, E. A. Brandes and G. R. Brook, Eds., Butterworth-Heinemann, Oxford, 1992, pp. **14**: 1-16.

73. ***ASM Metals Handbook***, Vol. 2, 9th Ed., 1979.

74. J. K. Stanley, *Electrical and Magnetic Properties of Metals*, American Society of Metals, Metals Park, Ohio, 1963.

75. G. Ghosh, J. Miyake and M. E. Fine, *JOM*, **49**, 1997, 56.

76. D. R. Poirier and G. H. Geiger, *Transport Phenomena in Materials Processing*, The Minerals, Metals & Materials Society, Warrendale, PA, 1994, p. 615.

77. R. A. Serway, C. J. Moses and C. A. Moyer, *Modern Physics*, Saunders College Publishing, New York, 1989, p. 328.

78. D. G. Ulmer, Personal communication/Unpublished Results.

79. J. Y. Huang, Y. K. Wu and H. Q. Ye, *Mater. Sci. & Eng.*, **A199**, 1995, 165.

80. R. R. Vance and T. H. Courtney, *Scripta Metall,* **26**, 1992, 1435.

81. R. Lerf and D. G. Morris, *Mater. Sci. & Eng.*, **A128**, 1990, 119.

82. *Binary Alloy Phase Diagrams*, T. B. Massalski, Editor-in-Chief, ASM International, Materials Park, OH, 1990, p. 1266 (Cu-Cr), 1440 (Cu-Nb), 837 (C-Cr), 863 (C-Nb).

83. M. Venkatraman and J. P. Neumann, *Bull. Alloy Phase Diag.*, **7**, 1986, 462.

84. JCPDS-International Centre for Diffraction Data, PCPDFWIN, v. 1.30, 1997, # 04-0836 (Cu), 06-0694 (Cr), 35-0789 (Nb), 05-0701 (Cr_2Nb), 12-0603 (ε-Cr_2Nb); 02-1031, 03-0857, 05-0658, 10-0181 (NbC_{1-x}); 14-0407, 35-0783 ($Cr_{23}C_6$).

85. A. Cottrell, *Chemical Bonding in Transition Metal Carbides*, The Institute of Materials, London, 1995, p. 13.

86. I. Barin, *Thermochemical Data of Pure Substances*, VCH Verlagsgesellschaft mbH, Weinhein, 1993, p. 431.

87. D. J. Thoma, F. Chu, P. Peralta, P. G. Kotula, K. C. Chen and T. E. Mitchell, *Mater. Sci. & Eng.*, **A239-240**, 1997, 251.

88. F. Chu, Y. He, D. J. Thoma and T. E. Mitchell, *Scipta Metall.*, **33**, 1995, 1295.

89. R. L. Fleischer, R. S. Gilmore and R. J. Zabala, *Acta Metall.*, **37**, 1989, 2801.

90. *Handbook of High Temperature Compounds: Properties, Production, Applications*, T. Ya. Kosolapova, Ed., Hemisphere Publishing, New York, 1990, pp. 499-500; 529-551.

91. G. E. Vignoul, J. K. Tien and J. M. Sanchez, *Mater. Sci. & Eng.*, **A170**, 1993, 177.

92. M. Takeyama and C. T. Liu, *Mater. Sci. & Eng.*, **A132**, 1991, 61.

93. G. S. Upadhyaya, *Nature and Properties of Refractory Carbides*, Nova Science Publishers, Commack, NY, 1996, p. 420.

94. R. Z. Valiev, N. A. Krasilnikov and N. K. Tsenev, *Mater. Sci. & Eng.*, **A137**, 1991, 35.

95. J. Lian, R. Z. Valiev and B. Boudelet, *Acta Mater.*, **43**, 1995, 4165.

96. R. Z. Valiev, *Mater. Sci. & Eng.*, **A234-236**, 1997, 59.

97. D. Tabor, *The Hardness of Metals*, Oxford University Press, London, 1951.

98. P. G. Sanders, J. A. Eastman and J. R. Weertman, *Acta Metall.*, **45**, 1997, 4019.

99. M. A. Morris and D. G. Morris, *Acta Metall.*, **35**, 1987, 2511.

100. A. Benghalem and D. G. Morris, *Mater. Sci. & Eng.*, **A161**, 1993, 255.

101. G. M. Michal: Case Western Reserve University, Private communication, 1993; G. M. Michal and D. L. Ellis, unpublished research, 1995.

102. J. R. Groza: *Mater. Charact.*, **31**, 1993, 133.

103. K. S. Kumar and C. T. Liu, *Acta Metall. Mater.*, **45**, 1997, 3671.

104. P. Pirouz and P. M. Hazzledine, *Scipta Metall.*, **25**, 1991, 1167.

105. T. Takasugi, K. S. Kumar, C. T. Liu and E. H. Lee, *Mater. Sci. & Eng.*, **A260**, 1999, 108.

106. A. V. Kazantzis, M. Aindow and I. P. Jones, *Mater. Sci. & Eng.*, **A233**, 1997, 44.

107. B. P. Bewlay, *et al.*, *Acta Metall. Mater.*, **42**, 1994, 2869.

108. D. A. Porter and K. E. Easterling, *Phase Transformations in Metals and Alloys*, Chapman and Hall, London, 1990, p. 147.

109. D. A. Porter and K. E. Easterling, *Phase Transformations in Metals and Alloys*, Chapman and Hall, London, 1990, pp. 101-103, 110.

110. J. Huang, M. Meyer, and V. Pontikis, *Phys. Rev. Lett.*, **63**, 1989, 628.

111. R. W. Balluffi and A. V. Granato, *Dislocations in Solids*, Ed. by F. R. N. Nabarro, North-Holland, Amsterdam, 1979, Vol. 4, p. 1.

112. C. S. Jayanth and P. Nash: *J. Mat. Sci.*, **24**, 1989, 3041.

113. F. J. Humphreys, W. S. Miller and M. R. Djazeb, *Mater. Sci. & Tech.*, **6**, 1990, 1157.

114. R. Elst, J. Van Humbeek and L. Delaey, *Acta. Metall.*, **36**, 1988, 1723.

115. N. Hansen, *Metall. Trans.*, **16A**, 1985, 2167.

116. D. P. H. Hasselman and L. F. Johnson, *J. Composite Mater.* **21**, 1987, 508.

117. A. L. Geiger, D. P. H. Hasselman and K. Y. Donaldson, *J. Mater. Sci. Lett.*, **12**, 1993, 420.

118. A. L. Geiger, D. P. H. Hasselman and P. Welch, *Acta mater.*, **45**, 1997, 3911.

119. J. Miyake, G. Ghosh and M. E. Fine, *MRS Bulletin*, **21**, 1996, 13.

120. J. D. Verhoeven, H. L. Downing, L. S. Chumbley and E. D. Gibson, *J. Appl. Phys.*, **65**, 1989, 1293.

121. V. L. Nordheim, *Azul. Phys.*, **5**, 1931, 642.

122. D. D. Pollock, *Electrical Conduction in Solids*, American Society of Metals, Metals Park, OH, 1985, p. 148.

123. J. Miyake and M. E. Fine, *Acta Metall.*, **40**, 1992, 733.

124. M. M. Antonova, L. N. Bashenova and I. I. Timofeeva, "The Production and Some Properties of Carbohydrides of Titanium, Vanadium, and Niobium," *Refractory Carbides,"* Ed. by G. V. Samsonov, Academy of Sciences of the Ukraine, Kiev, Ukraine, 1974, p. 47.

125. M. L. Öveçoglu and W. D. Nix, *Int. J. Powder Metall.*, **22**, 1986, 17.

126. D. R. Maurice and T. H. Courtney, *Metall. Trans.*, **21A**, 1990, 289.

127. W. A. Spitzig, A. R. Pelton and F. C. Laabs, *Acta Metall.* **35**, 1987, 2427.

128. C. L. Trybus and W. A. Spitzig, *Acta Metall.* **37**, 1989, 1971.

129. J. D. Verhoeven, S. C. Chueh and E. D. Gibson, *J. Mater. Sci.*, **24**, 1989, 1748.

130. J. D. Verhoeven, W. A. Spitzig, L. L. Jones, H. L. Downing, C. L. Trybus, E. D. Gibson, L. S. Chumbley, L. G. Fritzemeier and G. D. Schnittgrund, *J. Mater. Eng.*, **12**, 1990, 127.

131. P. Le Brun, E. Gaffet, L. Froyen and L. Delaey, *Scripta Metall.* **26**, 1992, 1743.

132. J. Naser, W. Riehemann and H. Ferkel, *Mater. Sci. & Eng.*, **A234-236**, 1997, 467.

133. J. Lian, R. Z. Valiev and B. Boudelet, *Acta Mater.*, **43**, 1995, 4165.

134. R. Z. Valiev, *Mater. Sci. & Eng.*, **A234-236**, 1997, 59.

135. A. H. Chokshi, A. Rosen, J. Karch and H. Gleiter, *Scripta Metall,* **23**, 1989, 1679.

136. K. Ichikawa and M. Achikita, *Mater. Trans., JIM*, **34**, 1993, 718.

137. C. C. Koch, *Nanostruct. Mater.*, **2**, 109, 1993.

138. J. S. Benjamin and R. D. Schelleng, *Metall. Trans.*, **12A**, 1981, 1827.

139. J. Weismuller, "Nanocrystalline Materials - An Overview," in: *Synthesis and Processing of Nanocrystalline Powder*, D. L. Bourell, ed., TMS, Warrendale, PA, 1996, pp. 3-19.

140. G. W. Nieman, J. R. Weertman and R. W. Siegel, *Nanostr. Mater.*, **1**, 1992, 185.

141. G. R., Shaik and W. W. Milligan, *Metall. Trans.*, **28A**, 1997, 895.

142. H. Hahn, J. Logas and R. S. Averbach, *J. Mater. Res.* **5**, 1990, 609.

143. A. Kats-Demyanets and R. Chaim, *Nanostr. Mater.* **6**, 1995, 851.

144. J. Eckert, J. C. Holzer, C. E. Krill, III and W. L. Johnson, *J. Mater. Res.* **7**, 1992, 1751.

145. M. A. Morris and D. G. Morris, *J. Mater. Sci.*, **26**, 1991, 4687.

146. K. R. Anderson, J. R. Groza and D. G. Ulmer, *Scripta Metall.*, **37**, 1997, 179.

147. A. Boltax, *Trans. Metall. Soc. AIME*, **218**, 1960, 812.

148. W. A. Spitzig, L. S. Chumbley, J. D. Verhoeven, Y. S. Go and H. L. Downing, *J. Mater. Sci.*, **27**, 1992, 2005.

149. A. Manzano-Ramirez, E. Nava-Vazquez and J. Gonzalez-Hernandez, *Metall. Trans.*, **24A**, 1993, 2355.

150. A. L. Gieger, D. P. H. Hasselman and P. Welch, *Acta Metall.*, **45**, 1997, 3911.

151. N. Fuschillo and M. L. Gimpl, *J. Appl. Phys.*, **42**, 1971, 5513.

152. L. S. Chumbley, H. L. Downing, W. A. Spitzig and J. D. Verhoeven, *Mater. Sci. & Eng.*, **A117**, 1989, 59.

153. E. Shapiro and J. Crane, "Optimizing Conductivity, Formabilitly, and Relaxation Resistance of Copper Alloys," *High Conductivity Copper and AluminumAlloys*, Ed. by E. Ling and P. W. Taubenblat, TMS/AIME, Warrendale, PA, 1984, p. 53.

154. S.C. Axtell, B.W. Robertson and R.J. DeAngelis, *Proc. of the 2nd Intern. Conf. on Struct. Appl. of Mech. Alloy.*, Vancouver, B.C., Canada, 1993, 445.

155. B. J. Aikin, NASA-John Glenn Research Center, Unpublished Research, 1997.

VIII. SYMBOLS LIST

A	Particle/Matrix Interfacial Area
a	Lattice Constant
b	Burgers Vector
c	Lattice Constant (z-axis) of e.g., hcp material
$C_{e,\infty}$	Equilibrium Solubility of Solute Atom in the matrix;
C_p	Heat capacity (specific heat) [J/kg-K]
D	Diffusivity of rate controlling solute in the matrix in m^2/s;
D	Average Grain size
d	Crystallite Size, Grain Size, Particle Size
D_o	Diffusion Coefficient of solute in matrix
e	Charge of an electron [1.602×10^{-19} C],
ε_t	True strain
E	Young's Modulus
$f(f_p)$	Volume Fraction of Second-Phase Precipitates/Particles/Dispersoids
f_{vg}	Volume Fraction of Grain Boundary Precipitates/Particles/Dispersoids
G	Shear Modulus
k_B	Boltzmann's constant, 1.3807×10^{-23} J/K
L	Lorentz Number
L_t	Total line length in lineal analysis count
M	Taylor Factor
M	Image Magnification for lineal analysis
m_e	Mass of an electron, 9.11×10^{-31} kg
n_e	Electron density (concentration)
N_L	Number of intercepts in lineal analysis
$\bar{L}_L$	Mean linear intercept length
Q	Activation Energy of Diffusion,
R	Universal Gas Constant, 8.314 J/mol·K; and
r	Particle Radius

$\bar{r}_o$	Average Particle radius at the onset of coarsening;
$\bar{r}_t$	Average Particle radius at time t [s] in m
T, T_m	Absolute Temperature in degrees Kelvin (K)
V_f	Volume Fraction of Second-Phase Precipitates/Particles/Dispersoids
V_m	Molar Volume of Particle
V_p	Volume Fraction of Second-Phase Precipitates/Particles/Dispersoids
K_p	Thermal Conductivity of Dispersoid/Particle
α_d	Thermal diffusivity [m^2/s]
γ/σ	Dispersoid/matrix interfacial energy in J/m^2;
κ_{el}	Thermal Conductivity due to electrons
λ	Mean planar Particle Spacing
λ	X-ray wavelength (usually $Cu_{k\alpha}$)
λ_{el}	Mean free path of electrons (average distance between collisions)
ν	Poisson's Ratio
ρ	Density of Material [kg/m^3], [g/cm^3]
σ	Flow/Yield/Frictional Stress
σ_e	Electrical Conductivity due to electrons
σ_m	Thermal Conductivity of Matrix
σ_p	Thermal Conductivity of Dispersoid/Particle
2θ	Bragg reflection/peak position in XRD
$\bar{V}_F$	Fermi velocity of electrons, i.e. velocity at the Fermi surface

APPENDIX A

Optical Microscopy of As-Extruded Cu-8 Cr-4 Nb and Cu-4 Cr-2 Nb Microstructures

Cu-8 Cr-4 Nb

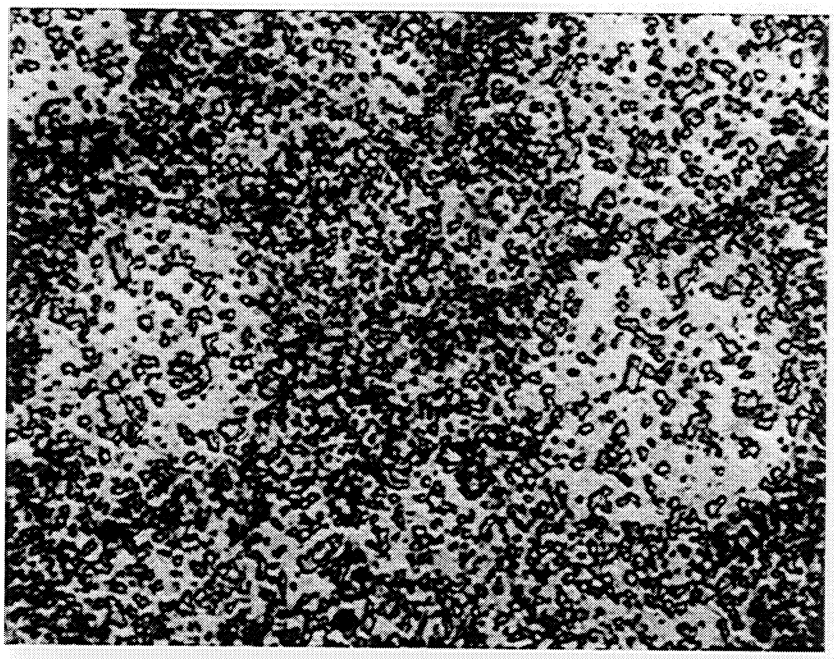

Cu-4 Cr-2 Nb **10 μm**

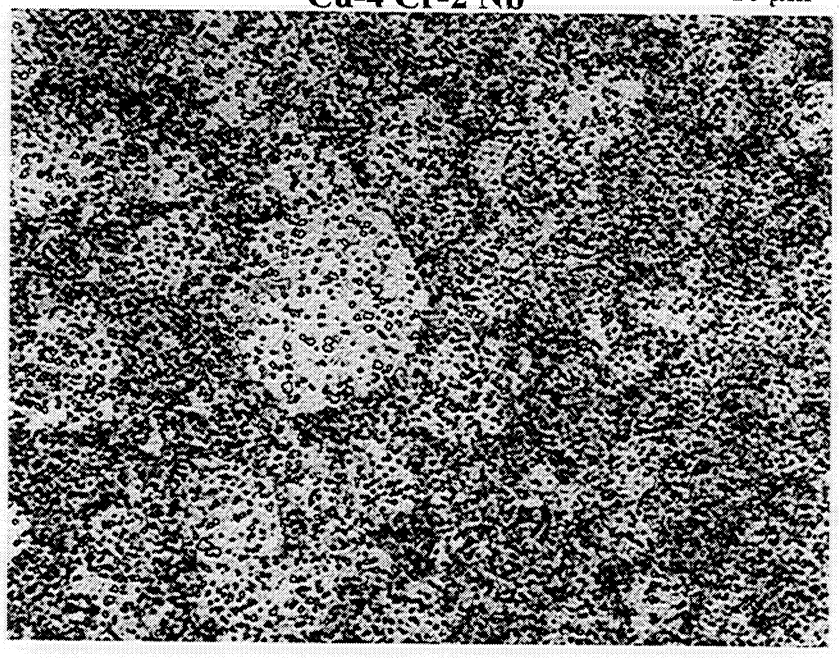

APPENDIX B

Vickers Hardness Vs. Rockwell B for Milled (Hot Pressed) and Non-Milled (Hot Pressed/Extruded) Cu-Cr-Nb Alloys

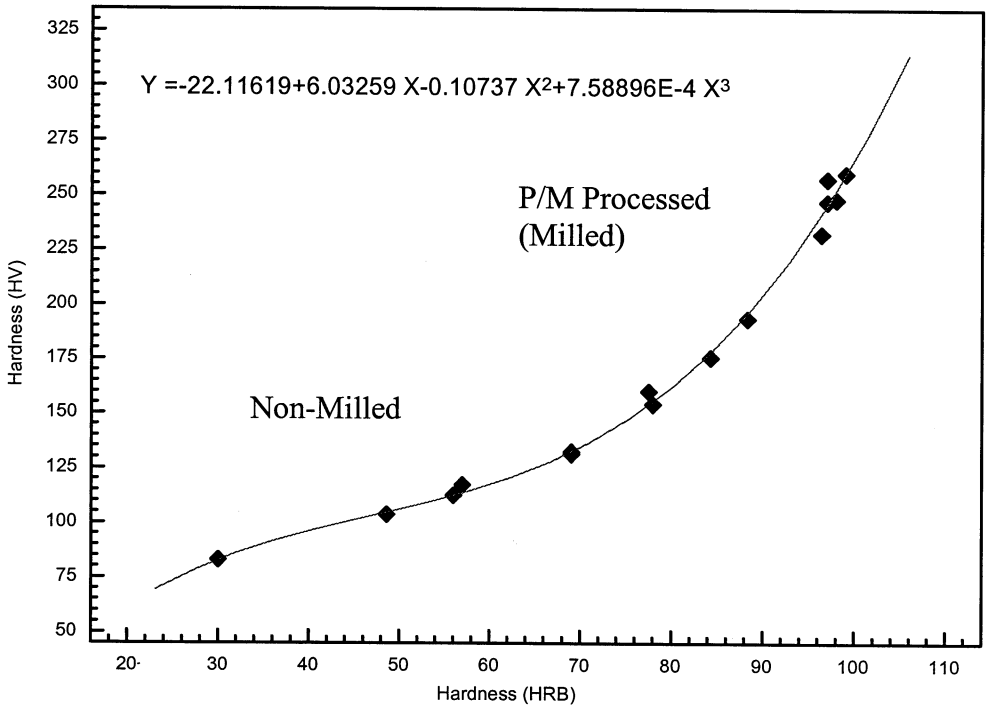

APPENDIX C

Cu-Cr_2Nb Pseudo-Binary Phase Diagram
as Calculated by Michal [101]

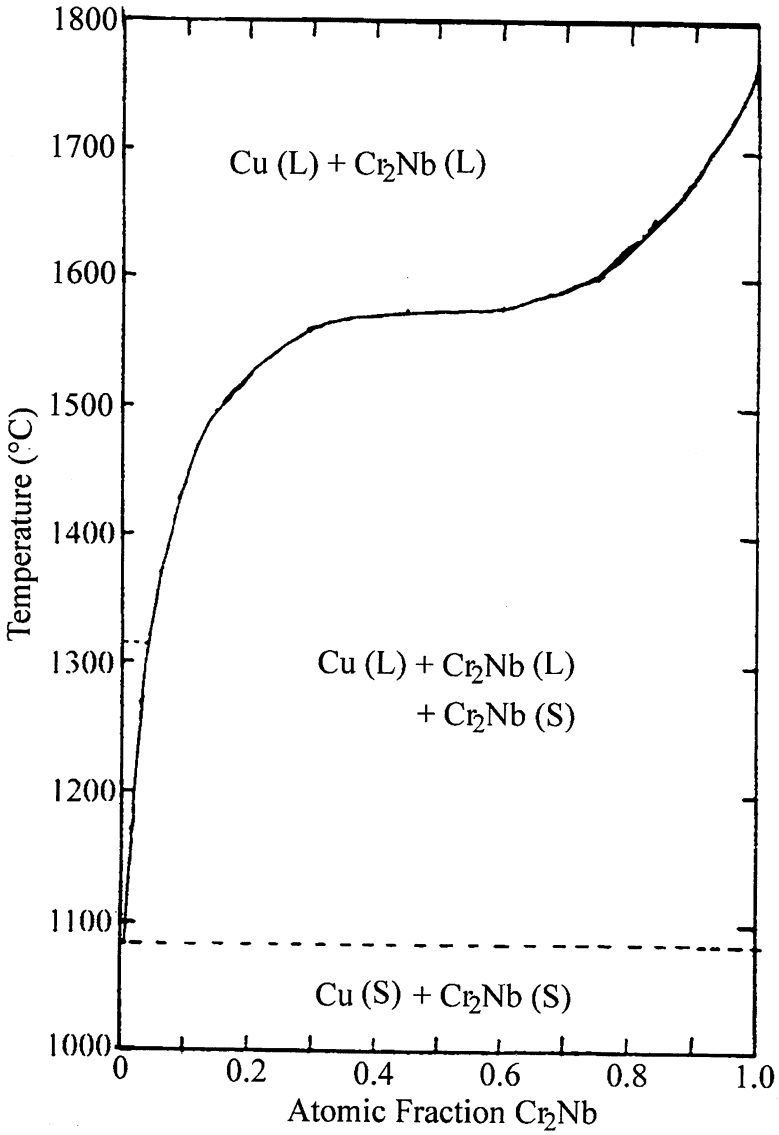

APPENDIX D

Orowan Strengthening (and Hillert-Gladman Grain Size) Calculations for Extruded Cu-8 Cr-4 Nb

$\frac{0.84M}{2\pi(1-\nu)^{0.5}}$	b (nm)	G (GPa)	$\frac{0.84\,MG\,\mathbf{b}}{2\pi(1-\nu)^{0.5}}$	f	r (nm)	λ_p (nm)	$\Delta\sigma$ MPa	d_{calc} (μm)	
0.505	0.256	45.0	5.82	0.022	81.5	795.2	50.6	4.94	
0.505	0.256	45.0	5.82	0.022	53.2	519.1	71.8	3.22	
0.505	0.256	45.0	5.82	0.022	85	829.3	48.9	5.15	
0.505	0.256	45.0	5.82	0.022	78.25	763.5	52.4	4.74	
0.505	0.256	45.0	5.82	0.022	74	722.0	54.8	4.48	
0.505	0.256	45.0	5.82	0.022	65	634.2	61.0	3.94	Secondaries
0.505	0.256	45.0	5.82	0.022	74	722.0	54.8	4.48	
0.505	0.256	45.0	5.82	0.022	68	663.5	58.8	4.12	
0.505	0.256	45.0	5.82	0.022	81	790.3	50.9	4.91	
0.505	0.256	45.0	5.82	0.022	67.75	661.0	59.0	4.11	
0.505	0.256	45.0	5.82	0.110	450	1963.6	22.1	5.45	← Avg. Primary
0.505	0.256	45.0	5.82	0.110	450	1963.6	35.4	5.45	
0.505	0.256	45.0	5.82	0.110	670	2923.5	25.0	8.12	

From using E~120 GPa[1]
ν = 0.343
[1]D. L. Ellis, Private Communication

$$\Delta\sigma = \frac{0.84MG\mathbf{b}}{2\pi(1-\nu)^{0.5}(\lambda-2r)}\ln\frac{r}{\mathbf{b}}$$

$$d_{calc} = \frac{4r}{3f}$$

APPENDIX E

Electron Mean Free Path Calculations for Cu and MM Cu-4 Cr-2 Nb

Material	Mass of Electron m_e	Fermi Velocity v_F (m/s)	Electon Density n_e	Electron Charge e (J)	Electron Conduction σ_e $(\Omega\text{-m})^{-1}$	Electron Mean Free Path λ_{el} (nm)	Resistivity ρ ($\mu\Omega$-cm)	Increase in Resistivity Compared to Cu, $\Delta\rho$
Cu	9.11E-31	1.57E+06	8.49E+28	1.60E-19	5.88E+07	38.6	1.70	0.00
Cu-4Cr-2Nb Milling Time (hr)								
0	9.11E-31	1.57E+06	8.49E+28	1.60E-19	4.86E+07	31.9	2.06	0.36
0.5	9.11E-31	1.57E+06	8.49E+28	1.60E-19	4.65E+07	30.5	2.15	0.45
1	9.11E-31	1.57E+06	8.49E+28	1.60E-19	4.01E+07	26.3	2.50	0.80
2	9.11E-31	1.57E+06	8.49E+28	1.60E-19	3.42E+07	22.4	2.93	1.23
4	9.11E-31	1.57E+06	8.49E+28	1.60E-19	3.27E+07	21.5	3.06	1.36
8	9.11E-31	1.57E+06	8.49E+28	1.60E-19	3.36E+07	22.0	2.98	1.28
4+ Anneal	9.11E-31	1.57E+06	8.49E+28	1.60E-19	4.24E+07	27.8	2.36	0.66

Data from Ref. [40]

$$\lambda_{el} = \frac{m_e \overline{V}_F \sigma_e}{n_e e^2}$$

Based on Eq. (7)

REPORT DOCUMENTATION PAGE

Form Approved
OMB No. 0704-0188

1. AGENCY USE ONLY (*Leave blank*)	2. REPORT DATE	3. REPORT TYPE AND DATES COVERED
	February 2000	Final Contractor Report

4. TITLE AND SUBTITLE

Effects of Thermal and Mechanical Processing on Microstructures and Desired Properties of Particle-Strengthened Cu-Cr-Nb Alloys

5. FUNDING NUMBERS

WU–523–61–13–00

6. AUTHOR(S)

Kenneth Reed Anderson

7. PERFORMING ORGANIZATION NAME(S) AND ADDRESS(ES)

University of California at Davis
Department of Chemical Engineering and Materials Science
Davis, California 95616

8. PERFORMING ORGANIZATION REPORT NUMBER

E–12121

9. SPONSORING/MONITORING AGENCY NAME(S) AND ADDRESS(ES)

National Aeronautics and Space Administration
John H. Glenn Research Center at Lewis Field
Cleveland, Ohio 44135–3191

10. SPONSORING/MONITORING AGENCY REPORT NUMBER

NASA CR—2000-209812

11. SUPPLEMENTARY NOTES

This report was submitted as a dissertation in partial fulfillment of the requirements for the degree Doctor of Philosophy to the University of California at Davis, Davis, California, 1999. Kenneth Reed Anderson, University of California at Davis, Department of Chemical Engineering and Materials Science, Davis, California 95616 (worked funded under the Summer Intern Program at Glenn Research Center). Project Manager, R. Dreshfield (retired), Materials Division, orgranization code 5120, (216) 433–9516. Responsible person, David Ellis, Materials Divsion, orgranization 5120, (216) 433–8736.

12a. DISTRIBUTION/AVAILABILITY STATEMENT

Unclassified - Unlimited
Subject Categories: 26 and 29 Distribution: Nonstandard

This publication is available from the NASA Center for AeroSpace Information, (301) 621–0390.

12b. DISTRIBUTION CODE

13. ABSTRACT ***(Maximum 200 words)***

Ternary Cu-Cr-Nb alloys, particularly Cu-8 Cr-4 Nb (in at.%), have demonstrated good thermal stability as well as high strength and conductivity at elevated temperatures. The initial powder material has a bimodal size distribution of Cr_2Nb precipitates. Primary Cr_2Nb precipitates are ~1 μm, and secondary Cr_2Nb particles are 30-200 nm. The particle coarsening was analyzed and found to follow LSW-type behavior. This study provides a detailed examination of the stability and strengthening effects of Cr_2Nb particles. This investigation also revealed that the primary particles provide direct grain boundary pinning and indirect grain boundary strengthening but virtually no Orowan strengthening. The secondary particles found within grains do provide Orowan strengthening. For extruded material, grain boundary strengthening (Hall-Petch effect) accounts for two-thirds of the strength with Orowan effects contributing the remainder. The proven advantages of Cu-Cr-Nb were the motivation to improve these attributes via microstructural refinement. Mechanical milling (MM) of Cu-4 Cr-2 Nb and Cu-8 Cr-2 Nb produced an increase in hot pressed Vickers hardness of 122% and 96%, respectively. The increase in hardness was more due to Cu grain-size refinement than to Cr_2Nb refinement. This study also demonstrated enhanced stability of MM Cu-4 Cr-2 Nb. Hot pressed 4 h milled Cu-4 Cr-2 Nb experienced only a 22% drop in hardness when annealed at 1273 K for 50 h versus a 30% drop for extruded Cu-8 Cr-4 Nb. The goal of improving the strength and stability of Cu-4 Cr-2 Nb to better than such properties for as-extruded Cu-8 Cr-4 Nb has been met. In addition, a figure-of-merit (FOM) coupling hardness and thermal conductivity was maximized for the case of 4 h milled Cu-4 Cr-2 Nb material. Overall, Cu-Cr-Nb alloys not only possess high strength, conductivity and thermal stability but also can be further developed to improve strength and stability.

14. SUBJECT TERMS

Cu-Cr-Nb alloys; Copper-based alloys; Powder metallurgy; Milling; Microsctruture

15. NUMBER OF PAGES

194

16. PRICE CODE

A09

17. SECURITY CLASSIFICATION OF REPORT	18. SECURITY CLASSIFICATION OF THIS PAGE	19. SECURITY CLASSIFICATION OF ABSTRACT	20. LIMITATION OF ABSTRACT
Unclassified	Unclassified	Unclassified	